The Development and Evaluation of a Compton Camera for Imaging Spent Fuel Rod Assemblies

Thesis submitted in accordance with the requirements of the

University of Liverpool for the degree of Doctor in Philosophy

by

Adam Caffrey

Oliver Lodge Laboratory

September 2019

Abstract

An investigation is presented into the application of a transportable Compton camera, developed at the University of Liverpool, for spent fuel assay. The system consists of three electronically cooled semiconductor detectors in a three tier configuration; two planar orthogonal-strip detectors, Si(Li) and Ge, and a coaxial HPGe detector. Pulse shape analysis (PSA) methods were developed to enhance the intrinsic position resolution of the system, improving the resolution of reconstructed point-source images by 30 % at a 10 cm stand-off distance. Additionally, a technique was created that allowed for gamma-rays which interacted twice in the Ge planar detector to be used in the image reconstruction algorithms. Incorporation of these events increased the system efficiency by 101 % at 662 keV.

A fuel phantom, produced in collaboration with the Defence Academy of the United Kingdom, was used to benchmark the detector's current imaging performance. The phantom comprised 6 Cs-137 and 6 Co-60 planchette sources in a steel housing. Phantom measurements were taken at a stand-off distance of 22.8 cm, before and after being submerged in water. After the application of PSA algorithms and other data processing techniques, the Compton camera was able to identify the isotope and orientation of planchettes placed perpendicular to the detector, but was unable to determine the order of planchettes placed parallel to the system at different stand-off distances.

To aid interpretation of experimental results, a GEANT4 simulation of the Compton camera was produced and its response validated against experimental data. Simulated phantom data highlighted the impact that position resolution has on the quality of reconstructed images. The results indicated that future planned-improvements should yield images with the quality required for spent fuel assay.

Contents

Chapter 1

Introduction

In 1968, the nuclear non-proliferation treaty (NPT) was established [1]. This agreement coordinated efforts to mitigate the threat of nuclear war and contains three binding commitments:

1. a move towards complete disarmament of current nuclear arsenals

2. cooperation in the development of nuclear energy for peaceful means

3. to prevent the spread of nuclear weapons and weapons technology

Stopping the transfer of nuclear material from fuel arrays for use in weapon production is an important staple of the treaty. A system of safeguards are implemented, under the scrutiny of the international atomic energy association (IAES), to ensure adherence to this goal [2]. To this effect, systems have been designed to detect the absence of some, or all, material from fuel modules. Gamma-ray spectroscopy for the non-destructive analysis of nuclear fuel is an effective, established technique. This thesis reviews the performance of the Gamma Ray Imaging system (GRI+), a three-tier Compton camera system designed for gamma-ray spectroscopy and imaging.

1.1 Thesis Outline and Accomplishments

This thesis reviews work undertaken to improve the image quality of GRI+, a Compton camera developed at the University of Liverpool. It describes in detail the improvements made and analysis performed on the system's abilities, and aims to document a logical narrative from the basic concepts of gamma-ray interactions to the acquisition of experimental data. The content of each chapter is summarised below:

Chapter 2: An overview of the fundamental physics pertinent to the thesis. This chapter discusses concepts related to gamma-ray interactions, semiconductor detectors and an overview of Compton camera workings.

Chapter 3: Properties of the GRI+ Compton camera are described. This includes the material composition, system geometry and various performance aspects. The novelty of the system's design is highlighted along with an overview of the data acquisition hardware.

Chapter 4: This chapter focusses on the stage between data acquisition and the retrieval of information for image reconstruction. The techniques created to manipulate preamplifier signals are described and their benefits qualified. Additionally, the implementation of pulse shape analysis (PSA) techniques to improve the resolution of reconstructed images is examined.

Chapter 5: This chapter describes the optimisation of the maximum likelihood expectation maximisation (MLEM) and ordered subset expectation maximisation (OSEM) image reconstruction codes, and the development of a new stochastic origin ensemble (SOE) code. Comparisons between the performance of image reconstruction algorithms are established and the best candidate for the reconstruction of spent fuel is justified. This chapter also quantifies the image resolution improvements from PSA and highlights additional considerations when producing Compton images.

Chapter 6: Experimental data of a fuel rod phantom are discussed. This chapter reviews the datasets acquired and information which can be gained from the corresponding reconstructions.

Chapter 7: Reconstructed simulated data for a fuel rod phantom are discussed. A simulated model of the Compton camera was formed and validated. Experimental data runs were replicated and the simulated performance of the system with improved position resolution was analysed.

Chapter 8: A final assessment of the device is made based on all of the information acquired. Future work is discussed which could improve the viability of the system for deployment in nuclear safeguarding.

The main objective of the research detailed in this thesis was to analyse and improve the current performance of GRI+. The main accomplishments made during the course of this investigation were:

- Pulse Shape Analysis (PSA) algorithms were developed to improve the precision to which gamma-ray interactions could be localised in the absorber detector. Preamplifier pulse data was obtained at each millimetre depth of the detector and was analysed to determine the relationship between pulse shape and interaction location. A method to compare and estimate the interaction depth of gamma rays from the shape of experimental preamplifier pulses was then created. Using a combination of this and a previously established technique to determine lateral interaction positions, a 30 % improvement in image resolution for a Cs-137 point source 10 cm from the detector was achieved.

- An SOE image reconstruction algorithm was developed. The code performed better than current methods when reconstructing point sources and a framework was developed to further improve the performance when multiple different isotopes are present.

- A method was developed to use utilise gamma rays that interacted twice in the absorber detector as input to the image reconstruction algorithms. By applying knowledge of the Compton scattering mechanism and evaluating the output image resolution for a sequence of thresholds placed on the energy depositions, an efficiency increase of 101 % was achieved at 662 keV. Only

a slight degradation in image quality was found when compared to a single-interaction-event reconstruction.

- A GEANT4 simulation was created which replicated the GRI+ system and experimental fuel phantom. Validation was performed by comparing the resolution of reconstructed data at various stand-off distances. The simulated results highlighted the importance of detector position resolution when imaging spent fuel.

Chapter 2

Fundamentals of Compton Imaging

Compton cameras rely on the interaction and detection of gamma rays, which are a form of ionising radiation. They are detectable through their interactions with the electrons of a material in which they deposit some or all of their energy. This chapter discusses the fundamental physics of the processes and materials used to detect gamma rays, and how manipulation of these principles are applied to a Compton camera.

2.1 Interaction of Gamma Rays with Matter

There are three main gamma-ray interaction mechanisms within the energy range used in this project (up to 1.5 MeV): photoelectric absorption, Compton scattering and pair production. For each of the three interaction types, the cross-sections are known to vary with the energy of the incident radiation and atomic number of the target material. Figure 2.1 shows this relationship and highlights the relative cross-sections for the detector materials used in this thesis, silicon and germanium. Understanding the relative contributions of these interactions is fundamental to the design and operation of a Compton camera. The linear attenuation coefficient is the probability of an interaction taking place per unit distance and is calculated from the cross section (υ).

$$\mu = N\upsilon = \left(\frac{N_a \rho}{A} \right) \upsilon \tag{2.1}$$

μ –   linear attenuation coefficient

N –   density of atoms

N_a –   Avogadro's number

ρ –   material density

A –   atomic weight
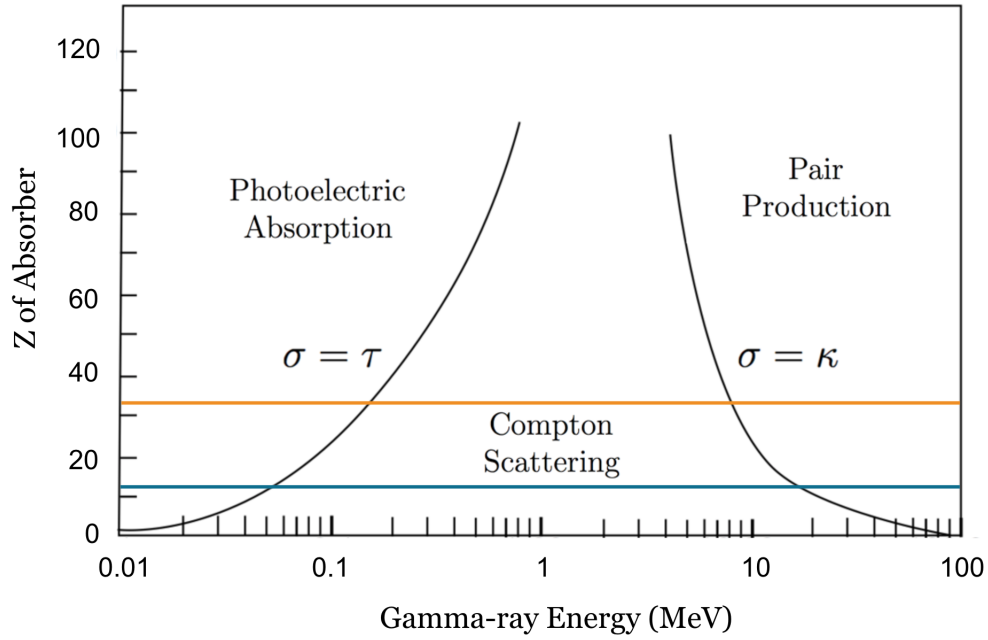
Figure 2.1: Relative cross-sections as a function of the atomic number of the attenuating material and the energy of the incident gamma-radiation, reproduced from [3]. Germanium (orange line) has an atomic number of 32. Silicon (blue line) has the atomic number 14.

For a collimated beam of gamma rays, the probability of any interaction occurring per a unit of distance is given by the total linear attenuation coefficient:

$$\mu = \tau + \sigma + \chi \tag{2.2}$$

τ –   photoelectric absorption linear attenuation coefficient

σ –   Compton scattering linear attenuation coefficient

χ –   pair production linear attenuation coefficient

This coefficient can be used to calculate the outgoing intensity (I) of a collimated beam of gamma rays travelling through a material (of thickness x) with a known incident intensity

(I_0), using equation 2.3. This relationship indicates the importance of detector thickness in Compton Camera design, a thicker detector is more likely to completely absorb the energy of an incident gamma ray.

$$I = I_0 e^{-\mu x} \tag{2.3}$$

2.1.1 Photoelectric Absorption

Photoelectric absorption is the complete absorption of an incident gamma ray in the vicinity of an atom. This causes an excitement resulting in the emission of a photoelectron. In order to conserve momentum and energy, this mechanism can only occur with a bound electron (usually K-shell) as the heavy atom acts to acquire the excess momentum whilst itself gaining little energy due to its large mass. The expression below gives the energy of the released photoelectron:

$$E_e = E_\gamma - E_b \tag{2.4}$$

E_e –   photoelectron kinetic energy

E_γ –   incident gamma-ray energy

E_b –   binding energy of the electron

The vacancy left by the electron, if it was not situated in the outermost shell, could be filled by a higher energy electron. This results in the release of a characteristic X-ray, which would likely be absorbed close to the photoelectric absorption site. Alternatively, excess energy could be transferred to another bound electron causing the liberation of an Auger electron. The photoelectric cross-section (v_{pa}), has been shown experimentally to depend strongly on the atomic number (Z) of the material and energy of the incident photon (E_γ) [4], as in equation 2.5 and in Figure 2.1. Photoelectric absorption is the dominant cause of gamma-ray attenuation at low energies and in high Z materials, (< 200 keV in germanium and < 60 keV in silicon).

$$v_{pa} \propto \frac{Z^5}{E_\gamma^{3.5}} \tag{2.5}$$

2.1.2 Compton Scattering

Compton scattering is the dominant energy loss mechanism of gamma rays in the energy range ~ 200 keV to ~ 8 MeV for germanium and ~ 60 keV to ~ 20 MeV for silicon. It is therefore dominant in the energy range of this study (up to 1.5 MeV) and an important process in the operation of a Compton camera. It is the inelastic scattering of an almost-free electron by a photon resulting in a decrease in the photon energy. The electron is assumed to be initially at rest and the direction of the gamma ray is subsequently altered. A schematic illustration of this process is shown in Figure 2.2.
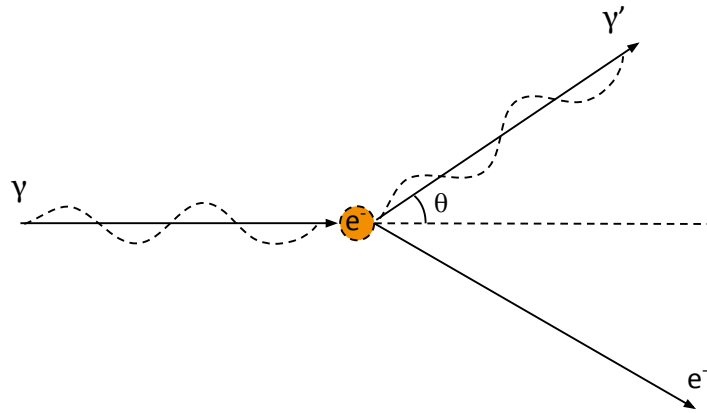

Figure 2.2: Illustration of Compton scattering.

Assuming the electron is initially at rest, conservation of energy and momentum yields the formula:

$$E'_\gamma = \frac{E_\gamma}{1 + \left(\frac{E_\gamma}{m_e c^2}\right)(1 - \cos\theta)} \tag{2.6}$$

E'_γ — outgoing gamma-ray energy

E_γ — incident gamma-ray energy

m_e — mass of an electron

c — speed of light

The fraction of the photon energy carried away by the electron depends upon the angle of scattering. This results in a feature in the gamma-ray spectrum known as the Compton continuum. Equation 2.6 shows a maximum outgoing photon energy equal to E_γ when no scattering takes place and a minimum outgoing energy of $E_\gamma / \left(1 + 2 \left(E_\gamma / m_e c^2 \right) \right)$ for a backscattered event at an angle of $180°$. Figure 2.3 shows the energy share between the scattered gamma ray and electron as a function of angle for an incident 662 keV photon that has undergone Compton scattering.
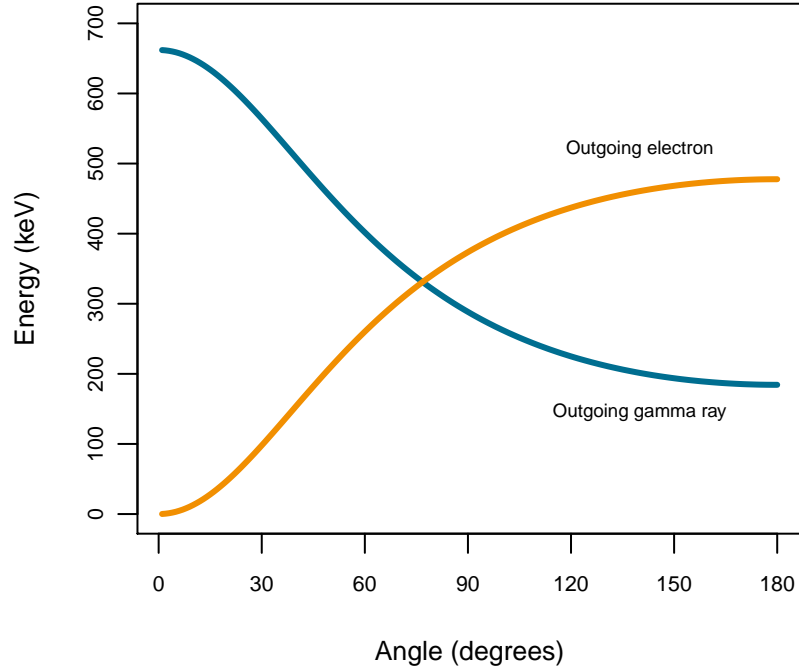

Figure 2.3: Energy of a gamma ray and electron following Compton Scattering as a function of scattering angle. The incident gamma ray has an energy of 662 keV.

The probability of a photon incident at an angle of θ scattering into the solid angle $d\Omega$ is given by equation 2.7, the Klein-Nishina formula. This is determined through a quantum mechanical calculation which gives the differential cross section [5]:

$$\frac{d\sigma}{d\Omega} = \alpha^2 r_c{}^2 P\left(E_\gamma, \theta\right)^2 \left[P\left(E_\gamma, \theta\right) + P\left(E_\gamma, \theta\right)^{-1} - \sin^2\left(\theta\right) \right] / 2 \qquad (2.7)$$

α — fine structure constant

r_c — reduced Compton wavelength of the electron, equal to $\hbar / m_e c^2$

$P\left(E_\gamma, \theta\right)$ — incident photon energy divided by final photon energy E_γ / E'_γ

Figure 2.4 shows the calculated scattering distributions for a select range of gamma-ray energies. As the energy of the incident gamma rays is increased, the probability of an interaction occurring per atom of the absorbing material gradually decreases and the likelihood of backscattering is reduced [4]. This effect is important for Compton Camera design as it indicates that forward scattering at shallow angles is dominant at the energies we are interested in detecting.
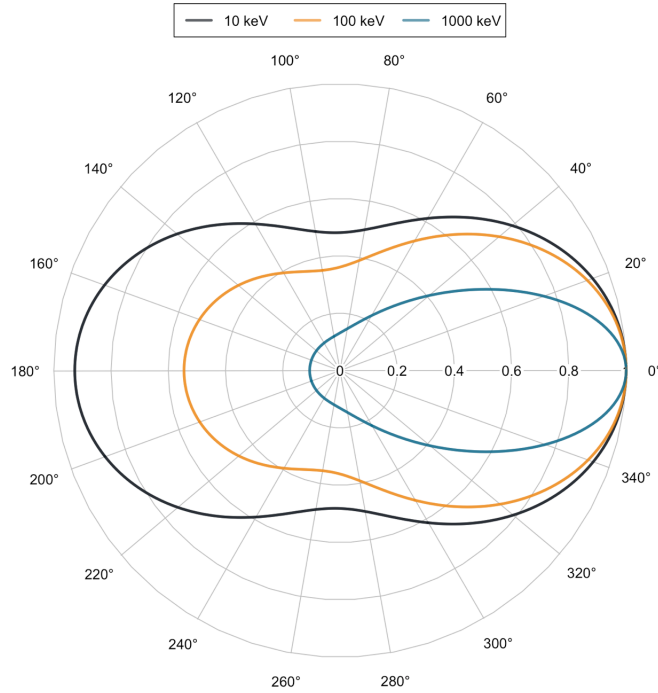

Figure 2.4: Scattering distributions for incident gamma rays of 10, 100 and 1000 keV calculated using the Klein-Nishina formula.

2.1.3   Pair Production

In the coulomb field of a massive nucleus a photon may disappear and in its place create an electron-positron pair. This pair production process dominates at photon energies greater than ~ 20 MeV in silicon and ~ 8 MeV in germanium. A heavy nucleus must be available to conserve momentum, and energy is conserved according to:

$$E_\gamma - 2mc^2 = T_{e^-} + T_{e^+} \tag{2.8}$$

E_γ — energy of the incident photon

mc^2 — rest energy of an electron or positron

T_{e^-} — kinetic energy of an electron

T_{e^+} — kinetic energy of a positron

There is a lower limit on energy for this process to occur, that being the energy required to produce an electron-positron pair, $2mc^2$. The positron will undergo annihilation with an electron a short distance after creation, producing a pair of 511 keV photons emitted at 180° from each other. These photons can then be attenuated in the material through the Compton scattering and photoelectric absorption processes.

2.2 Semiconductor Detector Principles

Solid state gamma-ray detectors come in one of two forms, semiconductors and scintillators. The higher density of these detectors compared to gas-based systems allows for the detection of gamma rays that would otherwise pass through a medium with few interactions. Scintillators are typically denser and can be made into larger bodies resulting in higher efficiencies relative to semiconductors, whilst the latter benefit from much smaller ionisation energies. More charge carriers are therefore produced per ionising interaction and the energy resolution of semiconductor detectors outperforms that of scintillators. GRI+ is made of three semiconductor detectors consisting of silicon and germanium. Semiconductors were selected for this project in order to distinguish between the photon energies emitted from nuclear fuel and because accurate measurement of energy is essential to the operation of a Compton camera.

2.2.1 Semiconductor Principles

Silicon and germanium are crystalline materials. The periodic arrangement of ions in crystals results in the formation of bands of allowed energy states for electrons. Forbidden regions exist between these bands, such that an electron must overcome the energy barrier in order to move between the two states. The size of this energy gap characterises a material into one of three categories; a conductor, semiconductor or an insulator, as illustrated in Figure 2.5.
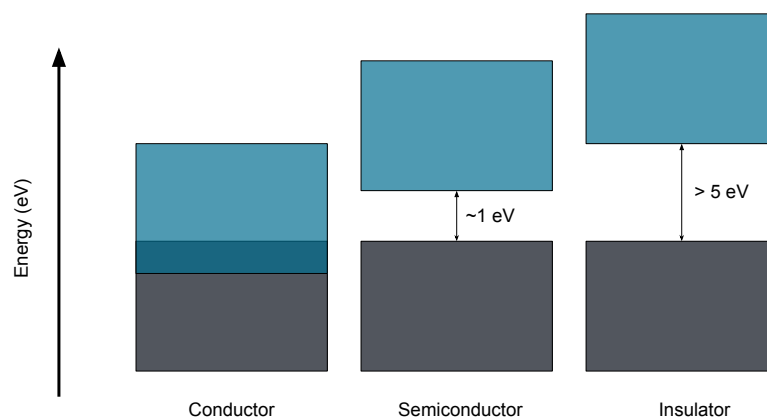
Figure 2.5: Illustration of band gaps in materials.

In a conductor these energy bands are overlapping, allowing for the easy flow of electrons. In an insulator this energy gap is too large to be overcome (> 5 eV) and so conduction does not occur. A semiconductor is a more interesting case because charge flow is possible under certain conditions. For the semiconductors relevant to this thesis, the energy gap falls around 1 eV (Si = 1.14 eV, Ge = 0.67 eV at T = 273 K). The lower of the two bands is known as the valence band. Electronic conduction occurs if an electron overcomes the energy gap and enters the higher energy band, which is known as the conduction band. When an electron is excited from the valence band to the conduction band there is an absence of charge in its wake. Relative to the remaining electrons, this absence is positively charged due to the reduced screening of the protons in the crystal. This is known as a hole and it acts as a positively charged carrier in the system. These charge carriers will drift to opposite sides of the semiconductor when an electric field is applied.

2.2.2   Semiconductor Doping

The band structure of semiconductors can be altered through a process called doping. If a semiconductor is made of a single, pure material it is known as intrinsic. In this case the number of electrons in the conduction band should be equal to the number of holes in the valence band. The purposeful, or accidental, addition of impurity atoms results in an extrinsic semiconductor. This is either described as p-type or n-type depending on

the dominant charge carrier in the system. To obtain a p-type semiconductor one adds acceptor atoms, which contain fewer than the required bonding electrons for a crystal lattice site. Placement of these atoms results in charge vacancies, known as holes, where once a covalent bond existed. This sets up a band of allowed carrier energies near the bottom of the forbidden region, above the valence band. An n-type semiconductor is created when one adds donor atoms with greater than the required number of electrons for a crystalline site. In this case additional electrons which are not part of a covalent bond lie on an energy band at the top of the forbidden region, just below the conduction band.

2.2.3   Semiconductor Detectors

Silicon and germanium radiation detectors are produced by combining a p-type and n-type semiconductor in thermal equilibrium to make a P-N junction. Under this condition, the difference in carrier concentrations causes the mass diffusion of free charge carriers across the junction. Recombination occurs leaving only the static charges in the crystalline lattice which set up their own internal electric field, halting further charge migration. The volume of material in which this happens is known as the depletion region. A schematic of this process is shown in Figure 2.6.
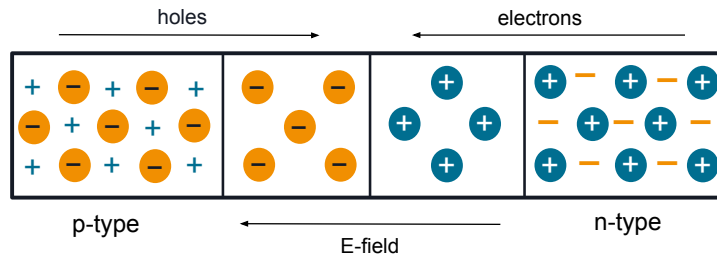

Figure 2.6: Basic illustration of a semiconductor P-N junction.

Under application of a bias (V_{app}) this internal field (V_{bi}) is further increased to obtain a larger depletion region width (W). The total depletion width is given by:

$$W = \sqrt{\frac{2\epsilon \left(V_{bi} - V_{app}\right)}{q} \left[\frac{1}{N_a} + \frac{1}{N_d}\right]} \approx \sqrt{\frac{2\epsilon V}{qN}} \tag{2.9}$$

ϵ $-$ dielectric constant

q $-$ charge of an electron

N_d $-$ donor concentration on the n-side

N_a $-$ acceptor concentration on the p-side

N $-$ dopant concentration on the least doped side

Electrons produced in this region shall be swept by the electric field producing a current. The bias of this field is chosen to encourage saturation of the carriers mobility without being so high as to cause a breakdown, and run-away current behaviour. The drift and collection of these charges due to the electric field is the basic principle that results in signal generation. Assuming the radiation is completely absorbed in the semiconductor material, the amount of liberated charge carriers is directly proportional to the incident energy of the radiation. Figure 2.7 displays a simple illustration of a P-N junction with liberated charges drifting to opposite contacts.
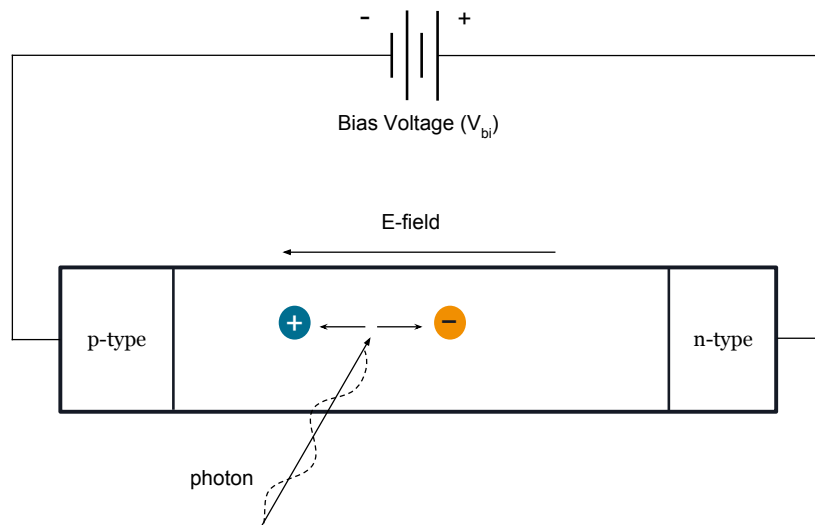

Figure 2.7: Illustration of a P-N junction performing as a radiation detector. Under irradiation, charge carriers are liberated and drift to opposite electrical contacts producing a detectable current.

Poisson statistics do not explain the statistical fluctuation in the number of charge carriers produced under irradiation (σ). Interactions along the path of the moving particles are not independent and so a correction factor is required to explain the variance:

$$F = \frac{\sigma}{N} \tag{2.10}$$

Where F is the Fano factor used to describe the statistical variance and N is the number of produced charged carriers according to Poisson statistics.

2.2.4 Signal Creation

It is important to understand signal generation in semiconductor detectors as properties of the signals are exploited to obtain information regarding the energy deposition and location of gamma-ray interactions. The electrons and holes produced in the detector medium induce a charge distribution on the surface of the surrounding detector contacts. As they drift under the influence of the electric field, the charge distribution on each contact electrode shall change. These changing charge distributions produce a measurable current. A total integration of the induced charge on the electrodes reveals the amount of charge liberated in the detector, which is proportional to the incident gamma-ray energy.
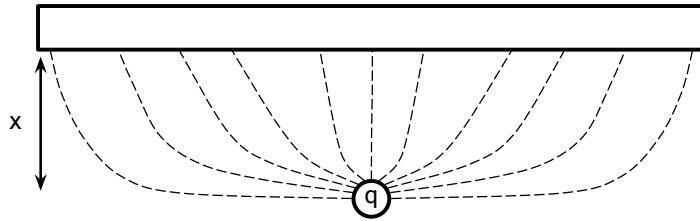

Figure 2.8: A schematic illustration of an external charge, q, at a distance, x, induces a charge distribution on an electrode.

The induced charge (Q) on the contacts due to electrostatic coupling between the contact and external charge (q) can be calculated using Gauss' law:

$$\oint \epsilon E.dS = Q \tag{2.11}$$

ϵ $-$ dielectric constant of the medium

E $-$ electric field

dS $-$ element of Gaussian surface surrounding the electrode

In order to determine the time-dependent signal produced by the detector it is required for this calculation to be evaluated at each unique position on the charge's path. Determination of the electric field at each instantaneous position is a complicated and tedious task alleviated through the application of the Shockley-Ramo theorem [6, 7].

Originally used to understand the induced charge on an electrode in a vacuum tube, the Shockley-Ramo Theorem states that the instantaneous current (i(t)) induced on a contact due to a moving external charge is given by:

$$i(t) = -qvE_0(x) \tag{2.12}$$

v –   instantaneous velocity of the external charge, q

E_0 –   weighting field

The total induced charge (Q) on an electrode from an external charge moving between locations is given by:

$$Q = -q\left[\phi_0\left(x_f\right) - \phi_0\left(x_i\right)\right] \tag{2.13}$$

ϕ_0 –   weighting potential

The weighting potential and weighting field are only a function of the external charges location and describe the electric potential and field at the location of the charge as a function of position. These equations hold true under the following assumptions:

1. There are no other sources of charge.

2. The electrode of interest set to unit potential.

3. All remaining electrodes have zero potential.

Furthermore, as the drift velocity of the moving charges are low compared to the speed of light in the materials, there are no magnetic field effects.

2.2.5   Preamplifier

The charge liberated in gamma-ray interactions to the silicon and germanium detectors is not substantial enough to be precisely measured. A preamplifier acts to increase the magnitude of the signal whilst maintaining low electrical noise. This is achieved by employing

a charge-sensitive preamplifier with an FET (field effect transistor) input stage, cooled to reduce thermal noise. A schematic of DC and AC coupled charge-sensitive preamplifiers is shown in Figure 2.9.

The collected charge is passed through a feedback loop where it is integrated over C_f and discharged over R_f. The time constant of the preamplifier ($\tau = C_f R_f$) is larger than the charge collection time to ensure the output voltage V_o is proportional to the deposited energy. To reduce capacitive loading in the system, the preamplifier is placed as close as possible to the detector. This reduces the input capacitance caused by cabling, ground loops, microphonics and radio-frequency pickup [8]. It is important that the preamplifier to has a large bandwidth to allow both low and high frequency components to pass, as the shape of pulses can be used in later analysis.
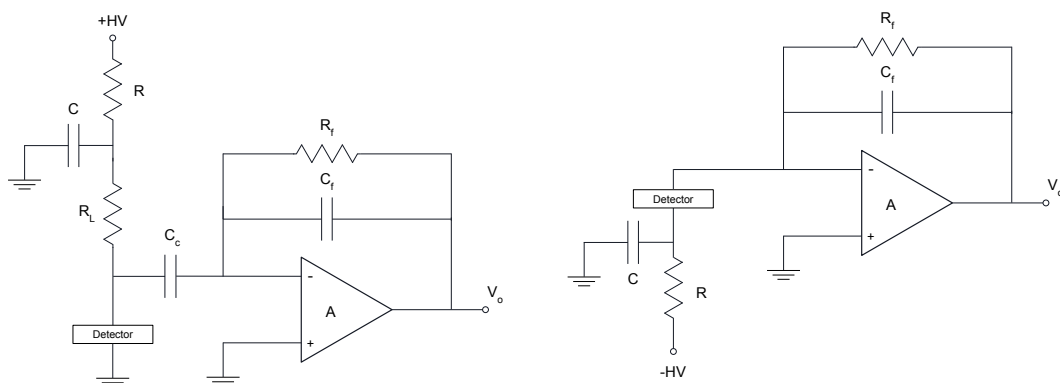

Figure 2.9: Circuit diagram of an AC [left] and DC [right] coupled charge sensitive preamplifier, reproduced from [9].

The preamplifier can either be AC or DC coupled to the detector. For an AC coupled preamplifier, the high voltage is applied through a load resister (R_L). The load resistance is chosen to be large enough to reduce noise in the system, but small enough as to not cause a voltage drop across the detector. Any leakage current from the detector is blocked from the preamplifier by a coupling capacitor (C_c). For detectors with little leakage current ($< 10^{-14}$ A), DC coupling can be implemented. In this case the preamplifier is directly connected to the detector. The main advantage of using a DC coupled preamplifier is that the load resister is removed which is a source of noise in the system [9]. Furthermore, the lack of a coupling capacitor can lead to better performance at high count rates. In both cases an RC filter is normally applied after the HV supply to reduce any noise.

17

2.2.6 Detector Efficiency

The performance of a semiconductor detector for gamma-ray spectroscopy is measured by its efficiency, peak-to-total and energy resolution. A higher counting efficiency for a gamma-ray detector results in reduced data acquisition times to collect sufficient statistics for spectroscopy. There are three forms of counting efficiencies; intrinsic, absolute and relative [4]. Absolute efficiency (ϵ_{abs}) is defined as the number of pulses recorded by the detector ($N_{recorded}$) per number of radiation quanta emitted by the source ($N_{emitted}$).

$$\epsilon_{abs} = \frac{N_{recorded}}{N_{emitted}} \tag{2.14}$$

The intrinsic efficiency (ϵ_{int}) is the number of pulses recorded by the detector per radiation quanta incident on the detector ($N_{incident}$).

$$\epsilon_{int} = \frac{N_{recorded}}{N_{incident}} \tag{2.15}$$

If the source is isotropic, the difference between the two is a geometric factor indicating the solid angle (Ω) from the source to the detector:

$$\epsilon_{int} = \epsilon_{abs} \frac{4\pi}{\Omega} \tag{2.16}$$

The relative efficiency (ϵ_{rel}) is an industry standard measurement which allows for the performance of detectors to be compared. It is calculated using a Co-60 point source, 25 cm from the centre of a detector's entrance window. The absolute efficiency of the 1332.5 keV photopeak is measured and divided by the same measurement made from a $3'' \times 3''$ Na(Tl) scintillation detector, under the same conditions.

2.2.7 Energy Resolution

The precision to which a semiconductor detector can measure deposited energy (charge) is known as the energy resolution. Generally this is defined as the FWHM of a photo-peak, if the distribution is Gaussian. The overall energy resolution (ΔE) is composed of three terms added in quadrature:

$$(\Delta E)^2 = (\Delta E_D)^2 + (\Delta E_X)^2 + (\Delta E_E)^2 \tag{2.17}$$

ΔE_D represents the fluctuation in the number of charge carriers created when a quanta of radiation interacts in the detector. This is based on the Fano factor previously mentioned in section 2.2.3:

$$\Delta E_D = 2.35\sqrt{\frac{F}{N}} \tag{2.18}$$

F –   Fano factor

N –   average number of charge carriers produced in an event

ΔE_D is a fundamental limit on the energy resolution of a semiconductor as, even with all other contributions minimised, the statistical fluctuation in the number of charge carriers is an intrinsic property of the selected material. Broadening due to incomplete charge collection and leakage current is represented by ΔE_X. ΔE_E accounts for any noise from electrical components in the post-detector signal processing chain.

2.3   Basic Principles of Compton Camera Systems

A Compton camera is used to determine the trajectory of incident gamma rays, in order to locate radioactive materials. The concept has its roots in astrophysics [10] where imaging high energy gamma rays with a high resolution and low background was required. The first lab-based system was developed for medical physics to act as an improved SPECT (Single Photon Emission Computed Tomography) system [11, 12]. Since this time it has found further use in nuclear decommissioning [13] and homeland security [14]. Unlike mechanically collimated imaging systems, the Compton camera is able to produce a three dimensional representation of a source from a stationary position. The absence of a collimator also provides an increased field of view and ensures a much greater fraction of incident gamma rays are detected by the device.

A typical Compton camera consists of two tiers, a front scattering detector and a rear absorber detector, as shown in figure 2.10. Each are sensitive to the energy deposited from an incident gamma ray and also the location of interaction. Ideally, events Compton scatter once in the first tier and then undergo photoelectric absorption in the rear tier. Events which undergo further interactions have additional uncertainties, use of these events are discussed in section 5.2.5. If a gamma ray Compton scatters once in the front detector, and

then undergoes photoelectric absorption in the rear detector, the total energy deposited by the gamma ray in the system is therefore:

$$E_0 = E_1 + E_2 \tag{2.19}$$

E_1 –   energy deposited during Compton scattering in the front tier

E_2 –   energy deposited during photoelectric absorption in the rear tier

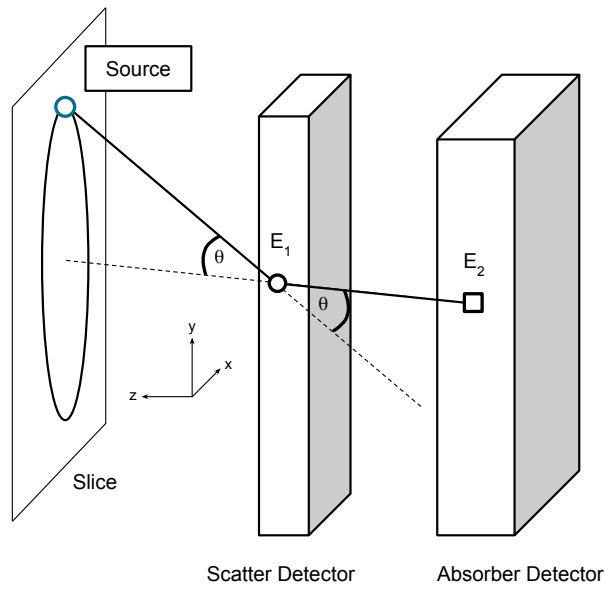E_0 –   total energy deposited in the Compton camera

Figure 2.10: Basic illustration of a Compton camera consisting of two tiers. The incident scattering angle is used to determine the location of the source. The projection of Compton cones onto an image slice determines the location of a source.

The total energy deposited in the system is displayed in an energy spectrum, known as the addback spectrum. If a gamma ray deposits all its energy within the Compton camera, this will be recorded in an addback spectrum photopeak, E_0. A gate is placed over photopeaks and events that fall into these limits are used in the image reconstruction. The vector which defines the cone's asymmetry axis is developed from the two of interaction locations, shown as the line between E_1 and E_2 in Figure 2.10. The precision to which an interaction can be localised is dependent on the segmentation of the detectors, this is discussed in chapter 3. The angle between the incident and scattered gamma ray can be calculated using the rearranged Compton scattering formula [15].

$$\theta = 1 + m_0 c^2 \left[\frac{1}{E_0} - \frac{1}{E_2} \right] \qquad (2.20)$$

θ —   angle between the incident and scattered gamma ray

$m_0 c^2$ —   rest mass of an electron

However, the direction of the Compton scattered electron is unknown, meaning the incident scattering angle limits the location of a radioactive source to a position on the surface of a cone. If the source is at a known distance from the camera then these cones are projected onto this distance slice, perpendicular to the face of the detector. These form a series of ellipses on the surface of the slice which overlap to indicate the position of the source. An example of this is shown in Figure 2.11 for 5, 50, 500 and 5000 overlapping cones. Figure 2.12 shows the profiles for the rows containing the greatest overlap values from Figure 2.11. It can be seen that a better representation of a source is obtained when more cones are used to produce the final image.
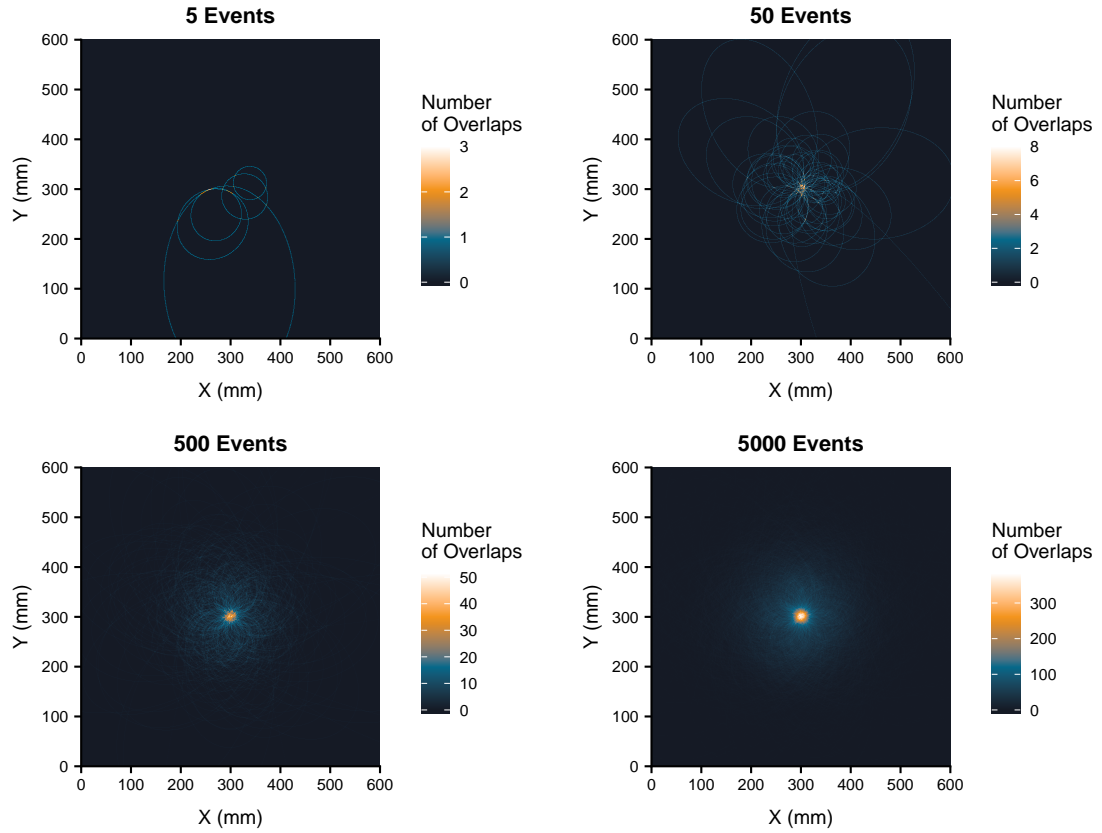
Figure 2.11: Images produced using experimental data for a Cs-137 point source 10 cm from the face of the Compton camera. Images made from 5, 50, 500 and 5000 cones. The overlapping of many Compton cones indicates the location of the radioactive source.
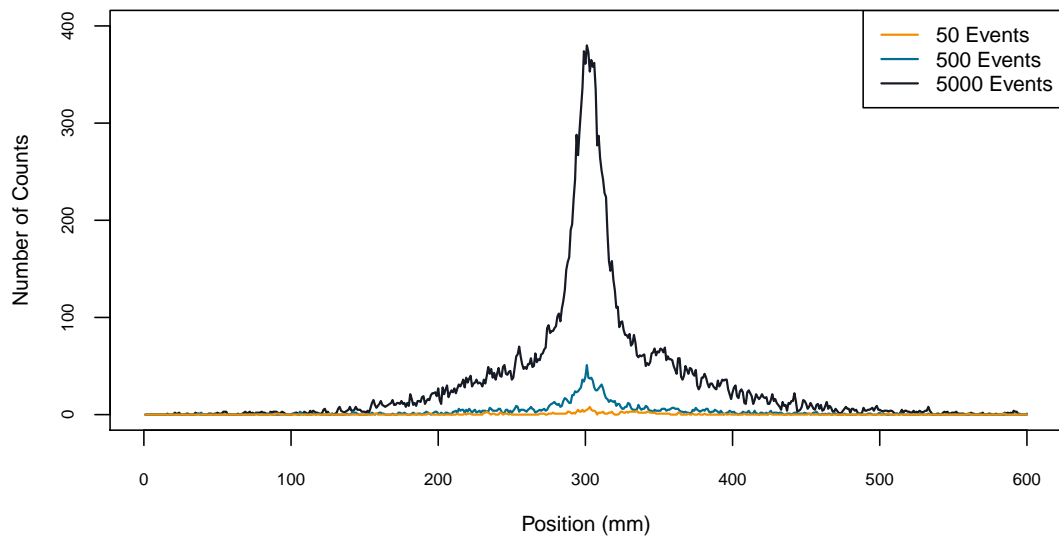

Figure 2.12: Image profiles for three of the slices shown in Figure 2.11.

22

The quality of a reconstructed image can be assessed using the point spread function (PSF). This is a common descriptor used to judge the performance of an imaging system based on the spread, or blur, of a point-like source of radiation. The PSF is represented by the FWHM of the reconstructed image profile in x or y through the pixel of greatest intensity in the image. It was determined in this work that the distribution best fitting the point source intensity profile for GRI+ is a Lorentzian peak sitting atop a Gaussian background. An example of this fitting is shown in figure 2.13. In this example, a Cs-137 point-like source was placed central to the face of the scatter detector and the image resolution was calculated to be 20.86 mm.
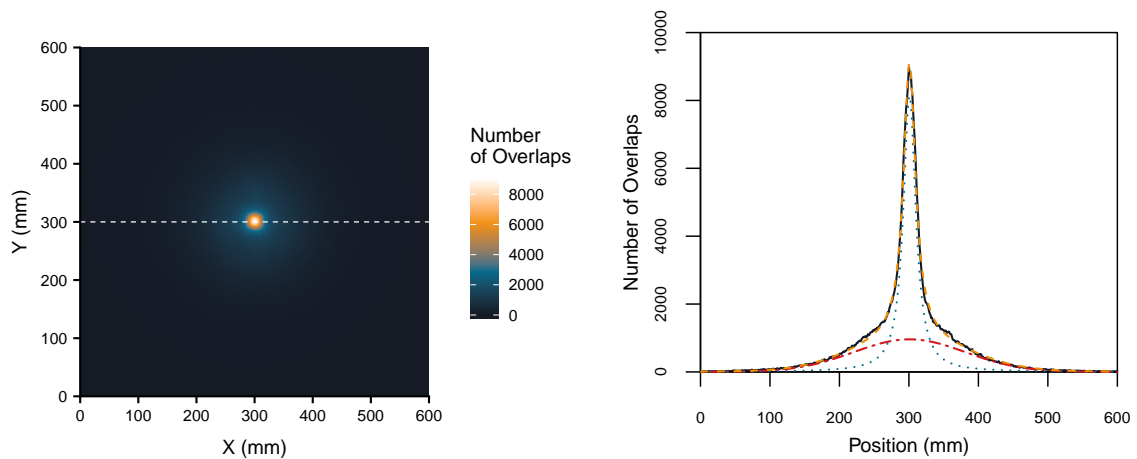
Figure 2.13: Reconstructed Compton image [left] and corresponding intensity profile [right]. The profile was taken at the row containing the maximum number of overlapping cones. The individual distributions used to fit the profile are overlaid.

Chapter 3

The GRI+ Detector System

GRI+ is a three-tier Compton Camera located at the University of Liverpool. It is comprised of three semiconductor detectors; two planar strip detectors and one coaxial detector. Each detector is held in an individual aluminium cryostat and the separation between each can be varied due to a custom-built frame. All three detectors were manufactured by Canberra for this project. Figure 3.1 shows a side view of the system. The signal cables can be seen for the first two detectors, the scatterer and absorber.

Figure 3.1: Photograph showing the side view of GRI+. The scatter detector, absorber detector and coaxial detector are displayed from left to right.

This chapter describes the properties of the individual detectors that form GRI+, and the influence that detector placement has on Compton imaging performance.

3.1 Scatter Detector

The scatter detector is the first tier of GRI+ and is shown schematically in Figure 3.2. It is named due to its desired role of Compton scattering the incident photons. It is cylindrical in shape, 8 mm thick and has a radius of 35.75 mm. It is electronically segmented by 26 orthogonal strips, 13 AC (p-type) vertical and 13 DC (n-type) horizontal strips on each face of the detector [16], which provide position of interaction information. Not all of these strips are used due to an insufficient number of digitiser input channels. Out of the 26 strips, 3 edge strips are unused and these are highlighted in Figure 3.2. The edge strips were chosen for removal to minimize efficiency loss as the surface area of these segmented sections are the smallest, proof of this is displayed in the appendix.
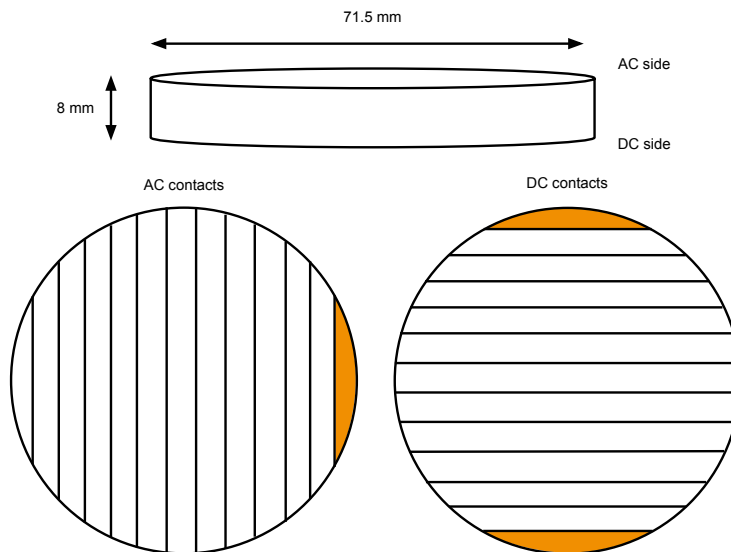

Figure 3.2: Illustration of the scatter detector. It is electronically segmented using 13 AC (p-type) and 13 DC (n-type) strips. Strips unused during data acquisition are displayed in orange.

The crystal is lithium drifted silicon (Si(Li)), and is housed in a cuboid aluminium cryostat of volume $33 \times 33 \times 5$ cm^3. The cryostat walls are 1 mm thick but this is reduced to 0.8 mm at each side of the crystal to minimise the attenuation of incident gamma rays,

as described by equation 2.3, thereby minimising efficiency loss. The detector is located at the central depth of the cryostat, as shown in Figure 3.3. A positive bias of 430 V is used to deplete the crystal. This runs lower than the recommended operating voltage of 600 V but is required to reduce the prominent leakage current, and is above the known depletion voltage of 150 V. Each strip has a pitch of 5.5 mm and an inter-strip gap of 500 μm which results in a voxelization of $5.5 \times 5.5 \times 8$ mm^3 for each interaction position. This volume is reduced towards the edges of the crystal, where the strip pitch is not uniform along the length of the strips. A 2.5 mm wide guard ring surrounds the crystal and acts to ensure uniformity of the electric field throughout its volume. Each strip is connected to a Canberra charge-sensitive preamplifier, housed in the cryostat, which provides a gain of 300 mV/MeV and is in a cold FET configuration. The crystal is electronically cooled to -175°C using a CryoPulse CP5 cooler.
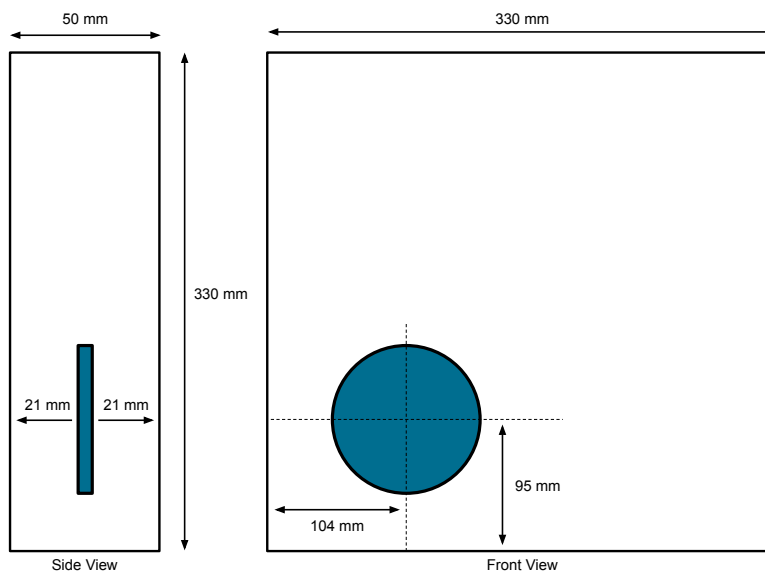
Figure 3.3: Schematic illustration to show how the Si(Li) crystal is placed in the aluminium cryostat. The walls of the cryostat are 1 mm thick with 0.8 mm thick entrance windows. Figure not drawn to scale.

3.2 Absorber Detector

Also manufactured by Canberra, the absorber detector is 20 mm thick with a height and width of 60 mm. It is electronically segmented into 24 orthogonal strips, 12 AC (p-type)

and 12 DC (n-type), each with a pitch of 5 mm, as shown in Figure 3.4. The position resolution provided from the voxelization localises an interaction to a volume of $5 \times 5 \times 20$ mm^3. The crystal has a depletion voltage of -1300 V and is operated at an applied bias of -1800 V. A CryoPulse CP5 cooler is used to electronically cool the crystal to a temperature of -192°C.
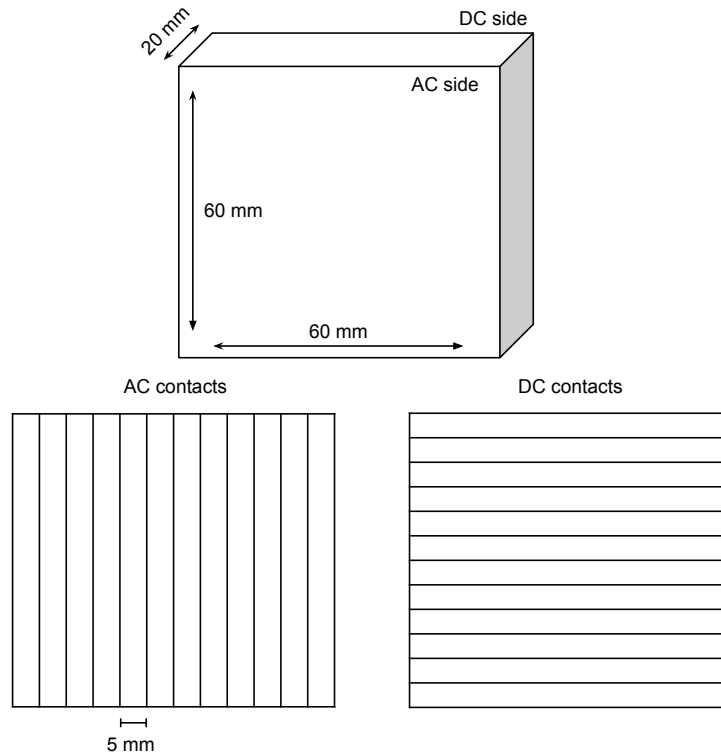

Figure 3.4: Illustration of the absorber detector. It is electronically segmented using 12 AC (p-type) and 12 DC (n-type) orthogonal strips.

The crystal sits at the central depth of an aluminium cryostat of dimensions $33 \times 33 \times 5$ cm^3, giving a wall-to-crystal separation of 15 mm as shown in Figure 3.5. The entrance windows to the crystal are 0.8 mm thick and a 3.5 mm guard ring surrounds the active area of hyper-pure germanium (HPGe). Each strip is connected to a Canberra charge-sensitive preamplifier, housed in the cryostat, which provides a gain of 200 mV/MeV and is in a cold FET configuration.
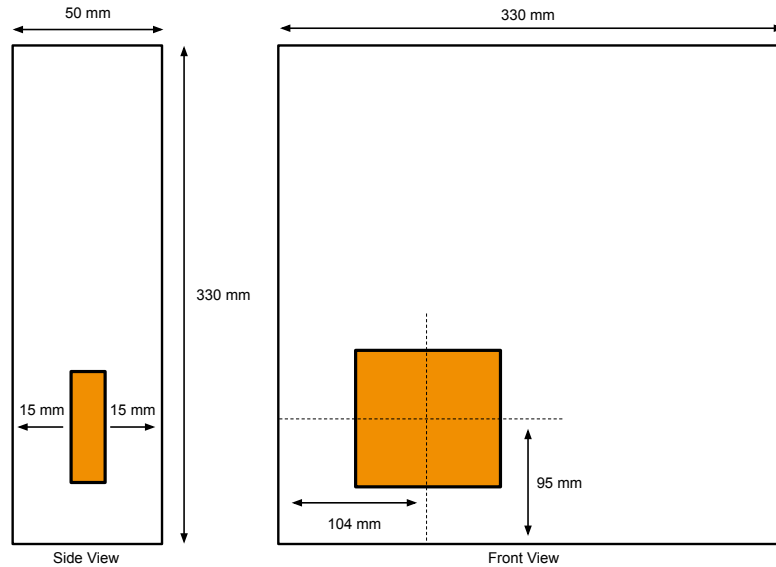
50 mm

330 mm

330 mm

15 mm   15 mm

95 mm

104 mm

Side View

Front View

Figure 3.5: The Ge crystal is placed centrally (within depth) in the aluminium cryostat. The walls of the cryostat are 1 mm thick with 0.8 mm thick entrance windows. Figure not drawn to scale.

3.3   Coaxial Detector

The coaxial detector is a standard electrode germanium detector (SEGe) manufactured by Canberra, model number GC4018. The detector performs with a relative efficiency of > 40 %. The crystal, which has a diameter of 66.5 mm and length of 50 mm, is offset by 6 mm from the aluminium endcap. The p-type coaxial detector consists of a germanium cylinder with an n-type contact on the outer surface and a p-type contact on the surface of an axial well [17]. The distance of the coaxial detector from the back of the absorber cryostat can be varied using the custom-built detector frame. A bias of +3000 V is applied to the crystal, far above the depletion voltage of 2500 V. The detector is electronically cooled using a CryoPulse CP5 cooler.
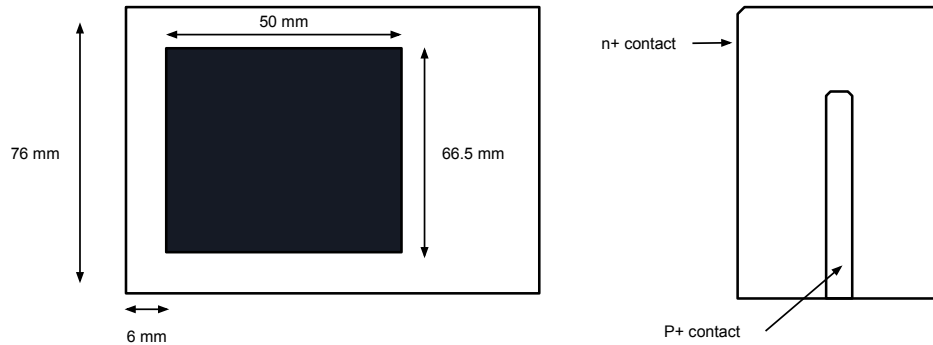
Figure 3.6: Illustration of the coaxial detector including the germanium crystal and aluminium cryostat [left] and a cross section of the crystal [right].

Unlike typical Compton cameras, GRI+ consists of three large volume detector tiers. The rear coaxial detector acts to improve the efficiency of the system, particularly at high energies. No information regarding interaction position is required from the coaxial detector as the reconstruction of Compton cones is accommodated using interactions in the front two tiers, the coaxial detector is only used for event selection. Events that Compton scatter in the first tier, and then undergo further Compton scattering in the absorber detector, can be absorbed in the rear coaxial detector and still be used in the image reconstruction process. Higher energy events, which are more likely to undergo Compton scattering in the absorber detector, benefit from this set-up most. Figure 3.7 displays the fraction of fold-1 events in which a gamma ray interacts in 2 and 3-tiers of the system. It can be seen that as the energies of incident gamma rays increase, the fraction that interact in all three detectors also increases and surpasses the fraction of 2-tier interactions at $\sim$ 1000 keV. An example energy spectrum recorded for a Eu-152 point source by the two and three tier configurations is shown in Figure 3.8, this highlights the usefulness of the third detector for higher energy events.
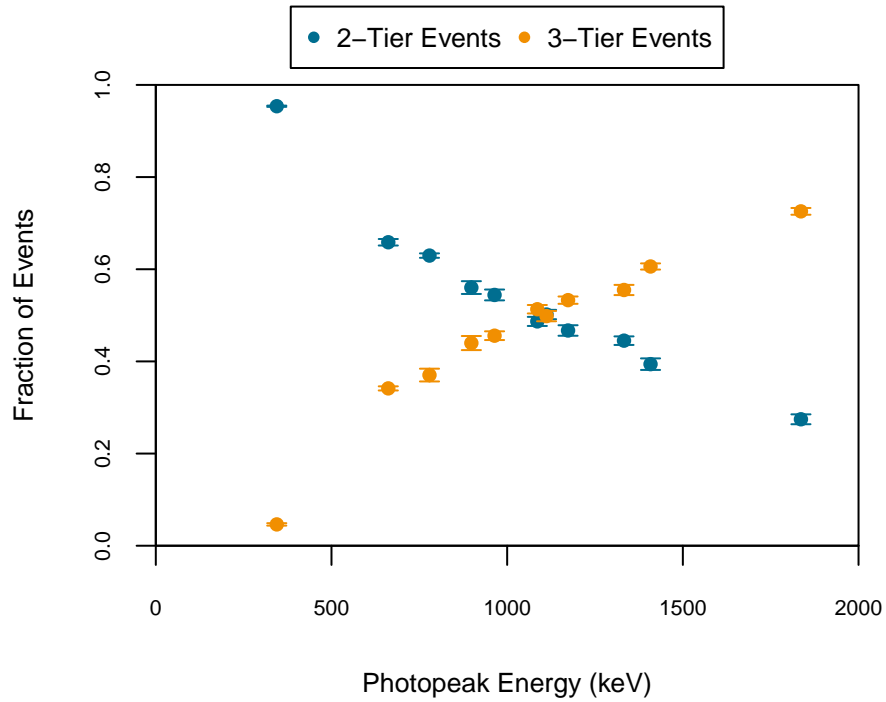
Figure 3.7: Shared fraction of fold-1 events for gamma rays interacting in 2 and 3-tiers of GRI+. Produced using Eu-152, Cs-137 and Co-60 point sources 10 cm from the detector.
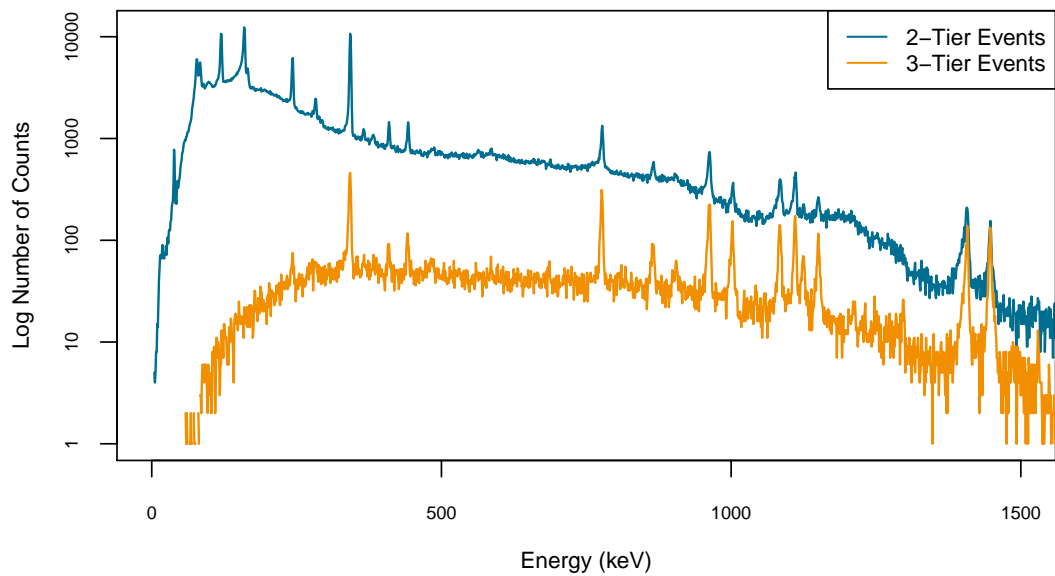

Figure 3.8: Energy spectrum created using fold-1 DC events for gamma rays interacting in 2 and 3-tiers of GRI+. Produced using a Eu-152 point source 10 cm from the detector.

3.4 System Geometry

The three detectors are configured as shown in Figure 3.9. The minimum achievable separation between the front two tiers is 7 mm. This is limited by bulky cooling arms which press against one another when the detectors are in the frame. The coaxial detector is placed as close as physically possible to the back of the absorber cryostat without risking impact of the two, which would damage to the delicate cryostat entrance windows. The approximate stand-off distance is around 2 mm with a likely error of 1 mm in either direction. It is placed as central as possible to the absorber detector's entrance window, and all three detector crystals are centrally aligned.
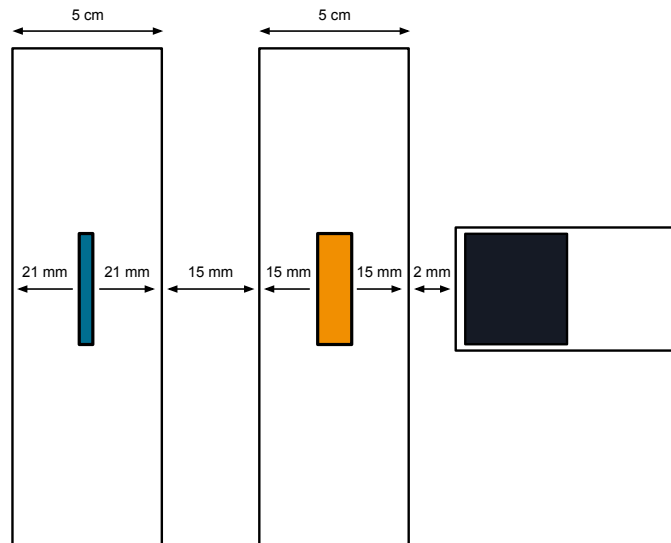

Figure 3.9: Schematic illustration of the Compton Camera layout.

The simplest usable event for image reconstruction requires a single Compton scattering interaction in the front detector, followed by photoelectric absorption in the absorber detector. The maximum scattering angle allowed in the front detector for this to occur is dependent on the position of the source, and separation between the two detector cryostats. An illustration of the maximum possible scattering angle is shown in Figure 3.10.
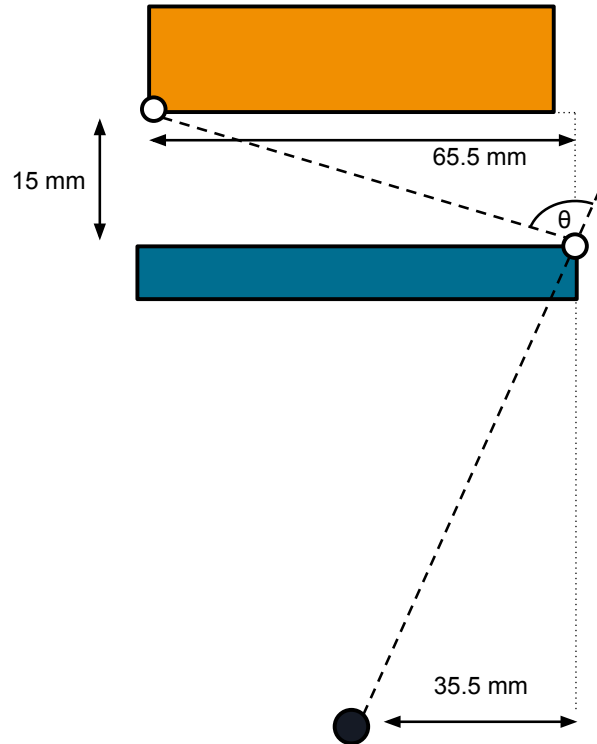
Figure 3.10: Illustration of the maximum scattering angle a gamma ray can undergo in the scatter detector to still interact in the absorber detector.

Figure 3.11 shows the relationship between source stand-off distance and cryostat separation on the maximum scattering angle. This was calculated assuming the source was central to the detector system. It can be seen that the maximum scattering angle decreases as the stand-off distance increases and when the cryostat separation is increased. This will determine the allowed range of energies which can be deposited in the detectors. For example, a point source 10 cm from the detector with a cryostat separation of 15 mm will have a maximum scattering angle of 67.5^o. Figure 3.12 demonstrates the range of energies that can be deposited in the front detector under this condition from a 662 keV gamma ray, it shows that the maximum energy which could be deposited in a single Compton scattering interaction is 292 keV. A further limit is placed on the system by the low energy thresholds implemented on the detector, described in section 3.6.
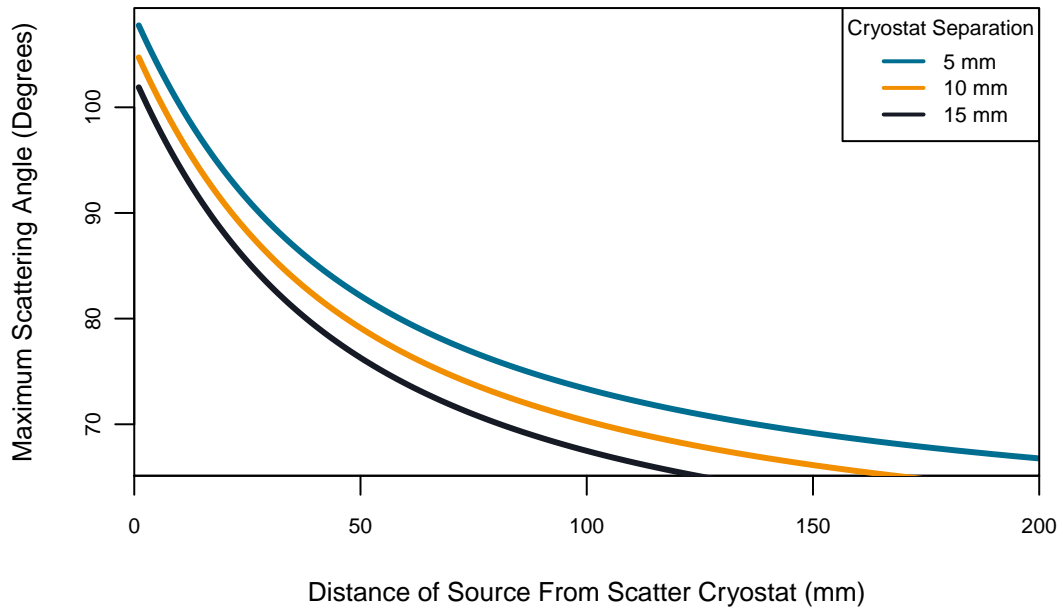
Figure 3.11: Relationship between the maximum scattering angle, source stand-off distance and separation of the two cryostats.
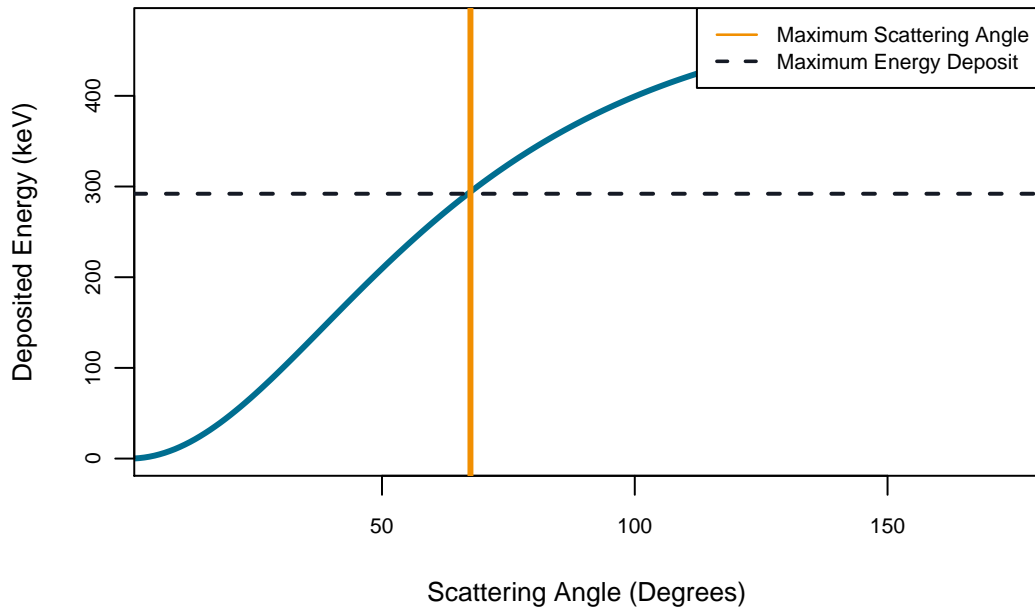

Figure 3.12: Deposited energy as a function of Compton scattering angle for a 662 keV gamma ray at a 10 cm stand-off distance. The maximum possible energy which could be deposited in a single scattering interaction is 292 keV.

3.5 Data Acquisition System

GRI+ uses a digital data acquisition system. This permits the preamplifier pulses output from the detectors to be stored and analysed for sophisticated online and offline measurements of the risetime and energy. A simple schematic illustration of the data acquisition system is shown in Figure 3.13.
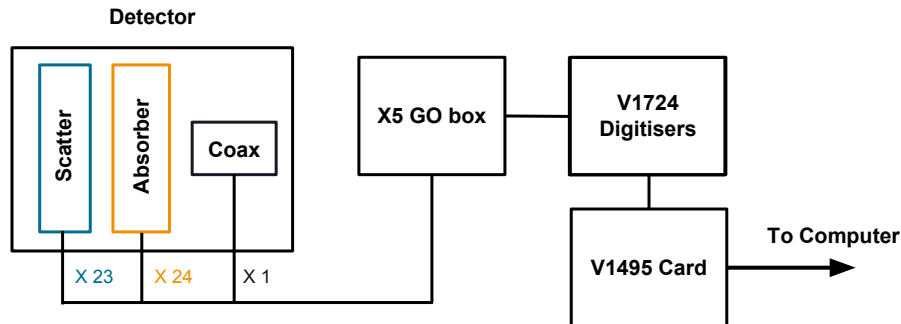

Figure 3.13: Illustration of the digital acquisition system used by GRI+.

CAEN V1724 digitiser cards [18] are used to sample the analogue pulses retrieved from the detector at 10 ns intervals (100 MHz) using flash analogue to digital conversion (FADC). In order to utilise the full dynamic range of the cards (2.25 V) gain and offset boxes (GO Boxes) are used to amplify the preamplifier signals by a factor of 5. In total, 6 digitisers are included in the set-up, with each feeding into one of the 6 channels of a V1495 global clock card. This card determines if an event meets criteria specified by the user (refer to section 4.1). The limited number of input channels on the card determines the number of digitisers that can be incorporated into the set-up. Each CAEN V1724 digitiser has 8 input channels. The output signals from the three detectors are split between the 6 digitisers, with the first three accommodating the scatter and coaxial detector whilst the remaining three receive signals from the absorber detector.

Signals that match user criteria are transferred to a computer using a V2718 VME to PCI Optical Link Bridge where they can be re-analysed using data acquisition software at a later time. This allows for methods to be applied to the data, such as pulse shape analysis (PSA), which can improve the overall performance of the system.

3.6   Noise Thresholds

Low energy thresholds for all channels of the Compton camera are implemented in the
V1724 digitiser cards. These must be set to discern between signals produced from gamma-
ray interactions and electrical noise in the system. Once a signal ascends above this
threshold, a proprietary algorithm built into the cards determines the energy of an event,
as described in section 4.1. Figure 3.14 shows the low energy thresholds set for each
detector channel. These represent the minimum energy that can be distinguished with
confidence from electronic noise, which is unique to each channel. Maximum energy de-
positions are constrained by the detector's geometry. In order to achieve the maximum
possible efficiency it is paramount that these thresholds be as low as possible, particularly
in the scatter detector where smaller energy depositions are expected from the Compton
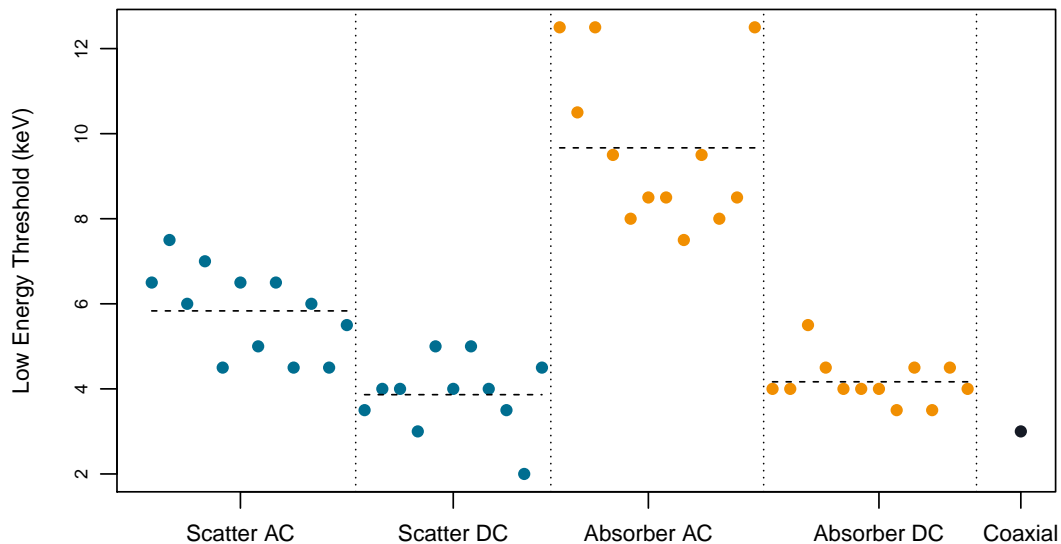scattering events.

Figure 3.14: Low energy thresholds for each detector channel. Average thresholds for each de-
tector face are displayed as dashed horizontal lines.

The DC side of each detector have thresholds lower than the corresponding AC sides.
This is a result of the preamplifier coupling discussed in section 2.2.5. AC coupled pream-
plifiers incorporate an additional load resistor which is a source of noise in the circuit. The
thresholds must therefore be increased on the AC sides to offset this additional noise.

3.7   Energy Resolution

The energy resolution of individual detector strips were determined using digital electronics at a gamma-ray energy of 122 keV in the front two tiers and at 344 keV in the rear two tiers. Energy resolution measurements were obtained from data acquired with a Eu-152 source. The energy resolution for each of the implemented Compton camera channels is displayed in Figure 3.15. The average energy resolution for the AC and DC sides of both detectors, displayed as bold horizontal lines on the plot, are displayed in table 3.1.
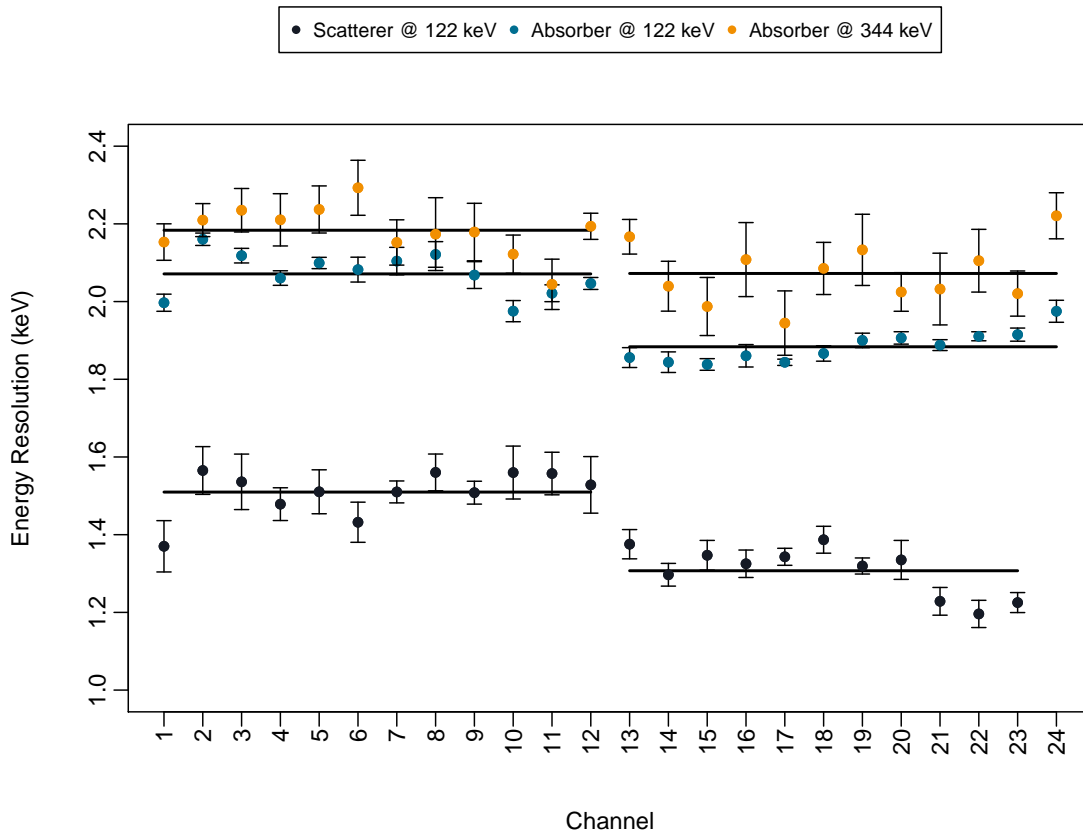

Figure 3.15: Energy resolutions of the detector channels calculated from the digital electronics. Energy resolutions were recorded at 344 keV in the absorber detector and 122 keV in both the scatter and absorber detectors. The average energy resolutions for the AC and DC sides at each energy is displayed as bold horizontal lines.

Detector	Energy (keV)	AC FWHM (keV)	DC FWHM (keV)
Scatterer	122	1.51 ± 0.05	1.31 ± 0.03
Absorber	122	2.07 ± 0.02	1.88 ± 0.02
Absorber	344	2.18 ± 0.06	2.07 ± 0.07

Detector	Energy (keV)	FWHM (keV)
Coaxial	344	1.75 ± 0.09

Table 3.1: Average energy resolutions.

Detector channels 1 through to 12 are AC coupled. The remaining 12 channels are DC coupled. The slightly improved energy resolutions of the DC coupled channels are a result of the preamplifier properties, discussed in section 2.2.5. As there is an improved energy resolution from DC coupled channels, the DC energies are chosen as input into the image reconstruction code.

3.8   Compton Camera Imaging Efficiency

The absolute Compton camera imaging efficiency for GRI+ was calculated according to equation 3.1. Only gamma rays which interacted once in each detector and deposited their full photopeak energy were considered to be 'recorded' events. These are the most simple type of event that can be used in the reconstruction of a Compton image.

$$\epsilon_{abs} = \frac{N_{recorded}}{N_{emitted}} \tag{3.1}$$

$N_{recorded}$	$-$	number of reconstructible events recorded by the detector
$N_{emitted}$	$-$	number of events emitted by the source $= A \times T \times P_\gamma$
A	$-$	activity of source
T	$-$	Time
P_γ	$-$	Branching Ratio

Point sources were placed 10 cm from GRI+, central to the scatter detector crystal. Each isotope was imaged separately and data were collected for more than 2 days apiece. Cs-137, Eu-152 and Co-60 were selected to obtain efficiency measurements throughout the full energy range important to this project (up to 1.5 MeV). Efficiencies were determined for

events which only interacted in the front two detectors (2-tier) and those which interacted in all three (3-tier), these are displayed in Figure 3.16. At low energies the efficiency of GRI+ for 2-tier events is low as gamma rays are mostly absorbed in the front detector. At higher energies the efficiency drops off as the likelihood of multiple interactions increases and gamma rays scatter through the system without depositing all of their energy. 3-tier efficiency cannot be calculated below 300 keV as it is very unlikely for gamma rays to scatter through the front two tiers without being fully absorbed. Above 662 keV the 3-tier efficiency falls away, but at a much smaller rate than the 2-tier efficiency. 3-tier efficiency is greater than 2-tier efficiency above $\sim$ 1000 keV, this relationship can also be seen in Figure 3.7. The relative increase in achievable system efficiency, when including 3-tier events, is displayed in Figure 3.17 and highlights the importance of the coaxial detector when imaging higher energies. It can be seen that above 1000 keV, an efficiency increase of more than 100 % is achieved, effectively halving data collection times.

Although the shape of the distributions shall be accurate, the absolute values calculated for efficiency may not. During the scope of this project, the firmware supplied with the CAEN digitisers encountered an issue. The data which is stored, to be interpreted by our sorting software, was found to not match the data processed by the digitisers. Differences in the number of detector segments encountering a gamma-ray interaction can be seen when looking at the hit distributions logged by the digitisers, and those logged by our sorting software. This issue is being studied and is expected to be fixed by a proprietary firmware update in the near future.
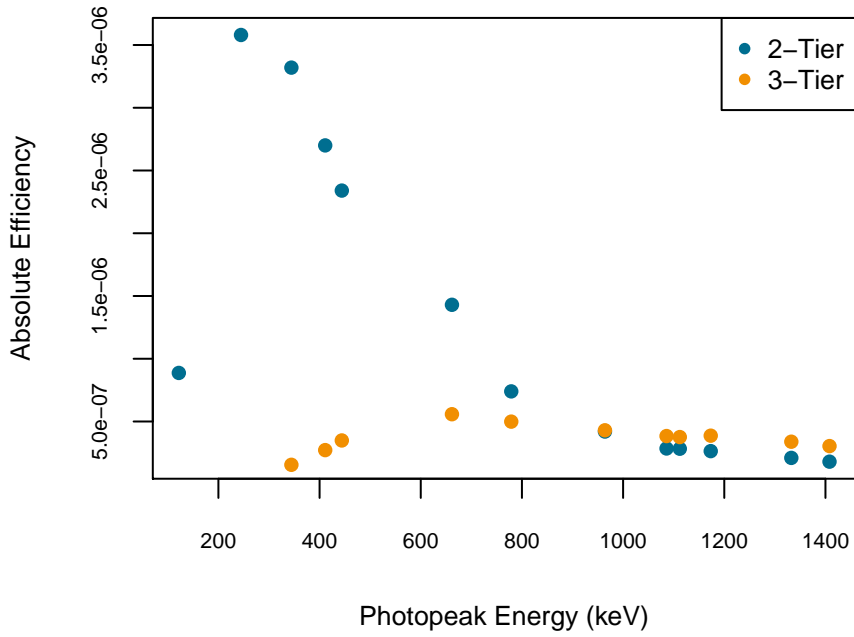
Figure 3.16: Compton camera efficiency for GRI+ calculated using reconstructible fold-1 events. Error bars are too small to see, sources placed 10 cm from the front of the detector.
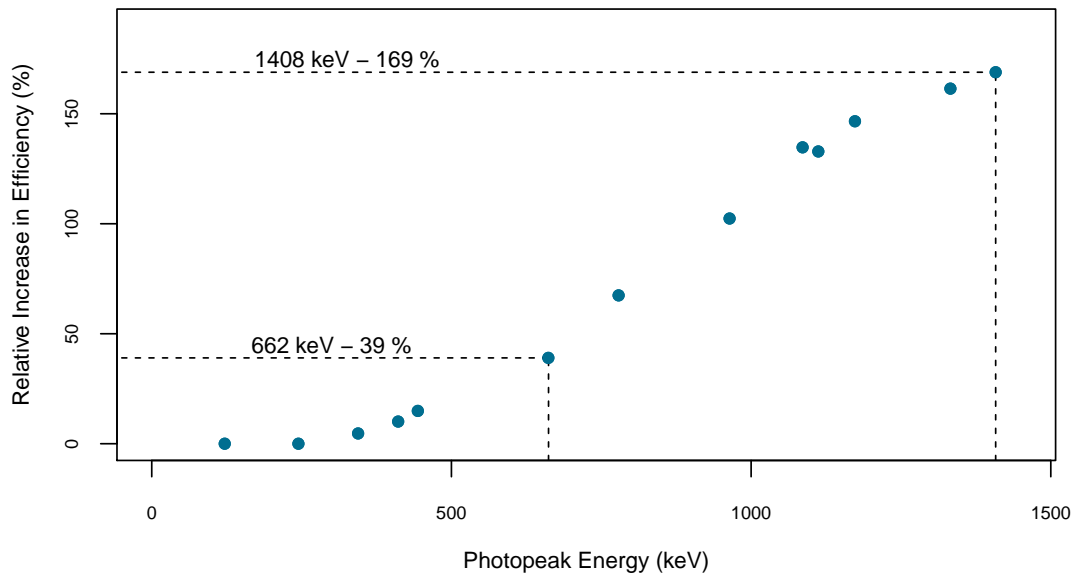

Figure 3.17: Relative increase in Compton camera efficiency due to the addition of 3-tier events for sources placed 10 cm from the detector.

Chapter 4

Digital Signal Processing

To produce an image of a gamma-ray source, the preamplifier signals retrieved from the GRI+ detectors must be digitised, analysed and formatted into a text file to be input into an image reconstruction algorithm. This chapter discusses the various steps between data retrieval and image formation, which will be described in the order shown as a basic workflow in Figure 4.1.
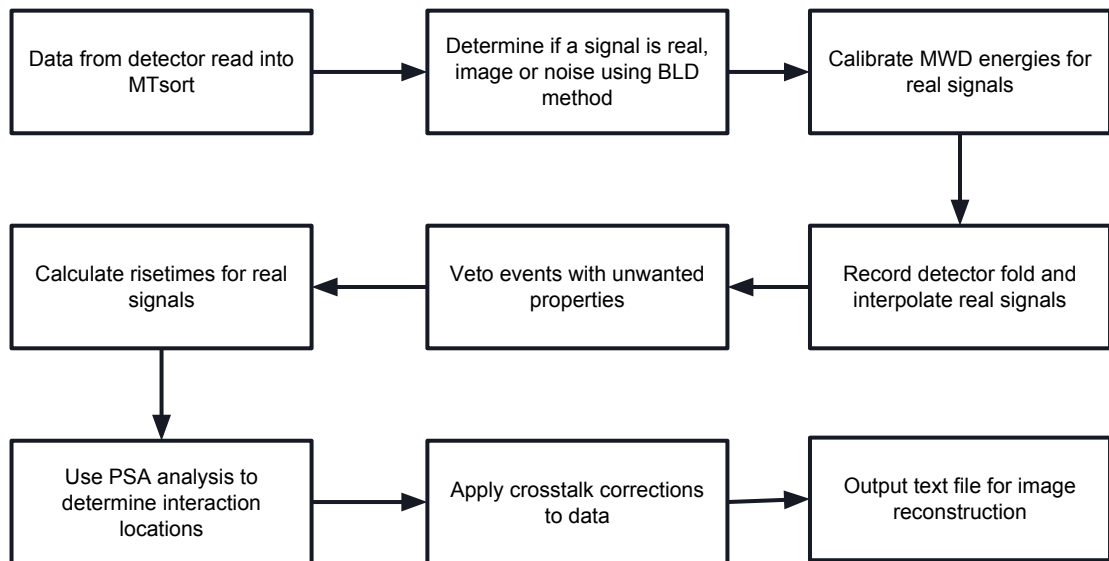
Figure 4.1: Workflow for data processing.

4.1 Data Acquisition Software

The data acquisition software coupled with our system is called MIDAS (Multi Instance Data Acquisition System) [19]. Its interface allows for the proprietary moving window deconvolution algorithm (MWD) [20] to be optimised through manipulation of several controlling variables, such as a trapezoid scaling factor and trapezoid rise time. Also set via the acquisition software are the user determined event criteria. In order for events to be registered as coincident in GRI+ it is required that at least one interaction is found on the AC face of the scatter and absorber detectors, with no criteria stipulated for the coaxial detector. A further logical parameter can be set which tells the system to either write out the signals from every channel when this benchmark is met (all masked mode) or just those channels which encountered a gamma-ray interaction (output as input masked). Although memory intensive, it is imperative to take data in all masked mode for future use of PSA algorithms.

The raw binary data obtained from the digitisers is analysed using the sorting software, MTsort [21], developed at the University of Liverpool. It is written in the coding language C [22] and allows for the manipulation and visualisation of the Compton Camera output before data is formatted for use in the image reconstruction codes. User created methods can be implemented alongside the MTsort script for sophisticated analysis of the signals from the detector. Natively, MTsort can be used for event selection, simple one and two dimensional plotting and energy spectrum calibration. Sorting can either be performed online, during data acquisition, or offline, post data acquisition. By conducting sorts online, the validity of the data can be ensured before disk storage has begun, and various histograms can be updated to inform the user of preliminary findings. Processing methods such as pulse shape analysis (PSA), which is used to better define the axis of the Compton cone, are written within C methods called by the MTsort code.

4.2 Pulse Information and Event Sequencing

Preamplifier pulses contain information in both their amplitude and shape. The storage and processing of these pulses by a digital data acquisition system permits the information contained to be extracted. Three signal types are attainable in the GRI+ detection system:

1. Real signals, which correspond to charge collection on a contact following a gamma-ray interaction.

2. Transient signals from strips in close proximity to the contact undergoing charge collection, also known as image charges. These are only present in the segmented GRI+ detectors.
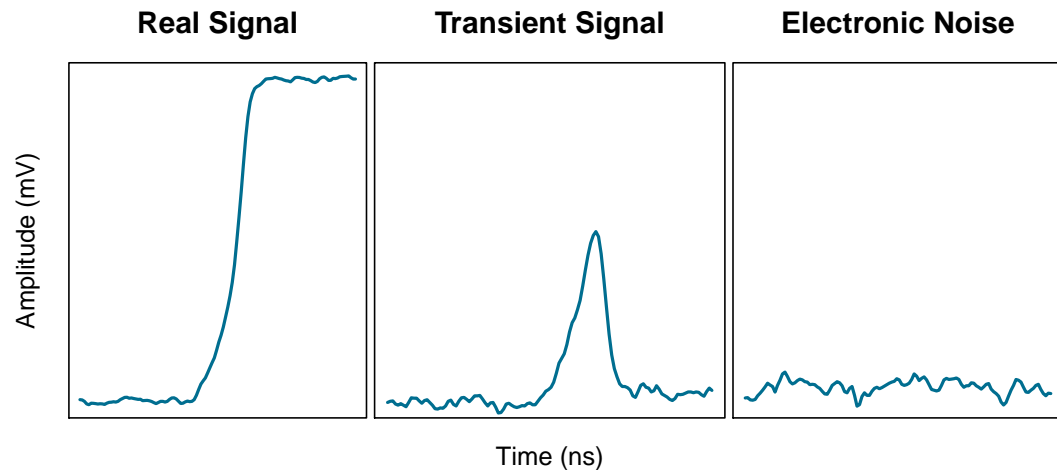
3. Electronic noise.

Figure 4.2: Examples of the three signal types from adjacent channels in a GRI+ strip detector. A real signal is produced in the strip where a gamma ray interacted [left], the neighbouring strips show transient signals [middle] and further strips display electronic noise [right].

To determine if a signal represents a gamma-ray interaction in a strip, 300 ns periods at the beginning and end of the digitised signal are analysed. If the average value of the latter period is three times greater than the standard deviation of the former, then an event is considered real. Figure 4.3 shows a signal from the absorber detector indicating the time periods used to calculate signal type.
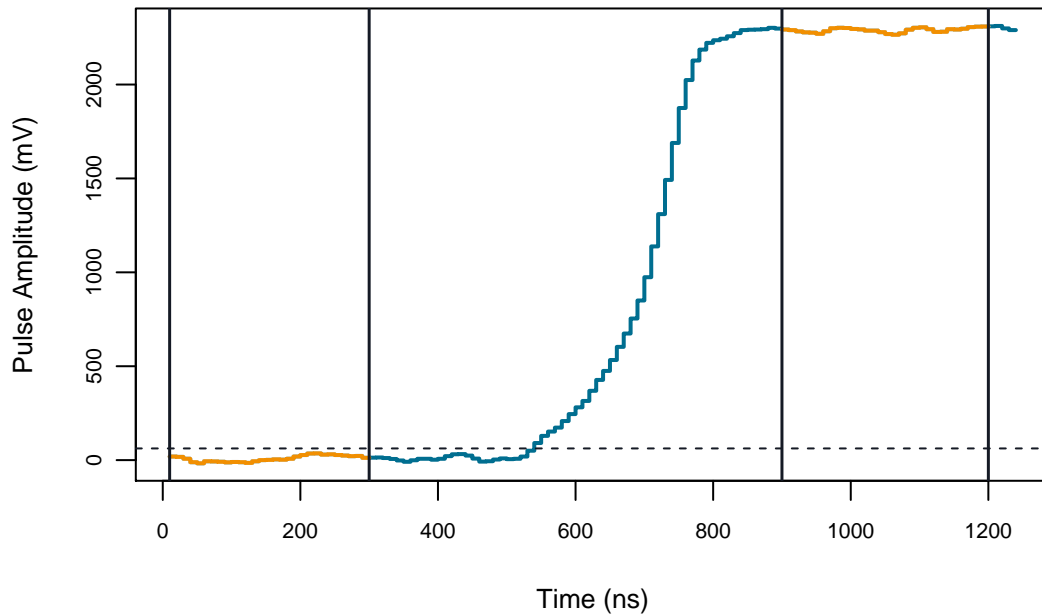
Figure 4.3: Signal from the absorber detector. The 300 ns periods used to categorise the signal are displayed in orange. Three times the standard deviation of the first 300 ns period is indicated by the dashed line.

If the signal is considered real then the deposited gamma-ray energy is calculated using the Baseline Difference (BLD) method. This method works by calculating the average value of the second 300 ns period, after the baseline offset has been removed. This is not as precise as the MWD algorithm programmed into the digitizer firmware, and so is not used when calculating the addback energies that are input to the image reconstruction codes.

4.3 Energy Calibration

Data acquisition for energy calibration is performed by running the system with no requirement on which face a signal is seen, and recording each signal. This is undertaken for each detector individually to avoid overloading the system, which can occur when too many signals are output at any one time.

The energies deposited in each of the detector's channels are calculated using a moving window deconvolution (MWD) algorithm built into the CAEN V1724 digitiser cards [18]. This algorithm must be optimised for each detector before data acquisition takes place and

works in four stages, as described in the appendix. The parameters selected were found to provide the best energy resolutions for each detector whilst also maintaining a high efficiency, these are further discussed in the appendix.

The calculated MWD energies must be calibrated. This is typically performed during an online sort taken before data is saved to disk. A quadratic fit is used to match the energies to the correct channels in a histogram. A python script was developed to help calibrate the 48 channels, saving several hours each time recalibration was necessary.

4.4   Detector Fold

GRI+ was designed to perform as an efficient Compton Camera, particularly for high energy gamma rays. In order to make use of this property, it is important to maximise the number of signals usable by the image reconstruction algorithms. Event fold is classified as the number of detector strips which detect a net charge above a given threshold and is calculated for each side of both detectors. The fold of the coaxial detector will always be 0 or 1, since there is no segmentation. The system fold is written as:

$$F\left[f_s AC, f_s DC, f_a AC, f_a DC, f_c\right] \tag{4.1}$$

$f_s AC$ –   Detector fold on the AC side of the scatter detector

$f_s DC$ –   Detector fold on the DC side of the scatter detector

$f_a AC$ –   Detector fold on the AC side of the absorber detector

$f_a DC$ –   Detector fold on the DC side of the absorber detector

f_c –   Coaxial fold

This format shall be used throughout the thesis when discussing detector performance. Figure 4.4 illustrates the fold for a series of different interactions by a single gamma ray as seen on the face of one detector.
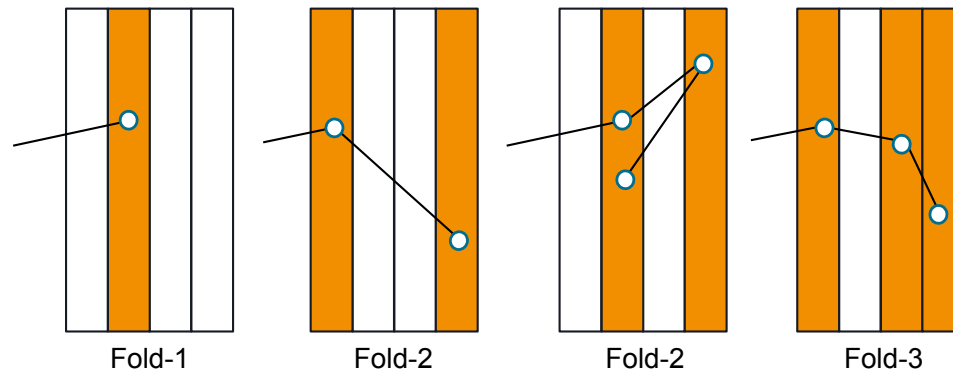
Figure 4.4: Illustration of fold classification for a single detector face. Gamma-ray interactions are shown as circles. The number of detector strips which detect a charge greater than a set threshold (orange) is known as the fold for that face of the detector.

It can be seen that this is a useful method to determine the number of interaction positions in the detector. It is possible that a gamma ray can interact more than once within a strip, however these events can be vetoed based on their signal properties (a discontinuity in the rising edge of the preamplifier pulse). Gamma rays with low energies are more likely to undergo photoelectric absorption, a fold-1 event. At higher energies Compton scattering can occur, which could result in any number of interactions in the detector crystal. Figure 4.5 shows the distribution of event fold in the absorber detector, calculated for a series of energy ranges. This data was obtained from a Eu-152 spectrum for the AC side of the absorber detector, displayed in Figure 4.6.

The distribution of events moves towards higher fold with increasing energy. It can be seen that for gamma rays above 900 keV, less than 50 % will be fold-1. By utilising fold-2 events, an increase in statistics can be obtained which, assuming the events are correctly ordered and introduce no additional uncertainties, results in a clearer reconstructed image. The inclusion of fold-2 events in image reconstruction is discussed in section 5.2.5.
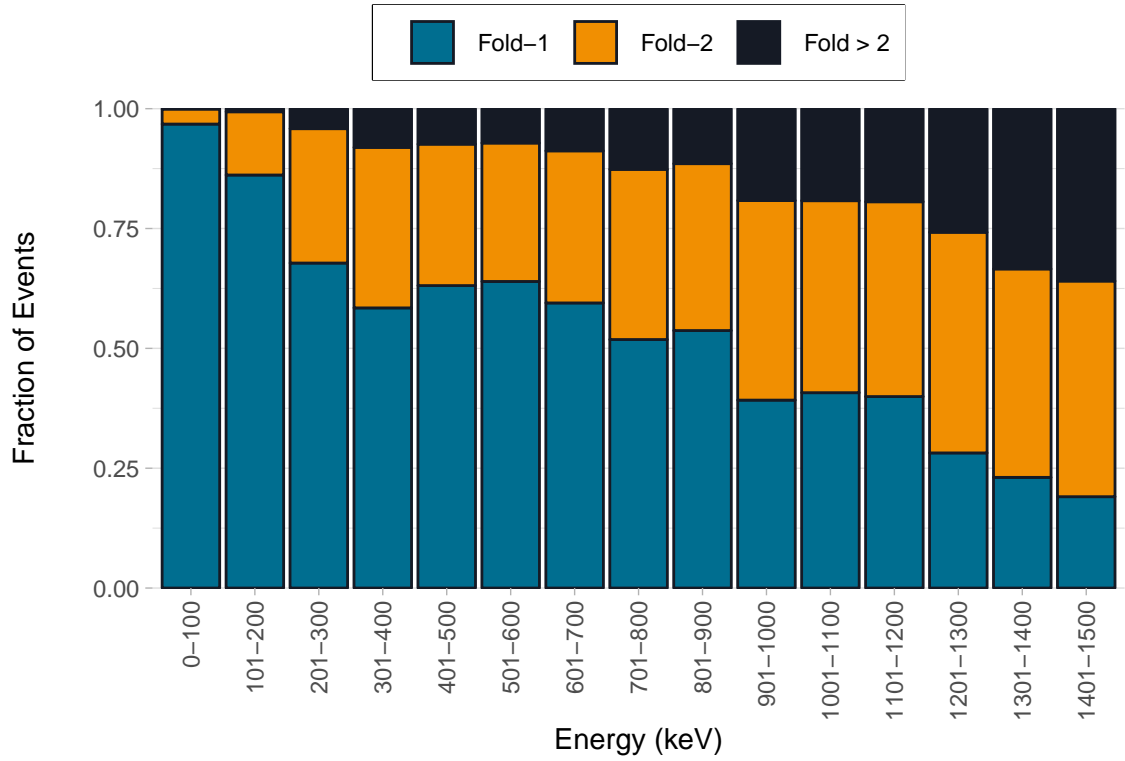
Figure 4.5: Distribution of event fold on the AC side of the absorber detector with energy. Each energy range has a normalised total count. Fold-1 events are indicated as blue, fold-2 events are orange and higher fold events are black.
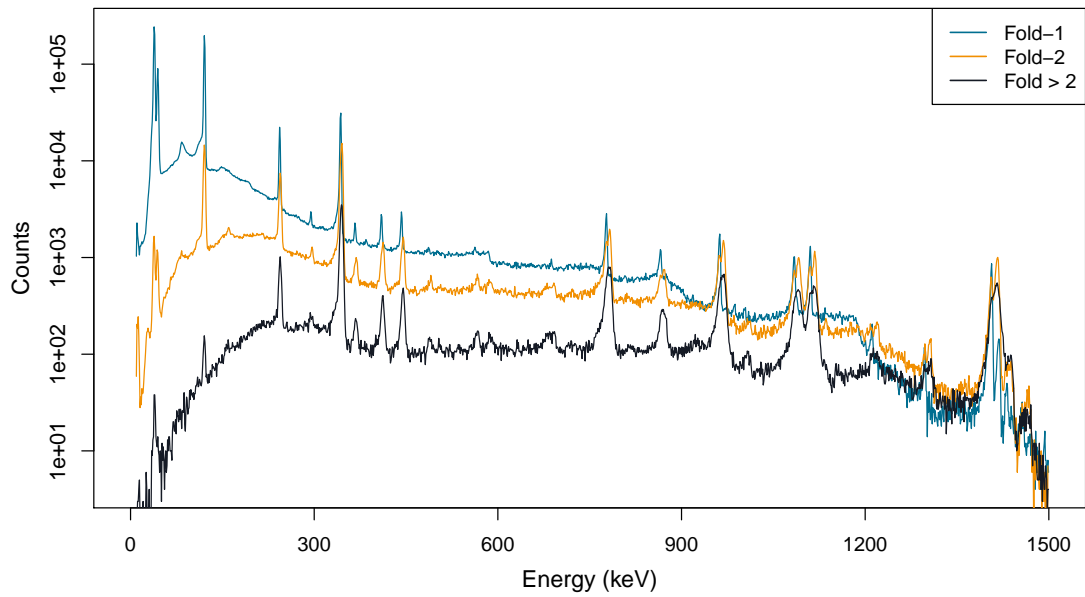

Figure 4.6: Eu-152 energy spectrum for fold 1, 2 and 3 events in the GRI+ system.

4.5   Pulse Interpolation

The CAEN V1724 digitiser cards sample the preamplifier pulses at a frequency of 100 MHz. Each recorded element that makes up the raw pulse is therefore separated by 10 ns. These signals are interpolated in MTsort before information is extracted in order to overcome limitations in the digitiser sampling rate, which impose high frequency noise and fluctuations on the signals. Once a signal is established as being the result of charge collection (a real pulse) and not electrostatic coupling with a neighbouring strip (an transient pulse) — an averaging filter is applied. An averaging filter of three elements was found to be adequate for removing the fluctuations.

$$y\,[i+1] = \frac{1}{3}\,(x\,[i-1] + x\,[i] + x\,[i+1])\tag{4.2}$$

where x is the amplitude at the time i and is stored in a second array, y. A linear interpolation of these pulses is applied to improve the sampling rate fivefold, this is shown in Figure 4.7. The implied additional points lie between the two readings to increase the perceived sampling rate to one element every 2 ns, 500 MHz. The outcome of this is a smoother signal, as shown in Figure 4.8.
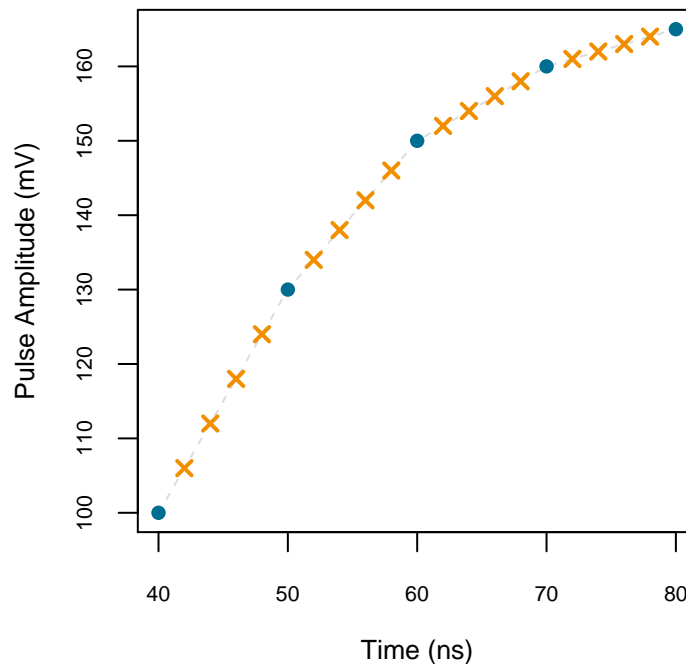

Figure 4.7: Example of the signal interpolation. Between each recorded element a linear fit is performed to improve the sampling frequency to 2 ns per element.
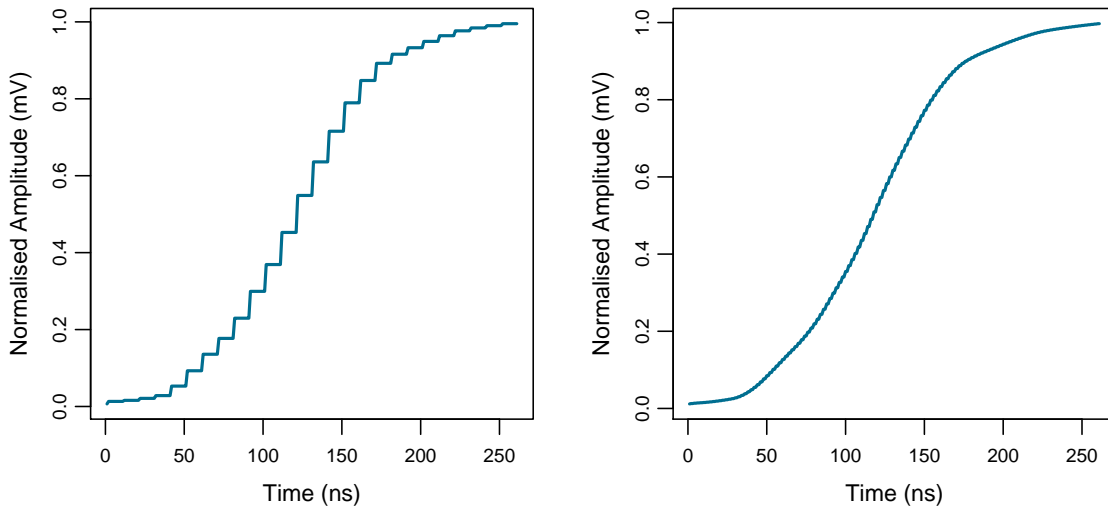
Figure 4.8: Preamplifier signals from the detectors are recorded using a 100 MHz digitizer [left] and interpolated to produce a perceived 500 MHz sampling rate [right]. Signals taken from the absorber detector.

4.6 Event Veto

During event selection it is important to veto signals with unusual properties such as those shown in Figure 4.9. In these examples, the signals are generated from two phenomena occurring within similar time frames. The first image shows the signal generated when 2 gamma-ray interactions are observed in the same detector strip [left]. The second image [right] shows the convolution of a real signal and a transient signal produced from an interaction in a nearby strip. The following methodologies are only performed for events occurring in the absorber detector where information on the shape of signals is required for further processing. These unwanted features can result in incorrect evaluations of signal properties and deposited energy. They are removed during sorting through differentiation and normalisation methods, which identify the particular features. Multiple-interaction signals can be characterised by identifying a gradient change. Differentiation of the convolved signal produced by these events displays a multiple-peak differentiation plot. This is shown for a signal produced by a single interaction and multiple interactions in Figure 4.10.
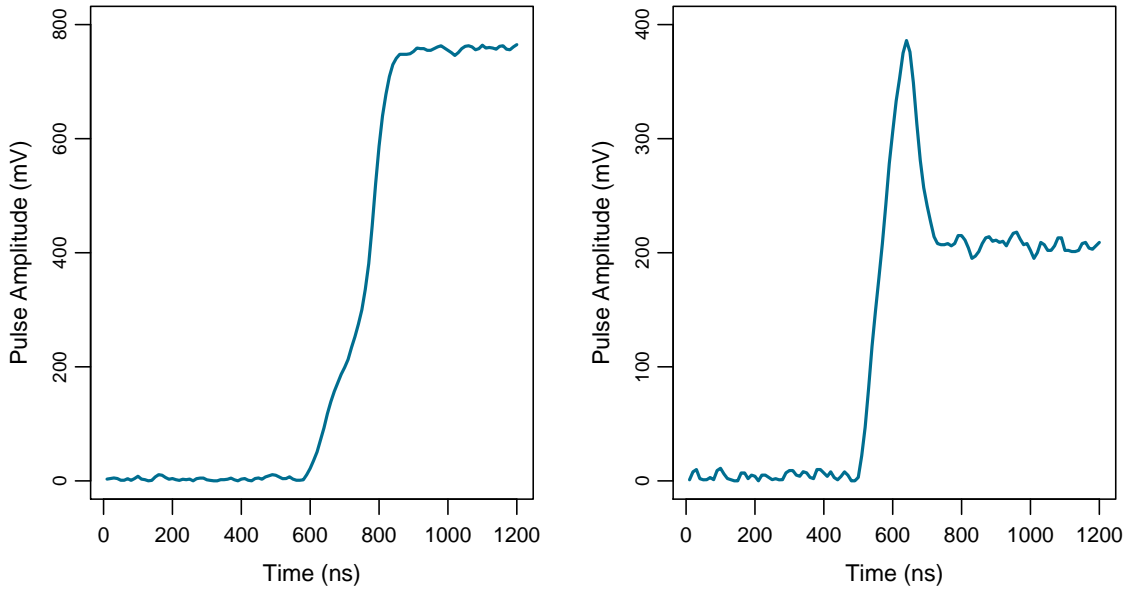
Figure 4.9: Signals produced from multiple interactions being recorded at the same time within the same channel [left]. An image charge and a real charge event being collected simultaneously [right].
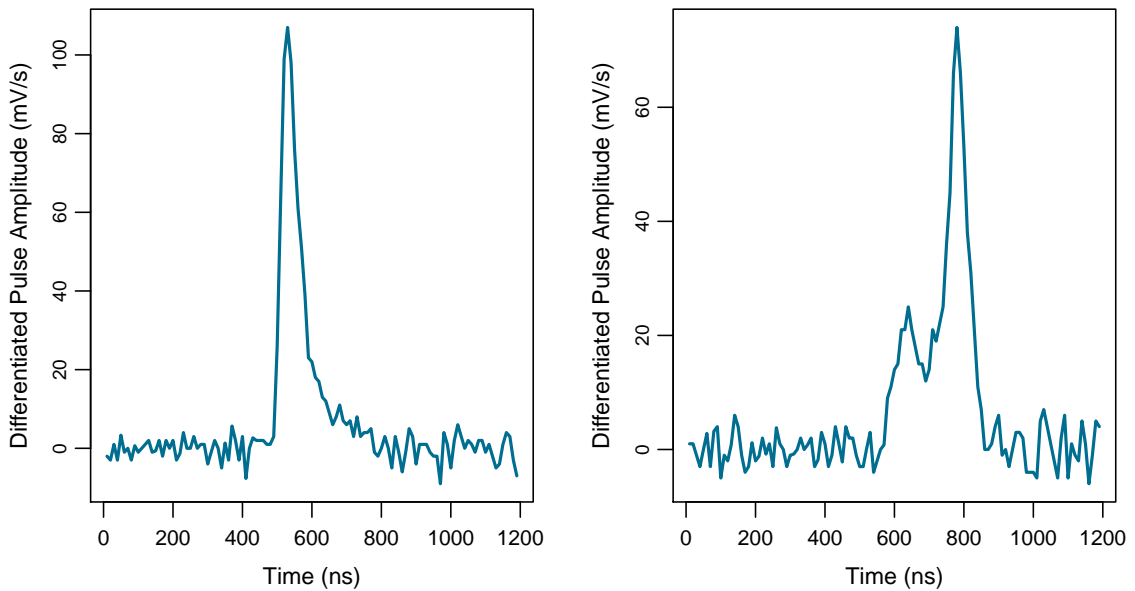

Figure 4.10: Differentiated single-interaction signal [left] and differentiated multiple-interaction signal [right].

By placing a threshold on the differentiated signal, it is possible to remove events that are composed of multiple interactions. For experimental data in this thesis, a threshold of

35 % the maximum gradient change was chosen. The systematic variance of thresholds was investigated and is addressed in the appendix. Lower energy signals, which contain a larger ratio of noise-to-signal, are predominantly removed using this method. This technique may therefore need to be bypassed completely when imaging energies below 400 keV.

Signals which consist of combined transient and real signals also lead to the incorrect calculation of energy and pulse shape. To avoid this, the signals are first normalised based on the last 200 ns, and then the maximum signal amplitude is calculated. As a pre-trigger window set in the digitisers ensures all signals are centred within the trace, the maximum height of convoluted image-and-real signals shall be greater, as shown in Figure 4.11. A maximum height threshold of 1.2 was selected from a visual assessment of signals with these signatures.
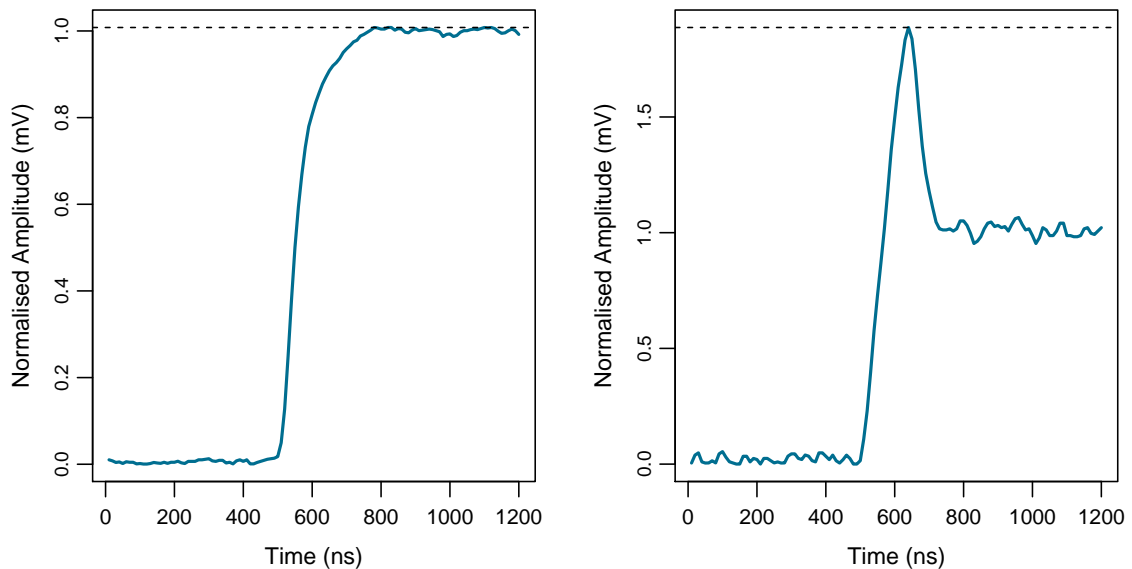

Figure 4.11: Normalised real signal [left] and normalised real signal with an image charge detected on the same strip [right]. The maximum height of the second signal is much larger than that of the first and so is removed via the static upper limit threshold of 1.2.

Both techniques to improve the quality of selected events result in a slight reduction of efficiency. The justification for this loss is the improvement found during image reconstruction and the enhanced performance of PSA algorithms.

4.7 Pulse Shape Analysis

Initially, gamma-ray interactions are assumed to occur at the central (x, y, z) coordinates of voxels. These are created in the front two detectors by the orthogonal strip contacts. The volumes represented by these voxels are $5.5 \times 5.5 \times 8$ mm^3 in the scatter detector and $5 \times 5 \times 20$ mm^3 in the absorber detector. This high degree of uncertainty, particularly within the depth of the absorber detector, results in significant errors in the cone axis geometry, and therefore overlaps, in the image. This uncertainty can be reduced with a technique known as pulse shape analysis (PSA). There are two ways by which pulse shape analysis is implemented. The first improves knowledge of the lateral interaction position through information extracted from the transient signals on neighbouring strips, known as XY-PSA. The other method utilises the risetime of preamplifier signals to estimate the depth of the interaction, namely Z-PSA.

4.7.1 XY-PSA

The movement of charge carriers towards a collecting electrode results in transient signals in neighbouring contacts due to electrostatic coupling with the moving charge. The size of these transient signals can be compared to estimate the lateral interaction position of a gamma ray. This methodology relies on the known relationship between image charge size and distance of an interaction from a neighbouring contact. The closer an interaction position is towards a contact, the larger the image charge collected upon that contact will be, and the smaller the image charge on the opposite side.

For each gamma ray that interacts once in the detector, an asymmetry parameter can be calculated using:

$$A = \frac{Q_L - Q_R}{Q_L + Q_R} \tag{4.3}$$

A — asymmetry parameter

Q_L — image charge area on the contact to the left of the real signal

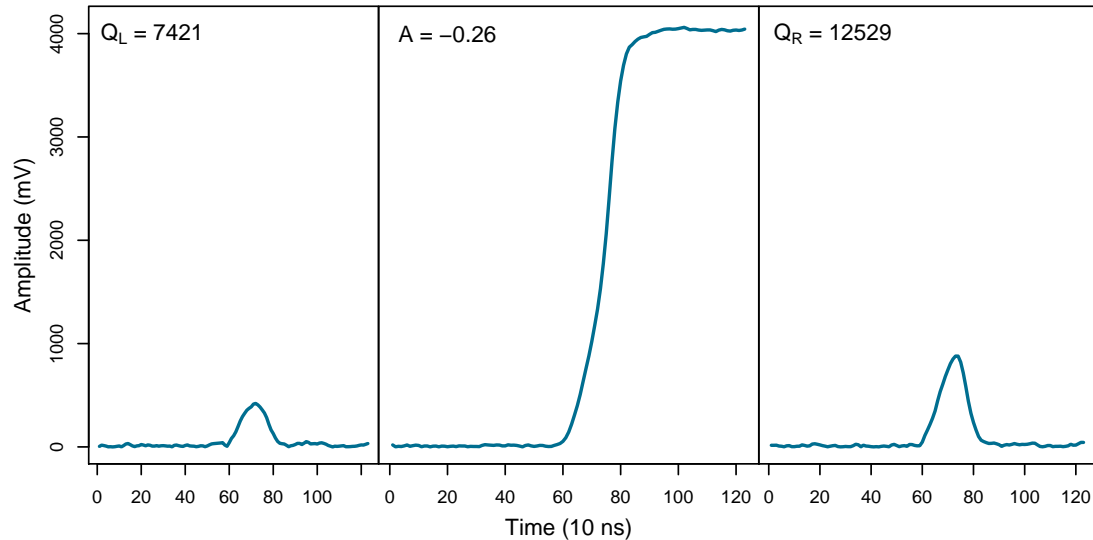Q_R — image charge area on the contact to the right of the real signal

Figure 4.12: The lateral position of an interaction is determined from the relative area of image charges. The asymmetry parameter and image charge areas, calculated from equation 4.3, are displayed for each signal.

The asymmetry parameter, A, shall take a value between 1 and -1. The closer this falls to zero the more central within the strip an interaction is believed to be. A value approaching 1 would indicate the charge was collected close to the neighbouring electrode on the left, and a value of approaching -1 would represent an interaction nearer to the right electrode. This value is scaled to fall between 1000 and 3000 for practical use in the MTsort script.

The distribution of asymmetry parameters is known to vary on a strip-to-strip basis and therefore calibration is required. Calibration of the asymmetry parameters is performed by placing Cs-137 and Eu-152 point sources at a stand-off distance of 10 cm from the detector. To ensure there is no bias from Compton scattering, no objects are placed between the source and detector being calibrated. There will be slightly fewer contact-edge events used in the calibration. This stems from the greater likelihood of events scattering into a neighbouring strip when interacting close to a strip boundary. Fold-2 events are disregarded so these are not used in the calibration.

The asymmetry distribution is then split into equal parts as shown in figure 4.13. As a gamma ray is equally likely to interact in one part of the contact as another — sectioning of the distribution effectively segments the strip. If the calculated asymmetry parameter for an event falls within a given section of the distribution, it can be assumed that the

interaction occurred at the corresponding lateral strip location. For both detectors, the distributions are split into 5 sections of equal area. This improves the lateral position resolution of the absorber detector to 1 mm, a factor of 5 improvement. The scatter detector lateral resolution is improved to 1.1 mm from the 5.5 mm strip pitch.
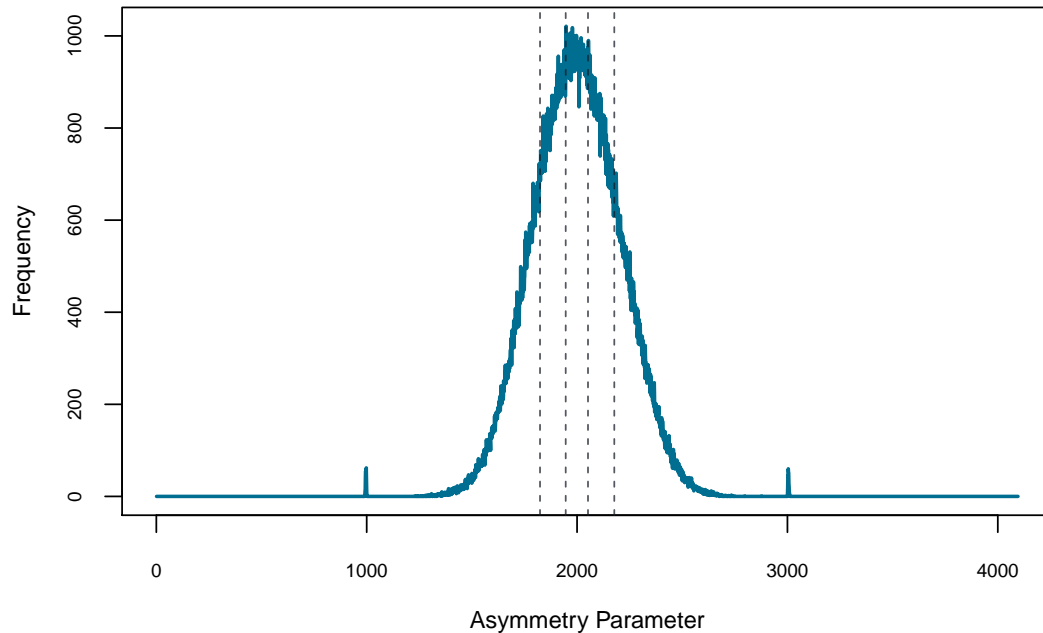

Figure 4.13: Distribution of asymmetry parameters for AC 6 of the absorber detector. The values have been shifted to centre around 2000. The peaks to the side of the distribution occur when no transient signal is found on the left or right contact. The distribution has been split into 5 equal parts to give a lateral position resolution of 1 mm from the 5 mm pitch of absorber strip contacts.

This methodology can only be performed for strips which have two neighbouring contacts. Strips on the edge of the detector cannot be calibrated in this way. Instead, an edge calibration method can be performed [23]. This method requires a face-scan of the detector and work is still ongoing to include XY-PSA for edge strips.

4.7.2 Z-PSA

The scatter and absorber detectors have a thickness of 8 mm and 20 mm respectively. Without any further knowledge of interaction positions it is assumed that all gamma-ray interactions occurred at the centre of these depths, and so the error on this position could be up to 4 mm and 10 mm in each corresponding detector. An electric field within the

volume of each detector saturates the velocity of charge carriers moving through the crystal. Therefore, the time it takes for these charge carriers to reach the detector electrodes shall be dependent on the gamma-ray interaction location. This information is stored in the risetime of real signals. Risetime is defined as the time it takes for a signal to reach a set fraction of its total amplitude. Figure 4.14 illustrates this concept for t90 (90% pulse amplitude), t50 (50%), t30 (30%) and t10 (10%). Short risetimes convey information on the charge carriers with the shortest drift time, whereas t90 offers improved signal to noise and is reflective of the complete charge collection time. Throughout this thesis, risetimes will be calculated as the difference in time for a signal to rise to a given fraction, relative to t10:

$$T90 = t90 - t10 \tag{4.4}$$
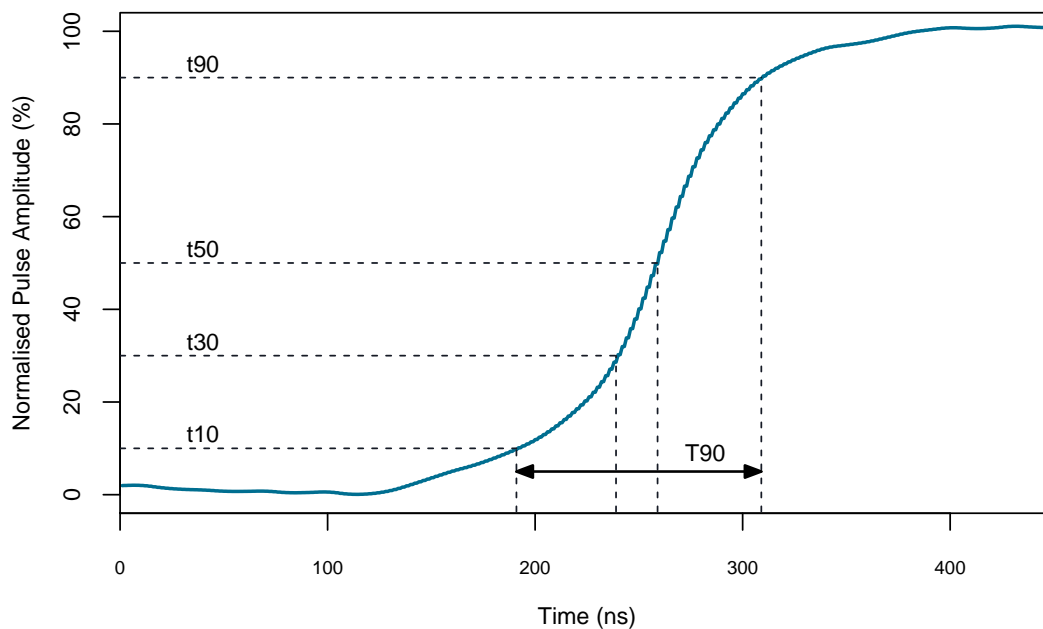
Figure 4.14: Risetimes for a pulse reaching 10%, 30% 50% and 90% of its full height.

Z-PSA utilises the risetime of a pulse to more precisely locate the interaction position of a gamma ray within the depth of a detector. Three Z-PSA methods have been tested to determine which resulted in the greatest improvement in image resolution. To begin, data to calibrate the detector response at known positions in the crystal was obtained. This is required to determine the relationship between risetime and event location. Due to time

constraints and the difficulty of obtaining the calibration data, Z-PSA was only developed for the absorber detector — which is the detector with the the largest uncertainty in Z. The detector was placed upon a Parker scanning table as orientated in Figure 4.15. Tungsten collimators were used to form a pencil beam from a 1 GBq Cs-137 source which scanned the detector in millimetre steps to produce a $60 \times 60 \times 20$ matrix of response points. At each scan position the collimator sat for 300 seconds, and 450 gamma rays were recorded per second [24].
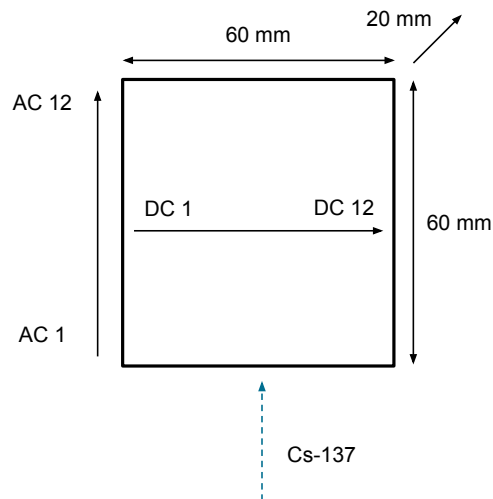
Figure 4.15: Illustration of the absorber detector crystal placed on the scanning table. The DC strips are located at 0 mm in depth.

The amount of data collected for each strip differed depending on its distance from the scanning table. Typically, all DC strips collected a similar number of events whilst the number of counts on AC strips decreased with increasing strip number. Each position collected over 600 signals corresponding to full 662 keV photopeak events. Not all the data collected could be used to determine the relationship between signal risetime and interaction location. For example, a gamma ray can undergo multiple interactions and therefore contain convolved risetimes components. The full selection of collected pulses for DC strip 6 at 10 mm are shown in Figure 4.16.
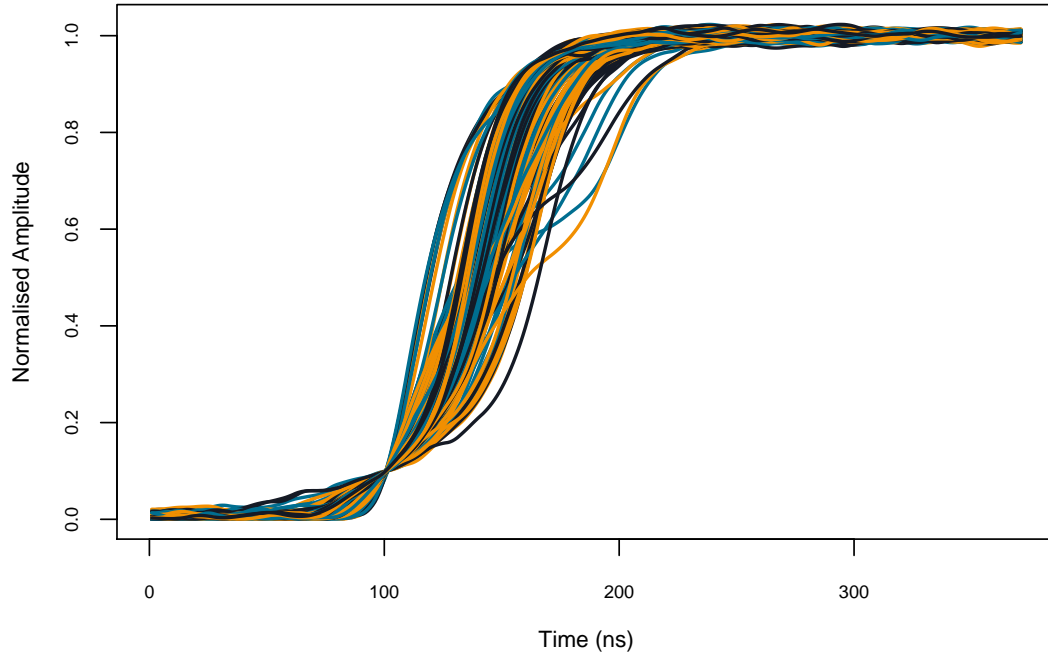
Figure 4.16: All signals collected from DC strip 6 on the absorber detector at an interaction depth of 10 mm. The signals were shifted to converge at t10. The variation in pulse shapes indicate the presence of additional events during charge transport.

A simple method was devised to remove pulses from calibration datasets which indicated the presence of multiple interactions, or other physical processes. Failure to separate these events would otherwise affect the calculated risetimes at each position in the crystal. The distributions of T90 minus T50, T90 minus T30 and T50 minus T30 for each position were investigated and any risetimes which deviated greatly from the average distribution were removed. For a given gamma-ray interaction position, the signal shape is expected to deviate in baseline noise only. Removing signals that show unusual risetime qualities ensures those remaining represent a single interaction at the depth of interest. The application of this method is shown in Figure 4.17 for signals collected on DC strip 6 at an interaction depth of 10 mm.
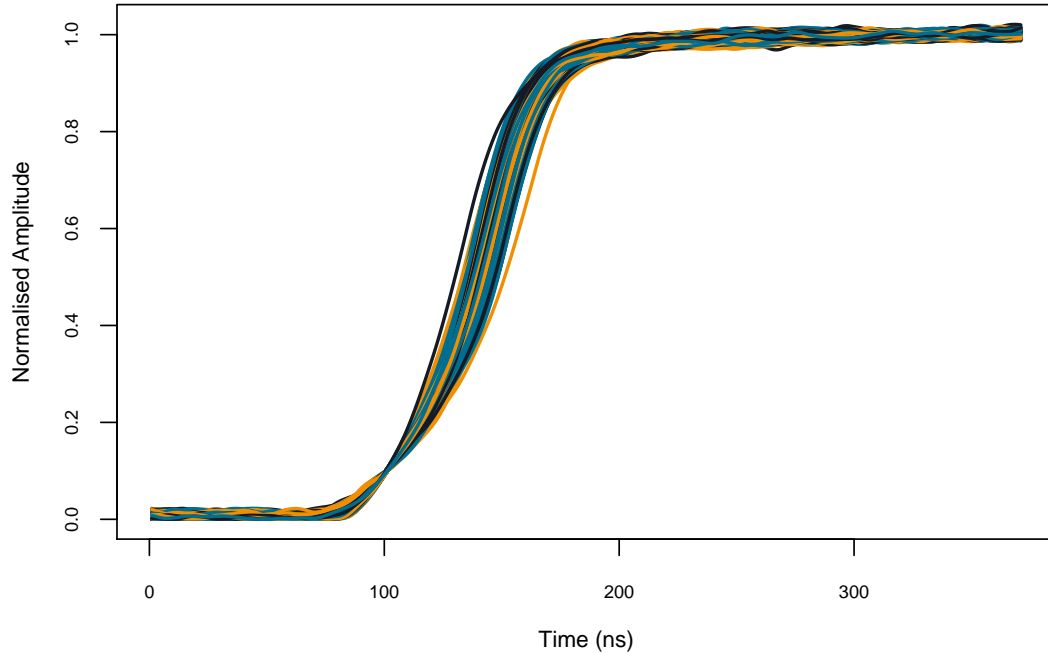
Figure 4.17: Signals collected on DC strip 6 which remained after using the simple cropping method. All pulses are aligned around t10.

To determine if the risetimes at each depth were uniform across each strip, the average risetime at each depth was compared, this is illustrated in Figure 4.18 for the 12 AC strips. A uniform distribution is observed for T30 and T50 but a more notable deviation is found in T90 risetimes. To highlight this, the standard deviation between calculated risetimes at each depth and the largest difference between risetimes for that depth, are displayed in Figure 4.19 for the AC face. The greater deviation seen for the calculated T90 values is likely a result of charge trapping or interference of carrier movement throughout the crystal as this relies on the almost-complete collection of electrons and holes. The increase in the maximum difference between risetimes at shallow depths (closer to DC strips) is not currently understood but is believed to be an effect caused by the electric field applied to the crystal. Further work is ongoing to investigate this phenomenon.
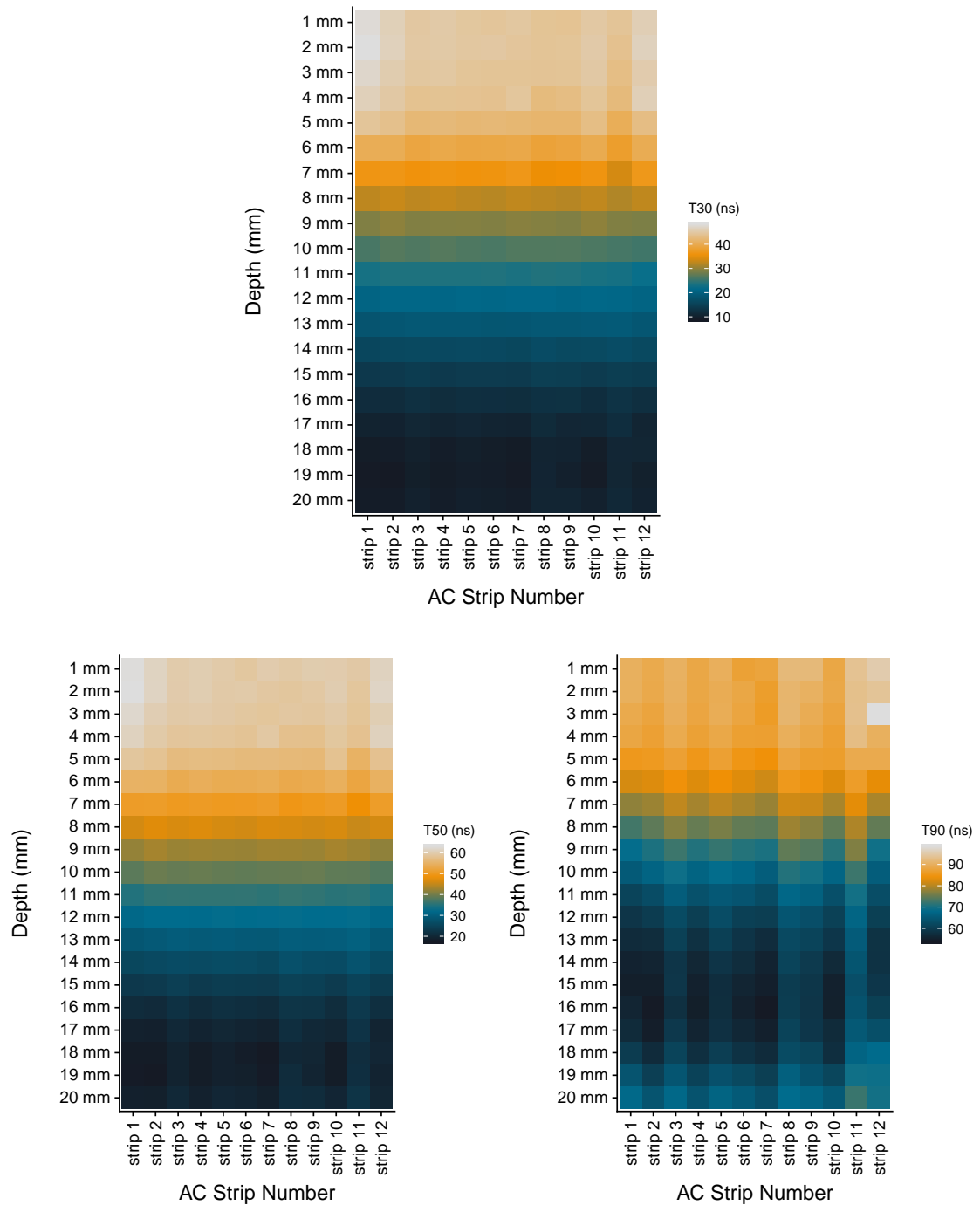
Figure 4.18: Heatmaps displaying the average T30 [top], T50 [bottom left] and T90 [bottom right] risetimes for all AC strips at all depths. Greater uniformity across strips is seen for T30 and T50. The colour represents risetime in nanoseconds.
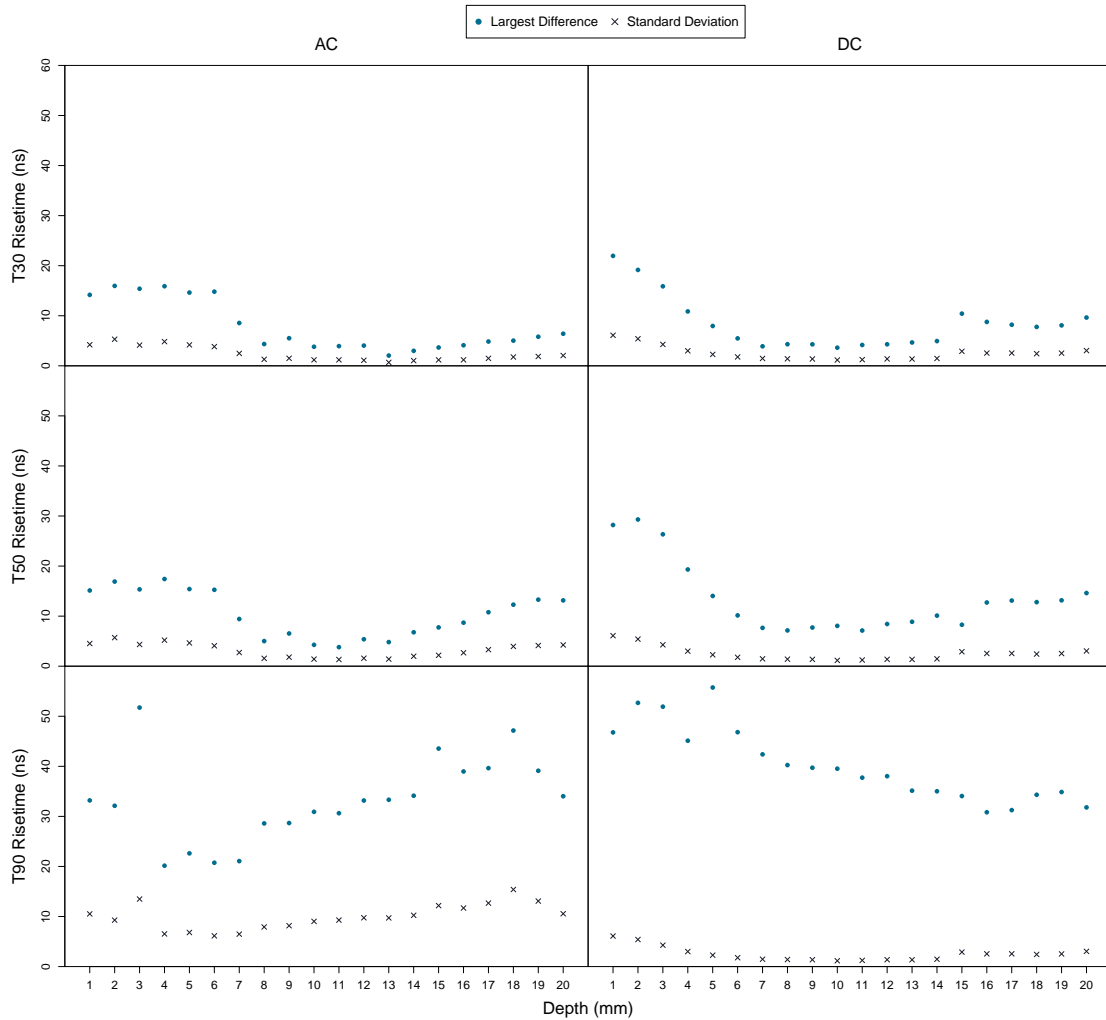
Figure 4.19: Standard deviations and the variation in risetimes for T30 [top], T50 [middle] and T90 [bottom] across each strip at each depth. Large risetime variations are seen for T90 for each depth across all strips.

Z-PSA Method 1 - T30 vs T90 Gates

The distribution in risetimes at each depth for a given strip indicates that a single value is not unique to any location. Large degrees of overlap in risetimes are observed between depths that are close to each other. This is illustrated in Figure 4.20.
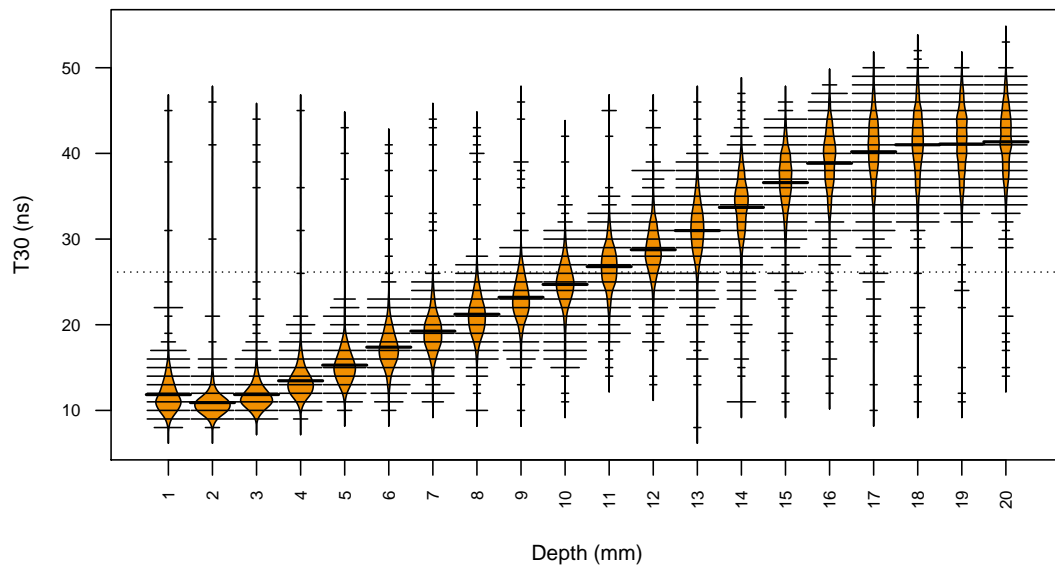
Figure 4.20: Beanplot of T30 risetimes for each depth (1 - 20 mm) for DC strip 6. The coloured regions indicate the distribution density. The horizontal lines show individual data points with wider lines indicating more data points. The dashed horizontal line is the average T30 across all depths. The overlap of risetimes indicates a single risetime will not be suitable for determining the depth of an interaction.

The percent of overlap between neighbouring distributions was calculated and used to determine groupings of detector depths which would result in the smallest overlap between grouped distributions. Table 4.1 shows the calculated overlaps between each interaction depth distribution for DC strip 6 and the overlap between the chosen groupings.

By combining various depth distributions, the detector can be segmented into volumes identified by risetime values. Combination of the distributions minimises the overlap in risetimes between different detector sections. The final grouping selected split the detector into three discrete sections; 1 - 4 mm, 5 - 13 mm and 14 - 20 mm, shown in Figure 4.21. A gamma-ray interaction that takes place at an unknown depth can be localised to one of the three positions using the risetime of the preamplifier signal, with only a small probability of the incorrect region being chosen.

Combined Depths (mm)	Amount of Overlap (%)
1 - 2	69.90
2 - 3	70.33
3 - 4	51.37
4 - 5	55.82
5 - 6	56.89
6 - 7	63.04
7 - 8	63.89
8 - 9	64.16
9 - 10	65.92
10 - 11	65.88
11 - 12	68.53
12 - 13	63.54
13 - 14	59.87
14 - 15	61.61
15 - 16	70.35
16 - 17	80.68
17 - 18	68.33
18 - 19	87.52
19 - 20	84.78

Combined Depths (mm)	Amount of Overlap (%)
[1 - 4] - [5 - 13]	13.17
[5 - 13] - [14 - 20]	13.35

Table 4.1: Percent overlap for neighbouring depth distributions before and after grouping.
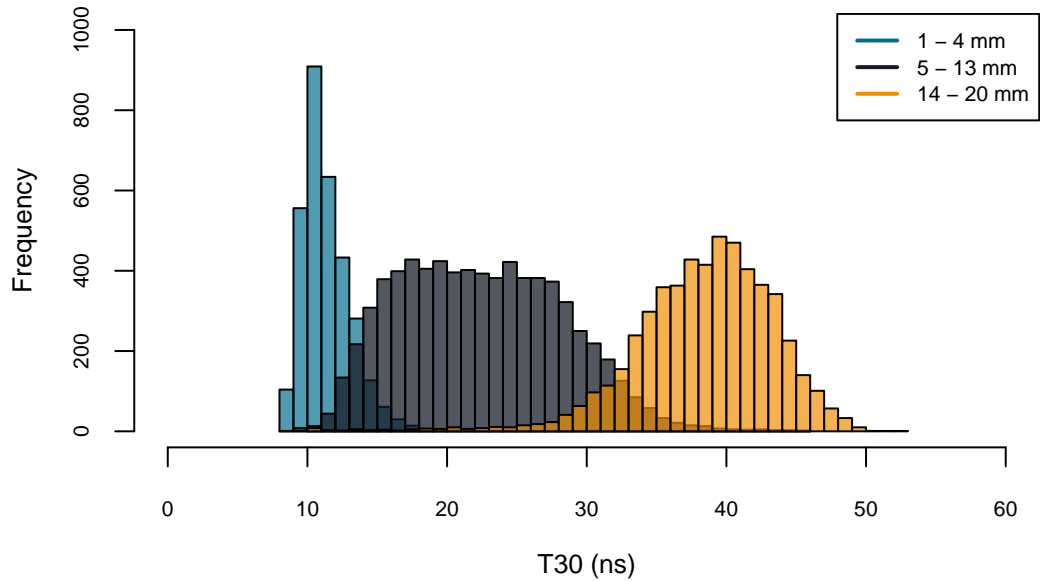
Figure 4.21: T30 risetime distributions on DC strip 6 for the three grouped depths.

Further precision on the depth of the interaction can be obtained by placing the same gates on T90. Figure 4.22 shows a beanplot of the T90 risetimes for DC strip 6 at each depth. An inflection can be seen in the T90 distributions along with large ranges and substantial outliers. Due to the inflection, no gates could be set on DC T90 as the same depth groupings must be placed on each risetime.
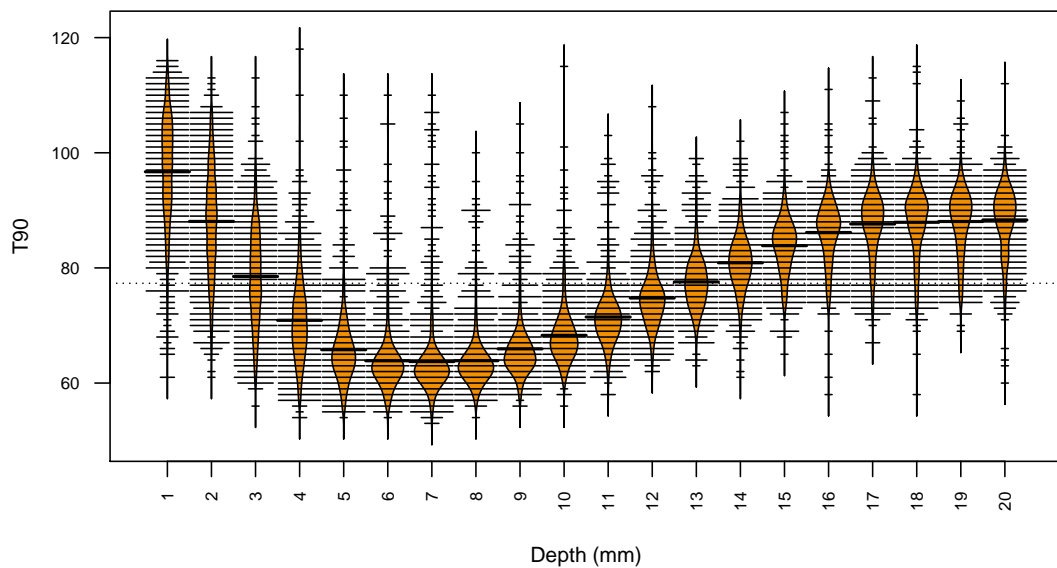

Figure 4.22: Beanplot of T90 for each depth for DC strip 6. The dashed horizontal line is the average T90 across all depths. An inflection is seen in the risetimes.

For the AC side of the detector, the optimum groupings of depths were calculated to be 0 - 7 mm, 8 - 14 mm and 15 - 20 mm to give distribution overlaps of 13.72 % and 10.52 % respectively for T30. The overlap for T90 was 14.48 % which consisted of two groups; 0 - 7 mm and 8 - 20 mm (AC groups 2 and 3 of T30 were combined). Using these gates the detector is split up into 3 discrete regions where an event can be localised through comparison of its risetime. This is illustrated in Figure 4.23 which shows AC T30 vs T90 for all depths and for each of the grouped depths.
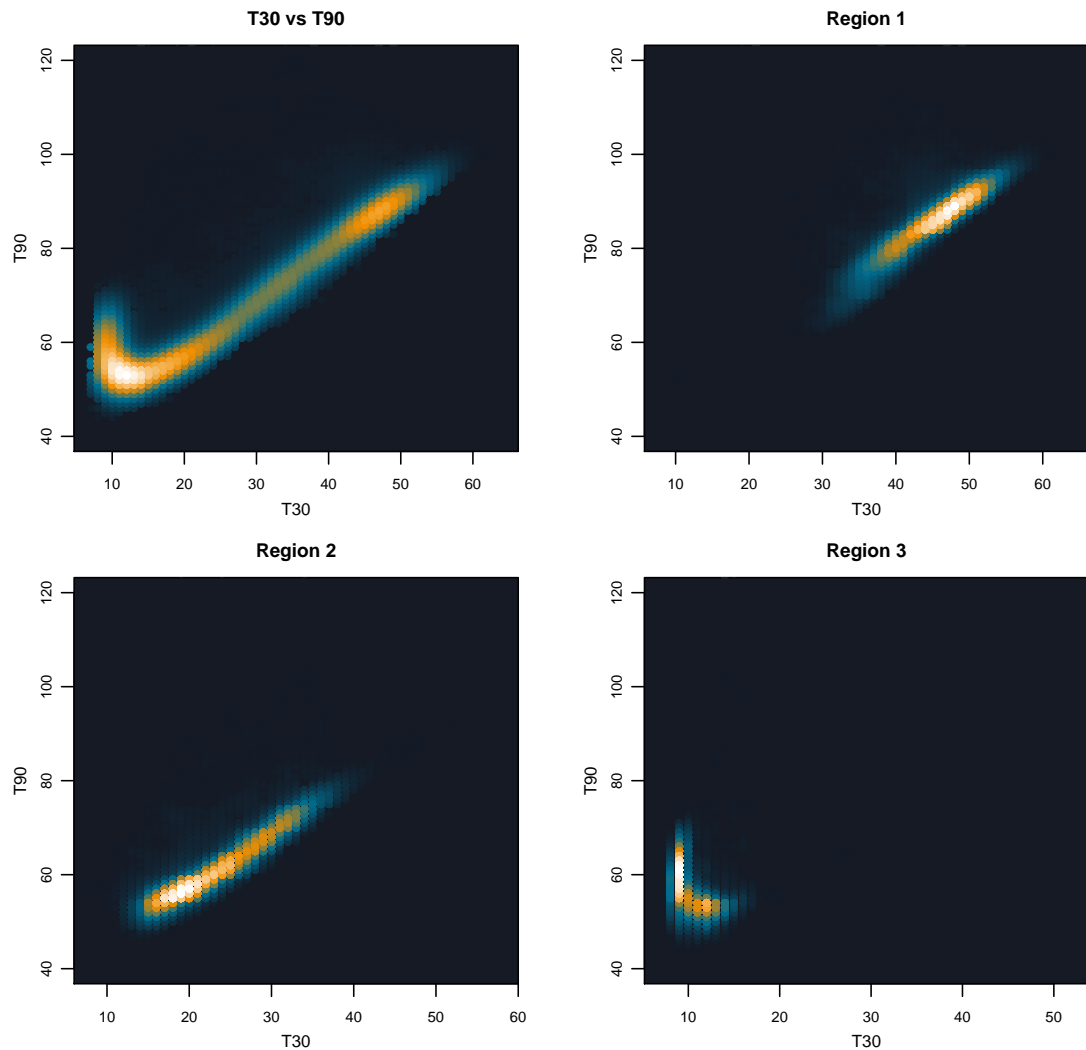
Figure 4.23: T30 vs T90 for AC strip 2. Plots show the full set of risetimes along with each of the risetimes in the combined depth regions. By comparing the risetime of an event occurring at an unknown depth with each of the regions it is possible to localise the event to one of three detector locations.

Z-PSA Method 2 - Risetime Correlation

T30 vs T90 risetime comparison methods can only localise an event to one of three positions within the absorber detector. By splitting the depth of the detector into a greater number of sections a better position resolution can be obtained, and therefore a clearer reconstructed image formed. The second method investigated for this system used risetime correlation. It compared the risetime found on one face of the detector to that found on the opposite face. For example, when an interaction takes place close to the AC side of the crystal, the DC side shall have a large T30 indicating a long period for charge transport. In this scenario, the AC side shall have a small T30 as the distance travelled by the charge to reach the contact will be minimal. By comparing the two it is possible to calculate the location an interaction occurred in the system.

As shown in Figure 4.18, the average T30 and T50 risetimes were more uniform across the detector strips than T90. For this reason, and the inflection in T90, T30 and T50 for each detector face were compared for this method. Figure 4.24 shows the calculated risetime correlations. Errors were calculated using the standard deviation of risetimes at each depth.
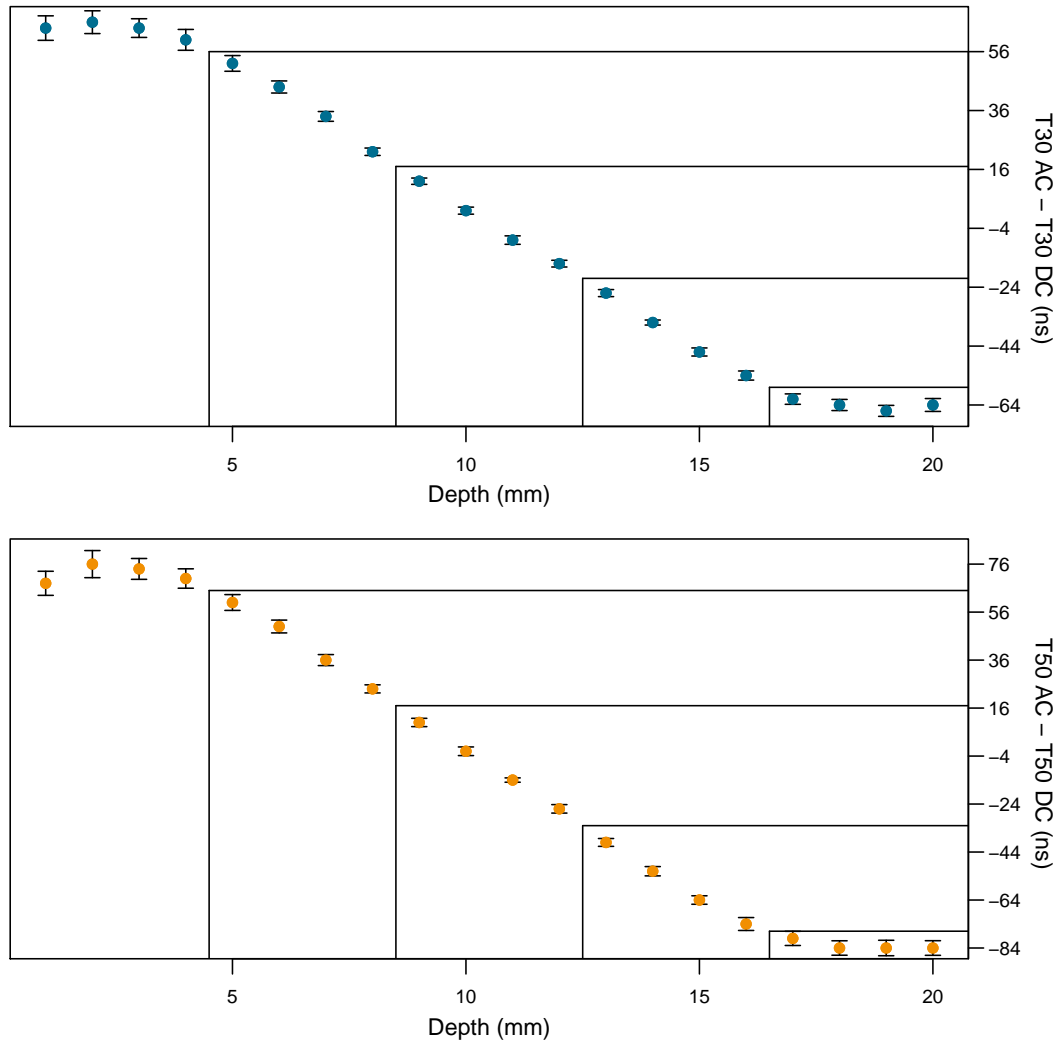
Figure 4.24: T30 AC minus T30 DC [top] and T50 AC minus T50 DC [bottom]. The calculated values have been split into five regions.

By comparing the risetimes from signals obtained during data acquisition, this method can segment the depth of the detector into 5 regions; 1 - 4 mm, 5 - 8 mm, 9 - 12 mm, 13 - 16 mm and 17 - 20 mm.

Z-PSA Method 3 - Chi-Squared Minimisation

The final technique compared the risetimes of an event from an unknown location in the absorber detector to the known average risetimes at each depth in the detector. Using a chi-squared minimisation of the differences between the two — an estimate of the interaction location is made. Figure 4.25 shows the average pulse shape at each millimetre depth for

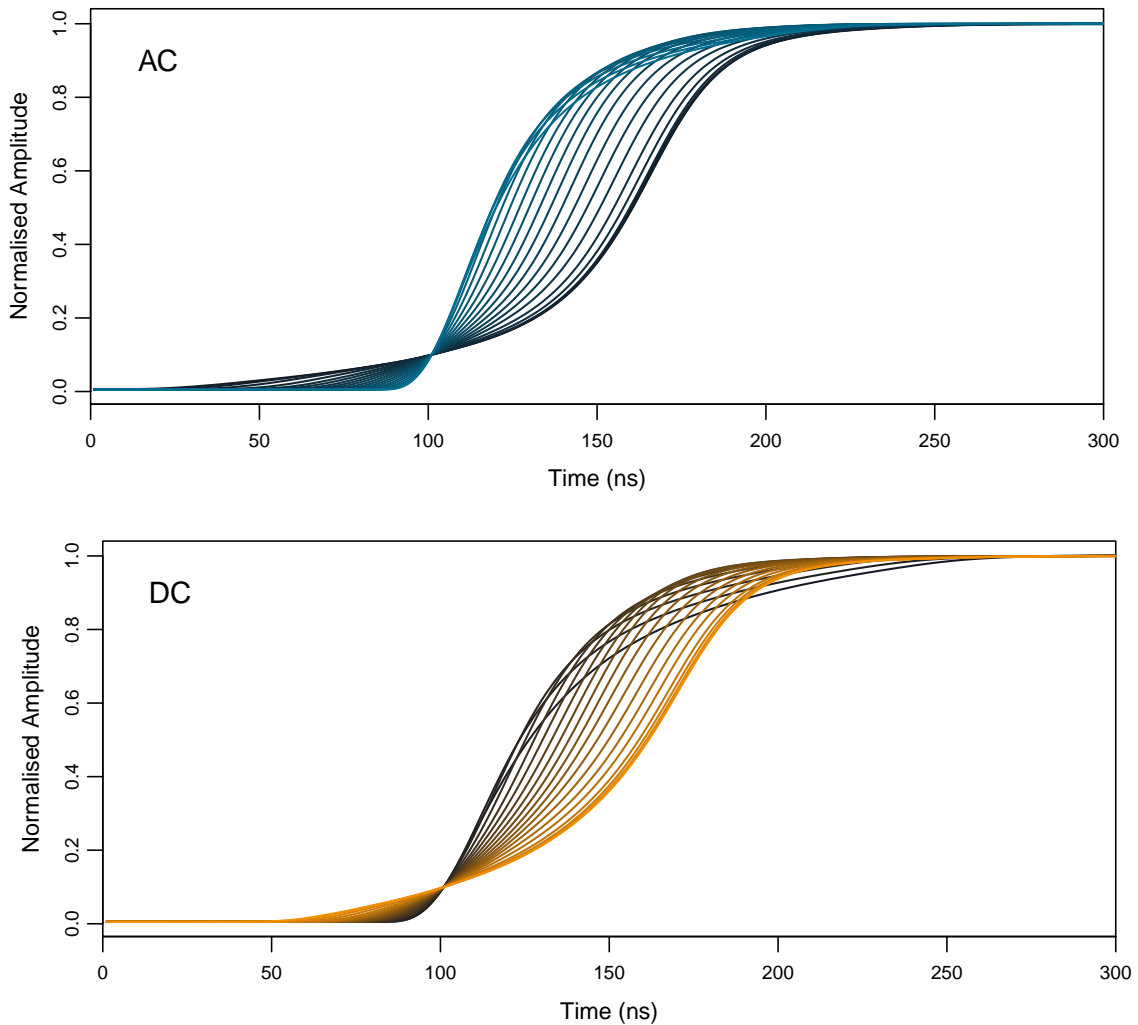the AC and DC sides of the detector.

Figure 4.25: Average AC and DC pulses from each position in 1 mm steps through the detector depth.

Theoretically this method segments the detector into 20 z-sections, giving an overall position resolution within depth of 1 mm. However, interactions which occur nearer to the edges of the detector show smaller risetime deviations than those from the centre of the detector. The result of this is a greater sensitivity within the bulk of the crystal and poorer performance when locating an event closer a face. Table 4.2 displays the calculated average risetimes at each depth in the detector.

Depth (mm)	Average Risetimes (ns)					
	T30 AC	T50 AC	T90 AC	T30 DC	T50 DC	T90 DC
1	89	119	180	25	50	192
2	88	119	180	23	45	172
3	88	118	180	24	45	152
4	88	117	177	28	48	136
5	84	114	173	31	54	128
6	79	108	166	35	59	126
7	71	100	158	39	64	126
8	65	92	150	42	69	128
9	58	84	141	46	74	132
10	52	77	133	50	80	138
11	47	70	126	53	84	145
12	42	64	120	57	91	152
13	36	58	116	62	98	159
14	32	52	113	68	104	166
15	28	46	111	74	110	172
16	24	42	112	78	116	178
17	21	38	114	82	118	180
18	19	36	120	83	120	182
19	19	36	127	84	121	183
20	19	38	133	84	121	184

Table 4.2: Average risetimes at each depth in the detector.

4.8 Crosstalk Correction

The front two detectors in GRI+ are segmented using orthogonal strip contacts. When the system is operated in all-masked mode each detector strip is read out simultaneously. Crosstalk is the production of a signal response in one circuit due to the undesired coupling with another. In GRI+, crosstalk due to capacitive coupling between neighbouring strip contacts results in the baseline shift of signals from the preamplifiers [25].

An addback energy spectrum shows the total energy deposition in a detector. It is calculated for each face of the detector by adding the energies deposited in individual strips. Transient signals neighbouring an event show small baseline offsets which would normally indicate a deposition of energy. The sum of energy depositions in higher fold events show peaks at greater energies than their fold-1 counterparts. The shift of gamma rays from the fold-1 position is seen to increase with fold and energy. This shift can be explained by higher fold events generally occurring between neighbouring strips. In these cases the baseline offset is combined with the real signal and the energies are therefore calculated to be higher. A correction for this shift must must be applied to remove the broadening and doubling of peaks in a spectrum containing multi-fold events. Figure 4.26 is an energy spectrum produced from the combined fold-1 and fold-2 events in the absorber detector and shows the broadening and splitting of peaks.
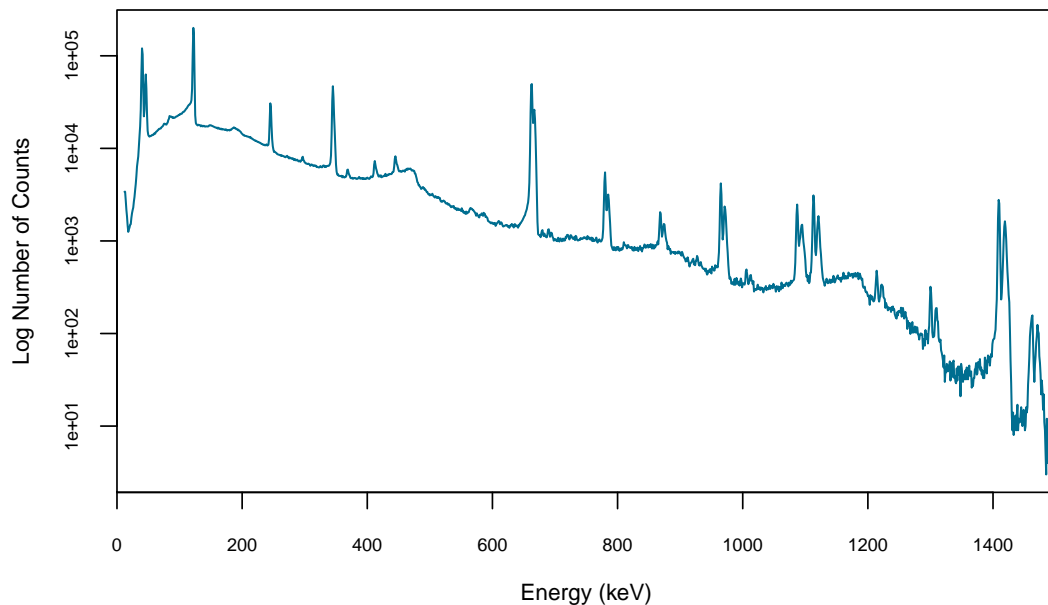
Figure 4.26: Addback energy spectrum consisting of fold-1 and fold-2 interactions from the AC side of the absorber detector showing the broadening and splitting of photopeaks with increasing energy.

Crosstalk is only apparent between neighbouring strips, where the associated strip electronics are at their closest. Figure 4.27 shows the addback energy spectra obtained from fold-2 events between adjacent and non-adjacent strips. The degree of energy shift increases with increasing energy indicating the effect is caused by a proportional form of crosstalk.
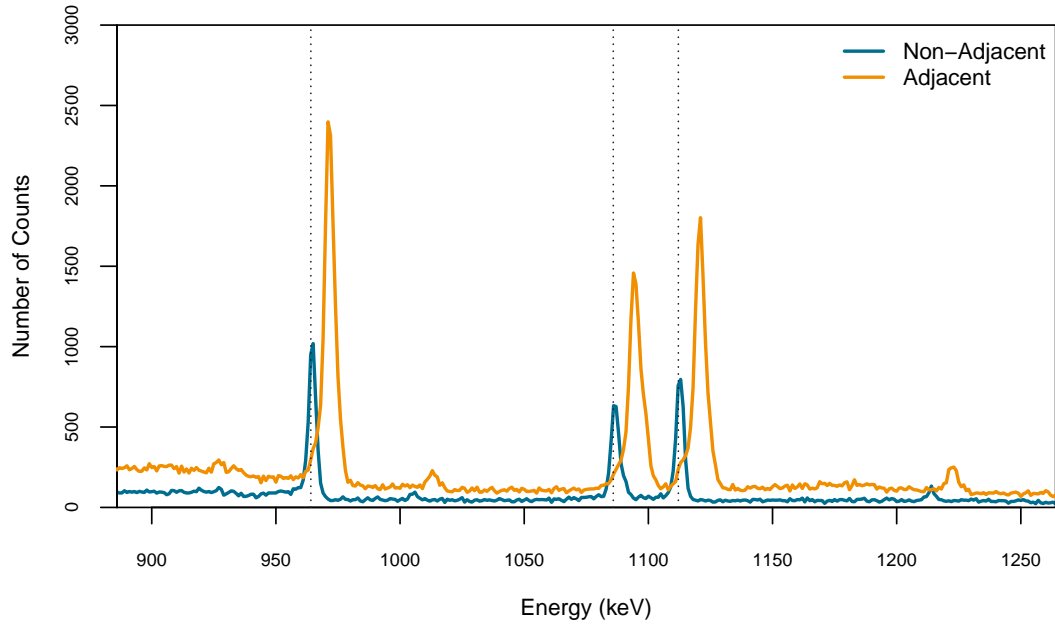
Figure 4.27: Addback energy spectrum for fold-2 events in adjacent and non-adjacent strips indicating the baseline shift for events which interact in neighbouring strips. The correct photopeak energies are indicated by the dashed vertical lines.

The incorrect calculation of energies deposited in the detector will result in the incorrect opening apex angles of Compton cones. Furthermore, these events shall be removed during image reconstruction if they lay outside chosen energy gates, leading to a reduction in the Compton camera's efficiency. A correction must therefore be applied to the calculated energies of fold-2 events interacting in neighbouring strips if they are to be used for image reconstruction. This correction factor is determined from the degree of photopeak shift from the expected location as a function of photopeak energy, shown in Figure 4.28. The plot was produced using the fitted centroids from a Cs-137 point source and Eu-152 point source in the MTsort software.
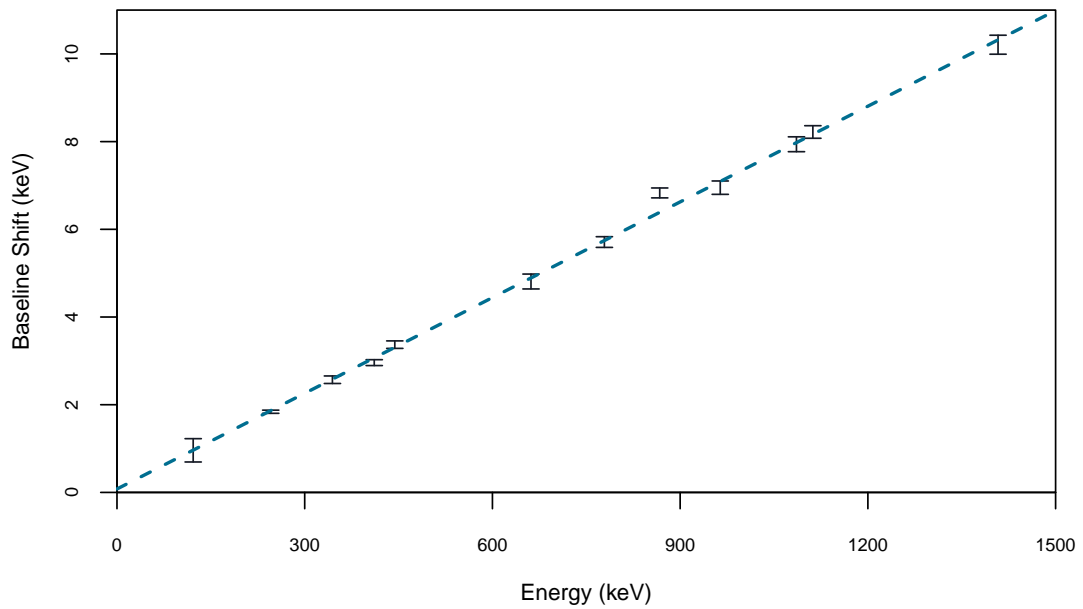
Figure 4.28: Baseline shift as a function of the photopeak energy. The gradient indicates the magnitude of proportional crosstalk in the system, 0.73 % on the AC side of the absorber detector and 0.26 % on the DC side.

The proportional nature of the crosstalk is shown in Figure 4.28. The degree of crosstalk is calculated from the gradient of the plot, found to be 0.73 % on the AC side of the absorber detector and 0.26 % on the DC side. Once the correction is applied, the total fold-2 addback spectrum shall contain only one peak as shown in Figure 4.29. This results in a stark increase in the number of reconstructible photopeak events. Once the energy and positions of real events are established, the data is formatted into a text file to be used in an image reconstruction code.
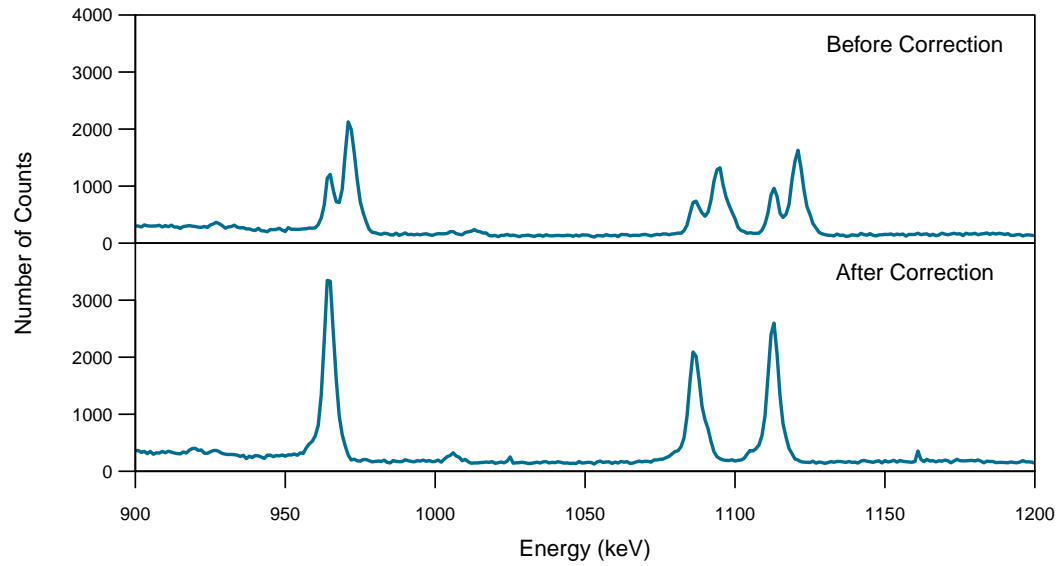
Figure 4.29: Fold-2 addback spectrum before and after the correction factor was applied for calculated fold-2 energies.

Chapter 5

Imaging with GRI+

Multiple image reconstruction algorithms are available for Compton imaging at the University of Liverpool (UoL). Algorithm choice is based on the needs of the user, such as time constraints and the geometry of the source being reconstructed. There are two methods of reconstruction, analytical and iterative. Analytical codes generally operate in a single step, determining the distribution of a source at a given distance using vector calculations. Iterative codes are based on the maximisation of probability, or another variable, and run multiple times at the users discretion, or up to some converging criteria. Iterative codes require greater amounts of processing time compared to analytical codes.

UoL codes are capable of processing fold-1 (F[1,1,1,1,1/0]) and fold-2 (F[1,1,1/2,1/2,1/0]) events and the format of input data is identical for each. For the purpose of this thesis most codes were rewritten into the languages of python [26] and R [27]. For code segments requiring a large number of repetitions, cython [28] was integrated to reduce run times.

This chapter shall discuss the various reconstruction codes available, the improvements achieved from PSA and further investigations into the quality of reconstructed images. A Cs-137 point source placed 10 cm from the front of the detector is used throughout this chapter when testing features of the imaging codes. This dataset was chosen due to its high statistics, single photopeak energy and short stand-off distance. The hardware on which the codes were run is an early 2015 Macbook pro, using a 2.9 GHz Intel Core i5 processor.

5.1 Image Reconstruction Methods

5.1.1 Analytical Image Reconstruction

The analytical reconstruction code is based on the simple back projection of cones [29]. The cones begin in the scatter detector and are projected outwards onto one or more x-y planes, known as slices. The input data are used to calculate the geometry of each Compton cone, which are discretised into a chosen number of points per angular degree as shown in Figure 5.1. This discretisation is known as conic sampling.
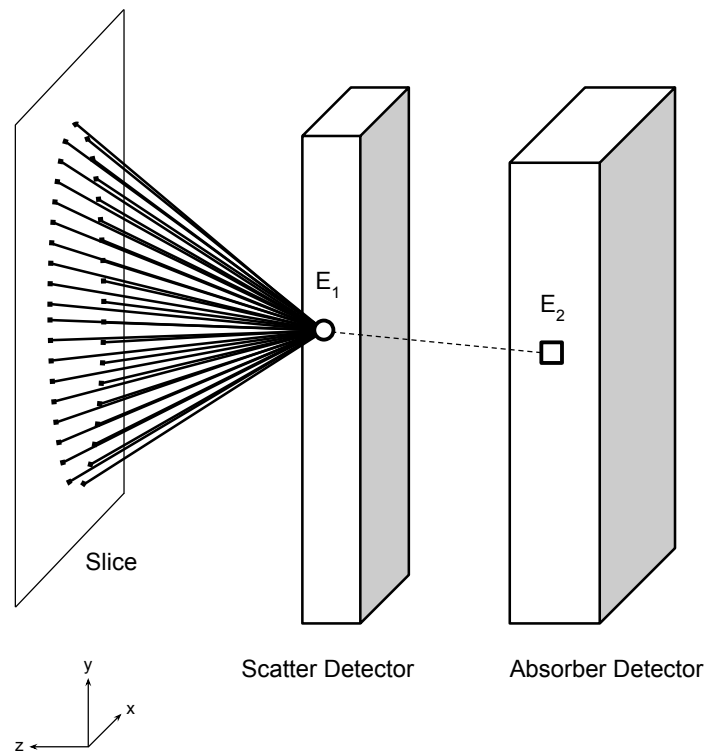

Figure 5.1: A Compton cone begins in the scatter detector and is projected onto a slice at a chosen distance. The Compton cone is discretised into a given number of points per angular degree of the cone.

The z-position of a slice is relative to the back of the absorber crystal, therefore it is important to know the separation of the detector cryostats and position of detector crystals within their housing. The user is prompted to filter the data before reconstruction, applying energy gates and cuts on the allowed scattering angles. In the original C-code, Root [30] is used to produce several key figures such as:

- The 2D imaging slice of overlapping cones, known as the 'Compton image'

- The FWHM of projections taken from the slice at the row and column containing the greatest number of conic overlaps

- A 3D plot of interaction positions within the detectors

- Energy spectrum with highlighted energy ranges used

- Angular distribution of events and highlighted fraction of events used

A fit is applied to the Compton image at the row and column containing the pixel with the maximum number of conic overlaps. An example slice and corresponding fits are shown in Figures 5.2 and 5.3 respectively. The data to produce these images was acquired using a Cs-137 point source 10 cm from the front of the detector, from the R version of the code.
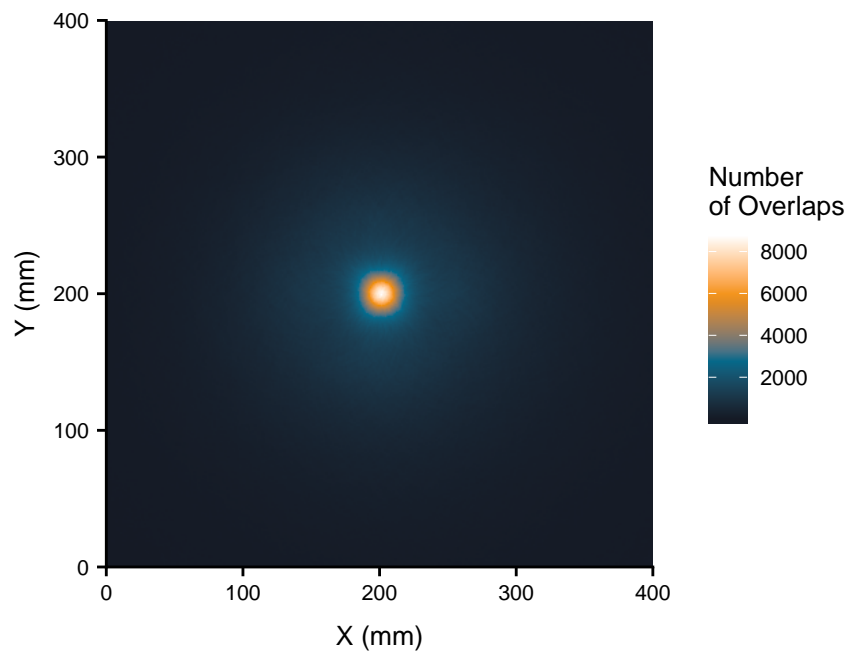
Figure 5.2: Image slice produced from the analytical image reconstruction code. The image was produced from a Cs-137 point source, 10 cm from the front face of the scatter detector cryostat.
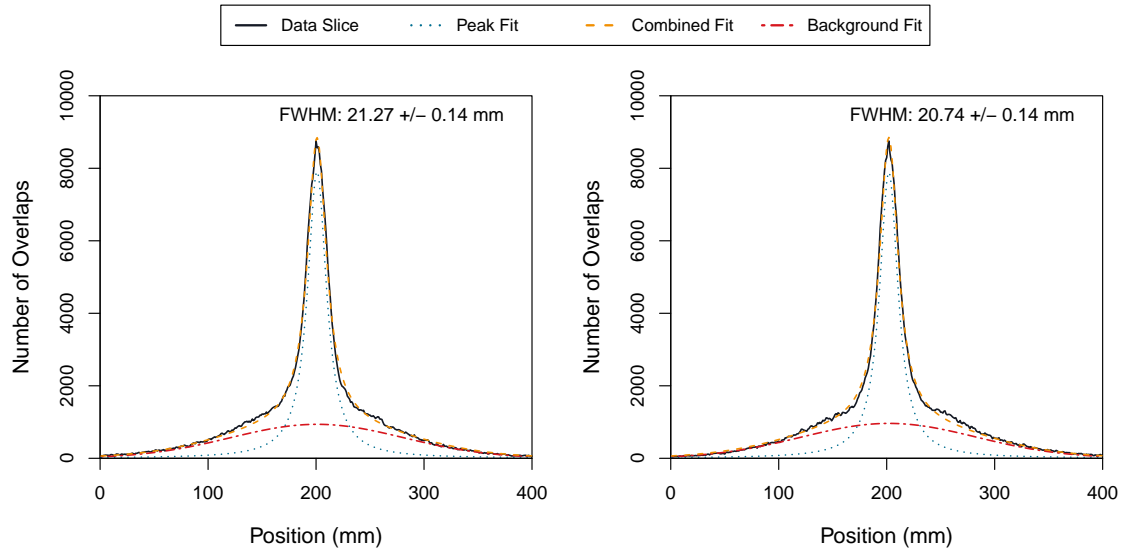
Figure 5.3: Analytical code output. The row [left] and column [right] containing the pixel with the maximum number of Compton overlaps has a distribution fitted to calculate the FWHM of the reconstructed image.

The time taken for a reconstruction is primarily determined by the size of the imaging slice, number of events to process and number of points drawn per degree of the Compton cone. For all reconstructions in this thesis a 400×400 mm^2 image slice is used. The time taken for an analytical reconstruction at various degrees of conic sampling is displayed in Figure 5.4. Times were calculated from the average of 200 reconstructions and errors were determined using the standard deviation of these values. A typical reconstruction takes less than 3 seconds, with the statistical noise of profiles reducing as the number of reconstructible events and conic sampling increases.
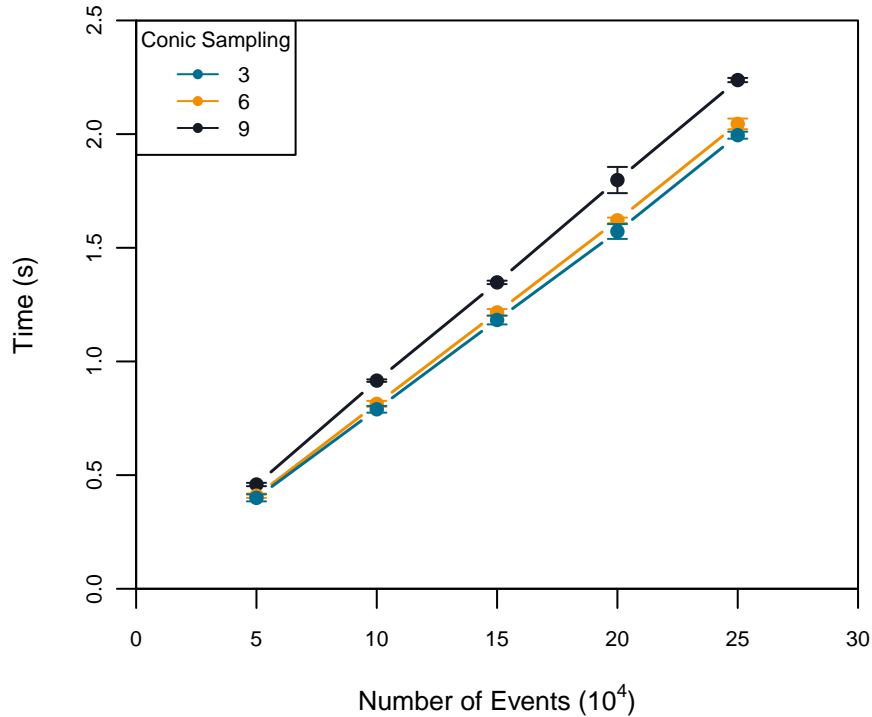
Figure 5.4: Time taken to reconstruct data using the analytical code as a function of the number of events and degree of conic sampling.

5.1.2 Iterative Image Reconstruction

Three iterative reconstruction codes are available at UoL; MLEM (Maximum Likelihood Expectation Maximisation), OSEM (Ordered Subset Expectation Maximisation) and SOE (Stochastic Origin Ensemble). For the purposes of this thesis the MLEM and OSEM codes were optimised anew and the SOE code was created from scratch.

MLEM

The MLEM code is based on an algorithm by Andriy Andreyev [31]. Cones are first projected into an imaging volume (a $400 \times 400 \times 400$ array) where each array element intersecting a cone is incremented. This first step produces an image comparable to the analytical code. Subsequent iterations forward-project the cones through the image volume to calculate weights associated with each cone. These weighted cones are then back-projected through an empty imaging volume to establish a probability matrix which is multiplied by the state of the previous imaging volume.

The time required for each iteration depends on the number of events to be reconstructed, size of the imaging volume and degree of conic discretisation. The MLEM code is by far the slowest of the available codes and a single reconstruction generally takes a day. The time taken for a single iteration from the C-version of the code for various settings is explored in Figure 5.5. Times were calculated by averaging over 10 iterations, and errors were established from the standard deviation of these values. For most reconstructions in this thesis the number of points per degree of Compton cone is set to 9 and over 100,000 events are used.
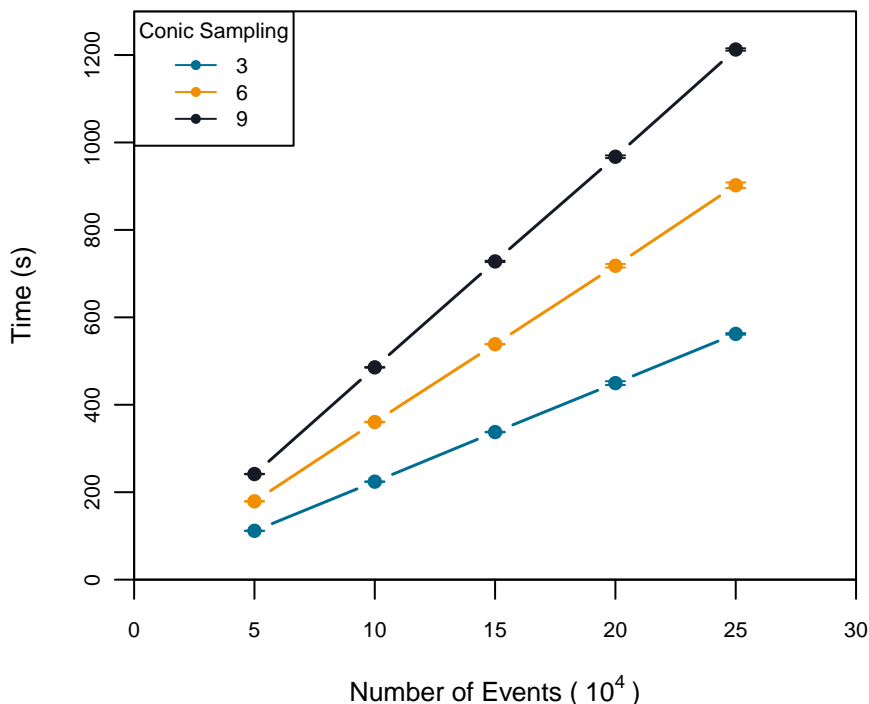
Figure 5.5: Time taken for an iteration from the C-version of the MLEM code for various degrees of conic discritisation. Imaging array size is $400 \times 400 \times 400$.

There is currently no converging criteria implemented into the MLEM code but future work is focused on addressing this issue along with the extended processing times. Figure 5.7 shows the image slice produced in three iterations of the MLEM code. With each iteration the respective intensity slices, displayed in Figure 5.6, further shift from a distribution described by a Lorentzian peak upon a Gaussian background. This means the FWHM of MLEM imaging slices and therefore quality of reconstructed images, cannot be quantitatively calculated using current methods.
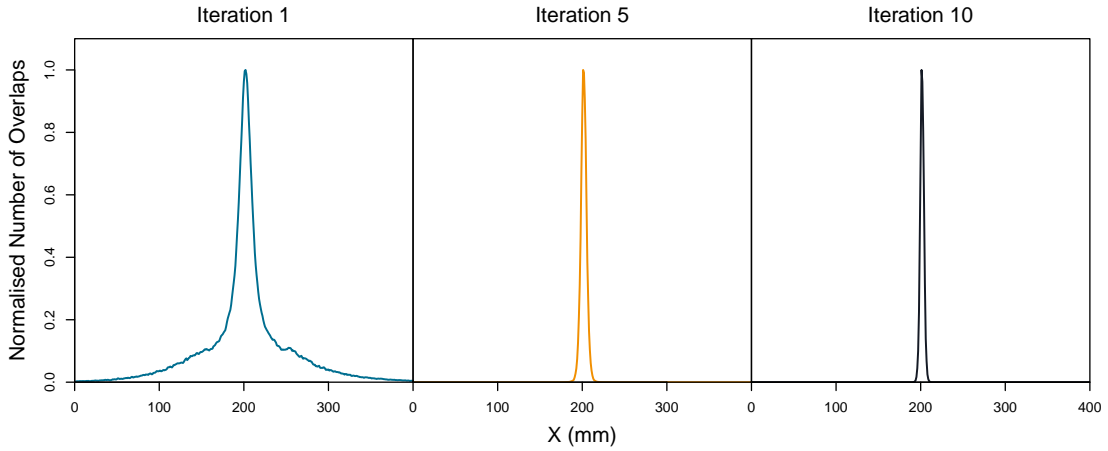
Figure 5.6: The first[left], fifth [middle] and tenth [right] intensity slices produced from the MLEM code. Data produced from a Cs-137 point source 10 cm from the front of the detector.
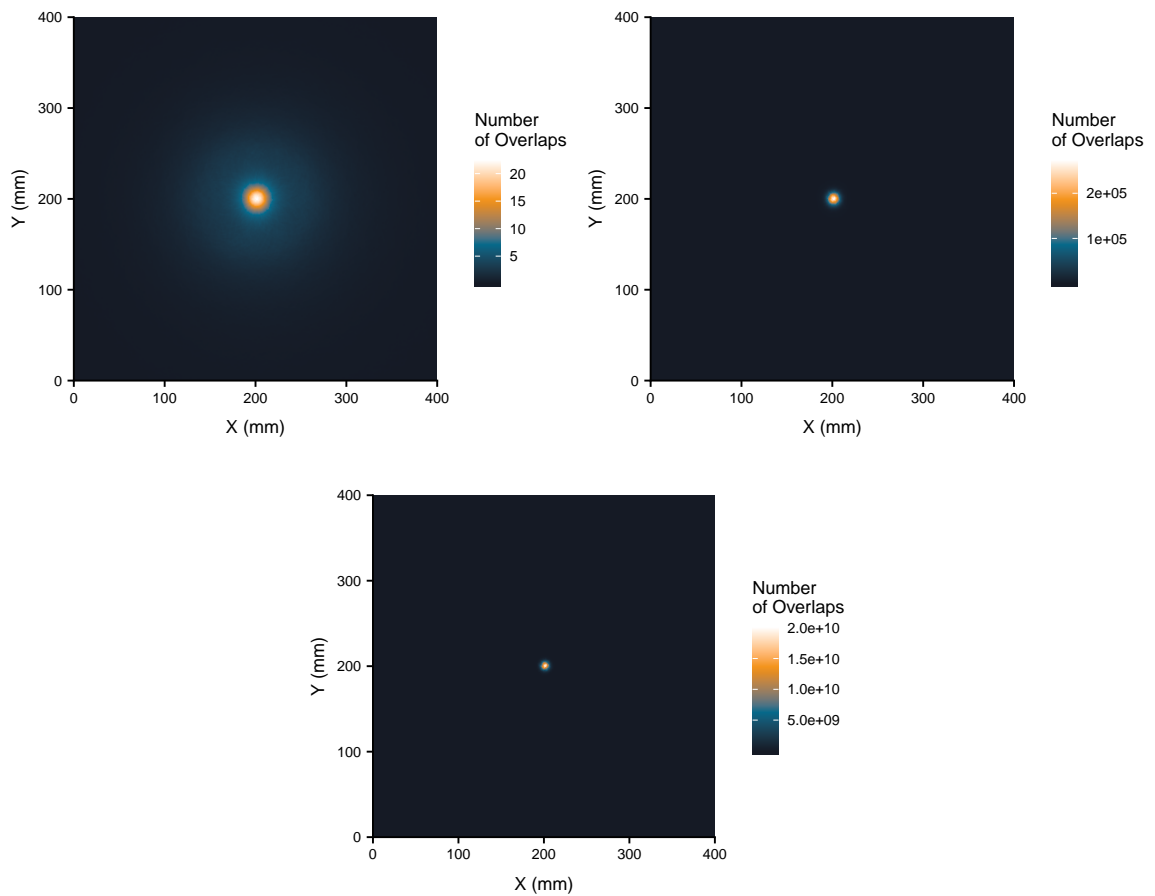

Figure 5.7: Output of the MLEM image reconstruction algorithm. The first [left], fifth [right] and tenth [bottom] iteration of the code for a point source 10 cm from the detector.

OSEM

The structure of the OSEM and MLEM codes are almost identical. The difference comes from the user's choice to run the events in batches, known as subsets. By calculating probability matrices for batches rather than the complete set of data, errors caused by global uncertainties are reduced. This uncertainty is further reduced by increasing the number of subsets which results in a better image resolution. The achievable resolution using the OSEM code with n iterations of m subsets is approximately what can be expected from the MLEM code running $n \times m$ iterations.

The time taken for an iteration of the OSEM code is identical to that of the MLEM code. The additional subset parameter of the OSEM code can result in over-iteration of an image whereby the actual distribution of a radioactive source falls between two iterations. The choice of optimum parameters for the OSEM code is more difficult when compared to that of the MLEM and work must be conducted to understand how to obtain the best results based on this selection. For the purposes of this thesis the MLEM code was used exclusively when reconstructing later experimental data due to this.

SOE

The SOE code was written entirely during this project. It is the fastest of the available iterative codes but favours point sources and performs poorly for extended geometries. A Compton cone projected onto a slice is represented by several points in the shape of an ellipse. A gamma ray which interacted in the detector only came from one of those many points. The SOE code works by displaying only one randomly selected point for each event. Subsequent iterations then move the points, one at a time, and establish whether the newly selected position is more or less likely to be the actual position of the gamma-ray source. This is based on the density of points in an n × n grid at the new position compared to the previous. The size of the averaging grid is determined by the user. Figure 5.8 illustrates the basic workflow of the algorithm.

Increasing the size of the averaging grid results in improved image resolutions and less clustering of points. The main contributors to the processing time of each iteration was found to be the number of events processed and the averaging grid size. This relationship is shown in Figure 5.9 for a 400×400 mm^2 image slice and discretisation of 9 points per angular degree of Compton cone. The degree of discretisation was determined to have no
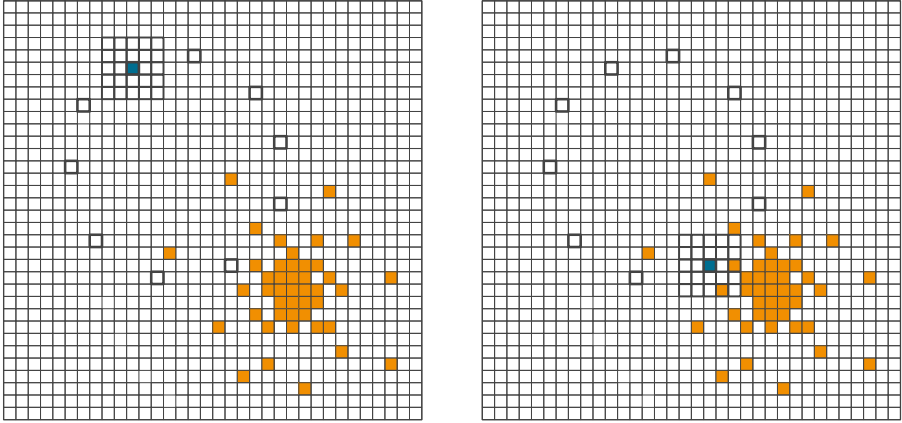
Figure 5.8: Each iteration selects one point from each ellipse and determines if the density at a
second point is greater than at its current position. The blue point on the left slice
has a lesser density than the one on the right, based on a 5 x 5 grid. If selected during
an iteration the point would be moved to the new position.

effect on the processing time as only one point is processed for each event per iteration,
regardless of the total number of coordinates making up an event. Time was calculated
by averaging over 50 iterations and errors were established from the standard deviation of
the values.
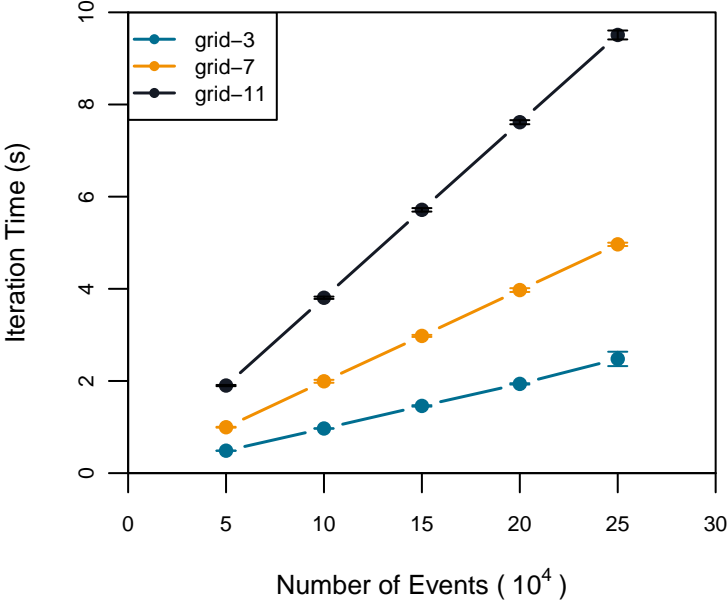
Figure 5.9: Relationship between grid size, number of points and iteration time for the SOE recon-
struction code. Times calculated from the average of 50 iterations, errors calculated
using the standard deviation of values.

The number of points moved per iteration is reduced as the optimum image is formed. Typically 40 iterations is sufficient to ensure the output image is representative of the source. The fraction of events moved per iteration for a Cs-137 point source 10 cm from the detector is shown in Figure 5.10. An averaging grid size of 11 was used to produce this plot.
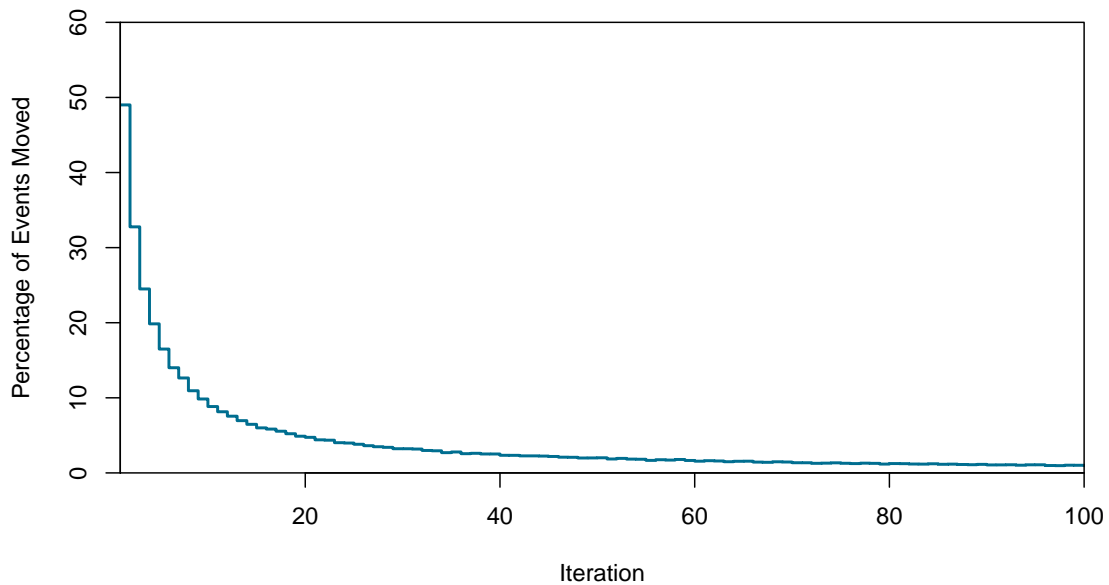

Figure 5.10: Percentage of points which are moved per iteration. Typically around 40 iterations is sufficient to produce a good representation of a source distribution.

Once the selected number of iterations have been processed, a final iteration is run. This takes each individual event, calculates the density at each point on the ellipse, and then places the point at the optimum position. Iterations are required before this step as the starting scenario greatly influences the output. If the source distribution is not already somewhat accurate then the outcome will not improve the image. Figure 5.11 shows several iterations from the SOE code.
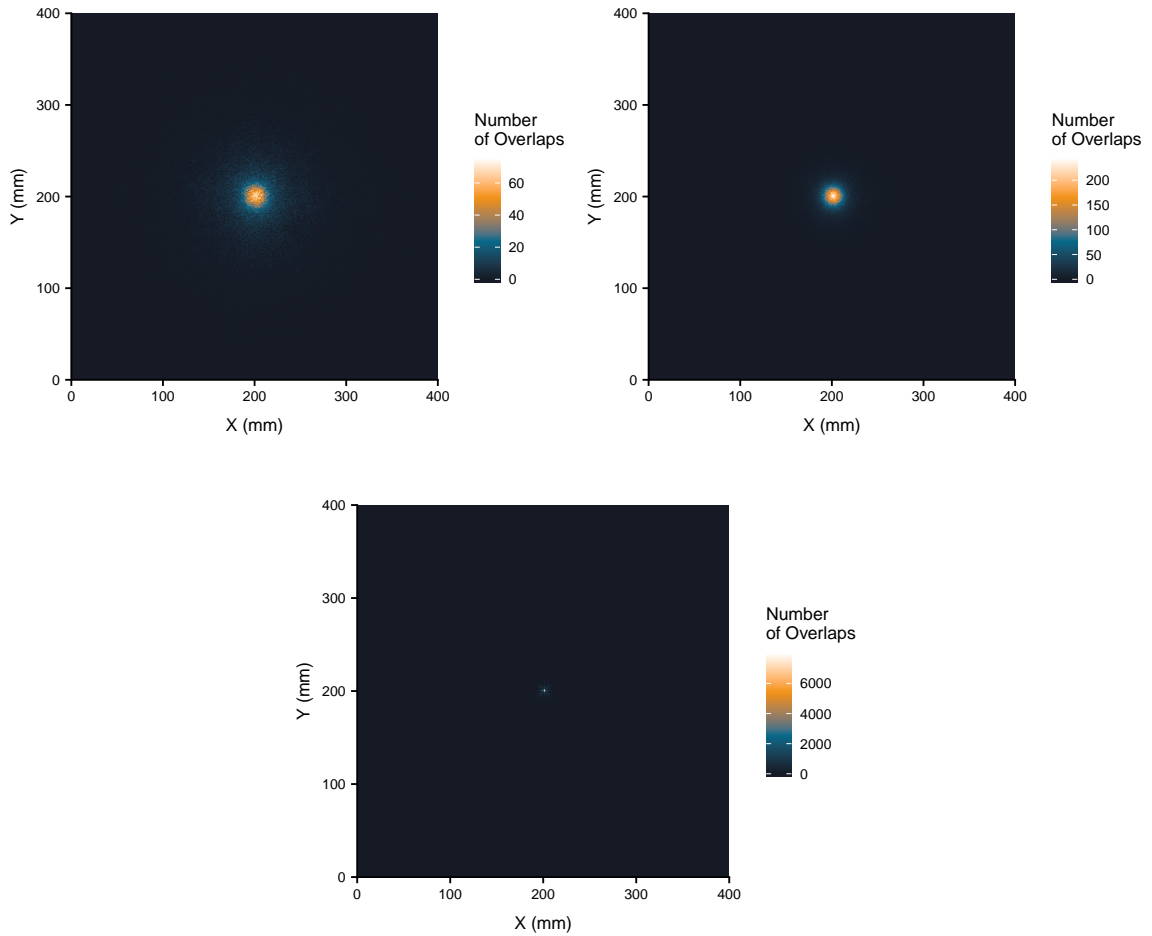
Figure 5.11: First [left], tenth [right] and final [below] iteration from the SOE code. The final iteration moves the points from the tenth iteration into the regions of highest density.

When imaging multiple gamma-ray sources, it is possible for an event from one source to be moved into the location of a different source if the density in that region is higher. For this reason, the user can specify which photopeaks are from different sources and the code reconstructs these points in a separate image space. These can then be recombined into the final output as displayed in Figure 5.12 — the reconstruction of Cs-137 and Co-60 point sources, 20 cm from the detector. This procedure to improve image resolution is only applicable to the SOE code.
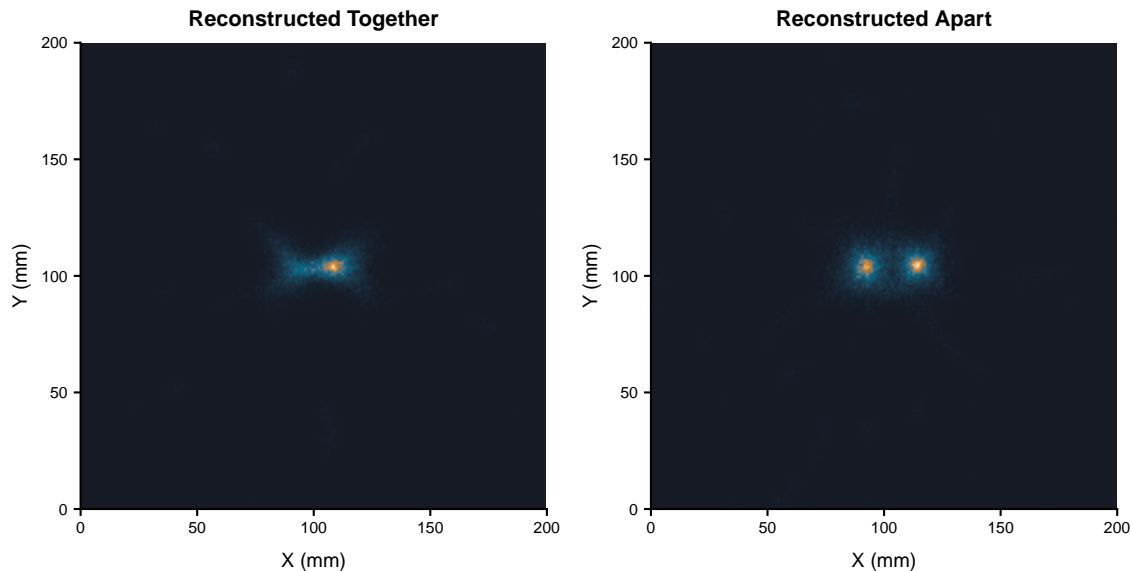
Figure 5.12: SOE reconstruction of Cs-137 and Co-60 point sources 20 cm from the detector. Sources reconstructed together [left] and in separate image spaces before recombination [right].

5.1.3 Comparison of Reconstruction Codes

Each reconstruction code has particular benefits and flaws. The choice of code must be made carefully by the user to suit the experimental data they wish to reconstruct. The analytical code is the fastest available at the university, it can work with both point and distributed sources and the selection of parameters is intuitive. The downside to this choice is the relatively poor image resolution. One possible solution to this limitation is to use a high pass filter (HPF) to remove the lower frequency 'blurred' sections of reconstructed images. An example of a HPF applied to a reconstructed image is shown in Figure 5.13, the corresponding intensity slices can be found in Figure 5.14. When applying a high pass filter, the user must decide on a cut-off frequency. Incorrect optimisation of this value can lead to ringing artefacts in the image slice. A high-pass filter shall be applied to experimental data later in this thesis to improve the resolution of reconstructed images.
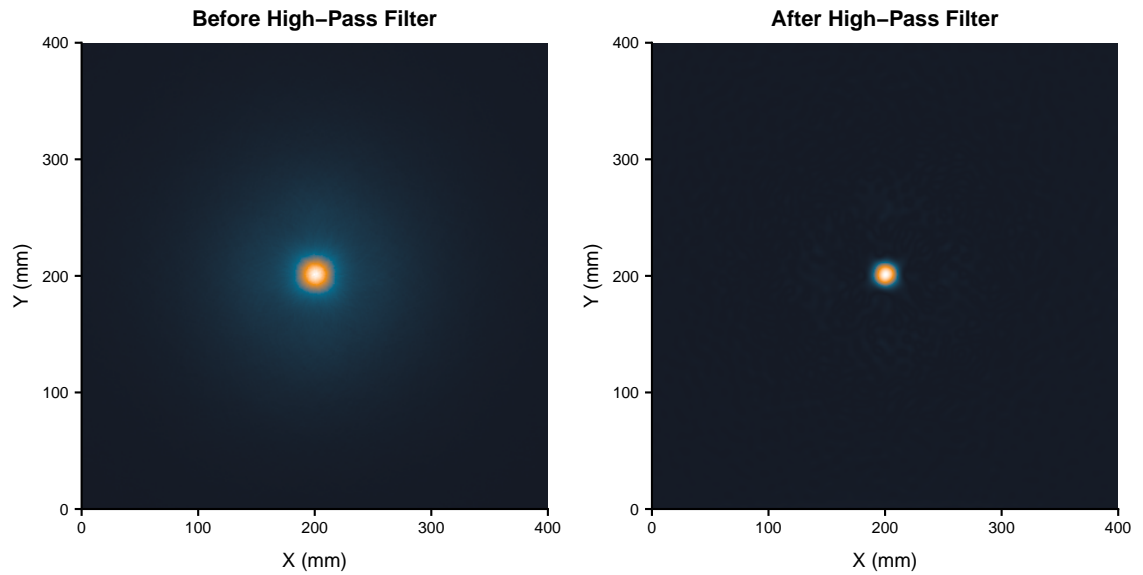
Before High–Pass Filter   **After High–Pass Filter**

Figure 5.13: Reconstructed images produced using the analytical code before [left] and after [right] the application of a high-pass filter.
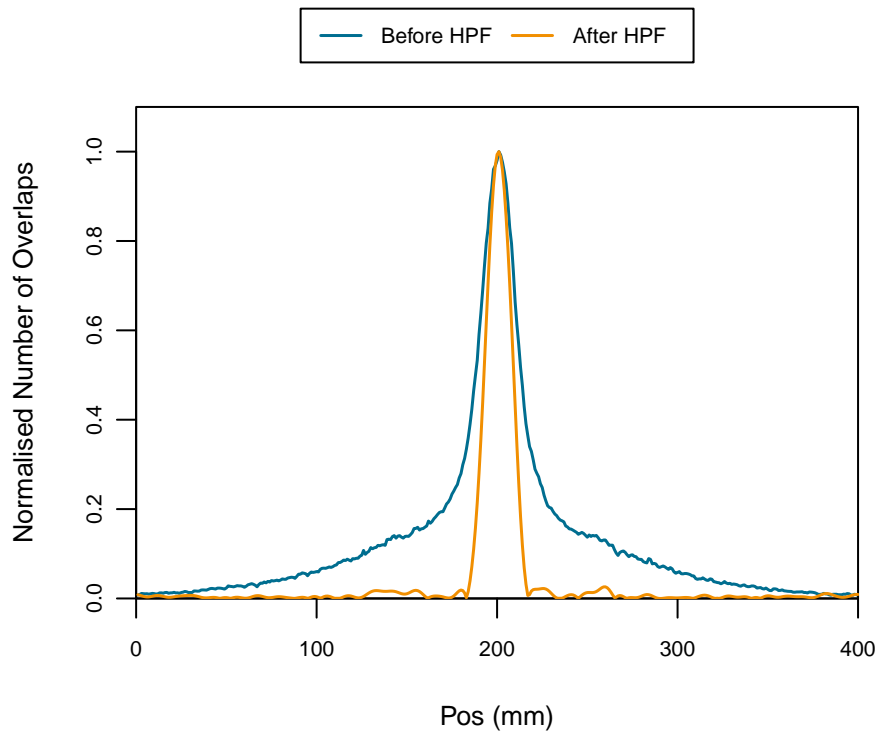

Figure 5.14: Profiles developed from an image slice before [blue] and after [orange] the application of a high-pass filter.

Even with this improvement, the SOE code produces much more precise representations of point sources. The time taken for an iteration is relatively short but around 40 iterations should be run, along with a finalisation step which can take several minutes. The disadvantage of the SOE code is clear when reconstructing several distributed sources of the same isotope. The code attempts to place points in regions of high density which results in a 'bridge' of points being allocated between objects. Multiple geometric sources are reconstructed as a continuous distribution because of this.

Ultimately, the code selected throughout this thesis for reconstructing experimental data is the MLEM code. The long processing times of the MLEM code can be sidestepped by simply increasing the available processing power, or running the algorithm on multiple systems to reconstruct several datasets at once. When reconstructing distributed or point sources the MLEM code performs equally well. The first iteration of the MLEM code is comparable to the analytical output. Subsequent iterations then further improve the image quality to obtain a resolution higher than what would be possible with the analytical code. A brief overview of the main qualities of each code is illustrated in Figure 5.15
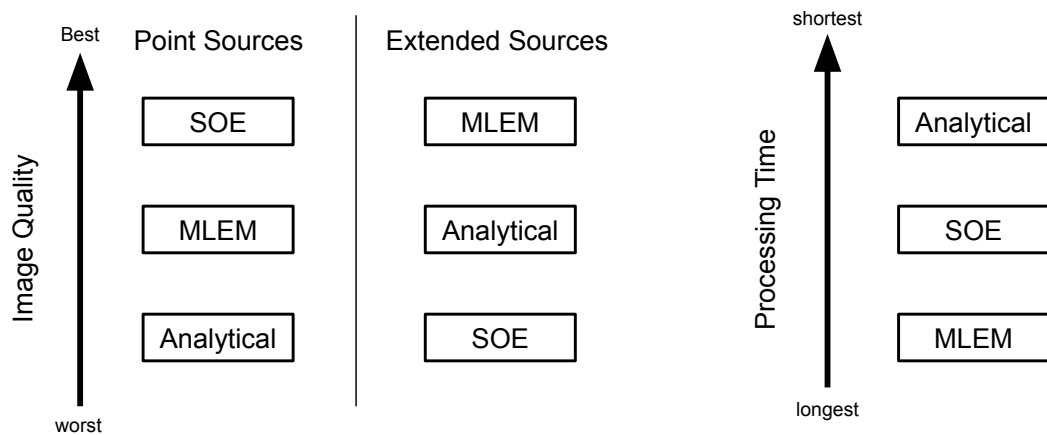

Figure 5.15: Comparison of reconstruction code abilities.

5.2   Benchmarking Image Performance

In order to image spent nuclear fuel, one must distinguish between multiple radioactive bodies a short distance from the front of the detector, housed within some medium. To accommodate this, a series of improvements to the imaging performance were researched. Section 6.2 shall discuss experimental data taken from a phantom used to simulate a fuel module. This section shall discuss the the factors influencing the quality of reconstructed images and benchmark their performance in the context of the phantom. The following factors of image reconstruction shall be explored:

- Impact of PSA on image quality

- Multiple source identification

- Reconstructing 3D source distributions with GRI+

- Imaging volumetric sources

- Impact of higher fold events

Throughout this section the analytical code is used to benchmark various aspects of GRI+. The intensity slices produced using this code can be fitted using a known distribution, discussed in section 2.3. This allows for quantitative metrics to be obtained from reconstructed images and improvements to be compared. The simplicity of the code also ensures nothing else, such as the number of iterations or stochastic nature of the SOE code, is responsible for differences between output. Additionally, the MLEM code dampens the intensity of objects offset from the centre of the detector's field of view. This would skew information when trying to understand effects from multiple point sources being imaged by the detector.

5.2.1 Evaluation of Pulse Shape Analysis Imaging Performance

The axis of a Compton cone is defined by the interaction locations of gamma rays in the detector system. Without any further analysis, lateral (X-Y) position knowledge is confined to the centre of voxels produced by orthogonal strip contacts. Additionally, no knowledge is directly obtained regarding the depth (Z) of an interaction within a crystal. Ultimately this limits the imaging performance because the cone axis is defined with a degree of uncertainty, determined by the detector's position resolution. PSA is the analysis of detector signals to infer greater precision on the interaction locations as discussed in section 4.7. Four PSA methods were implemented, three gave improved estimates of the interaction depth (ZPSA-1 (T30 vs T90), ZPSA-2 (risetime correlation), ZPSA-3 (chi-sq minimisation)) and one determined the lateral interaction positions on non-edge strips (XY-PSA).

To evaluate the improvement in Compton image quality through the application of PSA for GRI+, data was acquired with a Cs-137 point source 10 cm from the detector and each PSA method was applied to the data during the sorting process. Z-PSA methods were only applied to the absorber detector, where risetime information has been determined from scan data. The analytical image reconstruction code was used to create an image slice from each dataset. The resulting intensity profiles for these are shown in Figure 5.16. Table 5.1 shows the percent improvement in FWHM from each of the applied methods, when compared to 'No PSA'. The improvement from Z-PSA methods increases with the number of segments the absorber crystal is split into. The greatest improvement in image quality was achieved by applying Z-PSA version 3 in conjunction with XY PSA, 29.3 %. All reconstructed experimental data uses this PSA combination for optimal results.
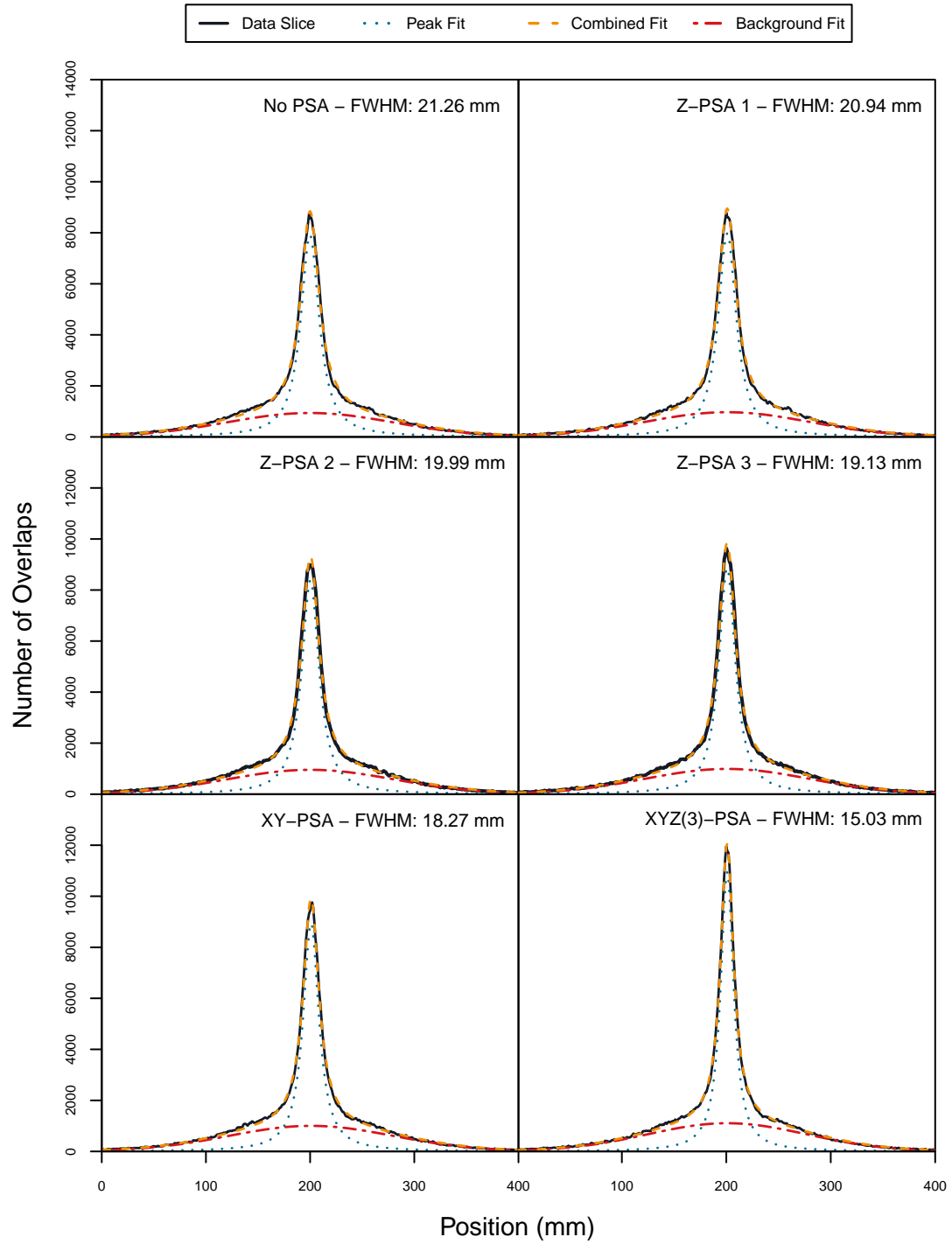
Figure 5.16: Intensity profiles from a Cs-137 point source 10 cm from the front of the detector with PSA methods applied.

PSA Method	FWHM (mm)	% Improvement	Number of Segments in X-Y	Number of Segments in Z
No PSA	21.26 ± 0.14		12	1
Z-PSA Ver. 1	20.94 ± 0.12	1.51	12	3
Z-PSA Ver. 2	19.99 ± 0.12	5.99	12	5
Z-PSA Ver. 3	19.13 ± 0.11	10.02	12	20
XY-PSA	18.27 ± 0.09	14.06	60	1
Z-PSA Ver. 3 and XY-PSA	15.03 ± 0.05	29.30	60	20

Table 5.1: Relative improvements in image quality from each PSA method when compared to no PSA applied during sorting.

The improvement to image quality from XY-PSA is greater than that from Z-PSA, even though the position of interaction within the depth of the absorber detector has the most uncertainty. This is likely to be due to the non-uniform sensitivity of the Z-PSA method implemented. Z-PSA version 3 works by comparing the risetime (T30, T50 and T90) of each interaction in the detector to the known average risetimes at each depth in the detector. The most likely interaction depth is then decided using a chi-squared minimisation. Figure 5.17 displays the distribution of calculated interaction depths in the absorber detector from a gamma rays which deposit between 500-600 keV. 21,000 events were used to create this histogram. Based on equation 2.3 the distribution of events are expected to take the form of an exponential. Imperfections in this method, and similarities in the average risetimes from interaction depths close the edges of the detector (as shown in Table 4.2), result in a reduced sensitivity at the faces of the crystal. This leads to the incorrect determination of interaction depths and a lesser improvement to image quality.
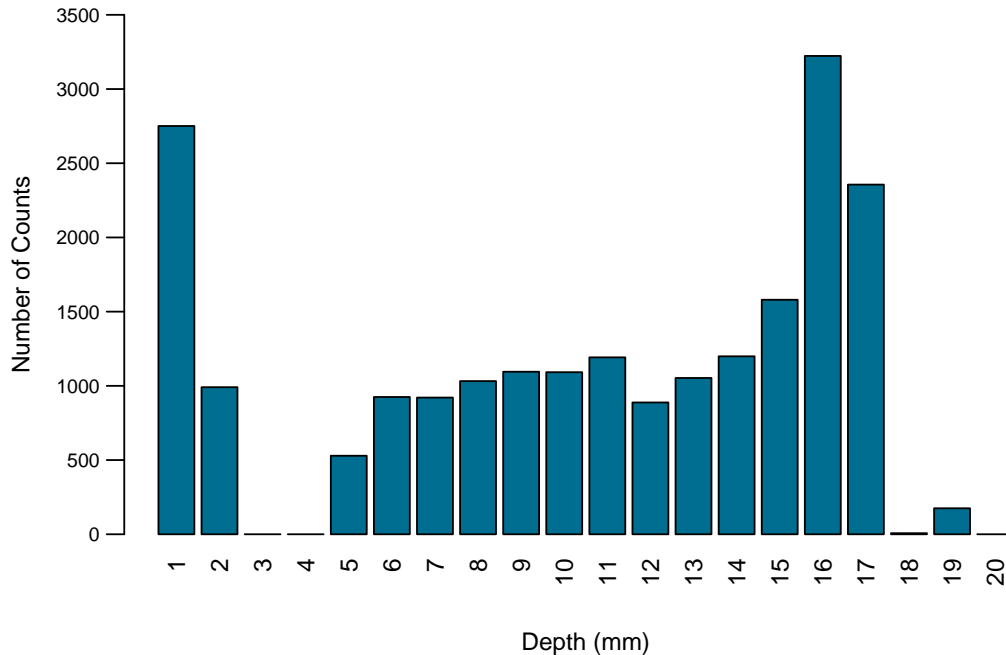
Figure 5.17: Depth distribution calculated for the absorber detector using Z-PSA version 3. The distribution is only made up of events which deposit between 500 and 600 keV in the absorber detector. A non-uniform sensitivity can be seen throughout and the back of the absorber detector is at 0 mm.

5.2.2 Distinguishing Multiple Point Sources

When imaging spent fuel modules, GRI+ is required to distinguish multiple fuel elements of various isotopes separated by short distances. Several datasets were acquired of point sources at set locations to investigate the resolving capability of GRI+. Two Cs-137 point sources were imaged at 3 distances (Z) from the detector. At each distance, data was taken for sources separated by 2, 4 and 8 cm (in X). The two point sources were chosen for their comparable activities and XYZ PSA was applied to all datasets. Figure 5.18 displays the intensity slices from these runs, produced using the analytical reconstruction code. It can be seen that the sources are more easily distinguished as separation increases and distance from the detector decreases. It is possible to identify the presence of 2 sources and their position from all data except 2 cm separation at 20 cm and 30 cm offsets. The same number of reconstructible events were used for each (40,000) and the fitting of peaks was performed automatically using a code developed in R [27, 32].
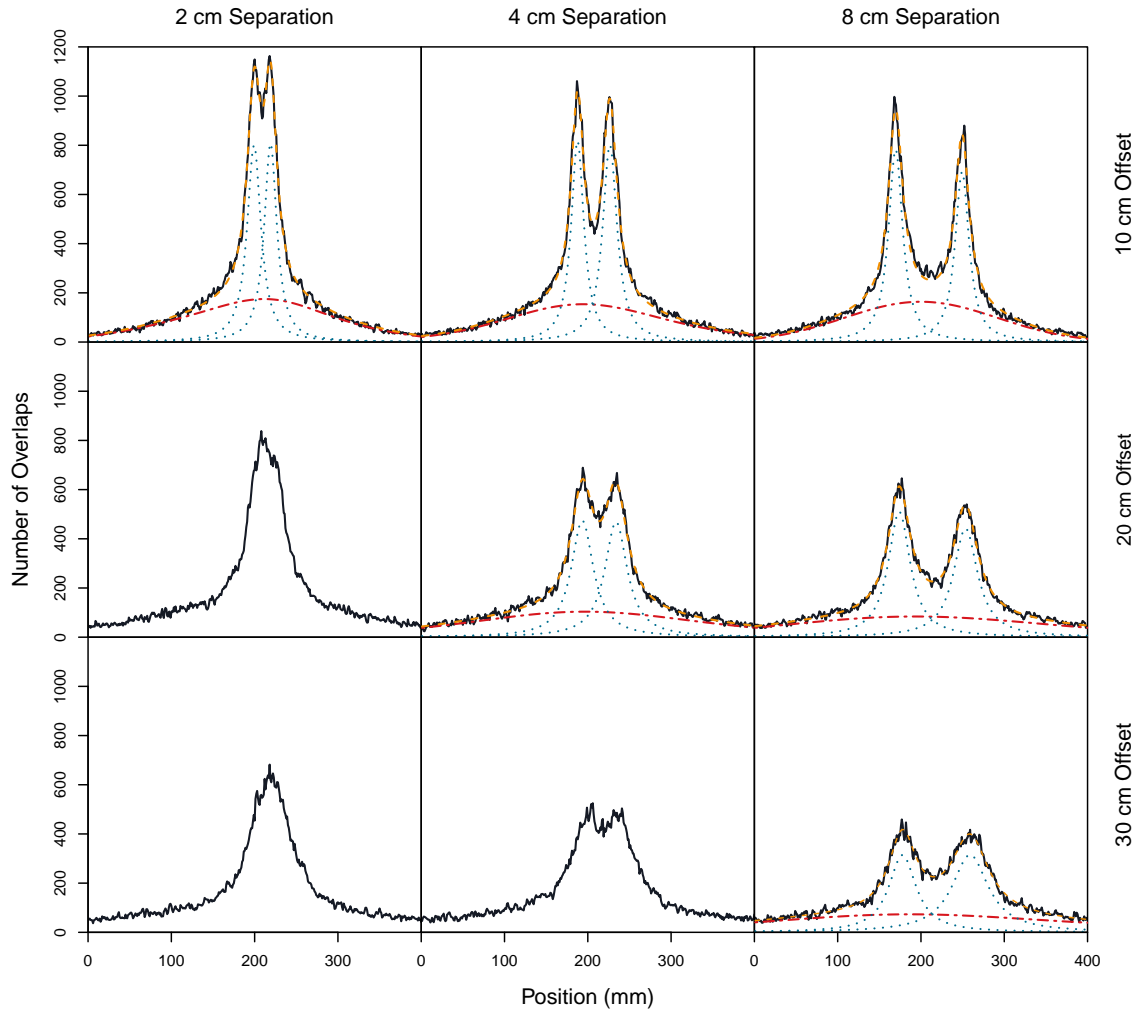
Figure 5.18: Image intensity slices for various stand-off distances and separations of Cs-137 point sources with XYZ PSA applied. GRI+ performs best for point sources close to the detector separated by large distances

GRI+ performs better when imaging point sources separated by larger distances with smaller offsets from the detector. As the stand-off distance is increased, poorer quality images are obtained as the FWHM of intensity profiles widen. This widening is caused by the amplification of errors in Compton cone geometries with increasing cone lengths. This effect is illustrated in Figure 5.19.
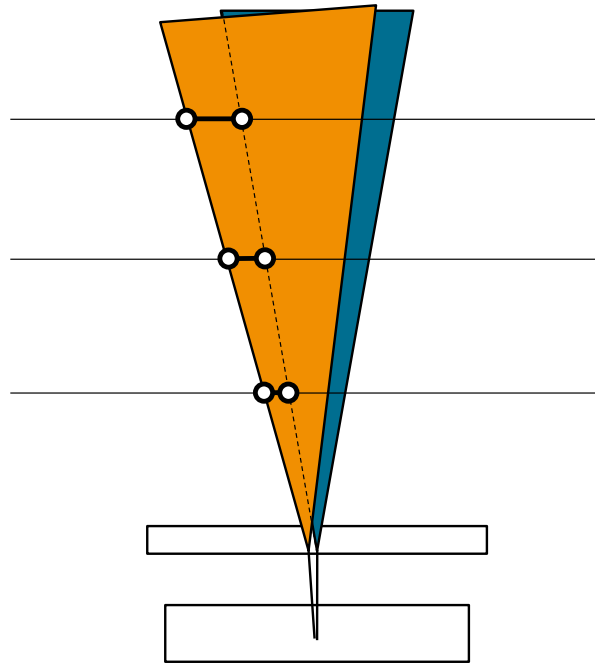
Figure 5.19: Illustration of a Compton cone with no geometric errors [blue] and small geometric errors [orange]. The difference between cones is amplified with increasing distance from the Compton camera.

Wider peaks naturally overlap when the separation between sources is too small. The offsets of 20 and 30 cm are comparable to that of the distance the fuel phantom was placed from the detector. Identification of individual sources is easier when each has different characteristic photopeak energies. Reconstruction can be performed individually for each photopeak and the separate intensity profiles overlaid to return the full distribution. This was performed for two point sources, Co-60 and Cs-137, separated by 2 cm (in X) and offset by 20 cm from the detector (Z). The energy spectrum with gated photopeaks is displayed in Figure 5.20 and the intensity profiles are displayed in Figure 5.21.
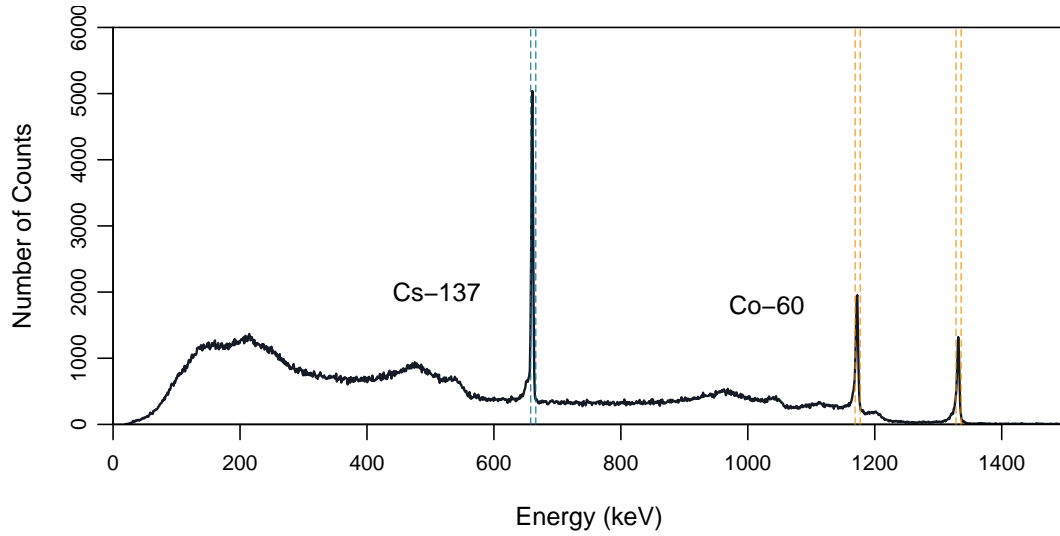
Figure 5.20: Cs-137 [blue] and Co-60 [orange] photopeak gates. Only events within the photopeak gates are used for image reconstruction.
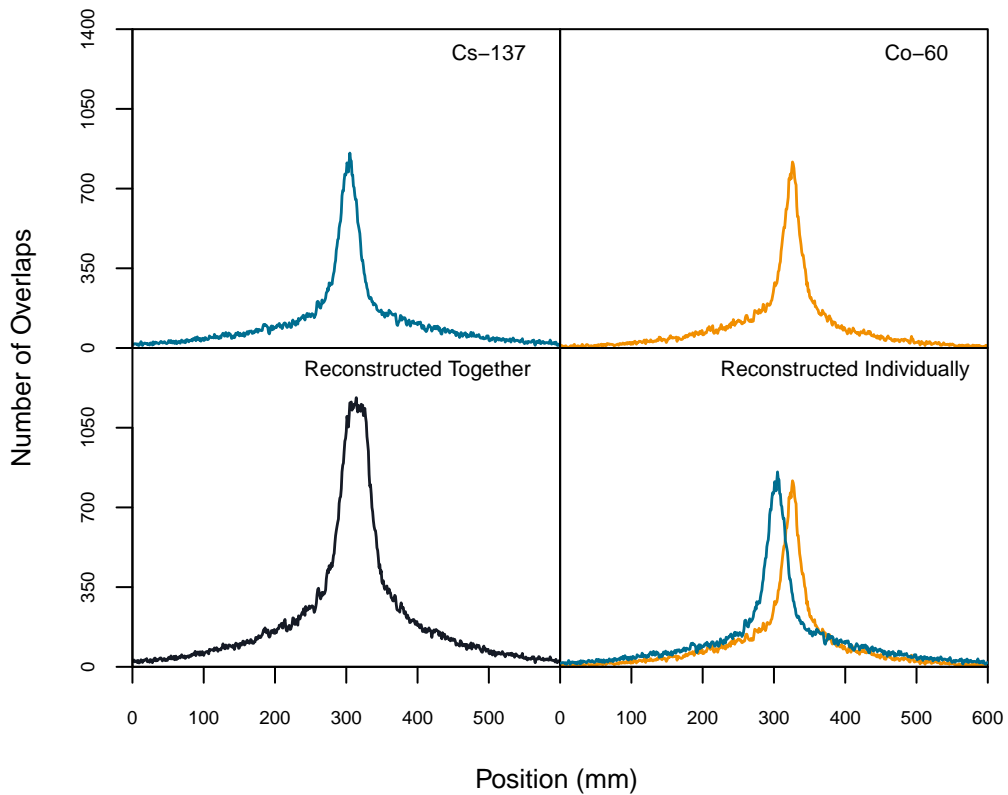

Figure 5.21: Co-60 and Cs-137 point sources placed 20 cm from the detector, separated by 2 cm. Individual isotopes can be distinguished by gating on photopeak energies to overcome the limitations in image resolution at small separations.

This result shows that it is possible to overcome the imaging limitations of identifying multiple sources separated by small distances by reconstructing each isotope individually. GRI+ is capable of identifying the position of individual point sources separated by small distances at stand-off distances up to at least 30 cm from the detector. This method of reconstruction, focussing on each isotope individually, shall be implemented into the analysis of phantom data to further improve the quality of images.

5.2.3 Reconstructing 3D Source Distributions

Using the analytical reconstruction code, GRI+ is capable of producing 3D source distributions by reconstructing multiple slices over a set distance. However, as the stand-off distance of radioactive sources from the front of the detector is increased, elongation of reconstructed images perpendicular to the detector is observed. This phenomena is believed to be related to uncertainties in the geometry of Compton cones and the degree of angular sampling available [33]. The allowed angular projections at two stand-off distances upon the scatter detector are shown in Figure 5.22.
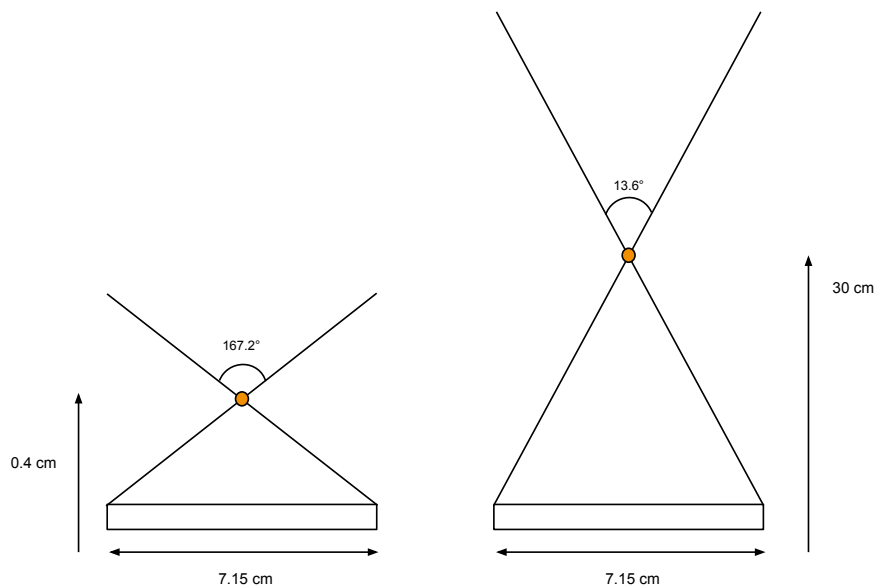

Figure 5.22: The angular projections are truncated with increasing source offset. Angles were calculated at 0.4 cm (167.2°) and 30 cm (13.6°).

To study this effect, data from a Cs-137 point source data was taken at 0.4, 10, 20 and 30 cm from the scatter detector cryostat and analytically reconstructed from Z = 0

mm (front of scatter detector crystal), to Z = 522 mm. The X-Z image slices, which lie perpendicular to the standard X-Y image slices, are displayed in Figure 5.23. The range over which the number of overlaps is greater than 80 % of the maximum overlap value in the images is identified by dashed horizontal lines. The same number of events were used to produce each image, 15,000.
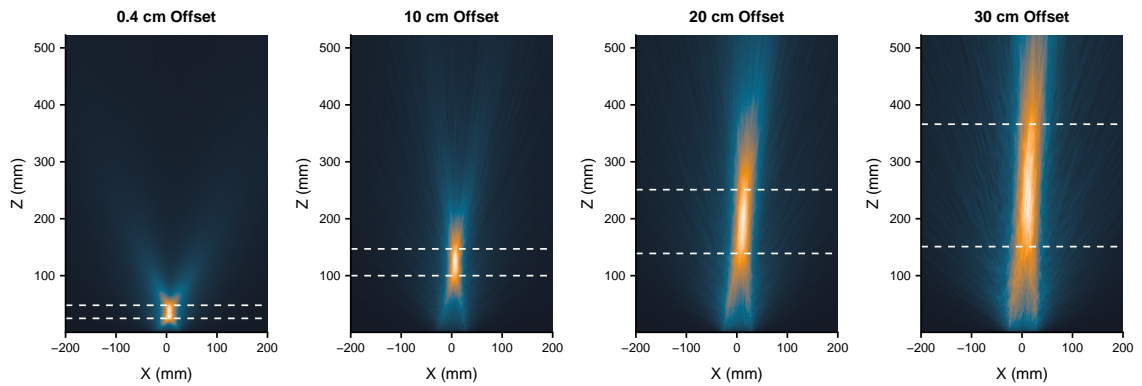

Figure 5.23: Increasing elongation of point sources is seen with increasing stand-off distances. Dashed lines indicate where the number of overlaps is greater than 80 % of the maximum overlap value. Z = 0 indicates the face of the scatter detector crystal.

As the source is positioned further from the detector, the range over which the number of overlaps is greater than the set threshold is increased. For each dataset the maximum overlap value as a function of distance is shown in Figure 5.24. As well as the notable increase in the width of each distribution, there is an increasing shift between the distribution maxima and actual location of each source. This relationship is displayed in Figure 5.25
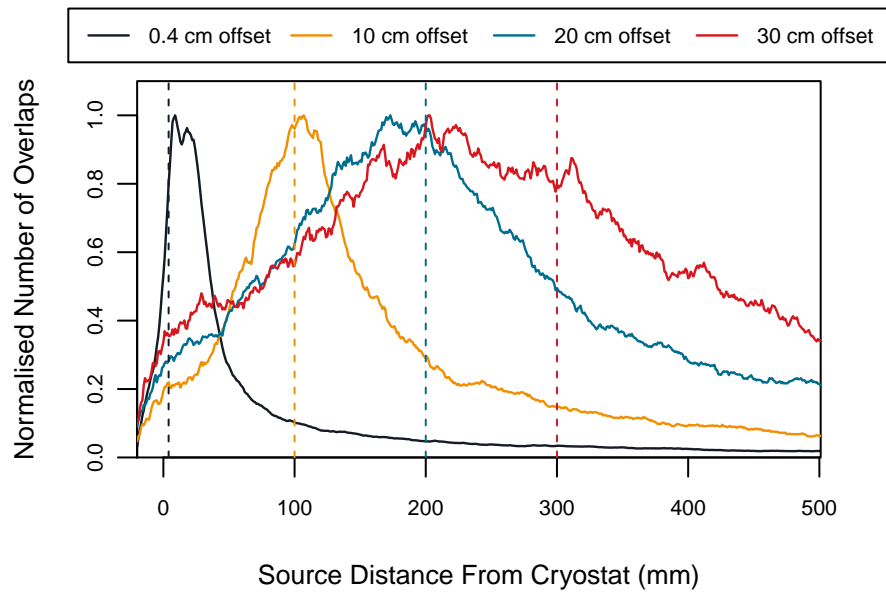
Figure 5.24: Maximum overlap value as a function of distance for each of the four datasets. As the source is stationed further from the detector the distribution of overlaps widens and the maxima further shifts from the actual location of the source (dashed lines).
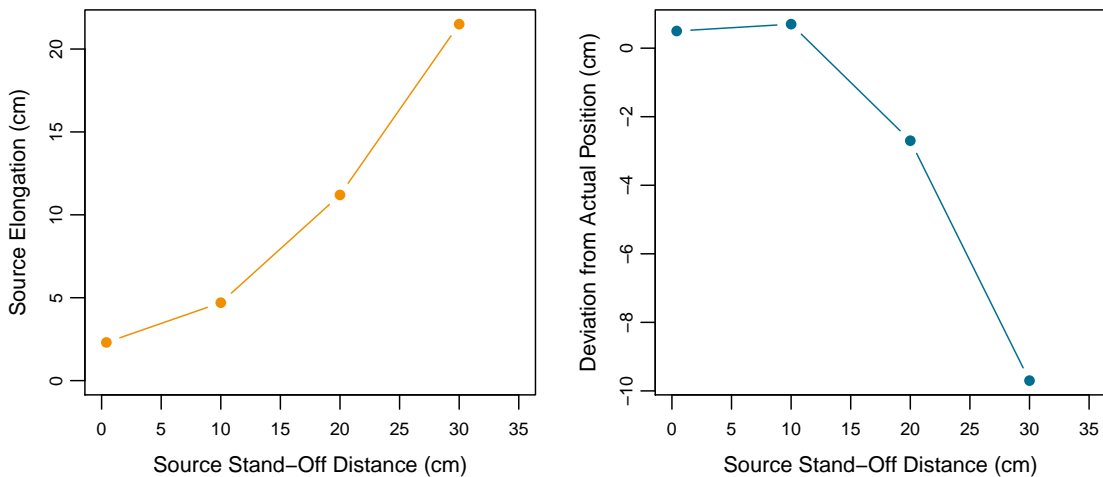

Figure 5.25: Elongation of source with increasing stand-off distance [left] and deviation between the location of maximum conic overlaps and known source location [right].

Any error in the calculated geometry of a Compton cone will result in a disparity between the actual position of the source and surface of the cone. This effect is amplified

at greater offsets and degrades the image resolution as the distance is increased. Both the energy resolution and dimensions of the scatter detector are intrinsic properties which cannot be altered. The widening of distributions and shift in maxima indicates cones are overlapping at incorrect locations. One approach to reduce this effect is to take a second Compton image, perpendicular to the first. This would increase the angular sampling but would require additional processing to couple the two reconstructions. The mobile cart housing GRI+ makes this a feasible option for improving image resolution and this is currently being investigated. Until this is achieved, in order to obtain the highest quality reconstructed images, spent nuclear fuel should be placed as close as possible to the front of the detector.

5.2.4   Geometric Source Imaging

Point sources are idealised distributions which are important for characterising imaging performance but are rarely equivalent to real-world measurements. Therefore it is imperative to investigate the performance of GRI+ when imaging extended distributions of radiation using the available image reconstruction algorithms. A Cs-137 vial was imaged at a distance of 10 cm from the detector and reconstructed using each of the available codes. The vial's active volume is a cylinder with a height of 3 cm and a radius of 1.5 cm, orientated as illustrated in Figure 5.26.
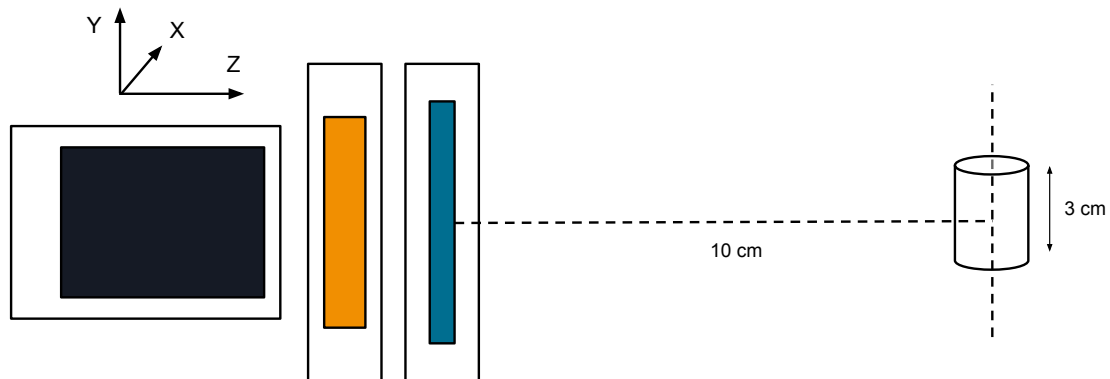

Figure 5.26: Orientation of the Cs-137 vial when imaged using GRI+.

The reconstructed image slices are shown in Figure 5.27 and corresponding profiles in Figure 5.28, where vertical lines indicate the width of the vial. It can be seen that

the analytical reconstruction method has the poorest signal to noise performance. The SOE algorithm, in its current form, is best suited for the reconstruction of point sources. Ultimately the SOE algorithm attempts to position all the conic overlaps in a pixel at the centre of the distributed points, rather than obtain a realistic impression of the radiation distribution. This results in a distribution with highly fluctuating statistics throughout the volume of the vial's expected location. The MLEM slice shows far less noise and a well defined vial geometry and therefore throughout this thesis, geometric sources shall be reconstructed using the MLEM algorithm.
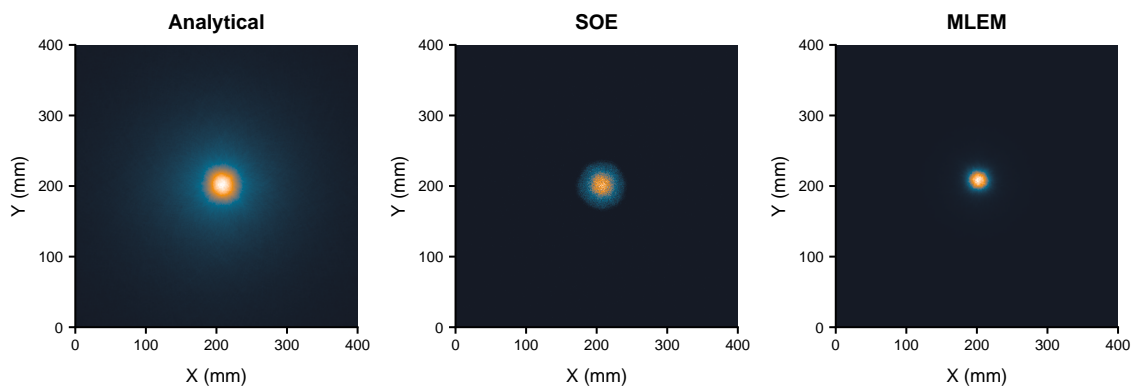
Figure 5.27: Cs-137 vial at 10 cm reconstructed using the analytical code [left], 50th iteration of the SOE code [middle] and 3rd iteration of the MLEM code [right].
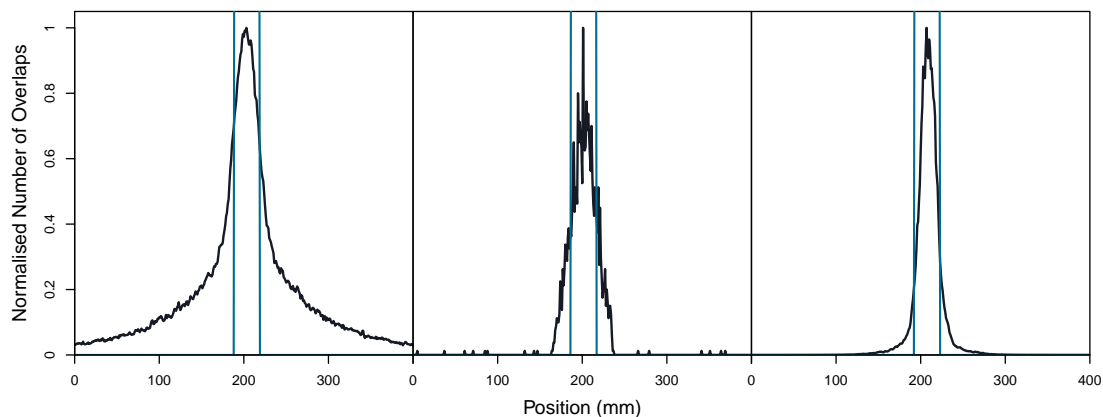

Figure 5.28: Reconstructed image slice of a vial at 10 cm using the analytical [left], SOE [middle] and MLEM [right] algorithms. The width of the vial is represented by the blue vertical lines.

The point spread function is not an appropriate descriptor for extended sources. In order to determine the quality of reconstructed images pertaining to distributed sources, the edge response function (ERF) is used. This estimates the dimensions of a source from an intensity slice. The steps to calculate the ERF are as follows:

1. Reconstruct an image and obtain a slice through the pixel of maximum intensity

2. Calculate the cumulative frequency of the normalised image slice

3. Find the difference (mm) between the amplitude at 10 % and 90 %

The ERF was calculated for each iteration of the MLEM code to determine which iteration best describes the vial. Figure 5.29 shows the ERF for each iteration of the MLEM code when the vial is placed 10 cm from the detector. It can be seen that the ERF improves from 162 mm to 14 mm between iterations 0 and 10. Iteration 3 was found to best match the geometry of the vial at 10 cm, with an ERF of 29 mm. Similar analysis was conducted at stand-off distances of 20 and 30 cm, these were best matched by iterations 4 and 5 respectively.
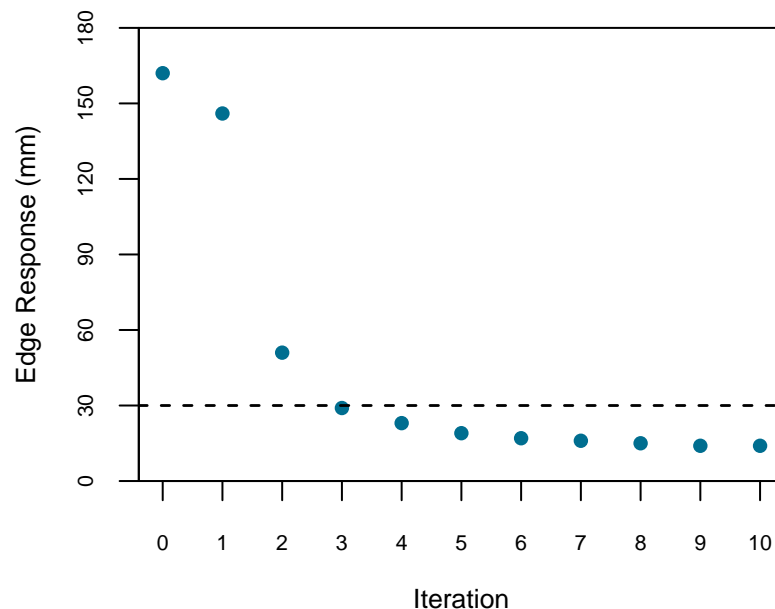

Figure 5.29: ERF for a reconstructed Cs-137 vial placed 10 cm from the detector for 10 iterations of the MLEM code. The actual width of a vial, 30 mm, is displayed as a dashed horizontal line.

The phantom shall contain a combination of Cs-137 and Co-60 planchette sources at stand-off distance of 20 - 30 cm from the detector. A final test was performed to assess the quality of images produced from a Cs-137 vial and Co-60 vial placed 30 cm from the detector, separated by 4 cm. The activity of the Co-60 vial is 1.85 MBq, the activity of the Cs-137 vial is 7.4 MBq. Both vials were imaged simultaneously and reconstructions were performed for each vial individually by gating on the relevant photopeaks. Figure 5.30 displays the resulting images.
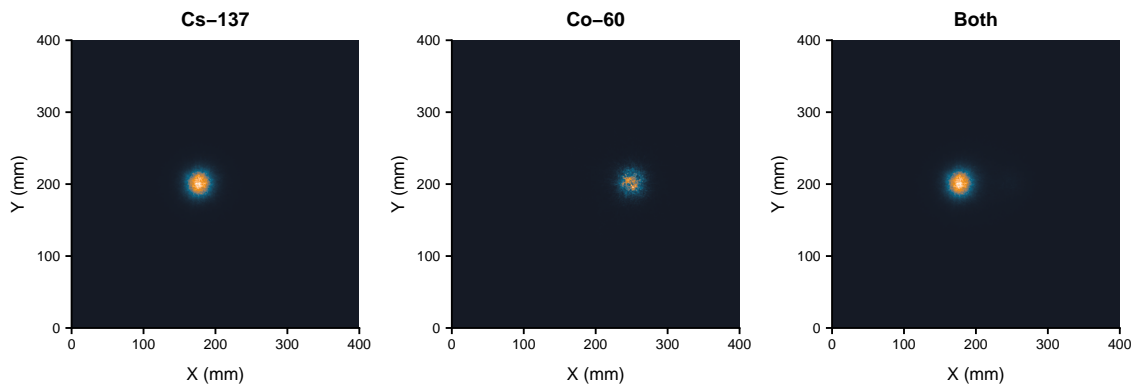

Figure 5.30: MLEM reconstruction of a Cs-137 vial and a Co-60 vial placed 30 cm from the detector. Both images are of the 5th iteration and each isotope was reconstructed individually by gating on the relevant photopeaks, Cs-137 [left], Co-60 [middle] and both sources together [right].

The MLEM code acts to suppress areas with few conic overlaps and will eventually iterate to the point containing the most overlaps. When both sources are reconstructed together this results in the complete loss of the Co-60 vial due to its reduced number of detected events. Figure 5.31 displays the gamma-ray spectrum from this dataset showing the reduced number of photopeak events.
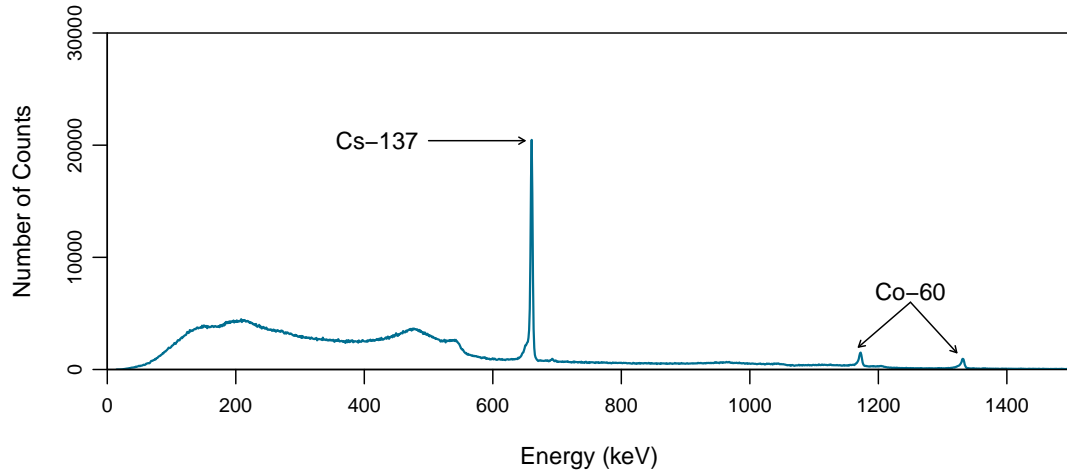
Figure 5.31: Energy spectrum produced from the Cs-137 and Co-60 vials.

When the number of reconstructed events differs greatly between sources, the optimum method to visualise distributions was determined to be by reconstructing each source individually. The profile should then be taken at the same row for each isotope, but the location of the pixel containing the greatest number of overlaps can differ greatly between distributions. Therefore, each column of the reconstructed images were averaged to develop the profiles instead. These averages were normalised before recombination to show the changing distributions of each isotope. The averaged profiles for the reconstructed vials are shown in Figure 5.32 before and after normalisation.
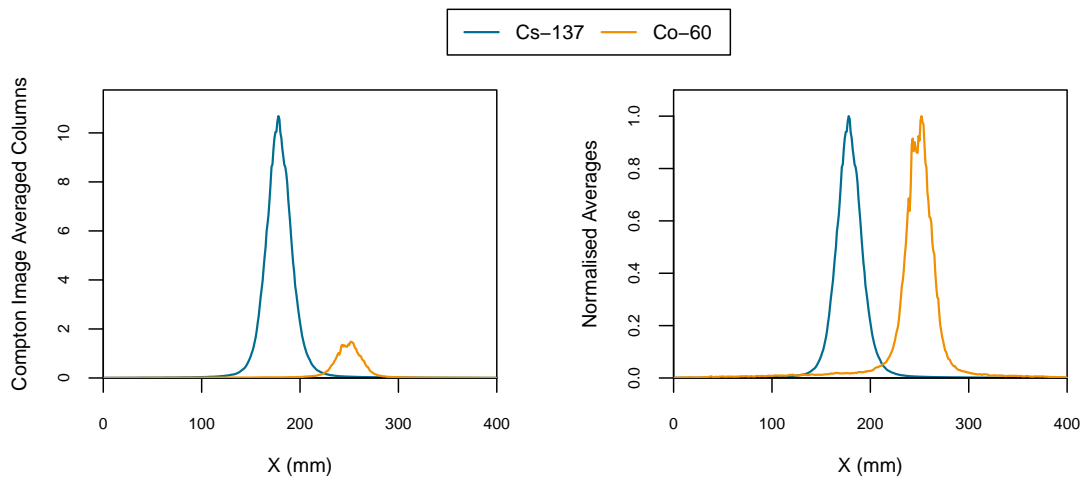

Figure 5.32: The distribution of radiation was found to be best described by averaging each distribution across one axis. This was done for each isotope individually [left] and normalised before being recombined [right].

101

In its current form, the MLEM code removes information relating to the activity of each source. Therefore, this normalisation does not remove any useful information stored in the image. This method of source visualisation is implemented into all runs using the MLEM reconstruction code.

5.2.5 Fold-2 Event Usage

As the energy of incident gamma rays is increased, events move towards higher fold interactions. This process is discussed in section 4.4 which displays the distribution of event fold with increasing energy. If a higher efficiency is required, GRI+ must be able to reconstruct these events. An event is classified as fold-2 if, on either face of the detector, 2 contacts collect a net charge above a set threshold. This can occur in the scatter detector, absorber detector or both. This section shall focus on the use of fold-2 events in the absorber detector for use in image reconstruction.

For an event to be reconstructible, the axis and apex angle of a Compton cone must be determined. Use of fold-2 scatter events would require the user to determine the order and precise vector between the two interactions. Any errors in this calculation would result in a large offset between the actual source position, and projection of the Compton cone. Miscalculating the order of multiple absorber events would result in a much smaller deviation. This is illustrated in Figure 5.33.
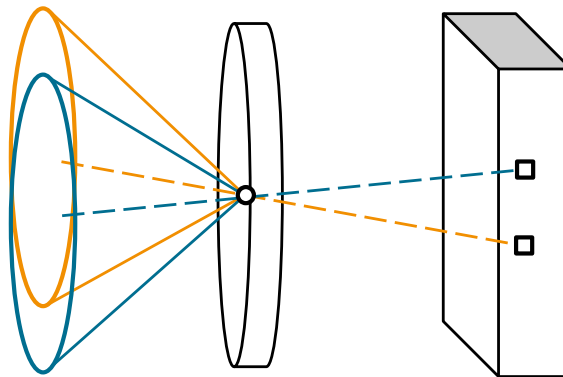

Figure 5.33: Illustration of fold-2 event usage in the absorber detector. Interaction positions in the absorber detector are indicated by squares. The event order must be determined correctly otherwise the geometry of Compton cones will be incorrect.

To determine the Compton cone axis for fold-2 absorber events, the interaction position in the scatter detector and location of the first interaction in the absorber detector must be known. The ordering of absorber interactions was investigated by imaging a Eu-152 point source 5 cm from the detector. Fold-2 absorber events were extracted from the dataset and reconstructed multiple times, each time the order of interactions was altered. This was performed for events which interacted in two tiers only, and a requirement was placed that the full incident gamma-ray energy was deposited within the two tiers. If the gamma ray did not leave the system then the first interaction should be caused by a Compton scattering event and the second, photoelectric absorption. The probability for either of these mechanisms to occur is dependent on energy. The order of interactions is therefore dependent upon the total energy deposited in the absorber detector. A threshold was set which, if the sum of interaction energies was below, the lowest energy interaction would be set as the first interaction. If this condition was not met then the order of events was reversed. This threshold was varied in steps of 50 keV and the FWHM of each reconstructed image profile was recorded. When the order of interactions is correct, the quality of reconstructed images should be greatest and therefore FWHM of the image profile should be at a minimum. An initial test was conducted by reconstructing Eu-152 events made up from ten photopeaks across the entire spectrum. The process was then repeated using the five lower energy photopeaks and then the five higher photopeak energies. The gated energy spectrum used for these tests is shown in Figure 5.34. A plot of the recorded FWHM at each threshold is displayed in Figure 5.35.

The optimum threshold for reordering events was determined using Figure 5.35 to be 450 keV. No PSA was applied during processing as XY-PSA cannot be implemented without neighbouring image charges, and fold-2 events were found to primarily occur between neighbouring interactions, as indicated in Figure 5.36. Accurate signal risetime information cannot be gained for fold-2 events which occur in neighbouring strips due to the convolution of real and transient signals. Therefore, Z-PSA could also not be applied to the data.
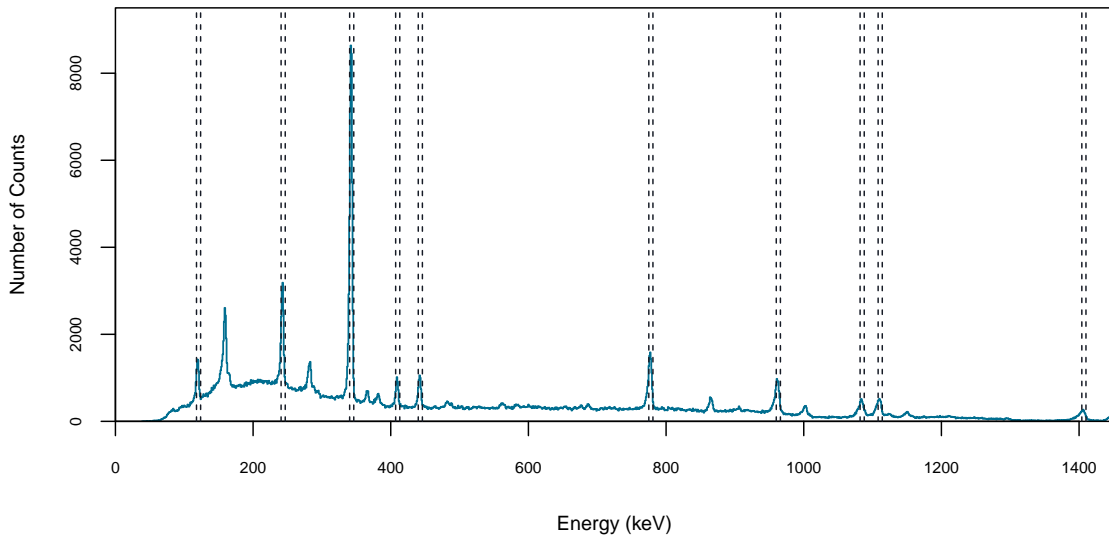
Figure 5.34: Eu-152 energy spectra produced using only fold-2 events. Photopeak gates placed on the spectrum are displayed as in black.
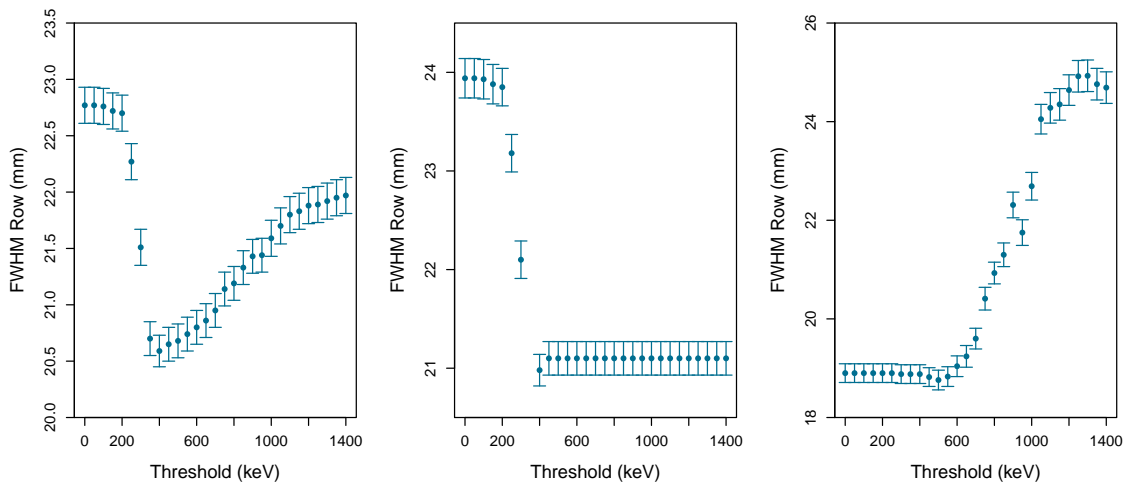

Figure 5.35: FWHM for the reconstructed fold-2 Eu-152 image at various set thresholds. The plots were produced by gating on 10 photopeaks across the entire energy spectrum [left], the 5 lower energy photopeaks [middle] and 5 higher energy photopeaks [right]. The optimum threshold was determined to be 450 keV.
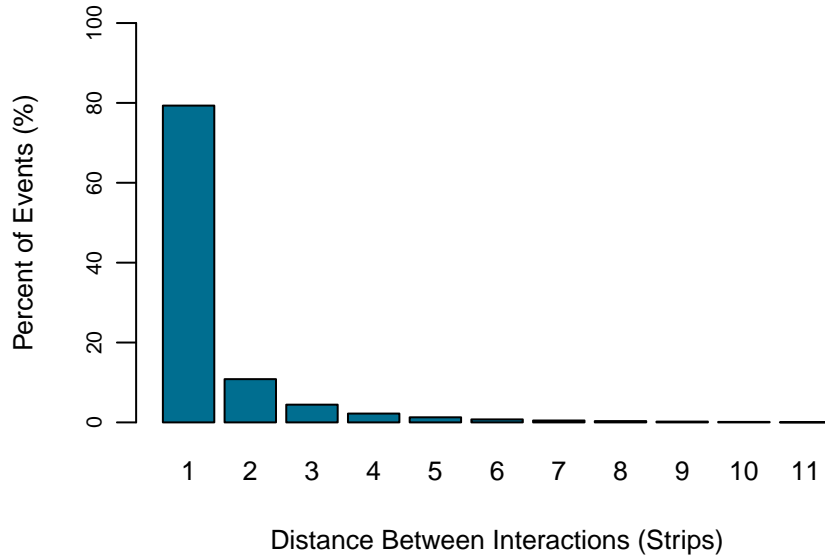
Figure 5.36: Distribution of hit strip separations for fold-2 events. Most fold-2 interactions occur between neighbouring strips.

A reconstructed image slice produced using only fold-2 events at the optimum threshold, and one produced using only fold-1 events (with XYZ PSA applied) are displayed in Figures 5.37 and 5.38 respectively. The same number of events were used to produce both slices, 71,186. The FWHM of the reconstructed images are 48.45 ± 0.49 mm and 31.06 ± 0.18 mm respectively.
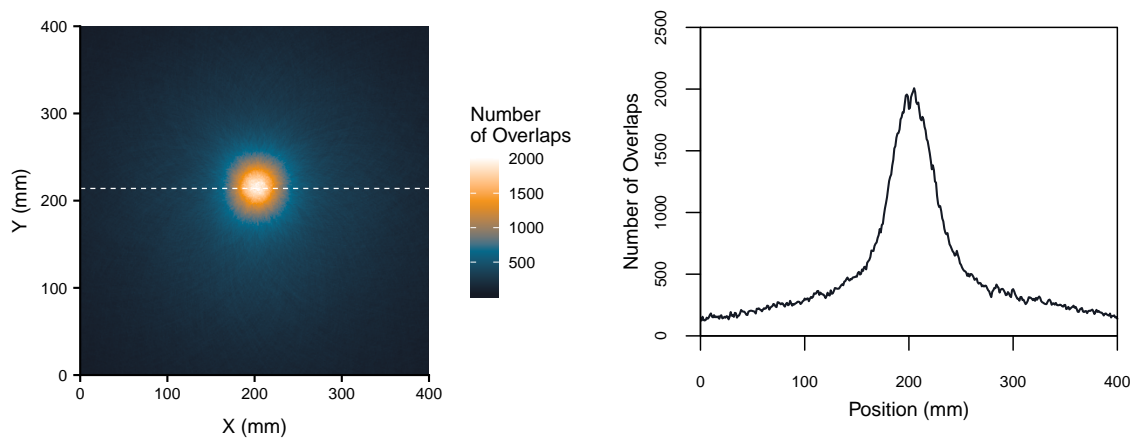

Figure 5.37: Reconstructed Cs-137 point source 20 cm from the detector produced using only fold-2 events [left] and the corresponding image profile [right]. No PSA was applied to the data during processing.
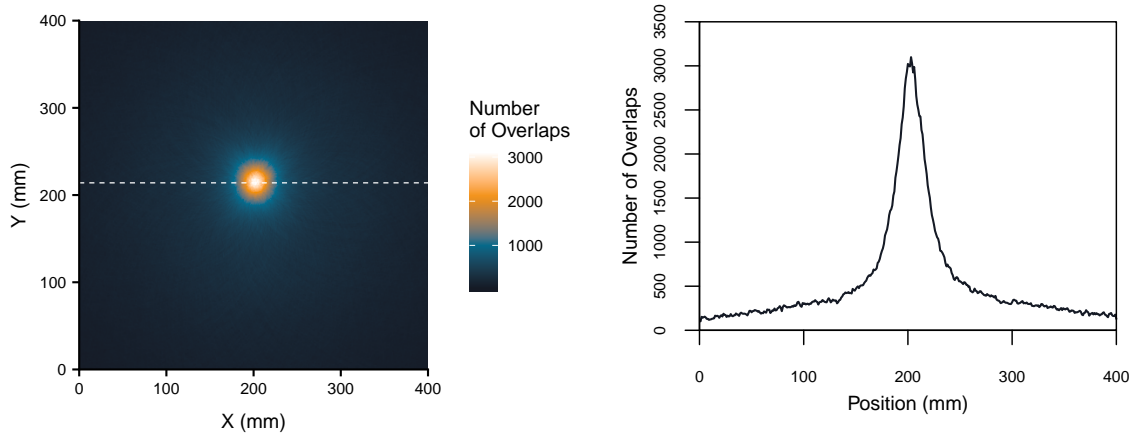
105

Figure 5.38: Reconstructed Cs-137 point source 20 cm from the detector produced using only fold-1 events [left] and the corresponding image profile [right]. XYZ-PSA was applied to the data during processing.

A comparison of each image profile is shown in Figure 5.39. The profiles were created using fold-1 events, fold-2 events, fold-1 events with XYZ PSA applied, and a dataset comprised of fold-1 (no PSA) and fold-2 events mixed equally. The best image quality is obtained when using fold-1 XYZ data, followed by fold-1 data without PSA implemented. By utilising fold-2 events in the image reconstruction algorithm, the number of reconstructible photopeak events is increased by 101 % for the Cs-137 point source, 20 cm from the detector. Incorrect decisions on the ordering of events increases the FWHM of the reconstructed fold-2 image. When imaging the phantom, the resolution of reconstructed images shall be prioritised over detector efficiency and so fold-2 events shall not be used. Figure 5.40 displays the various FWHM of image profiles for each dataset.
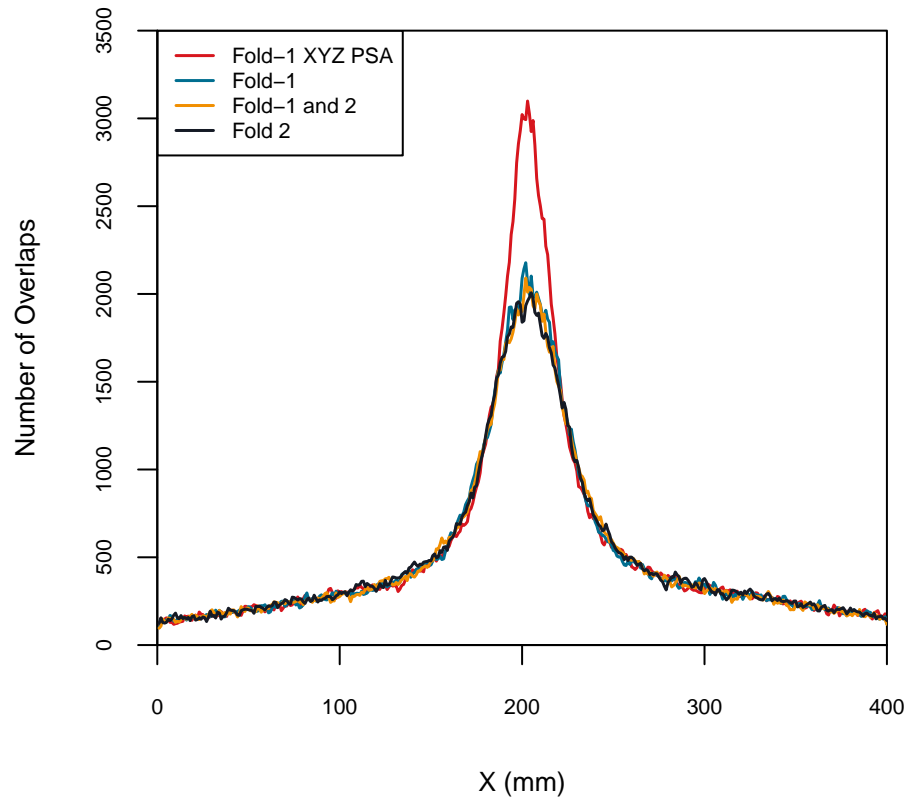
Figure 5.39: Comparison of image profiles from various reconstructions. Fold-1 data is found to consistently produce higher resolution images than fold-2 data.
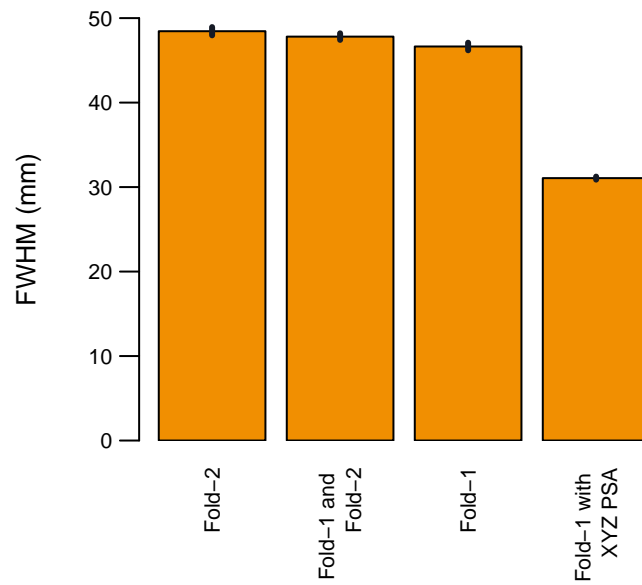

Figure 5.40: FWHM of intensity profiles of a Cs-137 point source 20 cm from the detector using different combinations of fold. Errors indicated by thick vertical lines.

Chapter 6

Evaluation of Experimental Phantom Data

Experimental data was acquired to assess the capabilities of GRI+ for imaging spent nuclear fuel. A phantom designed to mimic the properties of several fuel modules was developed in collaboration with the Defence Academy of the United Kingdom. Data were acquired for the phantom before and after being submerged in water. This data consisted of:

1. A single Cs-137 and Co-60 planchette source imaged without water.

2. The phantom placed 22.8 cm from the detector before submersion.

3. The phantom placed 22.8 cm from the detector, submerged in water.

This chapter describes the phantom design, experimental data acquisition and analysis of results.

6.1   Fuel Phantom Description

A fuel phantom was designed to mirror various properties of plate-type nuclear fuel with the purpose of assessing GRI+'s imaging capabilities. The prospective application of GRI+ is to image fuel placed in water containment after 10-20 years of cooling. After this duration Cs-137 ($T_{1/2}$ = 30.1 years), Cs-134 ($T_{1/2}$ = 2.1 years) and Eu-154 ($T_{1/2}$ = 8.6 years) dominate gamma-ray spectra [34]. Table 6.1 indicates the photopeaks of interest from

these isotopes, and also for Co-60, which is not present in fuel rods but is used in this experimental work.

Isotope	Photopeak Energy (keV)	Emission Probability (%)
Cs-137	661.657	85.1
Cs-134	604.721	97.62
	795.864	85.53
Eu-154	123.071	40.79
	1274.436	35.19
Co-60	1173.237	99.97
	1332.501	99.99

Table 6.1: Primary photopeaks of interest from Cs-137, Cs-134, Eu-154 and Co-60.

The phantom, photographed in Figure 6.1 and illustrated in Figure 6.3, is a stainless steel box with dimensions $180 \times 180 \times 225$ mm^3. Internally, it is split into four equal sections by a cruciform. Steel inserts can be placed in the four cuboid volumes which hold up to two planchette sources each. 6 Cs-137 and 6 Co-60 planchette sources were supplied with the phantom, the activity of each was 300 kBq. These isotopes were selected to simulate the spectral properties of Cs-137 and Eu-154 and cover the expected energy range emitted from spent fuel. Co-60 was used in place of Eu-154 due to its attainability and similar photopeak energy (1332 keV) to that of Eu-154 (1274 keV). Each planchette source is a disk with a diameter of 50 mm, edge thickness of 5 mm and an active-area diameter of 35 mm, as illustrated in Figure 6.2. The steel slides are separated by acrylic inserts to replicate the properties of water within the module. The phantom was placed into an open-top perspex container, $(60$ cm$)^3$, and sat upon a perspex ledge to ensure it lay in the centre of the detector's field of view (FOV). A silicon seal, attached to the underside of the lid, guaranteed no water entered the phantom once submerged. An illustration of the phantom is displayed in Figure 6.3.

Figure 6.1: Photograph of the fuel phantom taken at the University of Liverpool.
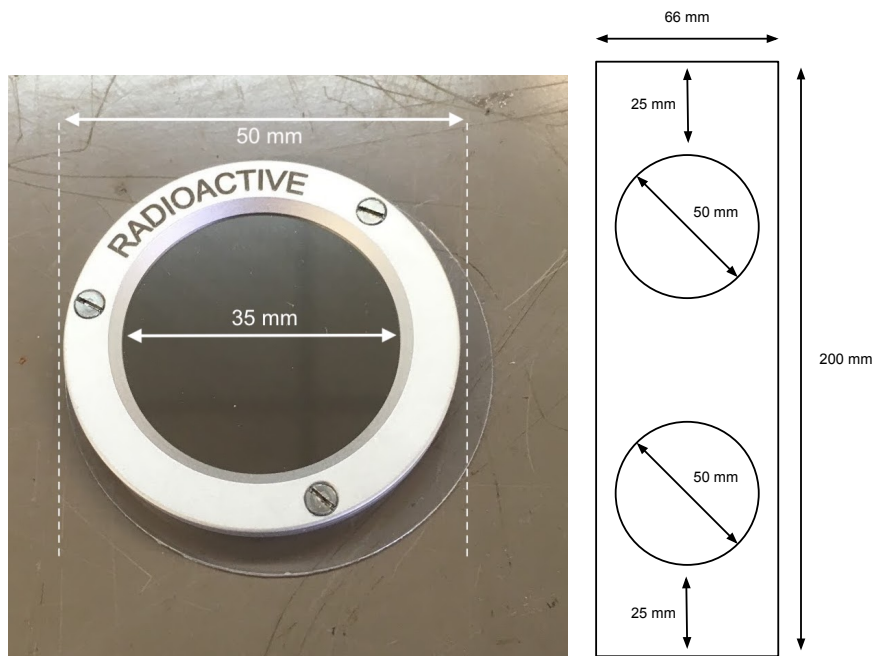

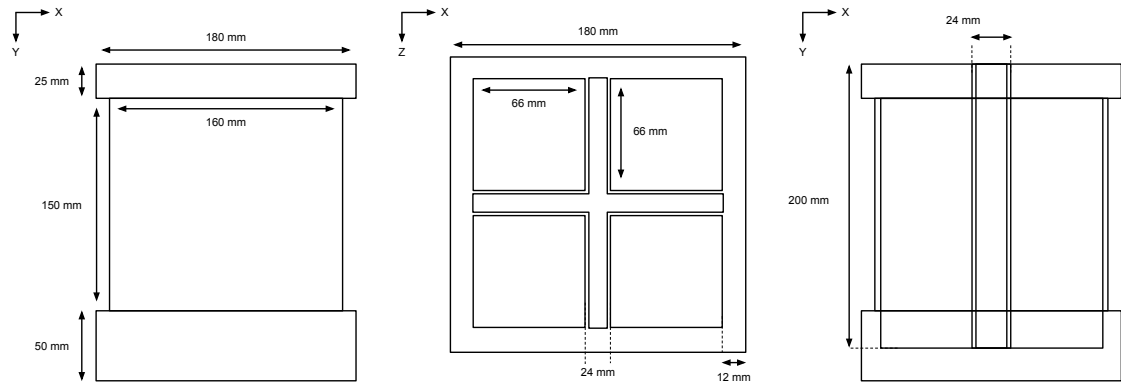**Figure 6.2:** Photograph of a Cs-137 planchette source [left] and illustration of a steel slide [right].

Figure 6.3: Illustration of phantom dimensions without the lid from the side [left], above [middle] and a cross section [right].

The phantom was manufactured according to a flexible design, allowing it to be representative of various fuel modules. The IRT-4M sandwich-type fuel assembly [35] from the VR-1 and LVR-15 reactors, located in Czech Republic, is one of the most complex fuel assemblies GRI+ would hope to image. This module type separates UO_2 fuel elements by 2.85 mm (1 mm of aluminium cladding and 1.85 mm of water) and has a length of 820 mm. An illustration of the 8 tube variant of IRT-4M is displayed in Figure 6.4, 6 and 4 tube variations are also used in the reactors. In order to effectively image such an assembly GRI+ will be required to distinguish elements of fuel, separated by very short distances. The minimum separation of planchette sources in the phantom when separated by an acrylic slide is 9.2 ± 0.1 mm, the error is due to slight deviations in the width of each acrylic slide. Although this is greater than the minimum separation of elements within IRT-4M fuel (2.85 mm), results from experimental data should indicate whether, with more research, GRI+ could image this type of fuel in the future.
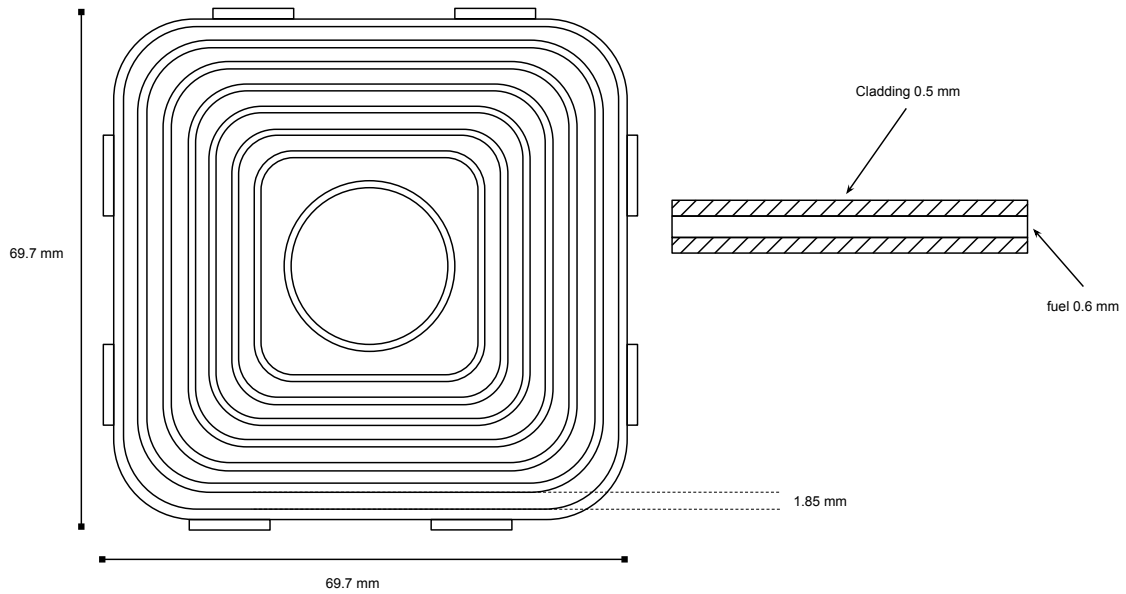
Figure 6.4: Illustration of the 8 tube IRT-4M fuel assembly.

The placement of Cs-137 and Co-60 planchettes is decided by the user. The orientation and positioning of elements can be easily adjusted allowing for specific scenarios to be tested. The focus of experimental work was primarily to identify individual elements. Safeguarding technologies act to find defects, such as some or all of a fuel element being missing from an assembly, in order to ensure no material has been diverted for illicit means [36]. By determining the degree to which individual planchettes can be identified with GRI+, an indication of the usefulness for detecting these flaws with this system can be established.

The fuel phantom was only available for a short period of time and so a limited number of experimental data were obtained. Data were acquired for the phantom positioned at 22.8 cm from the detector's face. The phantom was submerged in water for one of these acquisitions. Figure 6.5 shows a schematic of the phantom positioning from above. The face of the phantom was positioned to be central to the scatter detector crystal. This section shall describe all of the data taken and analysis of the reconstructed images. The 4th and 5th iterations of the MLEM code were used to reconstruct slices from the front and rear phantom compartments respectively. Justification for these iteration choices are discussed in section 5.2.4, they have been found to best represent the extent of a source at the given distances. Only fold-1 events were used in the reconstruction algorithm to

ensure the resolution of images were of the highest quality, and XYZ-PSA was applied during event processing.
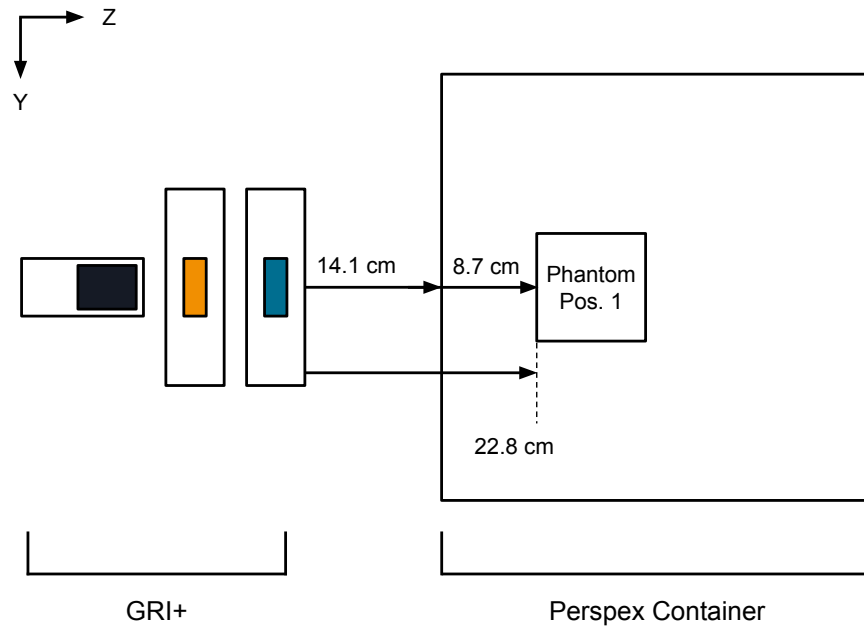

Figure 6.5: Top-down view of fuel phantom placement relative to the front of the detector.

6.2 Experimental Study

6.2.1 Multi-isotope Planchette Imaging

An initial acquisition was performed to determine whether individual planchettes could be distinguished at the phantom stand-off distance of 22.8 cm from the detector. One Cs-137 planchette and one Co-60 planchette were placed in neighbouring phantom compartments and imaged simultaneously, as illustrated in Figure 6.6.
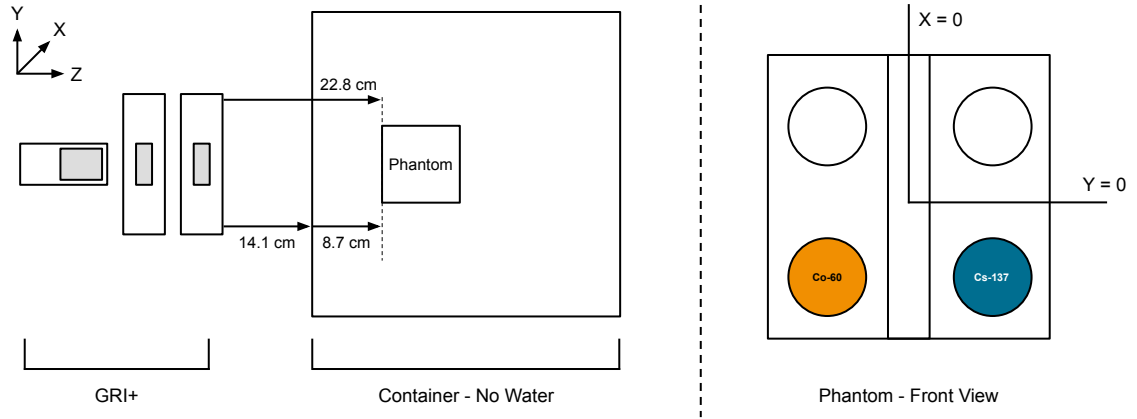
Figure 6.6: Illustration of the phantom placed 22.8 cm from the detector with no water filling the perspex box. A Cs-137 [blue] and a Co-60 planchette [orange] were placed in the front compartments of the phantom, parallel to the face of the detector.

Data was acquired for 22 hours. A total of 21,246 reconstructible Cs-137 photopeak events, and 12,926 reconstructible Co-60 photopeak events were collected during this time. Reconstructible events are defined as fold [1,1,1,1,0] or fold [1,1,1,1,1] as described in section 4.4. The low activity of the planchette sources, combined with their distance from the detector, meant run times of more than half of a day were required to record a substantial number of reconstructible events. Figure 6.7 displays the energy spectrum of reconstructible events from this data set. The following gates were placed around each of the photopeaks:

- Cs-137 662 keV gate: > 658 keV & < 664 keV

- Co-60 1173 keV gate: > 1169 keV & < 1177 keV

- Co-60 1332 keV gate: > 1328 keV & < 1336 keV

Each source was reconstructed separately, these gates are displayed in Figure 6.8.
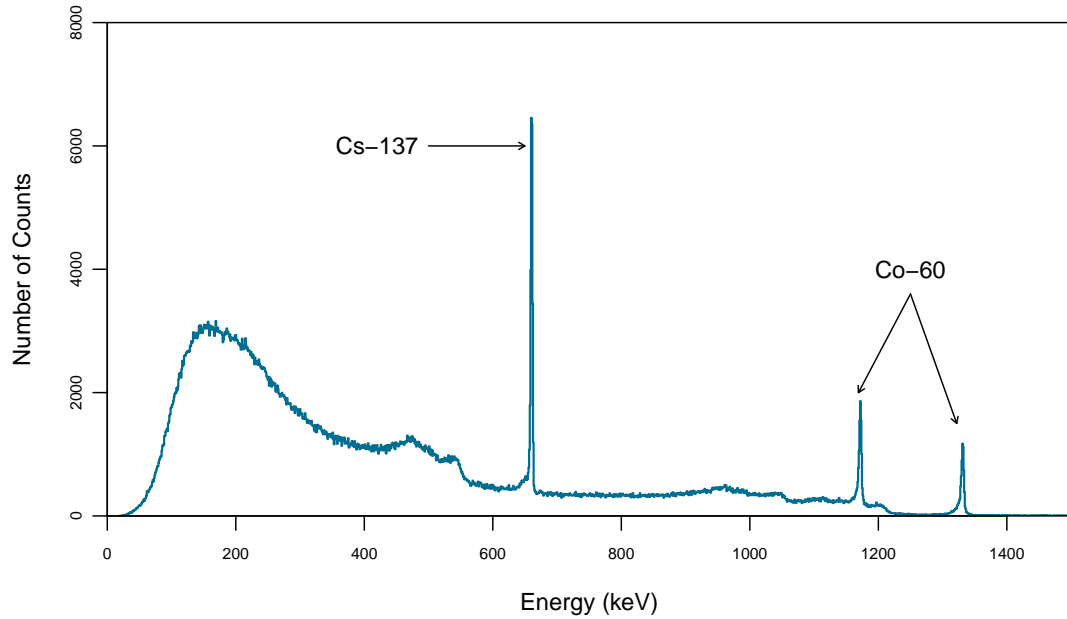
Figure 6.7: Energy spectrum from imaging a Cs-137 and Co-60 planchette in the phantom.
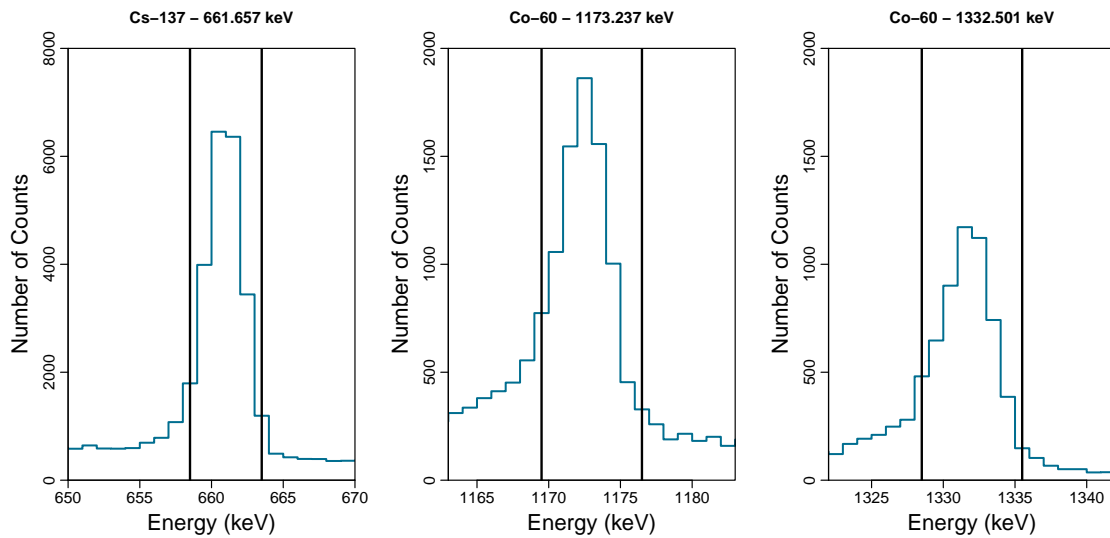

Figure 6.8: Reconstructible photopeak events were selected by applying energy gates for each isotope.

The MLEM iterative reconstruction code was used to image the planchettes. The profiles of each source were calculated as described in section 5.2.4. No water was present for this run, a series of dry runs were performed before water was introduced to ensure viable data would still be acquired in the case of a mechanical fault. The output of the

MLEM code is displayed in Figure 6.9 where the left image shows the reconstructed Co-60 events, the central image shows the reconstructed Cs-137 events and the final image is of the two isotopes reconstructed simultaneously. The 4th iteration of the MLEM code was used to produce these images.
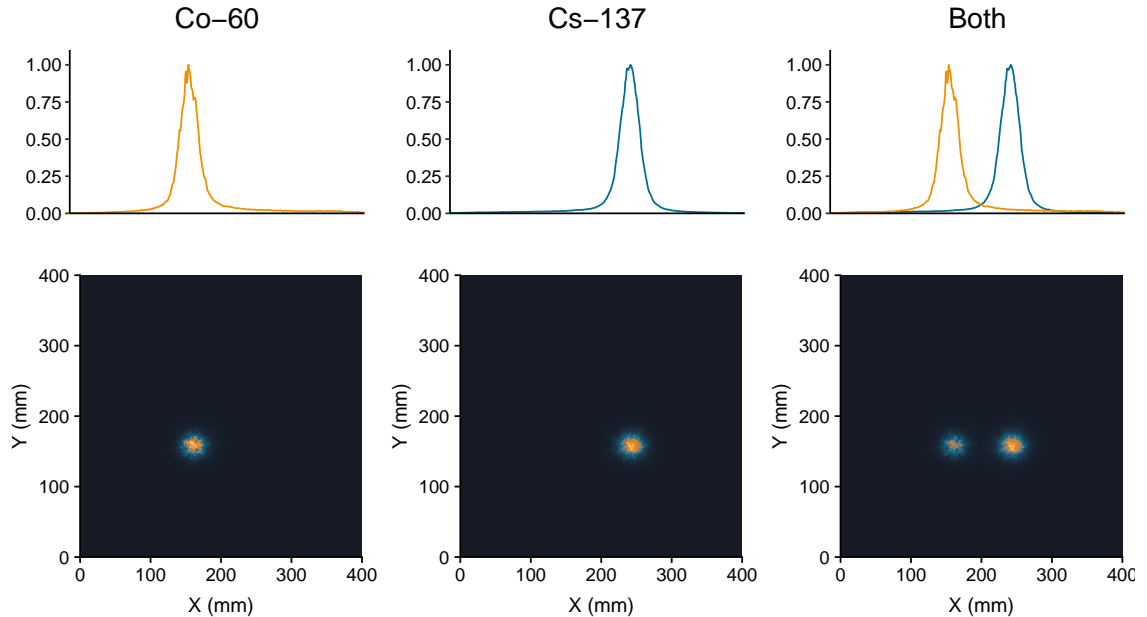

Figure 6.9: Reconstruction of a single Co-60 [left] and Cs-137 [centre] planchette in the phantom using the MLEM code. The combined reconstruction [right] shows easy identification of each planchette.

The reconstructed image slices clearly show each planchette as well defined distributions. Fewer reconstructible Co-60 events were collected during data acquisition. This is a result of GRI+'s reduced efficiency for collecting fold-1 events at higher energies, as discussed in section 3.8. When the two reconstructed isotopes are combined into one image, the relative difference in the number of conic overlaps results in a diminished appearance of the Co-60 planchette. The image profile for each of the isotopes is normalised and so this effect is removed in the combined profile distribution. The fewer reconstructible Co-60 events accounts for the additional statistical noise in the corresponding image profile.

The edge response function (ERF) was applied to the individual isotope profiles. This function attempts to calculate the width of the radioactive media used to produce the profiles, as described in section 5.2.4. Each planchette has an active area diameter of 35 mm. Figure 6.10 displays the ERF-transformed profiles for each planchette. Vertical lines

indicate the locations where the distributions reach 15 % and 85 % of their maximum height, the extent of a radioactive body is estimated by the difference between these two points. The estimated widths of each planchette were calculated to be 41 and 54 mm for Cs-137 and Co-60 respectively. The larger deviation from the actual active planchette width of 35 mm for Co-60 is likely a result of the greater statistical fluctuation in the image profile. In section 5.2.4, the difference between 10 % and 90 % of the maximum cumulative distribution was chosen to represent the width of a source. These values didn't accurately fit the distribution for the planchettes due to the gentle sloping of each distribution towards the centre of the FOV. A single Cs-137 point source at a distance of 20 cm has a FWHM of $\sim$ 32 mm as determined from the analytical reconstruction code. Given that this is the resolution attainable from a body less than 1 mm in diameter, and that a distributed source can be expressed as the combination of many point sources in a volume, the differences between the expected and calculated widths are well within acceptable bounds. These results indicate that the chosen iteration value of the MLEM algorithm has been correctly calibrated for this dataset, and GRI+ is capable of distinguishing individual planchette sources and identify the size of their active area within a reasonable degree of uncertainty.
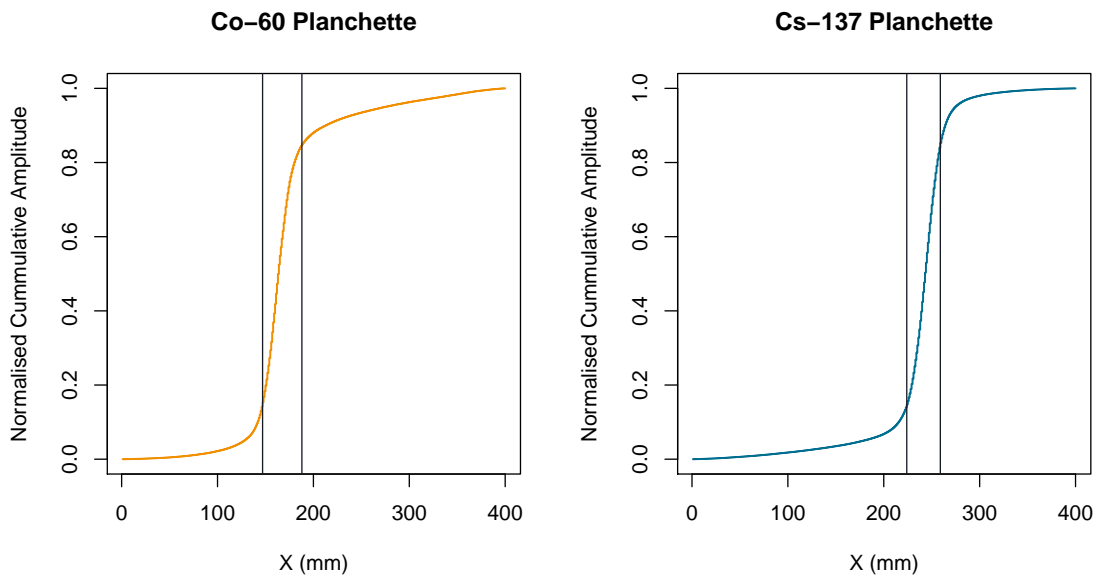

Figure 6.10: Edge response function applied to the Co-60 profile [left] and Cs-137 profile [right]. Vertical lines represent the points where distributions reach 15 % and 85 % of their maximum height.

In this orientation, with planchettes housed in adjacent steel slides, the separation between active areas is 55 mm. The centres of the two planchettes are separated by 90 mm. An illustration of this geometry is displayed in Figure 6.11.
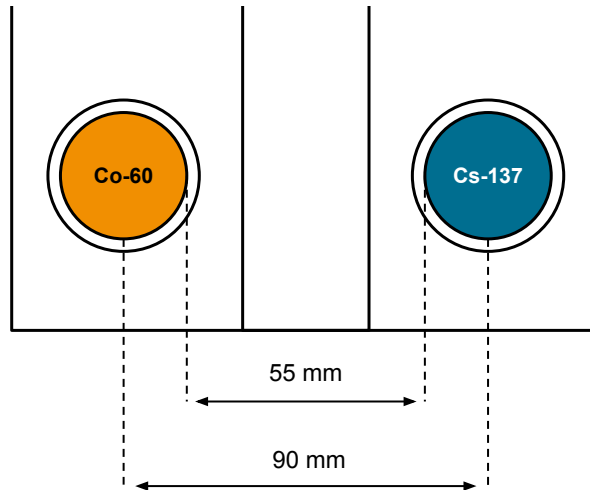

Figure 6.11: Illustration of the separation between planchettes when they are placed in neighbouring compartments.

The difference between the maxima of the two reconstructed profiles was calculated as shown in Figure 6.12. The separation was calculated to be 84 mm, different from the known value of 90 mm. One possible source of error is the fluctuation in the distribution of the Co-60 profile which has already been shown to produce uncertainties in the determination of the planchette's active area. With a higher number of statistics a more accurate separation could be calculated. Additionally, the maxima of each distribution are not equal distances from the centre of the image space. This could indicate an experimental error in the positioning of the phantom. Previous work has also found a radial distortion between the actual and reconstructed location of point sources [37]. This phenomena shifts the location of reconstructed sources closer to the centre of a slice and could explain the separation between planchettes being calculated as smaller than the experimental value. It is recommended that, in the future, more research must be focussed on this topic and the implementation of a correction within the MLEM code.
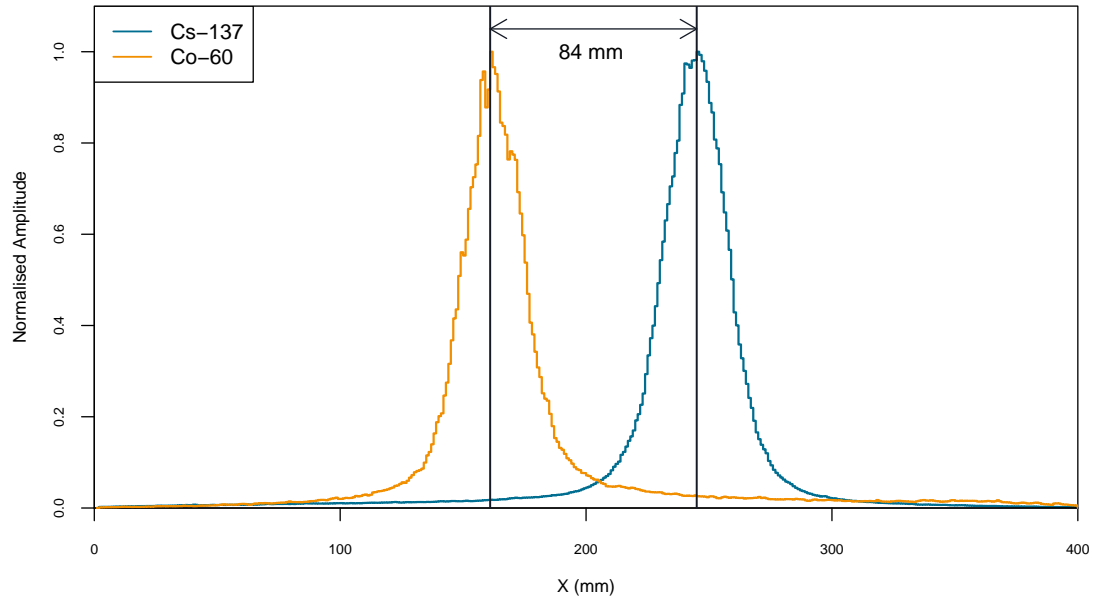
Figure 6.12: The separation between the Cs-137 and Co-60 profile maxima is 84 mm.

Ultimately, the results obtained from this dataset demonstrate that:

1. Photopeaks can be readily gated in the energy spectrum, owing to the good energy resolution of the detector system.

2. Individual planchettes can be easily identified when the phantom is placed 22.8 cm from the detector

3. The calculated widths of each planchette are representative of the known active region within a reasonable degree of uncertainty

6.2.2 Imaging the Phantom with a Complete Set of Planchettes

This section describes experimental data taken with the most complicated arrangement of planchettes. The phantom was placed 22.8 cm from the detector, as shown in Figure 6.13. The perspex box was not filled with water for this run, and two image slices were reconstructed using the MLEM algorithm. All 12 of the supplied planchettes, 6 Cs-137 and 6 Co-60, were present in the phantom. The planchettes were placed in a complex orientation to assess whether, either parallel or perpendicular, sources could be individually identified by GRI+. A slice through the closest compartments was first reconstructed using the 4th iteration of the MLEM code, at a distance of 27.3 cm from the detector. The rear

compartments were reconstructed using the 5th iteration at a distance of 36.3 cm from the detector. The individual isotopes were again reconstructed separately, by gating on specific photopeak energies, and combined into a final image. The processed slices are displayed in Figures 6.14 and 6.15. Data was acquired for 22.73 hours, in which 67,584 reconstructible Cs-137 photopeak events and 41,481 reconstructible Co-60 photopeak events were collected.
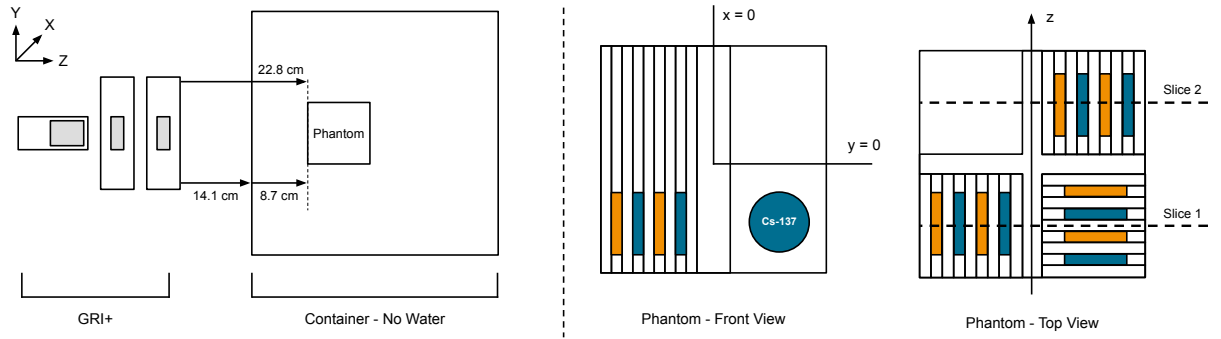

Figure 6.13: Illustration of the phantom filled with all Cs-137 [blue] and Co-60 [orange] planchettes, 22.8 cm from the detector. The perspex container contained no water during data acquisition.
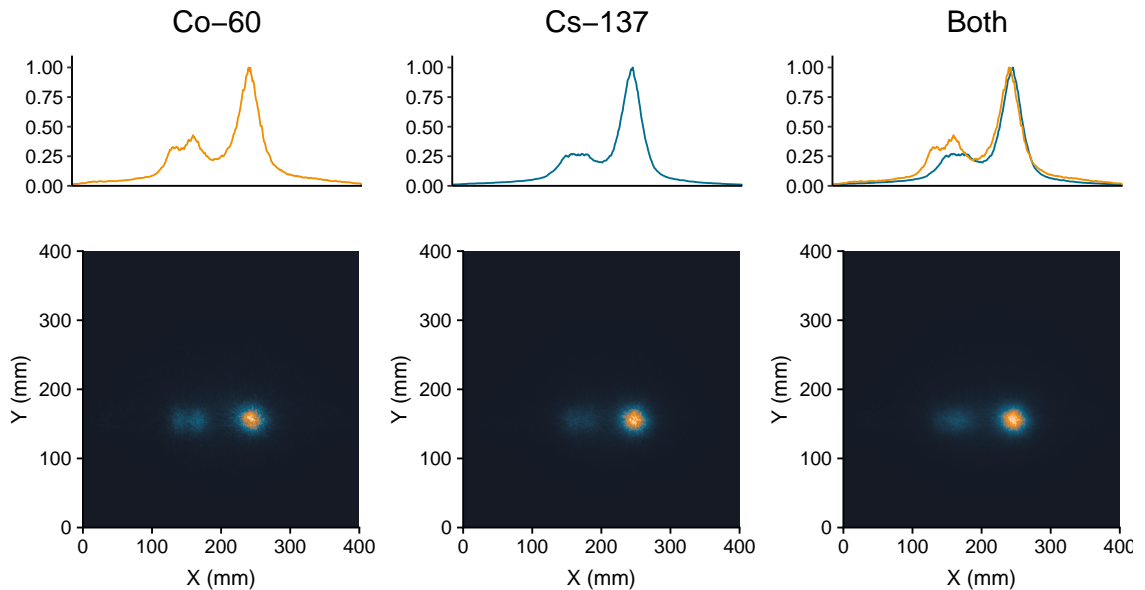

Figure 6.14: Reconstruction of the front phantom compartments with no water filling the perspex box. The phantom was placed at 22.8 cm from the detector.
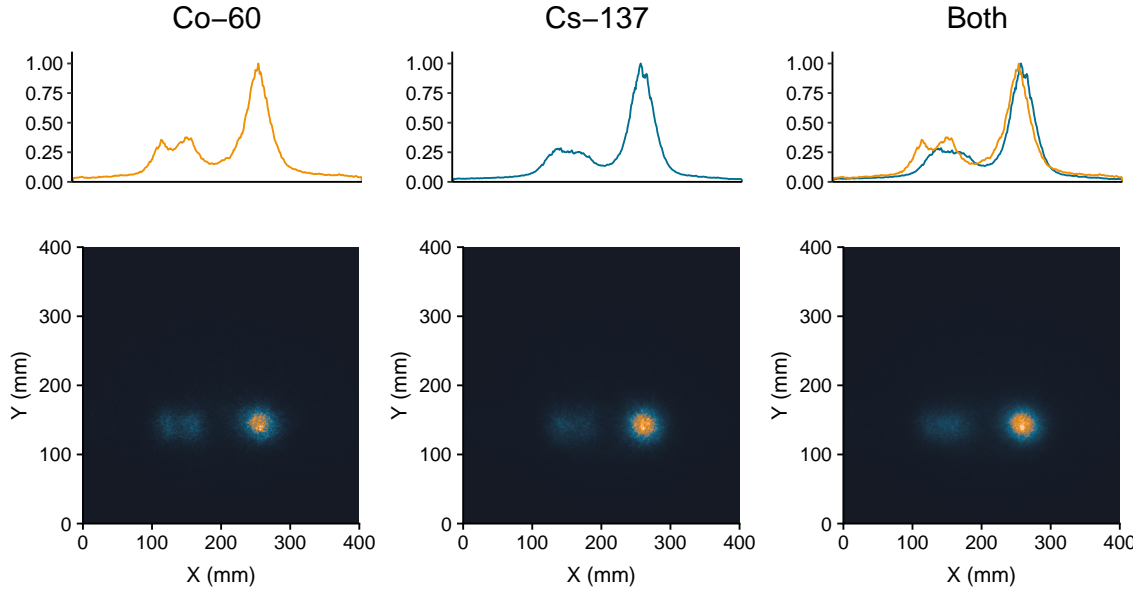
Figure 6.15: Reconstruction of the rear phantom compartments with no water filling the perspex box. The phantom was placed at 22.8 cm from the detector.

The reconstructed profiles from the front and rear phantom compartments are almost identical. This is not consistent with the actual placement of planchettes. One cause for this could be the elongation of sources in the plane perpendicular to the detector, coupled with the disparity found between experimental and reconstructed locations of a source, as reviewed in section 5.2.3. The analytical reconstruction code was used to develop X-Z image slices from this run, these can be seen in Figure 6.16 when gating on Cs-137 photopeak events and Co-60 photopeak events. Dashed lines are used to indicate the position of the phantom during data acquisition. A notable deviation can be seen between the position of the phantom and areas of maximum conic overlaps. The X-Z slice was produced from the Y slice containing the maximum number of overlaps (Y = 140 mm). This discrepancy can explain the similarities between the front and rear compartment slices. Specifically, the elongation of reconstructed images perpendicular to the front of the detector, coupled with the increased likelihood of events being collected from the planchettes in the front compartments, results in the rear slice being almost identical to the front slice. By reconstructing the rear slice using events which most likely originated from the front compartments, a distribution similar to what is expected from the front compartments is contained in these images.
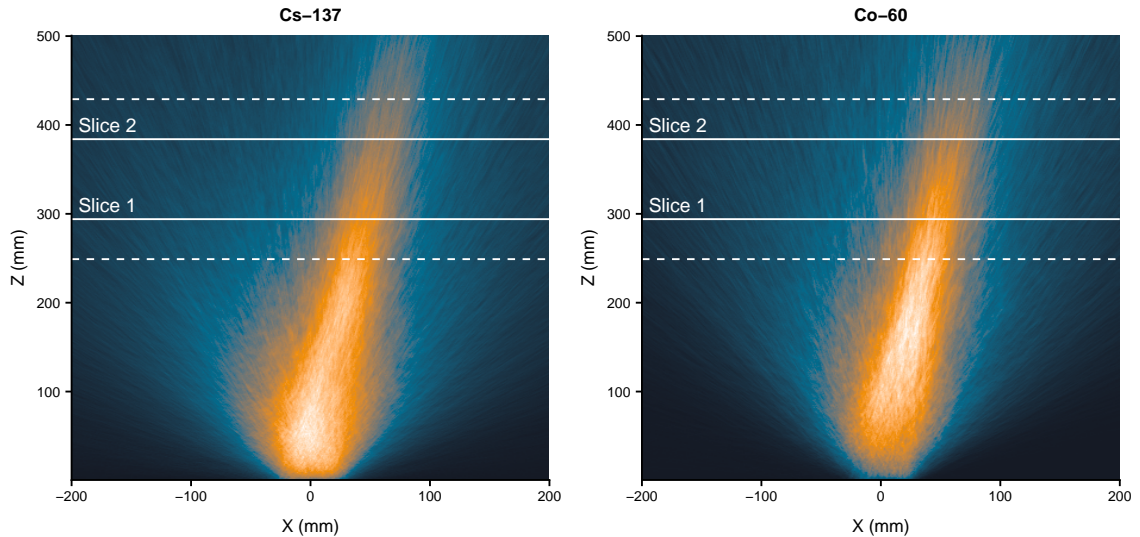
121

Figure 6.16: XZ-image slices of the phantom produced using the analytical reconstruction code. Reconstructions gated on individual isotope photopeaks. Dashed lines indicate the position of the phantom during data acquisition.

The left and right compartments of the phantom house planchettes which are orientated differently. This difference is translated into the reconstructed image profiles. In the right compartment the planchettes are parallel to the detector. The surface area, and therefore solid angle, of these planchettes is greater than those in the left compartment. This difference, in addition to the detection of reconstructible events from the planchettes in the rear compartment, results in a greater profile amplitude in the right compartment compared to the left. The Cs-137 and Co-60 profiles in this compartment overlap almost exactly. There is a slight offset in the location of the two peak's maxima of ~ 3 mm, this is likely to be an effect caused by the collection of events from the perpendicular planchettes in the rear compartment and the staggered distances of the parallel planchettes close to the reconstructed slice. From the profiles it can be inferred that the front-right compartment contains the planchettes which are parallel to the detector, and that both Cs-137 and Co-60 can be found in this section.

The front-left compartment consists of planchettes orientated perpendicular to the detector. The corresponding Co-60 intensity distribution does indicate the presence of more than one planchette through the multiple maxima of the intensity profile but it is impossible to determine the number of planchettes from the Cs-137 profile. A high-pass filter, discussed in section 5.1.3, was applied to the reconstructed slices. By reducing the

low-frequency noise in the image, individual planchettes perpendicular to the front of the detector can now be identified, as shown in Figures 6.17 and 6.18.
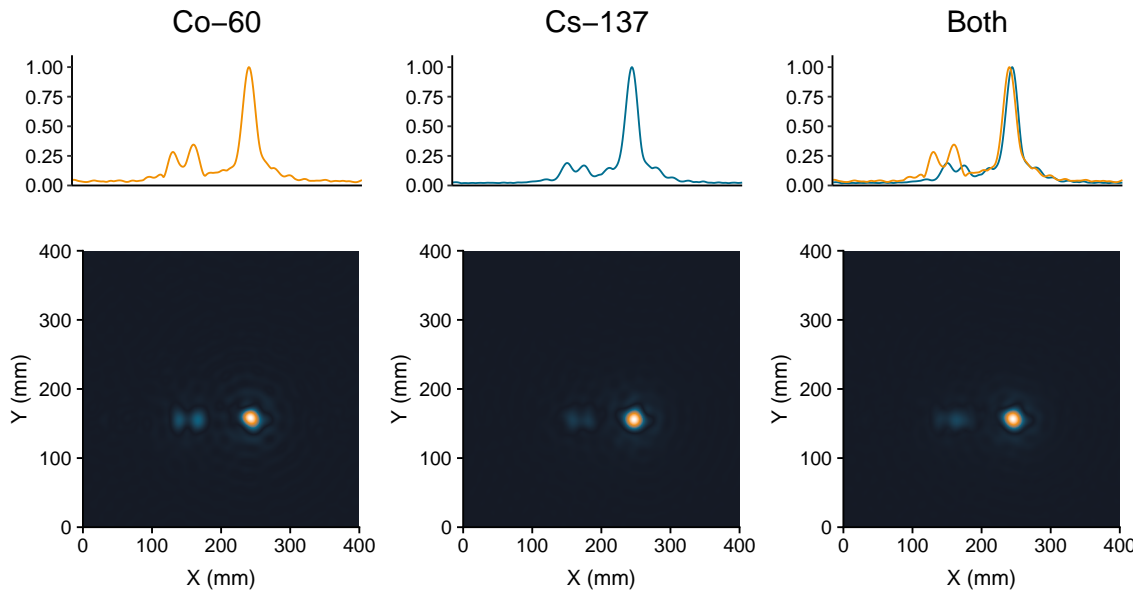

Figure 6.17: Reconstruction of the front phantom compartments with no water filling the perspex box after the application of a high-pass filter.
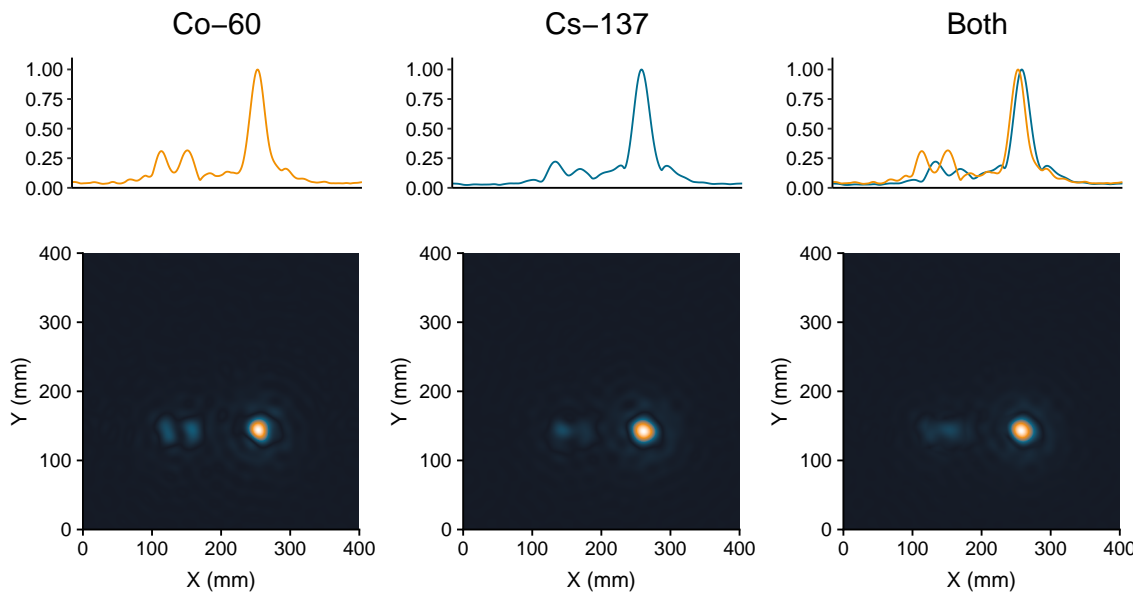

Figure 6.18: Reconstruction of the rear phantom compartments with no water filling the perspex box after the application of a high-pass filter.

Some ringing artefacts from the filter are present in the Compton images but the effect is minimal as the HPF was carefully optimised. Even with this filter applied, the Compton images of the rear phantom compartments do not reflect the known orientation of the planchettes and a new method of imaging objects at differing stand-off distances must be devised. The profile representing the rightmost Cs-137 planchette perpendicular to the detector has a smaller amplitude relative to the leftmost perpendicular planchette. The fewer reconstructible events collected for this planchette, and therefore smaller profile, is consistent with the gamma rays needing to travel through a greater volume of steel to reach the detector due the central phantom partition. Figure 6.19 displays an illustration of the planchette separations in the front compartments of the phantom. Each perpendicular planchette is separated by ~ 9.2 mm of perspex and their centres are 14.2 mm apart. The distance between the centre of the parallel and perpendicular planchettes is 68.7 mm and perpendicular planchettes of like-isotopes are separated by 28.4 mm.
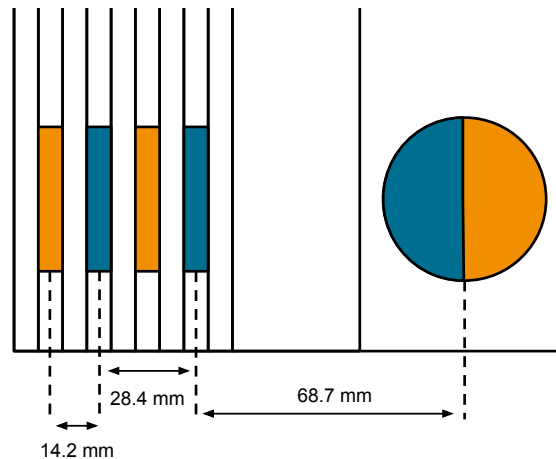

Figure 6.19: Illustration of Cs-137 [blue] and Co-60 [orange] planchette separations in the front phantom compartments.

The combined image profiles developed from the Compton images are displayed in Figure 6.20 along with calculated geometries. From the profiles, the perpendicular planchettes were found to be separated by 19, 10 and 14 mm. Perpendicular Co-60 planchettes were separated by 24 mm and Cs-137 planchettes were separated by 29 mm. The parallel Cs-137 planchette and rightmost perpendicular planchette were separated by 66 mm. A comparison of the experimentally-determined and known planchette separations is displayed in Table 6.2. Slight differences are found between the values, far smaller than the FWHM

of a point source situated at 25 cm from the detector, reconstructed using the analytical code (~ 40 mm). Experimental errors of up to 1 mm are expected due to manufacturing constraints resulting in small gaps between the steel slides and walls of the phantom. These differences could also be influenced by the radial distortion effect which is believed to be a function of both gamma-ray energy and source position.
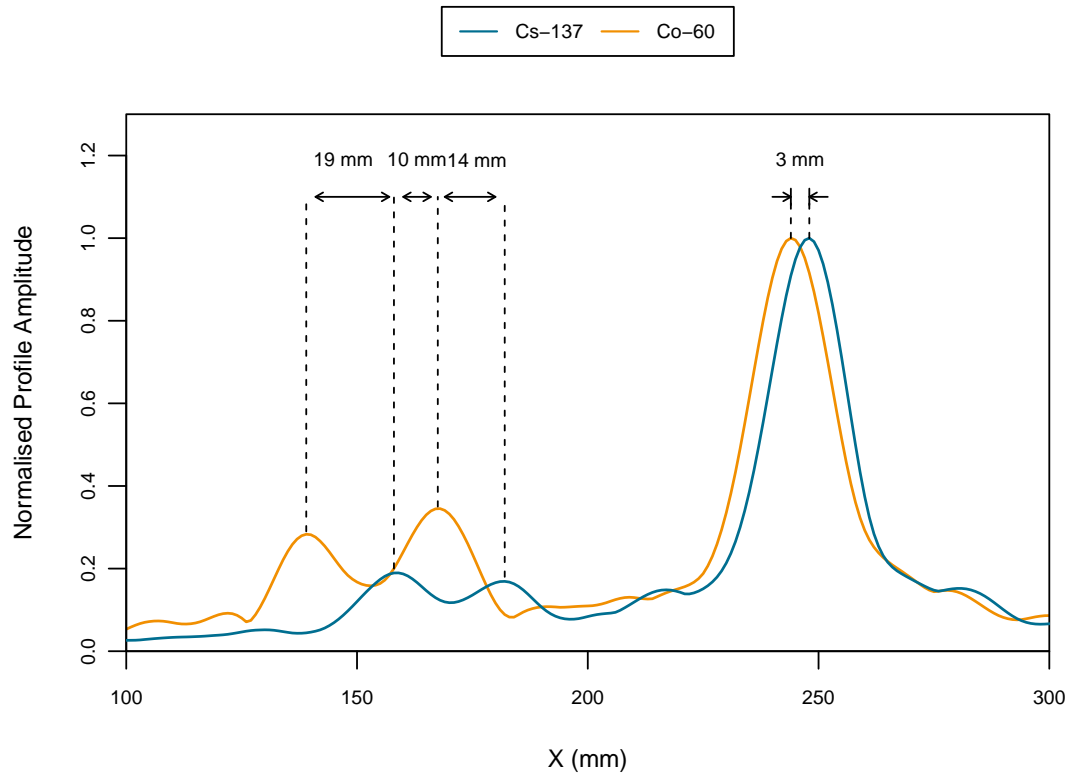

Figure 6.20: Overlaid Cs-137 and Co-60 planchette profiles from the front compartments of the phantom displaying the separation of features. A high-pass filter has been applied to the reconstructed images.

	Calculated Separation (mm)	Known Separation (mm)	Difference (mm)
Perpendicular Co-60 Planchettes	29.0	28.4	0.6
Perpendicular Cs-137 Planchettes	24.0	28.4	4.4
Leftmost Perpendicular Planchettes	19.0	14.2	4.8
Central 2 Perpendicular Planchettes	9.0	14.2	5.2
Rightmost Perpendicular Planchettes	15.0	14.2	0.8
Parallel Cs-137 Planchette and Rightmost Perpendicular Cs-137 Planchette	66.0	68.7	2.7
Parallel Co-60 Planchette and Rightmost Perpendicular Co-60 Planchette	76.0	82.9	6.9

Table 6.2: Known and experimentally determined separations of the planchettes within the phantom. Slight deviations can be seen between the values.

Using a combination of the MLEM reconstruction algorithm and a high-pass filter, it is possible to determine the orientation and isotopic properties of planchettes in the front compartment of the phantom using GRI+. The physical locations of planchettes can be determined within ~ 5 mm at a phantom stand-off distance of 22.8 cm and, for perpendicular planchettes, it is possible to determine their sequence of placement. Planchettes can be identified as being parallel to the detector but it is not possible to determine the ordering of planchettes from a single Compton image when multiple are placed at different distances. Rotation of the phantom to obtain a secondary Compton image, could be used to overcome this limitation and determine the orientation of planchettes in the rear compartment.

6.2.3 Imaging the Phantom Submerged in Water

Fuel is placed in spent fuel pools (SFP) upon their removal from a reactor. The water acts as coolant and shielding, absorbing outgoing radiation. The effect on imaging performance due to the introduction of water was investigated by examining the energy spectra and images produced. Figure 6.21 illustrates the positioning of the phantom relative to the detector and the orientation of planchette sources during data acquisition. This dataset

is identical to the previous run, with the inclusion of water. Data was collected for 45.47 hours, 70,744 reconstructible Cs-137 photopeak events and 50,020 reconstructible Co-60 photopeak events were collected during this time.
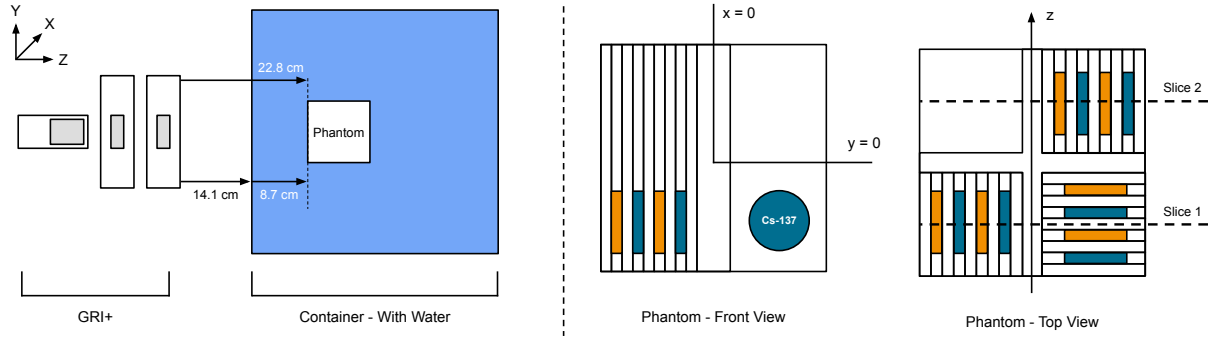

Figure 6.21: Illustration of the phantom filled with all Cs-137 [blue] and Co-60 [orange] planchettes, 22.8 cm from the detector. The phantom was submerged in water.

Figure 6.22 displays the fold-1 energy spectra obtained from the phantom placed 22.8 cm from the detector, with and without water filling the perspex box. An equal number of events were used to create each spectrum, 4,438,096. Figure 6.23 displays a focussed view of the spectrum photopeaks.
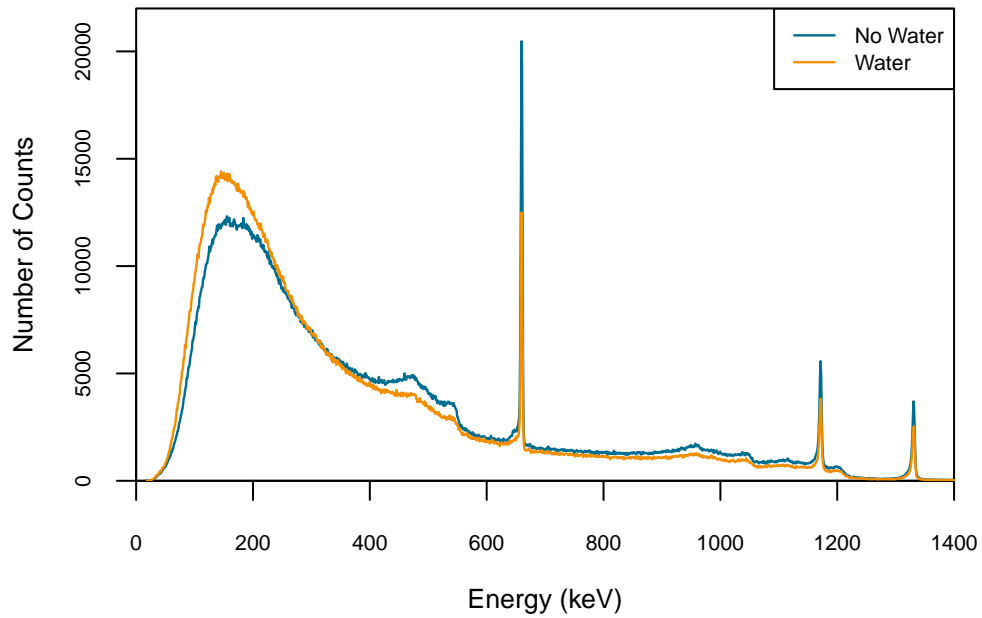
Figure 6.22: Spectrum produced from the phantom placed 22.8 cm from the detector with and without water filling the perspex container.
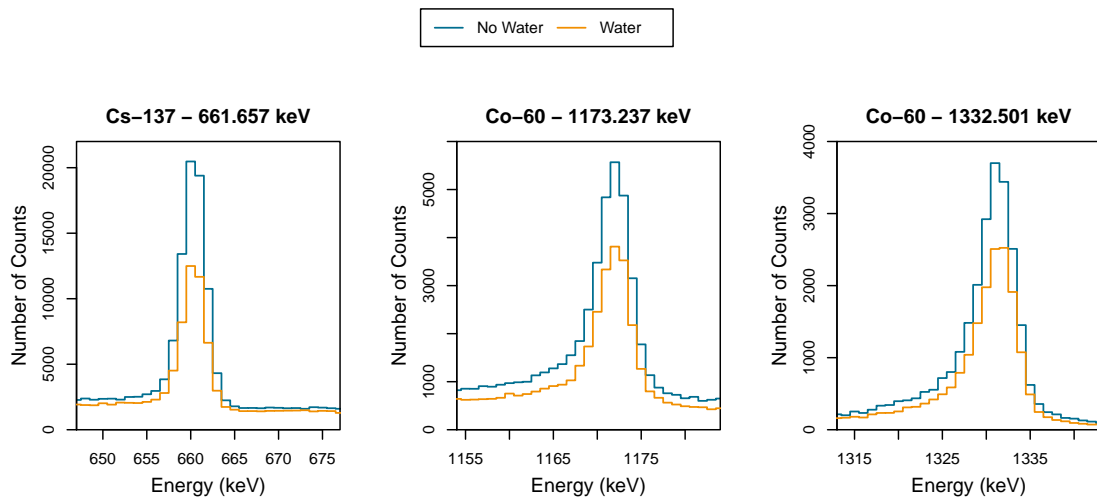

Figure 6.23: Spectrum produced from the phantom placed 22.8 cm from the detector with and without water filling the perspex container, focussing on individual photopeaks.

The body of water scatters and absorbs outgoing radiation according to the physical principles discussed in section 2.1. When water is present, the spectrum shows an increased Compton scattering region, along with fewer photopeak events. The FWHM for each peak was calculated, with and without water, and are displayed in Table 6.3 along with the

percentage decrease in the number of photopeak events. Only a slight difference between the FWHM is seen. In each case the photopeak energies are well defined and can be readily gated thanks to the energy resolution attainable from GRI+. The percentage decrease in the number of photopeak events is reduced with increasing energy. This relationship was described in section 2.1.2, as gamma-ray energy is increased the probability of an interaction taking place within a medium is reduced. As the volume of water between the detector and fuel assembly is increased this effect will be amplified and data collection times shall need to be extended to collect a sufficient number of reconstructible events, particularly at lower energies.

	FWHM (mm)		Percentage Decrease in Photopeak Events
Energy (keV)	No Water	Water	due to the Inclusion of Water
661.657	3.19 ± 0.01	3.16 ± 0.02	38.07
1173.237	4.52 ± 0.05	4.50 ± 0.05	29.82
1332.501	5.11 ± 0.06	5.26 ± 0.07	28.23

Table 6.3: FWHM of photopeak energies with and without water filling the perspex box.

The reconstructed phantom images are displayed in Figures 6.24 and 6.25. the images were produced from the 4th and 5th iterations of the MLEM reconstruction code respectively. The profiles for each slice are very similar to what was seen for the phantom before water was introduced. From the profiles it is difficult to identify the individual perpendicular Co-60 planchettes and impossible to determine the number of Cs-137 planchettes.
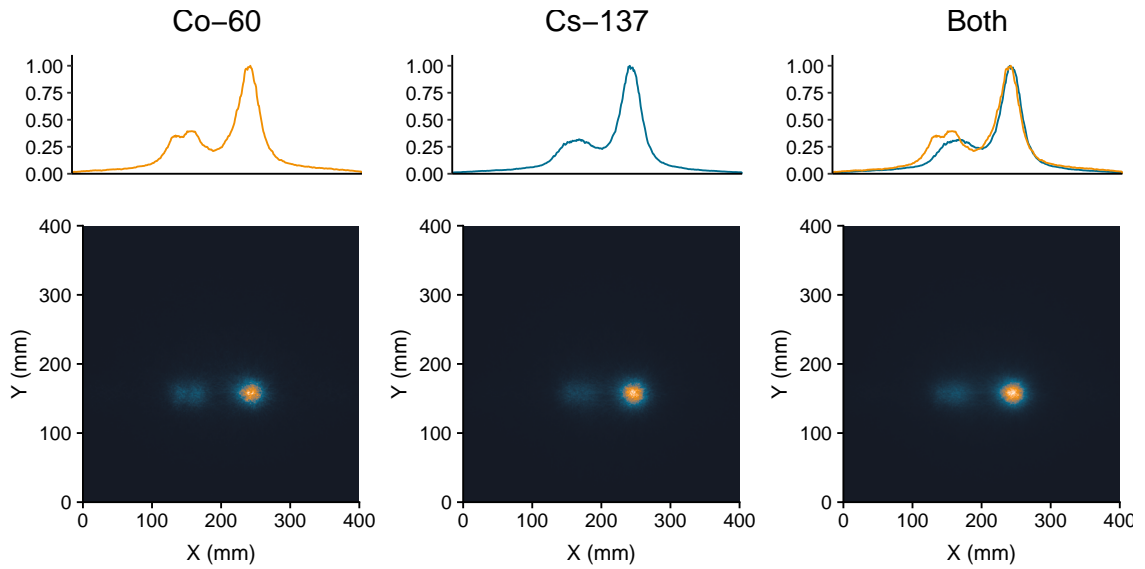
Figure 6.24: Reconstruction of the front phantom compartments with water filling the perspex box. The phantom was placed at 22.8 cm from the detector.
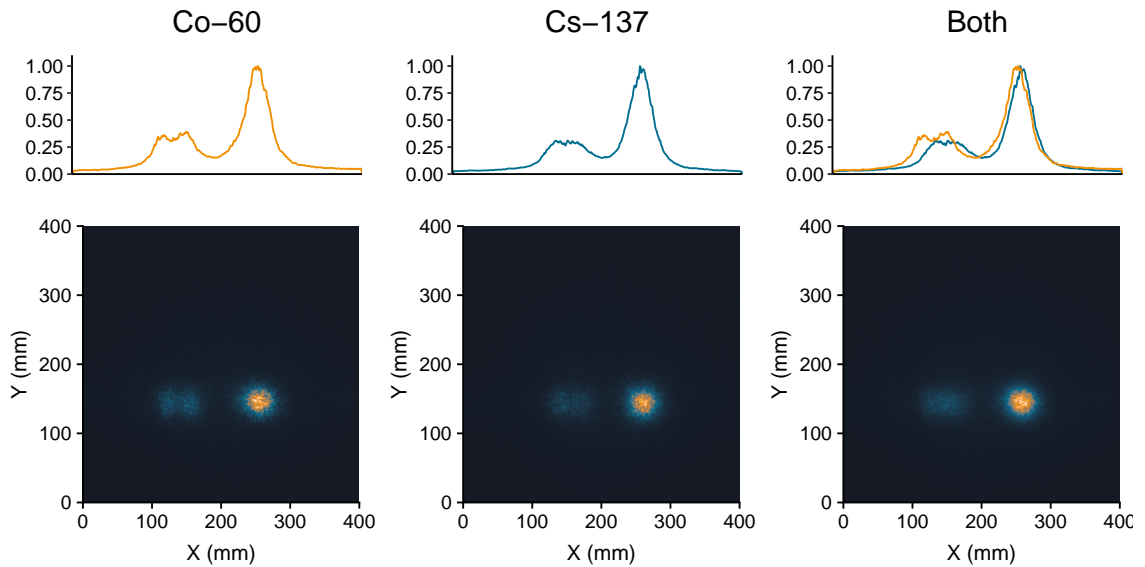

Figure 6.25: Reconstruction of the rear phantom compartments with water filling the perspex box. The phantom was placed at 22.8 cm from the detector.

A high-pass filter was applied to the slices to improve the resolution of the reconstructed images. The resulting Compton images are displayed in Figures 6.26 and 6.27. From the filtered slices it is now possible to place individual perpendicular planchettes, demonstrating the importance of the HPF.
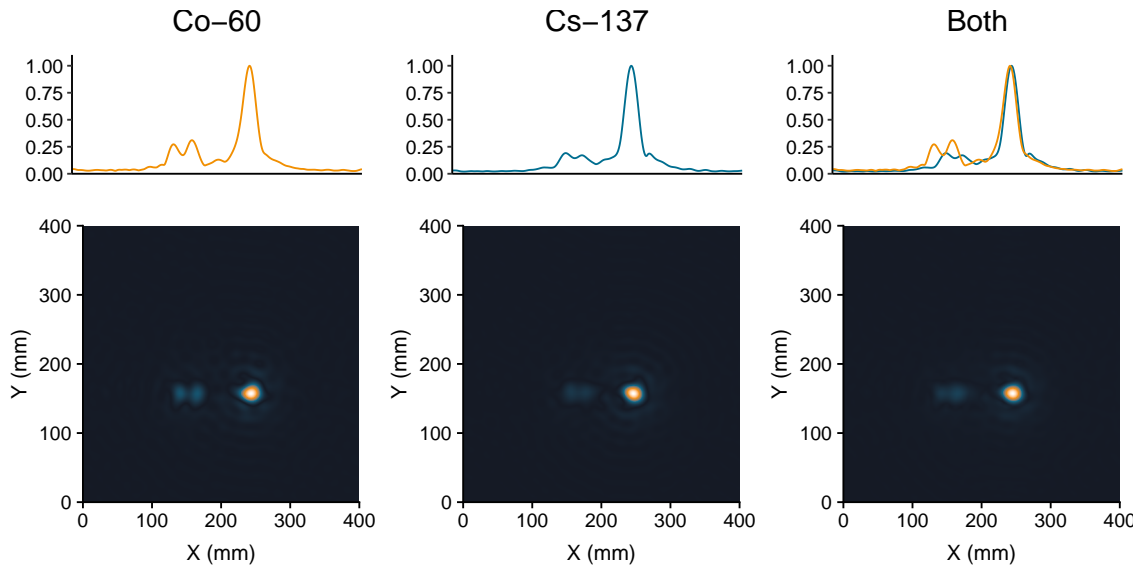
Figure 6.26: Reconstruction of the front phantom compartments with a high-pass filter applied. The phantom was placed at 22.8 cm from the detector, submerged in water.
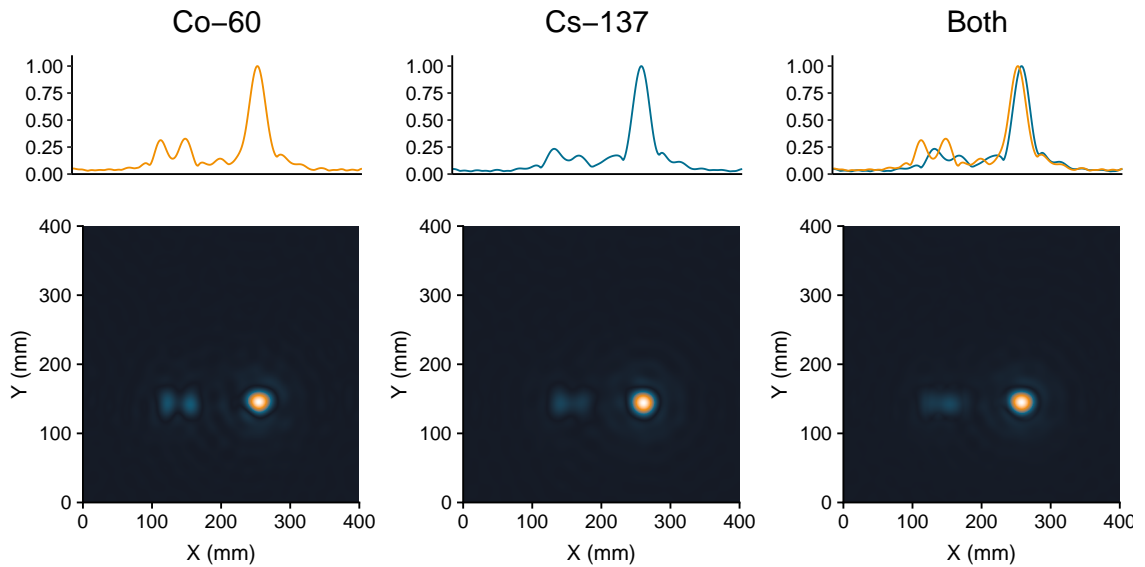

Figure 6.27: Reconstruction of the rear phantom compartments with a high-pass filter applied. The phantom was placed at 22.8 cm from the detector, submerged in water.

As the planchette sources are housed within the steel phantom, a large degree of Compton scattering is already observed before water is introduced into the system. This affects the signal-to-noise of the lower-energy gated photopeak events. Co-60 gamma rays which scatter within the phantom or water could lose enough energy to fall into the lower en-

131

ergy photopeak-gates, increasing the background noise in the images. Figure 6.28 displays the intensity profiles for the phantom at 22.8 cm from the detector with and without water filling the perspex box. Only the front phantom compartments are displayed. The rear compartments show very similar profiles to the front compartments and a new reconstruction technique must be devised in order to obtain information from these slices. Additionally, Figure 6.29 displays these profiles overlaid on the same plot. In each case the profiles are again normalised to the maximum count in the profile.
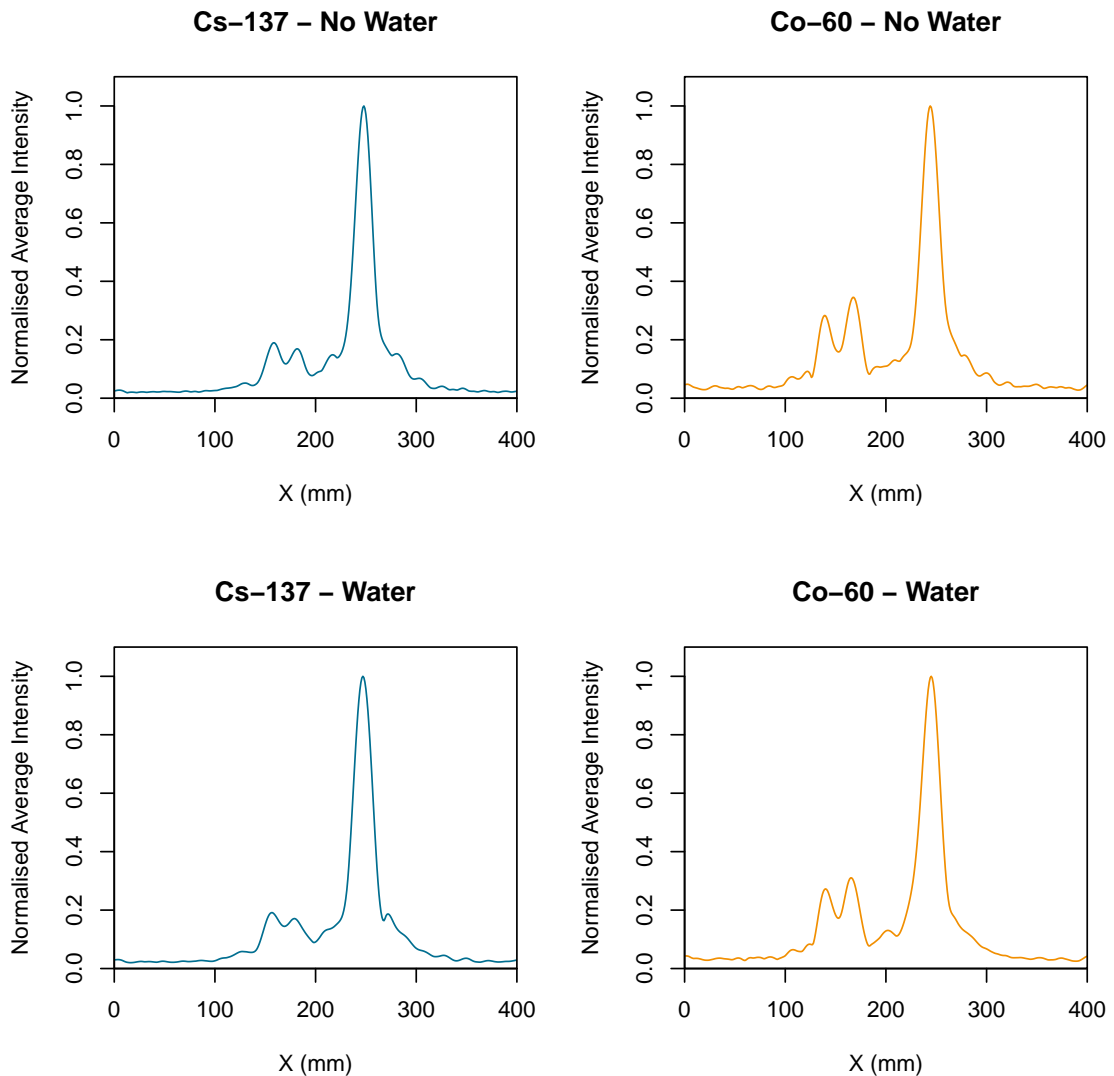

Figure 6.28: Intensity profiles for the phantom placed 22.8 cm from the detector with [bottom] and without [top] water filling the perspex box, after the application of a high-pass filter.
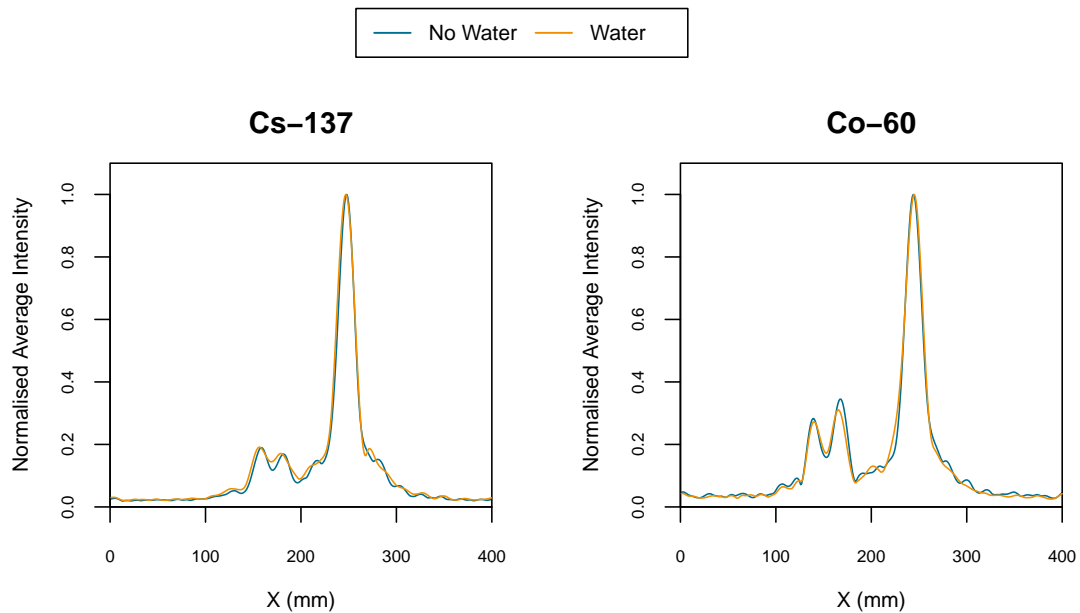
Figure 6.29: Overlaid intensity profiles for the phantom placed 22.8 cm from the detector with and without water filling the perspex box, after the application of a high-pass filter. Reconstructions produced by gating on Cs-137 photopeak events [left] and Co-60 photopeak events [right].

There is very little difference between the reconstructed phantom intensity profiles with and without water filling the perspex box. The planchettes in the left compartment are slightly less well-defined when the phantom is submerged in water. This is a result of the additional scattering gamma rays undergo introducing further uncertainties into their point of origin. Between the two environments, features are located at the same position. The biggest difference between imaging with and without water is the time it takes to obtain reconstructible events. When water is absent, $\sim 2{,}973$ reconstructible Cs-137 photopeak events and $\sim 1{,}825$ reconstructible Co-60 photopeak events are collected per hour. When water is introduced to the system these values reduce to $\sim 1{,}556$ for Cs-137 and $\sim 1{,}100$ for Co-60 per hour.

In conclusion, by submerging the phantom in water, the rate at which reconstructible events are recorded by GRI+ is reduced. Features which were apparent when the system was in a dry environment are still visible and little change is observed in the reconstructed profiles. The good energy resolution attainable from GRI+ limits the degradation in

resolution between the two environments as the photopeaks are well defined and easily gated.

6.2.4 Overview of Experimental Data Findings

Reconstructed phantom images show potential in the use of GRI+ for imaging spent fuel. The most notable indicators that warrant future work in this system are:

1. The energy resolution of GRI+ allows for the easy identification of peaks in gamma-ray spectra, even when the phantom is submerged in water.

2. GRI+ can identify the isotope and orientation of planchettes in the front compartments of the phantom.

3. It is possible to identify the order and position of planchettes placed perpendicular to the detector in the front compartments after the application of a high-pass filter.

Conversely, the reconstructions indicate limitations when using GRI+ for imaging spent fuel:

1. Information cannot be gained on planchettes stationed behind compartments with other planchettes in.

2. The order of planchettes parallel to the detector cannot be determined.

Future improvements can be made to the system to enhance the quality of reconstructed images. A new reconstruction algorithm could be developed which can account for the disparity between reconstructed and actual source positions. This refers to both the radial aspect reviewed in previous work [37] and the elongation of reconstructed sources perpendicular to the detector, discussed in section 5.2.3. A new method which allows for the reconstruction of images using fold-2 events could be investigated to increases the system's efficiency which doesn't degrade the quality of reconstructed images. This would reduce the lengthy acquisition times required for the system to collect an adequate number of reconstructible photopeak events. And finally, in its current form, GRI+ is unable to attain information regarding the position of planchettes in the rear compartments. A possible solution to this issue is to rotate the fuel module during imaging to produce a 3D model of the assembly.

Chapter 7

GEANT4 Phantom Simulation

GEANT4 is a Monte Carlo toolkit, written in the C++ coding language [38], to simulate the tracking of particles through media [39]. It is utilised in multiple fields, such as astrophysics, medical physics and high energy physics to simulate real world systems without the requirement of a physical environment or expensive equipment. GEANT4 is maintained, tested and improved by a large collaboration of specialised computer scientists and physicists. There are an extensive suite of features available to users, and all simulations should be compared to physical systems to validate implemented choices. As GEANT4 has an object orientated structure, simulations are generally split across several files with each controlling a different aspect of the simulation.

A simulation was developed to determine the impact detector position resolution has upon the quality of reconstructed images. In the near future database PSA algorithms are to be implemented for GRI+. This offline-technique matches the signals produced by the detector preamplifiers to a simulated database of signals taken from known positions. At optimum performance, this method should localise events in the scatter detector to $1.1 \times 1.1 \times 1$ mm^3 voxels and events in the absorber detector to $1 \times 1 \times 1$ mm^3 voxels. The simulation was created to mimic the improved position resolutions we hope to obtain from the system. The information can then be used to determine the highest quality image obtainable by GRI+ of the phantom, and then compare this image to what it is possible to produce using current PSA methods. The simulation was designed as a stepping-stone for later, more thorough, investigations into the effect various imaging parameters have on the performance of GRI+. This chapter shall discuss the GEANT4 implementation of both GRI+ and the phantom, and the steps used to validate the simulation.

7.1   GEANT4 Detector Geometry

Objects in GEANT4 are defined by their shape, material and position. A complete visualisation of the implemented geometry is displayed in Figure 7.1. The principal elements of the GRI+ system were included to ensure the simulation was as accurate as possible. The final simulation included:

- Detector crystals

- Detector cryostats

- Detector guard rings

- Detector dead layers

Each detector is sensitive to the location radiation interacts and the amount of energy deposited. This information was recorded for each of the crystals and stored for offline analysis. Post processing methods were used to add uncertainties to the energies deposited in each tier based on the known energy resolution response of GRI+. Additionally, low energy thresholds were applied to each detector segment, and events which occurred in the channels unused by the digital acquisition system were vetoed.
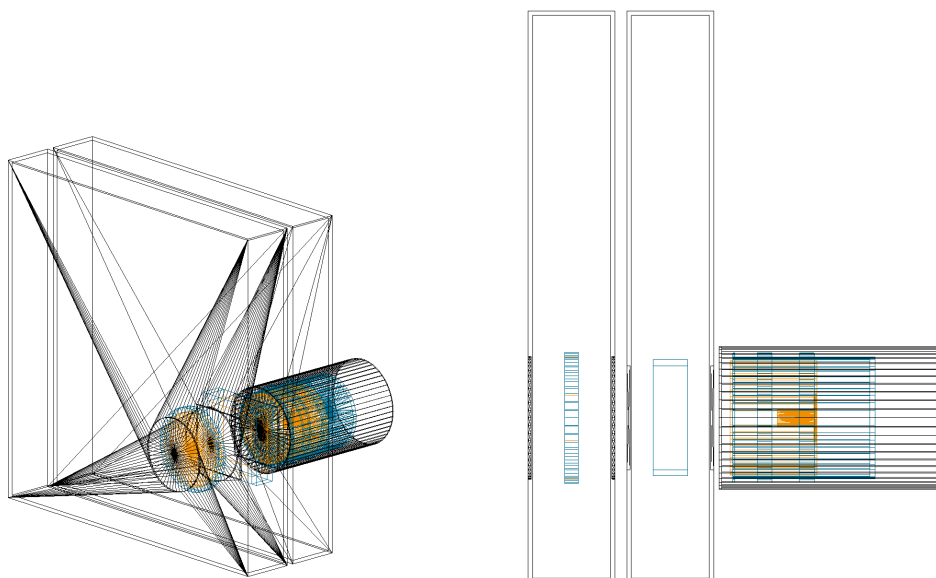

Figure 7.1: Geometry of GRI+ implemented in GEANT4, angled [left] and side [right] view. Cryostats are displayed as black, crystals as orange and dead layers as blue.

7.2 GEANT4 Physics List

The user must specify which interaction mechanisms particles can undergo. This is done by selecting a pre-made list of physics processes or by defining a custom set of rules cherry-picked from available classes. The cross-sections for each interaction type differ across physics lists. For simulating GRI+, it was decided that the low energy electromagnetic package 'G4EmLowEPPhysics' was a suitable choice. The energy depositions recorded in GRI+ fall far below 2 MeV and the selected list is validated for energies ranging from a few eV to several GeV. A default cut value was chosen for all particles in the simulation, this value decides the point after which a particle shall no longer be tracked.

7.3 GEANT4 Sensitive Detector Description

The scatter, absorber and coaxial crystals are defined as sensitive materials in the simulation. When radiation enters one of these volumes, the simulation was developed to store the following information:

1. Type of particle being tracked

2. Energy deposited from interactions in the volume

3. Identifier of the sensitive volume

4. Time of each interaction

5. Location of each interaction

Each simulated gamma ray in GEANT4 is given a unique identifier upon initial creation which is maintained throughout its life-cycle. Crystals were segmented by placing gates on the position of each interaction, where each gate represented a strip on the detector. Energies deposited from multiple interactions within one segment were summed and this information was used to produce an output format comparable to the physical system.

7.4 Validation of the GEANT4 Simulation

To validate the simulation, reconstructed images produced using simulated and experimental data were compared. Several datasets were acquired for this purpose. The same

number of reconstructed events from both the experimental and simulated datasets were input to the analytical reconstruction code, and FWHM from the reconstructed slices were calculated. For the purpose of validation, PSA was not applied to experimental or simulated data. The PSA method developed to determine the depth of an interaction, described in section 4.7.2, is not uniformly sensitive throughout the depth of the absorber detector. Interactions near either face of the crystal show very similar risetimes (T30, T50 and T90) to the positions a few millimetres before the respective faces, as shown in Table 4.2. This results in a 'bunching' effect, where events are placed away from the faces of the crystal. Furthermore, XY-PSA is not currently implemented for strips with no neighbouring contacts. Simulated data would not display these phenomena and interactions would be identified perfectly. Therefore, to achieve the most suitable comparison, event locations were localised to the voxels created by intersecting contacts and only fold-1 events were used to reconstruct images.

Cs-137 datasets were used to validate the system as, along with Co-60, this is the isotope of interest and will be representative of the response expected from the planchettes supplied with the phantom. Co-60 could have also been used but the reduced efficiency of GRI+ for higher energy photopeaks meant the simulations would have required longer processing times. The GEANT4 simulation was ran on an early 2015 Macbook Pro, using a 2.9 GHz Intel Core i5 processor. Processing times of around 24 hours were required for a Cs-137 point source at a 10 cm stand-off distance to collect 10,000 reconstructible fold-1 events. Figures 7.3 and 7.4 display the reconstructed images and corresponding profiles produced from the simulated and experimental data runs, and Table 7.1 displays the calculated FWHM. The FWHM of slices were taken through the row and column of the pixel containing the maximum number of conic overlaps from the simulated and experimental images. Agreement for each comparative pair was achieved within an allowed margin of 3 standard deviations. This demonstrates the validity of the simulation for Compton imaging and gives confidence in other, more complex output. A minimum of 10,000 events were used to reconstruct each image. Additional validation steps, such as comparing the efficiency of simulated and experimental detectors, had to be foregone due to an unforeseeable DAQ issue affecting the system. The result of this issue is that the efficiency and energy response of the detector cannot be reproduced and so this simulation shall act as the foundation for future, more thorough, investigations. However, the simulation is currently only

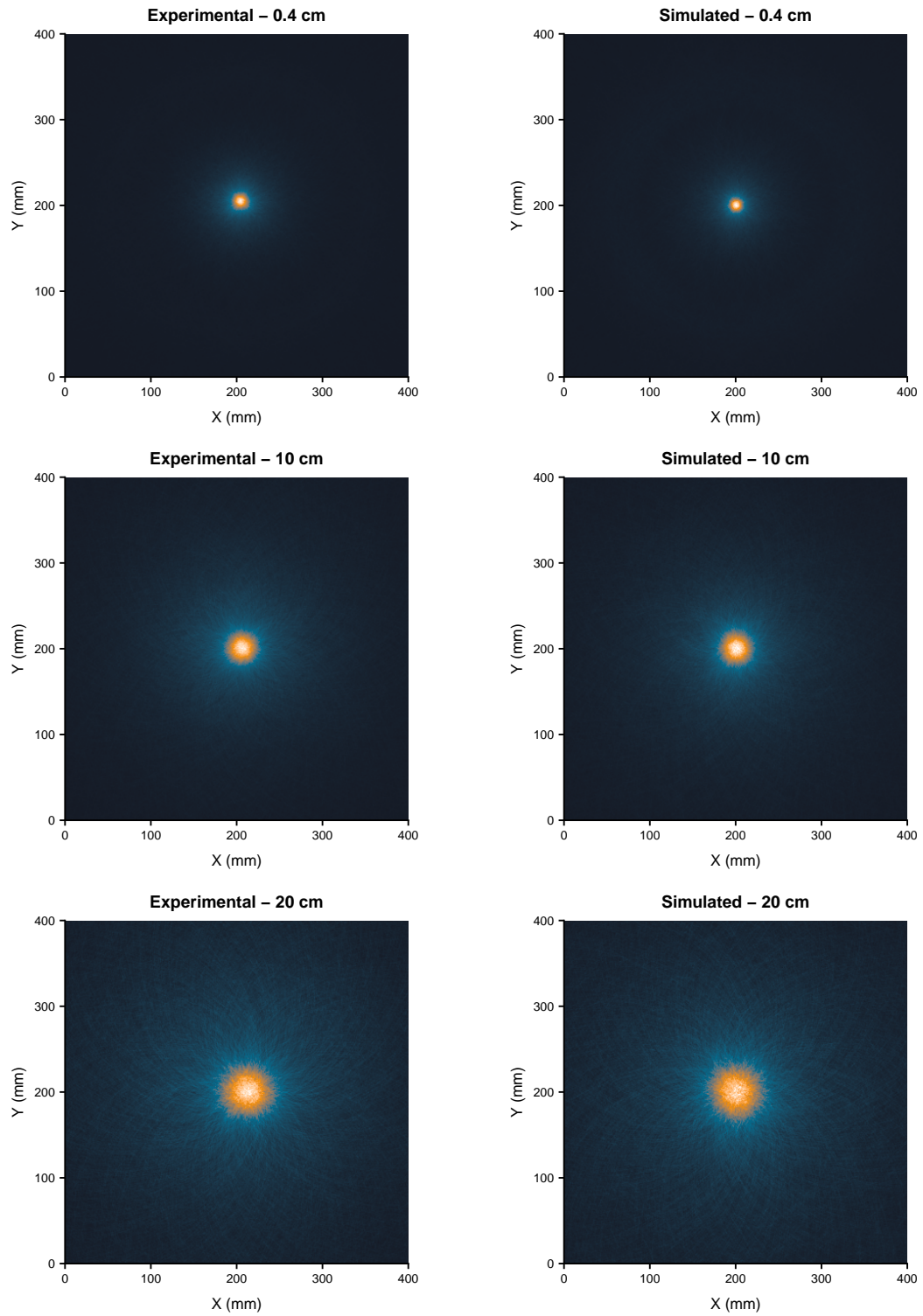to be used to evaluate image quality, which is shown to be valid.

Figure 7.2: Experimental and corresponding simulated image slices. This figure continues on the next page.
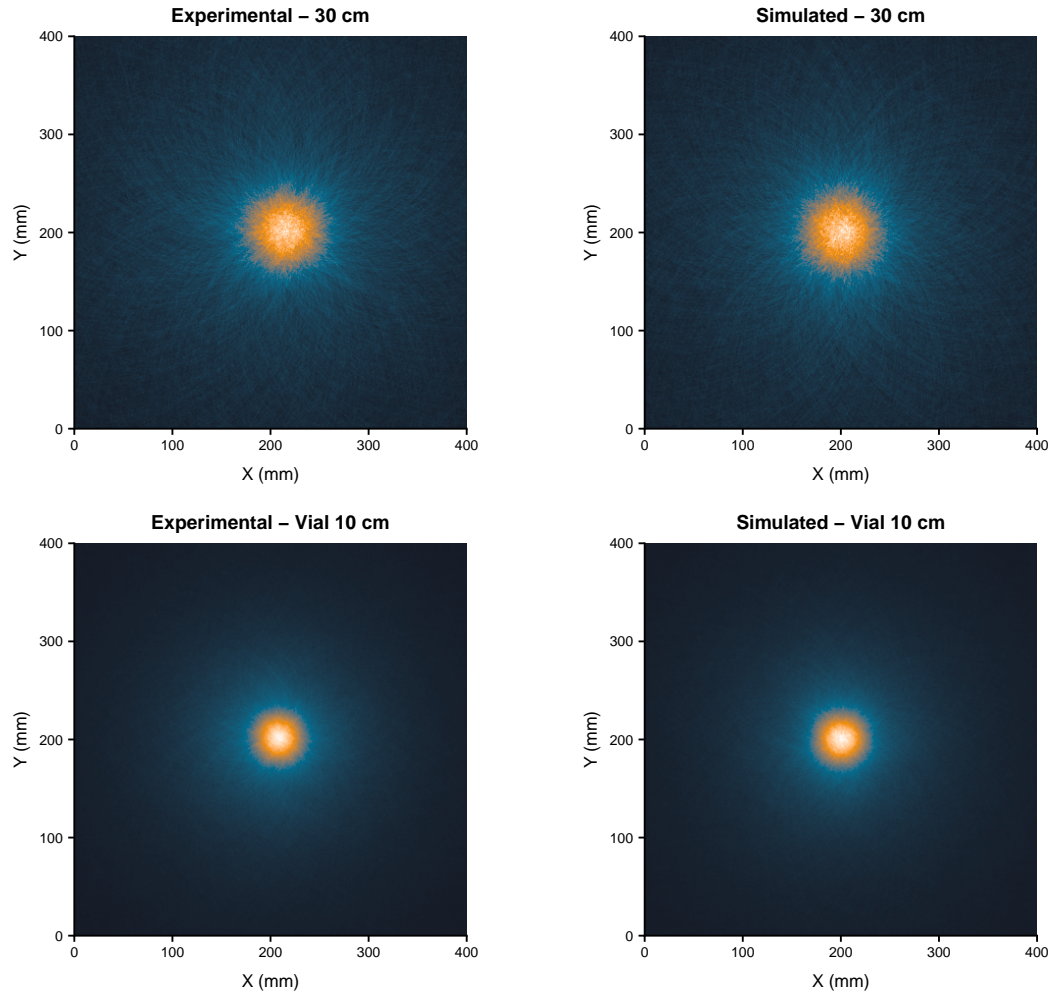
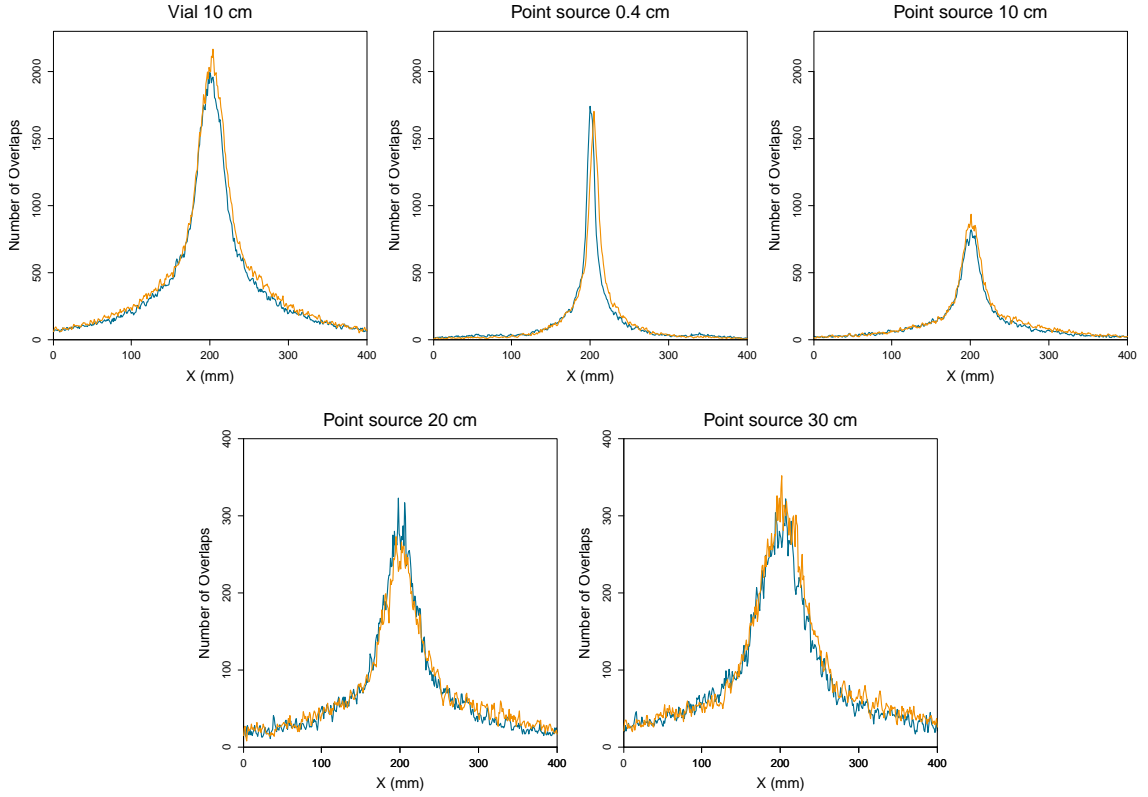**Figure 7.3:** Experimental and corresponding simulated image slices.

Figure 7.4: Experimental [orange] and corresponding simulated [blue] image profiles. These profiles represent the rows containing the maximum number of conic overlaps from the image slices.

Isotope	Source Location (cm)	Experimental FWHM (mm)	Simulated FWHM (mm)
Cs-137 Point Source	(0, 0, 0.4)	13.66 ± 0.18	13.23 ± 0.12
Cs-137 Point Source	(0, 0, 10)	27.72 ± 0.22	27.89 ± 0.31
Cs-137 Point Source	(0, 0, 20)	48.12 ± 0.74	47.47 ± 0.94
Cs-137 Point Source	(0, 0, 30)	63.13 ± 0.96	67.49 ± 1.1
Cs-137 Vial	(0, 0, 10)	40.48 ± 0.36	41.09 ± 0.36

Table 7.1: Comparison of experimental and simulated image resolutions. FWHM calculated from intensity slices at the row (Y) containing the greatest number of conic overlaps, column slices show similar consistency.

7.5 Simulating the Phantom in GEANT4

The phantom was simulated according to the schematics described in section 6.1. Both the steel and perspex materials required for the simulation are available within GEANT4's material database. These were used to simulate the phantom body, planchette slides, perspex separating volumes and surrounding box. Figure 7.5 displays a wireframe illustration of the implemented phantom geometry. Two experimental data runs were replicated in GEANT4; the phantom containing only two slides, and the phantom containing a full set of slides without water filling the perspex container. Substantial run times were required to obtain the equivalent number of reconstructible Cs-137 and Co-60 events in the simulation as from experimental data. Even when biasing the direction of emitted gamma rays towards the detector system, each simulation required approximately 10 days of processing.
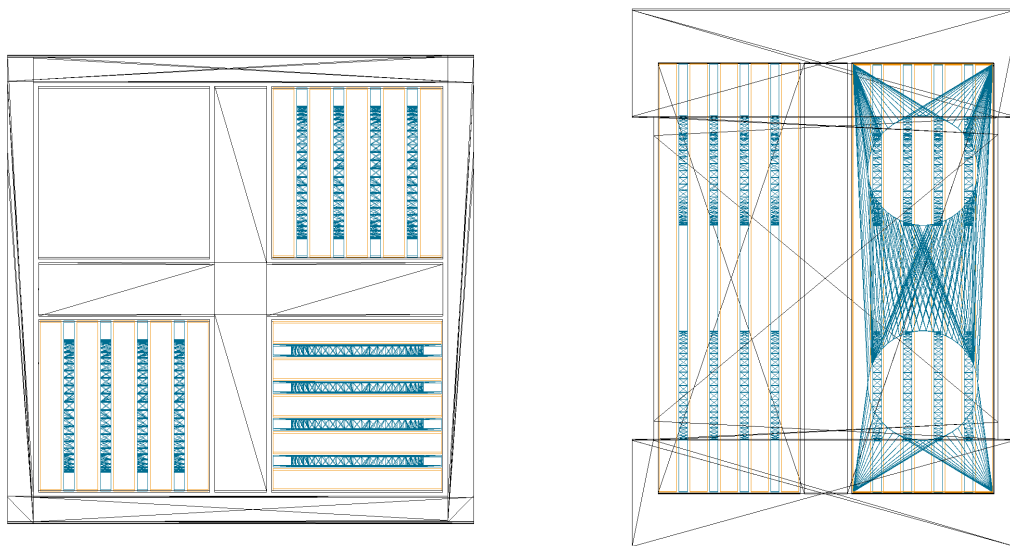

Figure 7.5: Wireframe visualisation of the phantom from the top [left] and front [right].

7.5.1 Simulation of the Phantom Containing 2 Planchette Sources

The first simulation replicated the first experimental dataset. The perspex box was not filled with water and the phantom, placed at a distance of 22.8 cm from the detector, contained a single Cs-137 planchette and Co-60 planchette. Figure 7.6 displays simulated wireframe illustrations of the implemented phantom and GRI+ geometries. Initially, no

PSA was applied in the simulation. This permits a direct comparison between the simulated and experimental data. By ensuring these images are similar, more confidence can be placed on the results obtained when applying improved position resolution to the detectors.
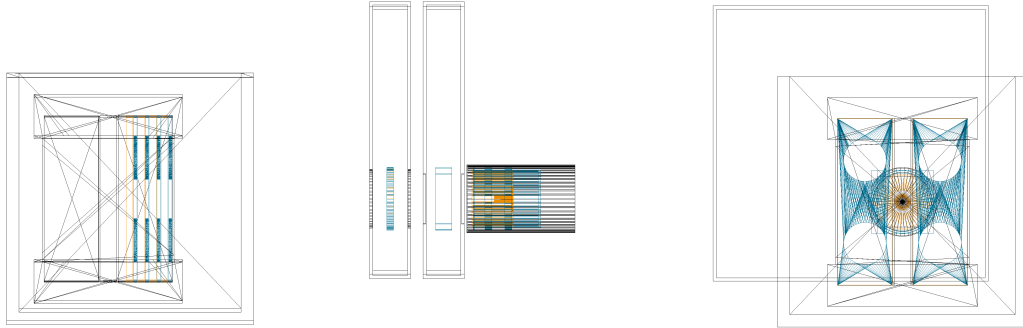

Figure 7.6: Wireframe visualisation of the phantom, detector and empty perspex container from the side [left] and behind the phantom [right].

Simulated data was reconstructed using the 4th iteration of the MLEM code. Figures 7.7 and 7.8 display the experimental and simulated reconstructed images. Both images were reconstructed using 21,246 Cs-137 photopeak events, and 12,926 Co-60 photopeak events. Applied energy gates and MLEM code settings were chosen to match previous experimental data reconstructions, as per section 6.2.1. The figures show the reconstructed Co-60 planchette on the left, Cs-137 planchette in the centre and the two reconstructions combined on the right.
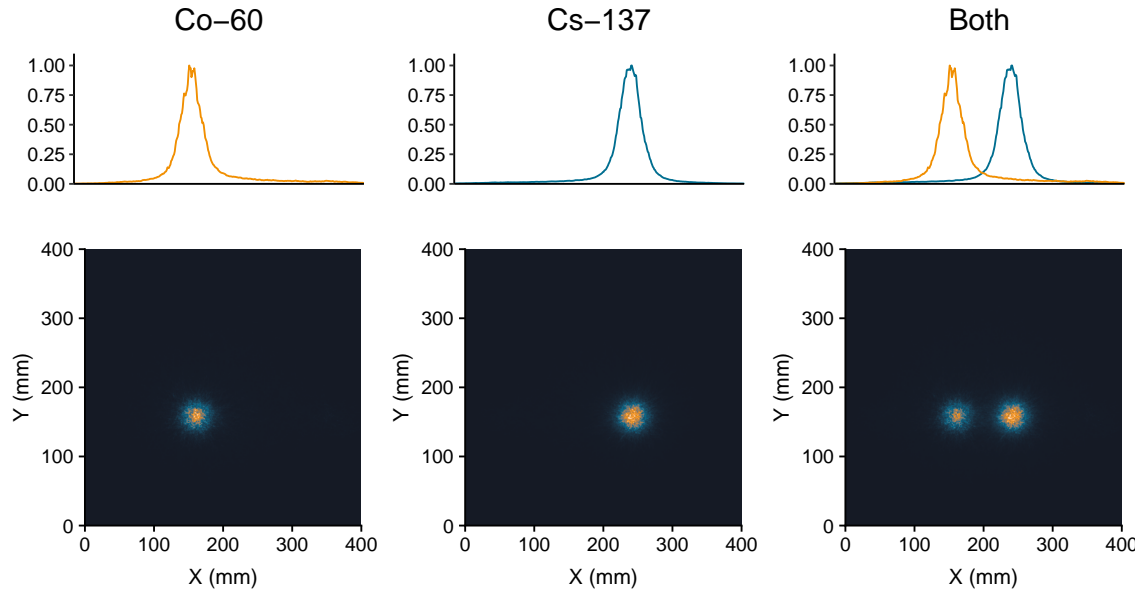
Figure 7.7: Reconstruction of experimental data obtained of the phantom containing two planchette sources with no water filling the perspex box. The phantom was placed 22.8 cm from the detector. No PSA was applied to data before reconstruction.

Figure 7.8: Reconstruction of simulated data obtained of the phantom containing two planchette sources with no water filling the perspex box. The phantom was placed 22.8 cm from the detector. No PSA was applied to data before reconstruction.
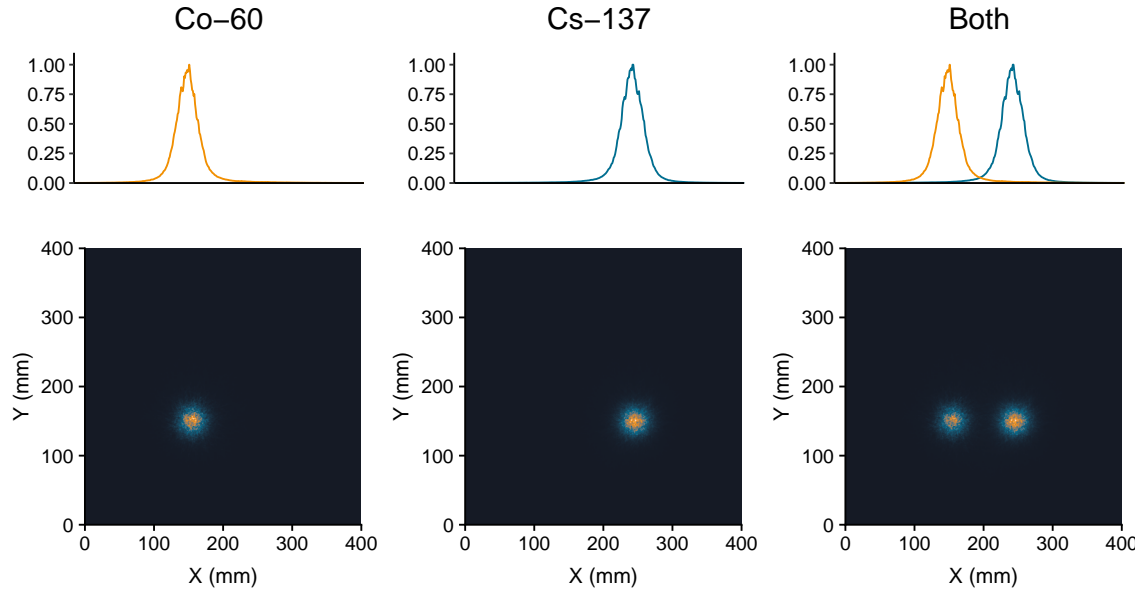
The reconstructed images produced using experimental and simulated data are very similar. In each case, the planchette sources are easily identifiable as standalone distributions. Differences are seen in the random statistical noise of the profiles but the position and width of the individual isotopes closely match, as can be seen in Figures 7.9 and 7.10. A perfect match between the two images cannot be expected as small inconsistencies shall exist between the two data sets; for example, experimental charge sharing effects, imperfect placement of objects, and scattering of gamma rays from the environment and frame are not simulated. The similarity of the Compton images indicates that the fuel phantom has been accurately simulated.
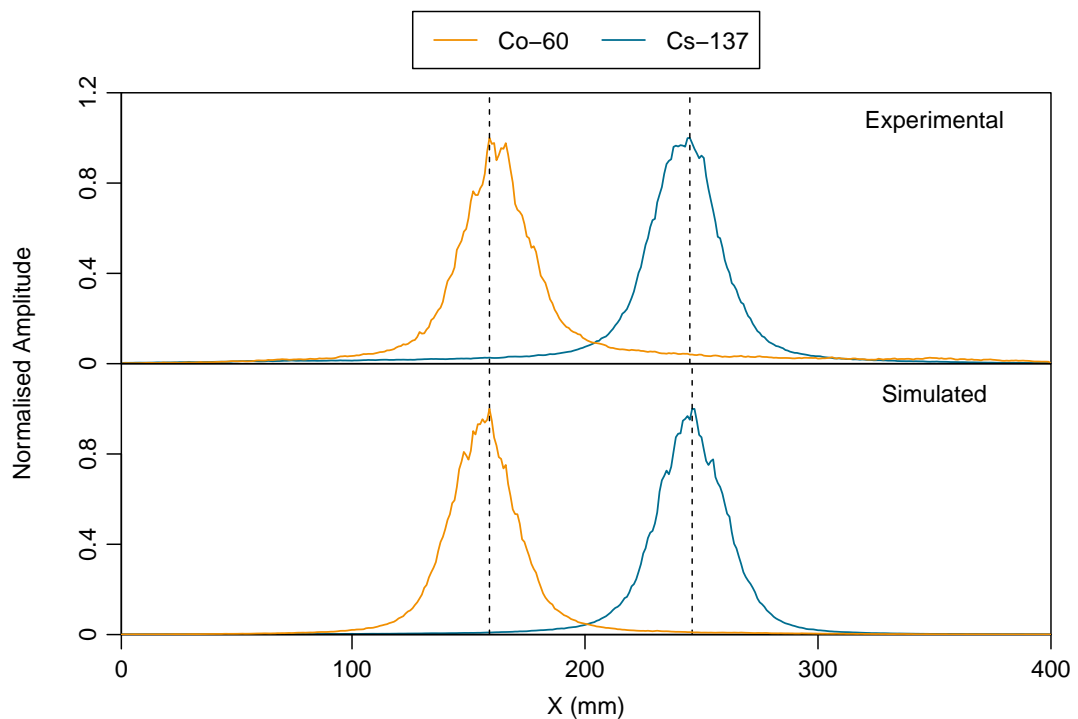

Figure 7.9: Comparison of the image profiles produced from experimental and simulated data of the phantom containing only 2 planchette sources. Dashed lines indicate the location of the profile's maximum amplitude and no PSA was applied during processing.
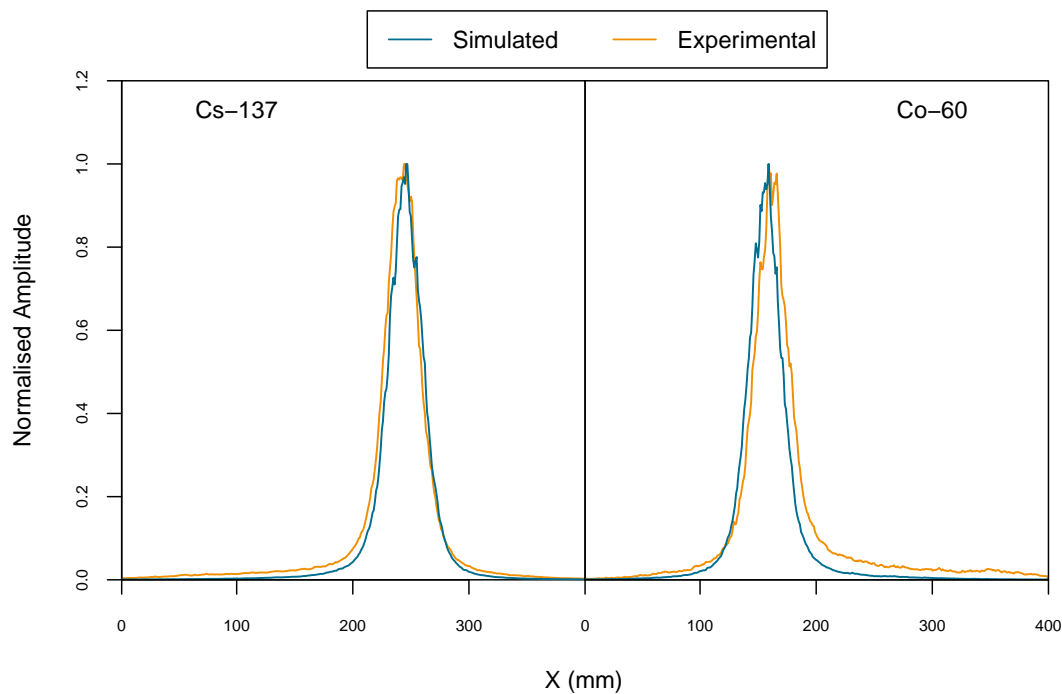
Figure 7.10: Comparison of the image profile widths from the experimental and simulated phantom containing only 2 planchette sources.

It is believed that, after the application of improved PSA algorithms, voxel sizes can be decreased to $1.1 \times 1.1 \times 1$ mm^3 and $1 \times 1 \times 1$ mm^3 in the scatter and absorber detectors respectively. As such, a second simulation was ran which segmented the crystals into these volumes to mirror the performance of future PSA algorithms. The same number of reconstructible fold-1 events were used in the production of this image as the non-PSA version. The reconstructed images are displayed in Figure 7.11. Figure 7.12 overlays the non-PSA and PSA simulated profiles. The width of each profile is greatly reduced when the position resolution of the detector is increased. This shall aid in the identification of individual planchettes when they are positioned at smaller separations.
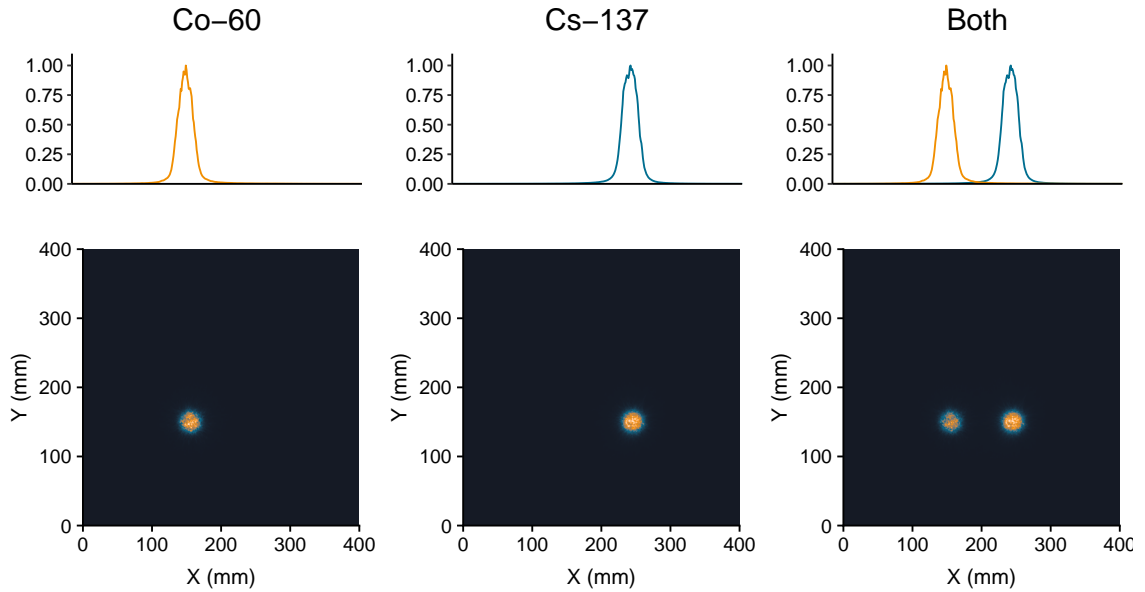
Figure 7.11: Reconstruction of the front phantom compartments with no water filling the perspex box. The simulated phantom was placed 22.8 cm from the detector. Optimum PSA has been applied to the data.
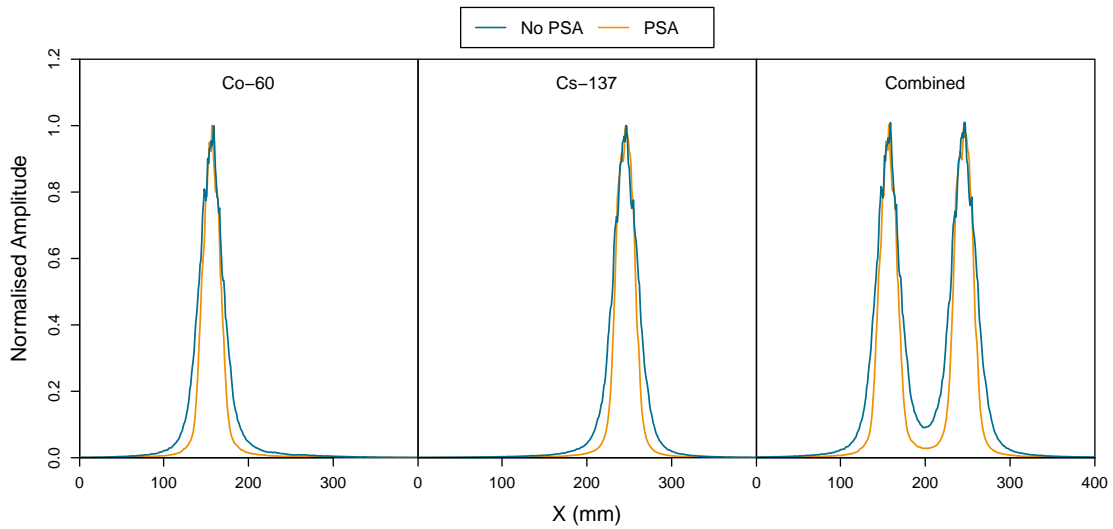

Figure 7.12: Comparison of the image profiles from the simulated phantom with and without PSA applied to the data.

The difference between profile maxima of the simulated data with and without PSA were calculated to be 90 and 87 mm respectively. The known separation of planchette sources is 90 ± 1 mm, the uncertainty is a result of the small amount of movement al-

lowed by the metal slides and planchettes. This indicates that the radial distortion effect could be a result of uncertainties in the positioning of Compton cone axes, more work must be conducted on this topic for full clarification. The edge response function was applied to the reconstructed phantom images produced from the simulation with optimal position resolution, this is shown in Figure 7.13. The improved localisation of interaction positions within GRI+ should result in a more precise measure of planchette width. The extent of the bodies were evaluated between the limits of 5 % and 95 % the height of the normalised cumulative distributions. These values were chosen based on the shape of the ERF responses which lacked the gentle sloping of previous evaluations. The widths of each planchette were determined to be 38 and 41 mm for Cs-137 and Co-60 respectively. This is a marked improvement over the previous experimental values of 41 and 54 mm calculated between the more generous limits of 15 % and 85 %, and much more in-line with the expected value of 35 mm.
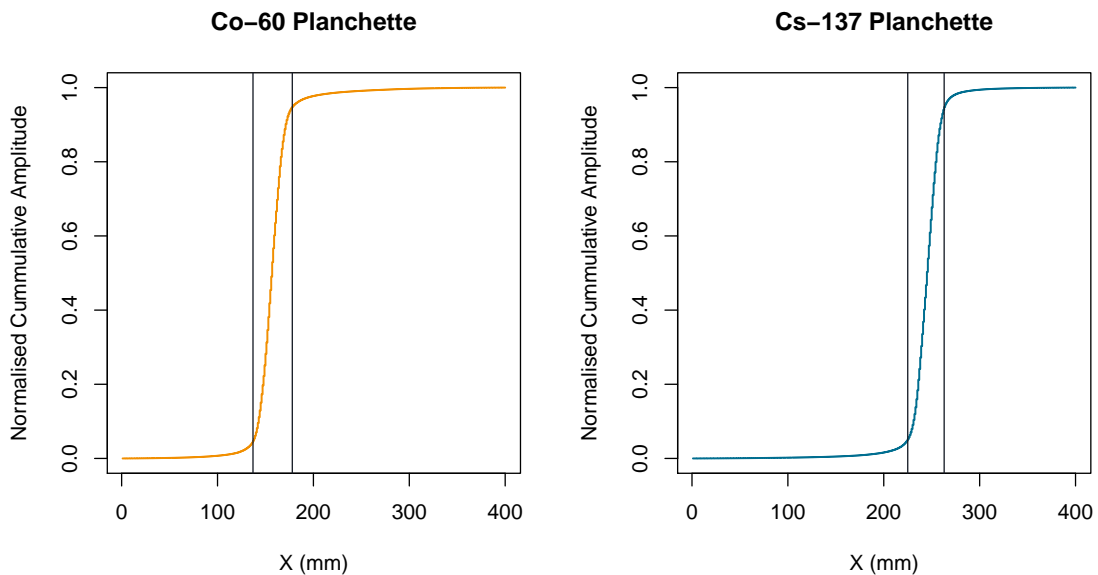

Figure 7.13: Edge response function applied to the Co-60 profile [left] and Cs-137 profile [right]. Vertical lines represent the points where distributions reach 5 % and 95 % of their maximum height.

The results of this first simulation indicate that:

1. The phantom has been correctly implemented as the reconstructed images produced using experimental and simulated data with no PSA applied are very similar.

2. The resolution of reconstructed phantom images improves with increasing detector position resolution.

3. As the segmentation of GRI+ is increased, the width of radioactive bodies, calculated using the ERF from reconstructed images, more accurately represents experimental widths.

7.5.2   Simulating the Phantom with a Complete Set of Planchettes

A simulation was developed to replicate the second experimental dataset of the phantom containing all 12 planchette sources, 6 Cs-137 and 6 Co-60. The planchettes were orientated as per Figure 6.13 to exactly match the experimental set-up, the GEANT4 wireframe geometry for this run is illustrated in Figure 7.14. A total of 67,589 reconstructible fold-1 Cs-137 photopeak events and 41,490 Co-60 events were simulated over several days. Slices were reconstructed at distances of 27.3 cm and 36.3 cm from the detector, through the centres of the front and back compartments. The slices were reconstructed using the 4th and 5th iterations of the MLEM code respectively and improved position resolutions were applied, these images are shown in Figures 7.15 and 7.16.
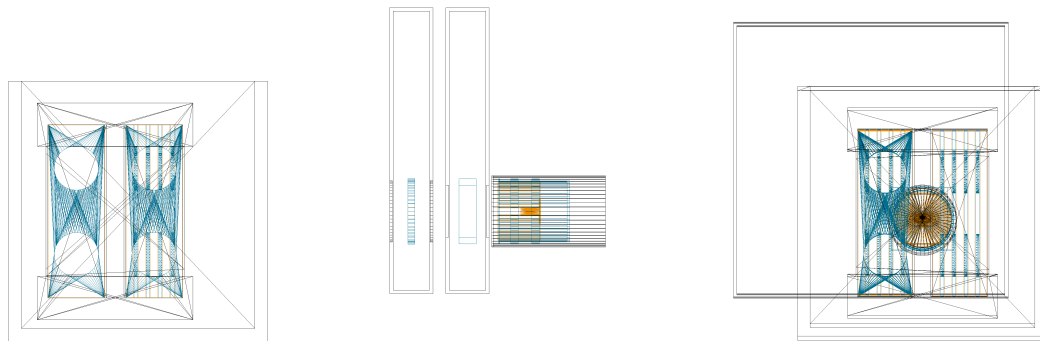

Figure 7.14: Wireframe visualisation of the phantom, detector and empty perspex container from the side [left] and behind the phantom [right].
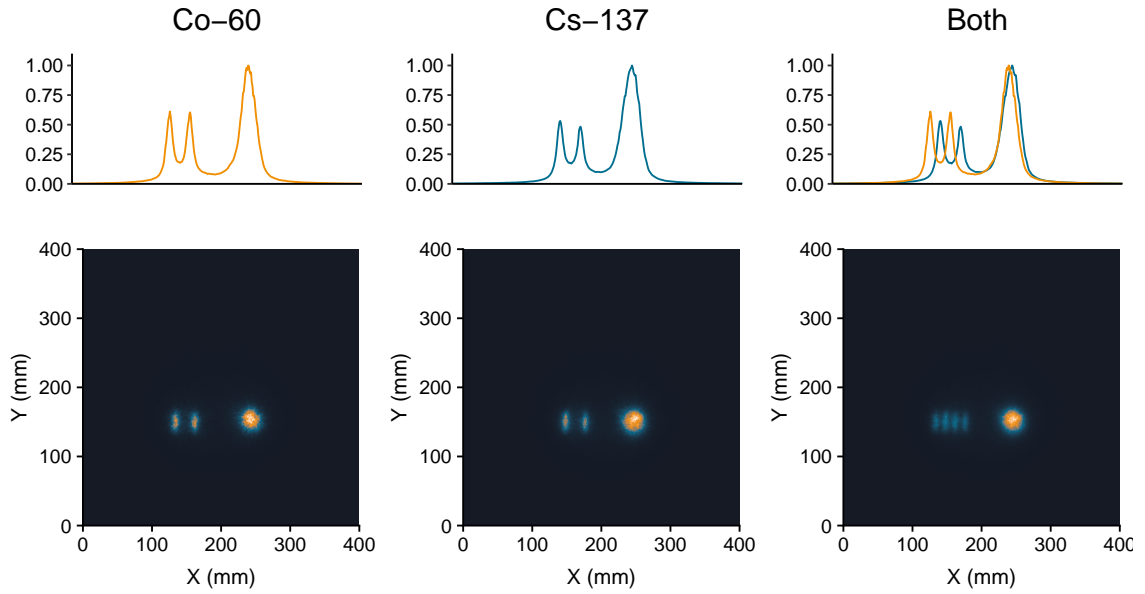
Figure 7.15: Reconstruction of the front phantom compartments with no water filling the perspex box. The simulated phantom was placed 22.8 cm from the detector. Optimal PSA has been applied to the data.

Figure 7.16: Reconstruction of the rear phantom compartments with no water filling the perspex box. The simulated phantom was placed 22.8 cm from the detector. Optimal PSA has been applied to the data.
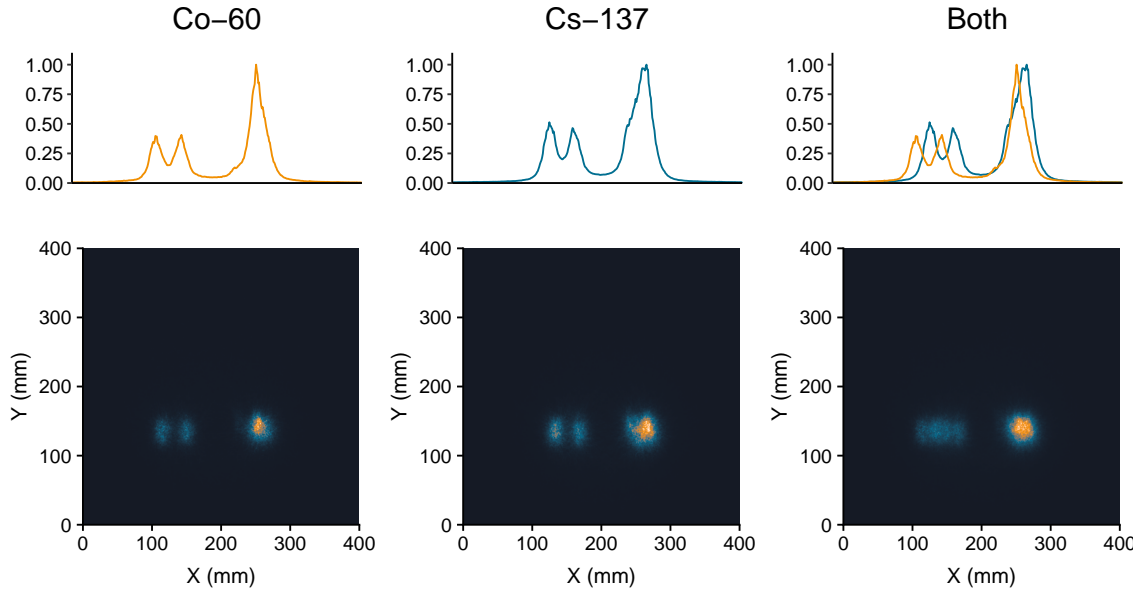
It is not possible to improve the image resolution of the reconstructed slices by applying a high-pass filter. Too little low-frequency noise is present and so the application of a filter results in significant ringing artefacts without improving the image resolution. Individual planchettes are easy to distinguish but, even with this optimal position resolution, the orientation of planchettes in the rear compartment cannot be determined. The Cs-137 and Co-60 profiles are displayed in Figure 7.17 indicating the relative position of each feature.
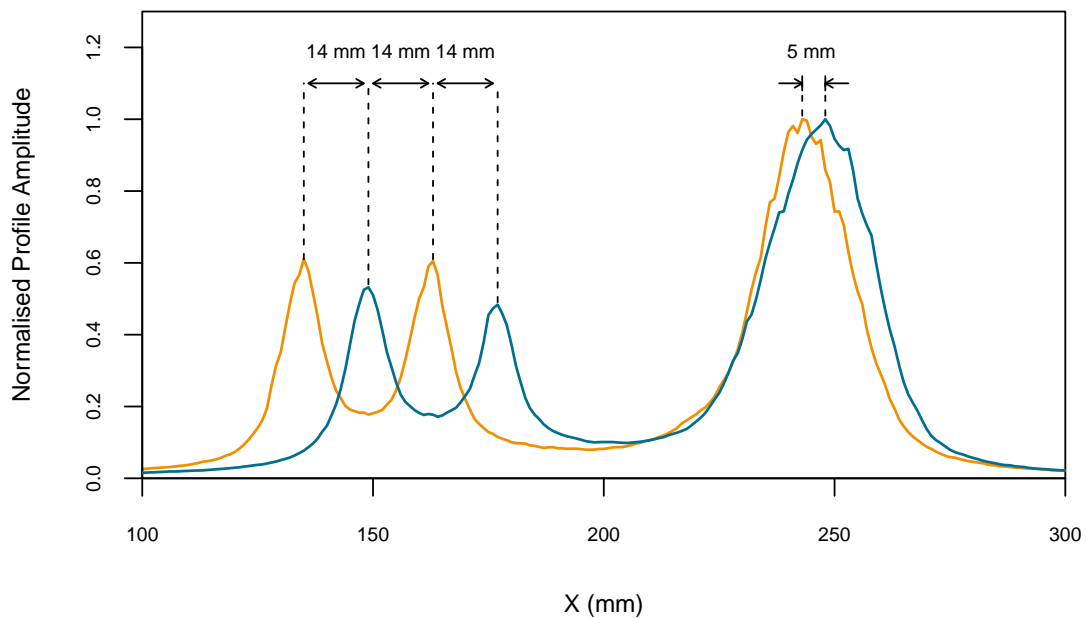

Figure 7.17: Overlaid Cs-137 and Co-60 planchette profiles from the front compartments of the phantom displaying the separation of features. Profiles were produced using simulated data with optimal position resolution applied.

The profiles clearly display the planchettes and each are located in the expected position. The distributions in the front-right compartment do not overlap exactly. This result matches the experimental findings and lends further credence to the simulation's accuracy. The simulation highlights the potential performance of GRI+ once improvements have been made to the algorithms which localise gamma-ray interactions. It indicates that, after future enhancements, GRI+ would be able to correctly identify both the isotope and orientation of any planchettes within the phantom to a degree more than satisfactory for

the application of imaging spent fuel.

A final simulation was created to replicate the current position resolution capabilities of GRI+. To match experimental data, XY-PSA was removed for any strips without neighbours on both sides and no Z-PSA was applied to the scatter detector. This simulation was produced by altering the positional information of the previous simulation data, and therefore the same number of events were used in each. The reconstructed slices from the front and rear tiers are displayed in Figures 7.18 and 7.19 respectively.
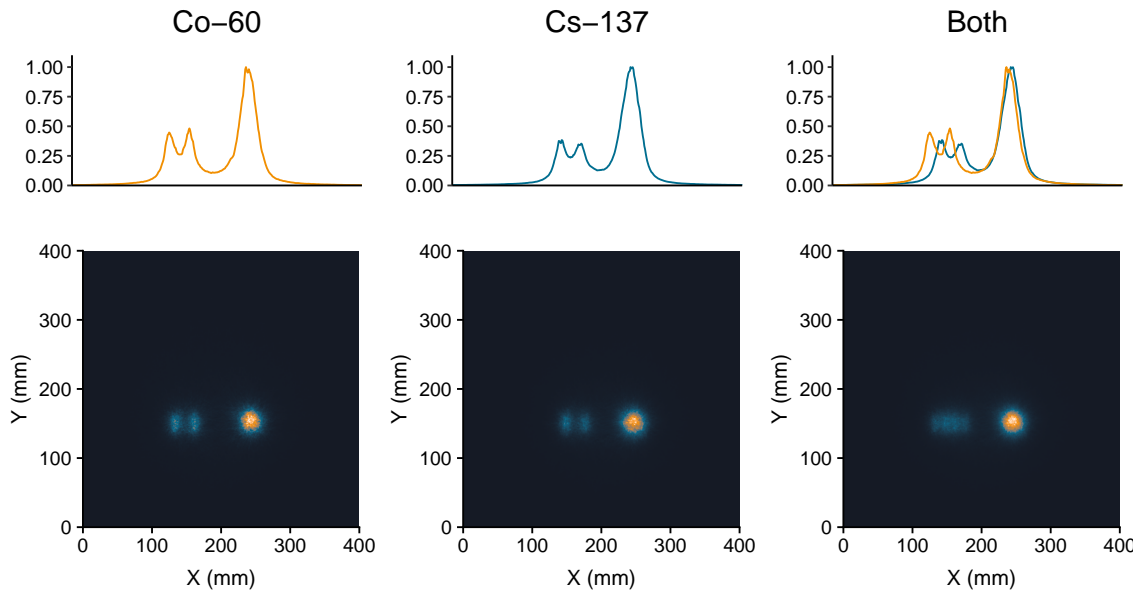

Figure 7.18: Reconstruction of the front phantom compartments with no water filling the perspex box. The simulated phantom was placed 22.8 cm from the detector. Current PSA capabilities have been applied to data.

Figure 7.19: Reconstruction of the rear phantom compartments with no water filling the perspex box. The simulated phantom was placed 22.8 cm from the detector. Current PSA capabilities have been applied to data.
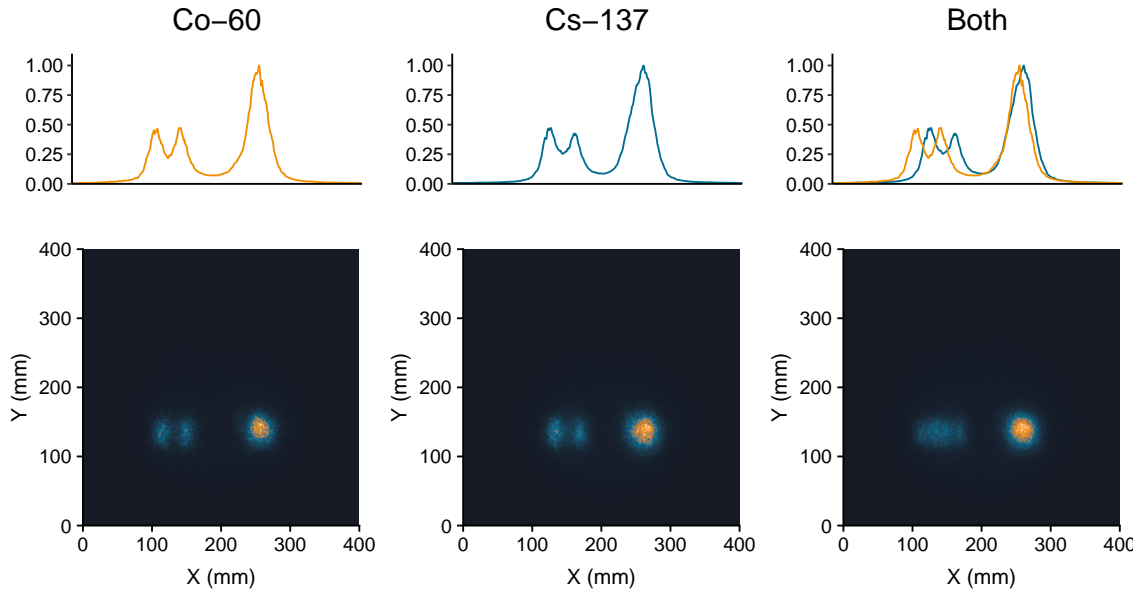
The profiles are less defined than when the position resolution of the detectors were simulated to be optimal, but both the Cs-137 and Co-60 planchettes can be distinguished in the front compartments. The two simulated profiles, along with the experimental dataset they aim to represent, are shown in Figure 7.20. No high-pass filters have been applied to these profiles to avoid any differences caused by poor filter optimisation, and dashed lines are used to represent the known locations of planchette sources. The experimental data differs from the simulated data in both the position of reconstructed planchettes and clarity of the distributions. Although the simulation aims to replicate the experimental performance, in reality, the current PSA methods do not operate perfectly. Z-PSA in the absorber detector is not uniformly sensitive through the entire crystal's volume, experimental errors in the system's set-up may exist, and the detector crystals may not be perfectly centered in the cryostats. These uncertainties, along with the increased background in experimental data from the presence of additional scattering materials in the environment, could explain the differences between the simulated and experimental profiles.
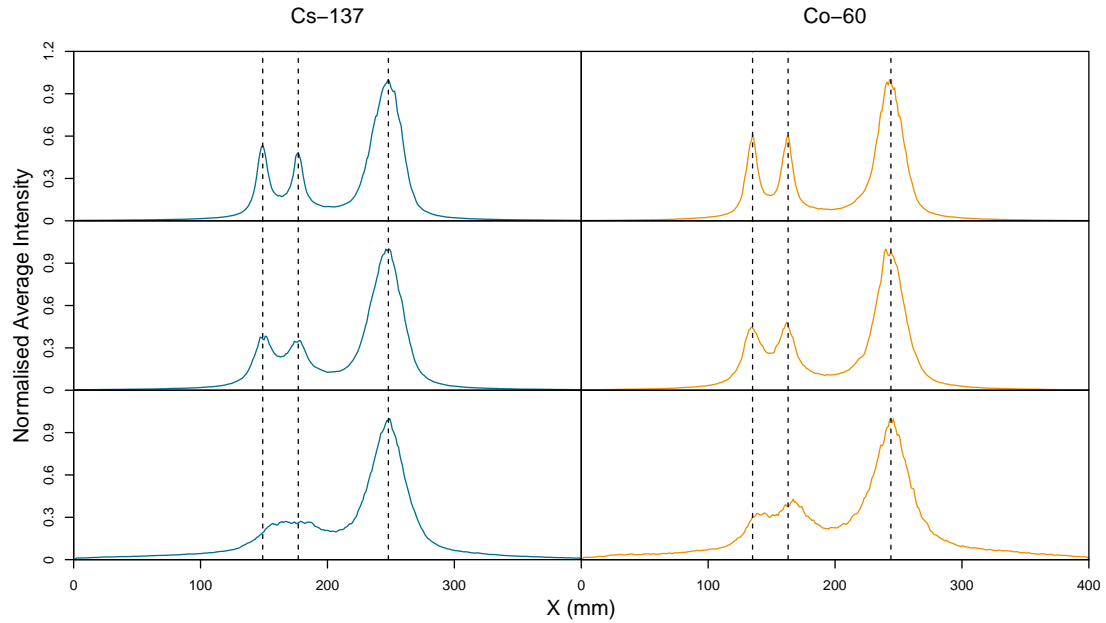
Figure 7.20: Profiles from the front compartments of the phantom, placed 22.8 cm from the detector. Simulated data with optimal position resolution [top], simulated data with current position resolution [middle] and experimental data [bottom]. Dashed lines indicate known planchette positions

Figures 7.21 and 7.22 display the simulated slices after the application of a high-pass filter. Individual planchettes are made more prominent, but notable ringing effects can be seen. These images indicate that, as the resolution of Compton images are improved with future PSA updates, the high-pass filter should become less utilised to avoid increasing noise in the data.

Figure 7.21: Reconstruction of the front phantom compartments with no water filling the perspex box. The simulated phantom was placed 22.8 cm from the detector. Current PSA capabilities and a high-pass filter have been applied to data.
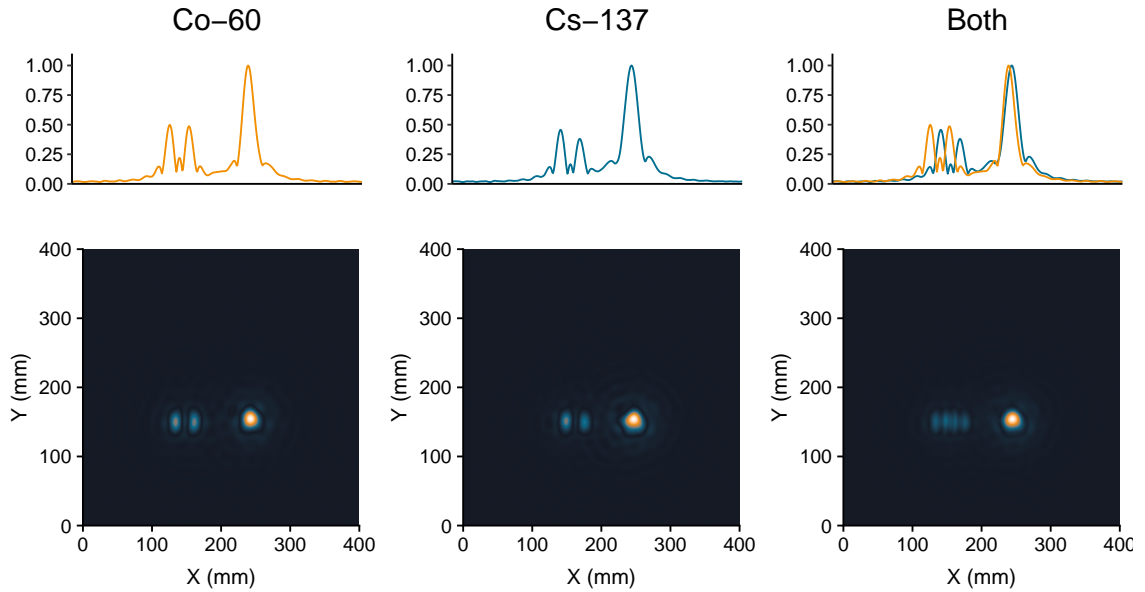

Figure 7.22: Reconstruction of the rear phantom compartments with no water filling the perspex box. The simulated phantom was placed 22.8 cm from the detector. Current PSA capabilities and a high-pass filter have been applied to data.
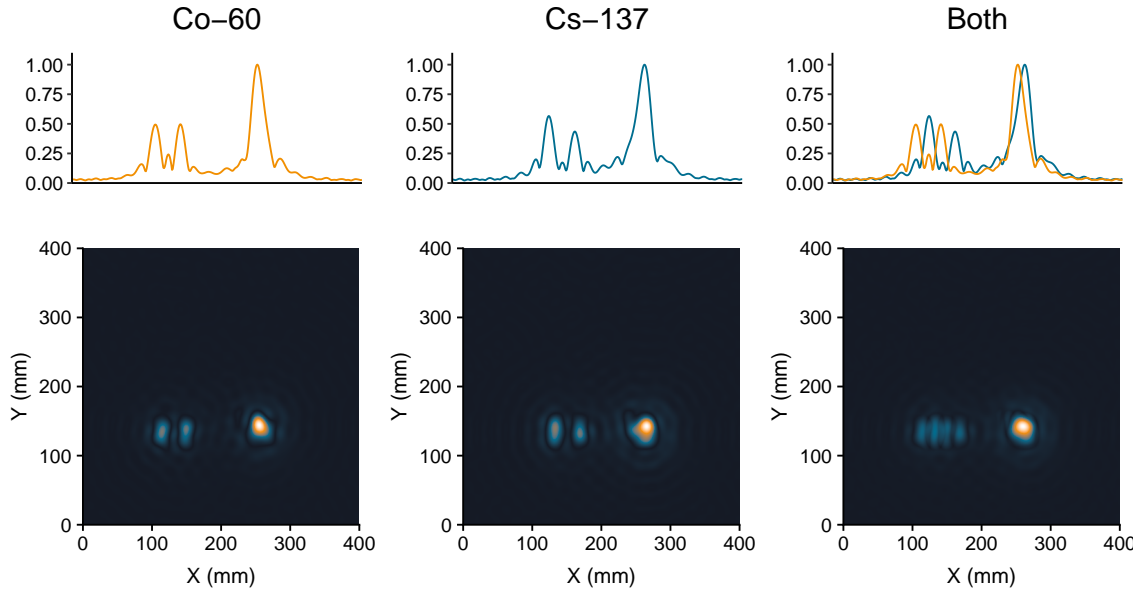
7.6 Overview of Simulated Data

The simulated data highlights the importance of position resolution on the quality of reconstructed images. It indicates that GRI+ should be able to identify the isotope and orientation of any planchettes once improvements are made to the current PSA algorithms. Additionally, the simulation which replicates the current performance of GRI+ displays much clearer profiles than what is found experimentally. This difference is likely to be due to a combination of non-simulated effects:

1. Scattering of gamma rays from non-simulated geometries in the environment, such as the detector frame, walls etc.

2. Uncertainties in the position of elements in the Experimental set-up.

3. A radial distortion effect believed to be absent, or not as prominent, in the simulation [37]. This is likely caused by inaccuracies in the positioning of the cone axis as a result of either the image reconstruction algorithms, physical properties of the detector system or a combination of the two.

Work is currently ongoing to replace the parametric absorber PSA methods with a database algorithm. This shall reduce the size of voxels to $1 \times 1 \times 1$ mm^3 volumes, with a much greater precision than available from the current method. It is believed that the application of this database PSA method should allow the experimental profiles to better match the simulated detector response.

Chapter 8

Conclusion and Future Work

This thesis has described the gamma-ray imaging performance of GRI+, a three tier Compton camera developed at the University of Liverpool, for the application of spent fuel assay. Multiple improvements were implemented to increase the quality of reconstructed images including; the creation of techniques to remove convoluted signals, development of PSA algorithms to improve on the intrinsic position resolution of the detectors and optimisation of current reconstruction algorithms for imaging of a fuel phantom.

The performance of three Z-PSA algorithms, which inform on depth-of-interaction in the absorber detector, were compared. Using a chi-squared minimisation between the average risetimes at each millimetre depth in the detector and the calculated risetimes of a signal from experimental data, the detector volume was partitioned into 20, 1 mm, segments. Combining this method with established XY-PSA algorithms resulted in a 30 % improvement in image resolution for a Cs-137 point source 10 cm from the detector.

The potential use of fold-2 absorber interactions for image reconstruction was investigated. The image resolution was recorded as a function of event order. The highest resolution images were obtained when, below 450 keV deposited in the absorber detector, the position of the lowest energy event constituted the cone axis, with the opposite being true above 450 keV. The resolution of a Cs-137 point source 20 cm from the detector was determined to be 48.45 mm when using only fold-2 absorber events, only a slight degradation in quality when compared to 46.64 mm from fold-1 events only. Including Fold-2 events in the reconstruction process increased the efficiency of GRI+ at 662 keV by 101 %. PSA cannot be applied to fold-2 events. To maintain the highest possible image resolution fold-2 events were mitigated from reconstructed phantom data.

Experimental data were acquired of a fuel phantom — a steel module containing 6 Co-60 and 6 Cs-137 planchette sources — before and after submersion in water. The orientation of planchettes were varied to benchmark the current imaging performance of the Compton camera. Using the many implemented improvements, it was possible to determine the isotope and orientation of planchettes perpendicular to the detector but the system was unable to identify the order of planchettes when placed parallel to the detector, at different stand-off distances. A GEANT4 simulation was created and validated through a comparison with experimental image resolutions. This simulation was designed to inform on the quality of images attainable by GRI+ once planned improvements have been made to the current PSA algorithms. It was found that, by further segmenting both detectors, the quality of images will be more than adequate for the application of spent fuel assay.

From this work several conclusions can be made:

1. PSA was successfully implemented and its inclusion greatly enhances the quality of reconstructed images. These methods should be applied to any future data.

2. When imaging multiple radioactive bodies, individual sources are easier to distinguish when the detector offset is minimised and the separation is maximised.

3. Elongation of reconstructed sources occurs in the direction perpendicular to the face of the detector. This phenomena becomes more potent with increasing offset and results in difficulties when identifying individual sources at different distances.

4. Fold-2 absorber events can be implemented into the image reconstruction process. This will increase the efficiency of GRI+ at the cost of a slight reduction in the resolution of reconstructed images. This event type should not be included when imaging spent fuel as, for these measurements, image quality is more important than efficiency.

5. The MLEM iterative reconstruction algorithm performs best for imaging distributed radioactive bodies when compared to the other algorithms available.

6. GRI+ can identify the isotope and orientation of planchette sources perpendicular to the detector but, using the current iterative reconstruction algorithms, could not determine the ordering of planchettes at different distances.

7. The energy resolution of GRI+ allows for the identification and gating of individual photopeaks from the planchette sources. The increased scattering of outgoing radiation due to water submersion increased photopeak width, but only a slight reduction in image quality was found.

8. A simulation of the Compton camera and phantom were created in GEANT4 and validated. This highlighted the importance of crystal segmentation for high-quality reconstructed images. Future work, focussed on the implementation of database PSA methods to achieve the required detector position resolutions, will greatly improve the resolution of reconstructed images.

8.1   Future Work

This thesis found potential in the application of GRI+ for the imaging of spent fuel but work is still required before the system can reach its full potential. Work is currently being devoted to the creation of database PSA algorithms. This development will localise any absorber detector interactions to $1 \times 1 \times 1$ mm^3 voxels, and shall work for both fold-1 and fold-2 events. The method of usage for fold-2 events discussed in this thesis, section 5.2.5, does not allow for the application of PSA and interactions are placed in the centre of $5 \times 5 \times 20$ mm^3 voxels. Database PSA is able to localise fold-2 interactions. This shall greatly improve the number of reconstructible events without degrading output image quality. Once completed, this technique shall be replicated for the scatter detector, allowing the system to achieve an imaging performance comparable to the GEANT4 simulation, described in section 7.

Another limitation is the performance of the MLEM code for extended sources. Research should be invested in the development of a new, or improved, iterative reconstruction algorithm. The current code iterates extended distributions to a point, no converging criteria is implemented and sensitivity should be adjusted with the changing efficiency of the detector's field of view.

Research must also be carried out to determine detector dead time, an important consideration given the flux of spent fuel at varied positions. Unfortunately, due to a firmware issue in the digital electronics throughout the duration of this PhD, information on the number of counts throughput in the digitisers could not be accessed. For an event

to be reconstructible in GRI+, radiation must interact in at least the first two tiers within a set coincidence window. If the flux of radiation is too high then false coincidences can be made between radiation quanta. This can lead to noise in reconstructed images or, if the flux is high enough, a complete inability to record any real coincident events.

Appendix

Moving Window Deconvolution

The energies deposited in the detector are calculated using a moving window deconvolution (MWD) algorithm built into the CAEN V1724 digitiser cards. This algorithm must be optimised before data acquisition takes place and works in four stages.

1. The first stage takes the preamplifier charge pulse, described in section 4.2. This pulse is characterised by its sharp risetime and long decay tail.

2. A correction is applied to the pulse to remove the signal's decay tail, converting it into a step function. The small variance in height for this step function accounts for the higher precision of the MWD algorithm relative to the BLD method.

3. Differentiation of this step function after a user defined time (Trapezoid Flat Top) is the third stage, producing a square pulse.

4. A moving average of a predefined width is then applied to this square pulse to achieve the trapezoid shape. This averaging filter removes any of the minute fluctuations observable in the previous stage. The final energy of an event is determined from the height of the flat top of the trapezoid pulse.
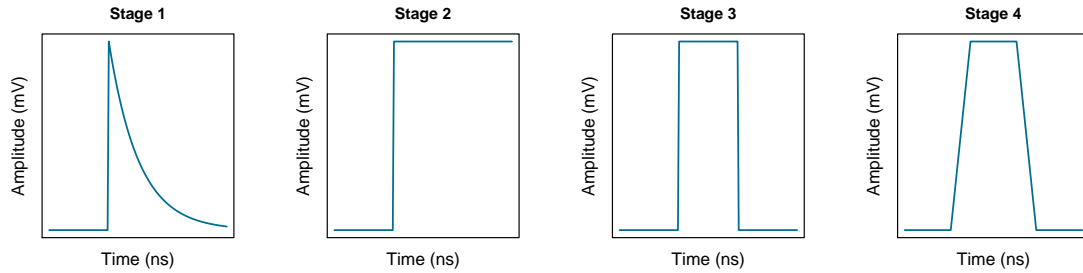
Figure 8.1: Illustration of the main four stages of the MWD algorithm.

The MWD algorithm is used to calculate the energy of events in the system but is avoided when determining the fold as even transient charges will be identified as having some energy by this algorithm. Instead, the raw pulses are analysed and those which are determined to be real events by the BLD algorithm have their energies calculated using the MWD algorithm. Multiple parameters must be set to optimise the performance of the algorithm. Those selected were found to provide the best energy resolutions for the detectors whilst also maintaining a high efficiency, and are displayed in Table 8.1.

	Scatter Parameters (μs)		Absorber Parameters (μs)		Coaxial Parameters (μs)
	AC	DC	AC	DC	-
Decay Time	50	50	50	50	50
Input Rise Time	0.025	0.025	0.025	0.025	0.025
Trapezoid Flat Top	2.5	2.5	2.5	2.5	2.5
Trapezoid Rise Time	5.5	5.5	5.5	5.5	5.5
Pretrigger Window	7.5	7.5	7.5	7.5	7.5

Table 8.1: Optimised MWD parameters for the GRI+ system.

Optimising Event Veto Criteria

The shape of signals are analysed to estimate the location an interaction took place within the volume of the detector. Not all signals are representative of charge carrier transport through the crystal. More than one interaction occurring in a detector segment results in a discontinuity in the rising edge of a signal. These signals must be removed in order to preserve the performance of implemented PSA algorithms. A detailed explanation of this process is described in section 4.6.

This phenomena is identified by differentiating the signals, and then analysing the number of peaks in the subsequent response. An example of a differentiated signal is displayed in Figure 8.2. It is difficult to determine the number of peaks due to the highly fluctuating baseline of the differentiated signals. Instead a threshold, set as a fraction of the signal's maximum height, is applied and the number of peaks above this threshold is determined, this is displayed as a dashed line on Figure 8.2.
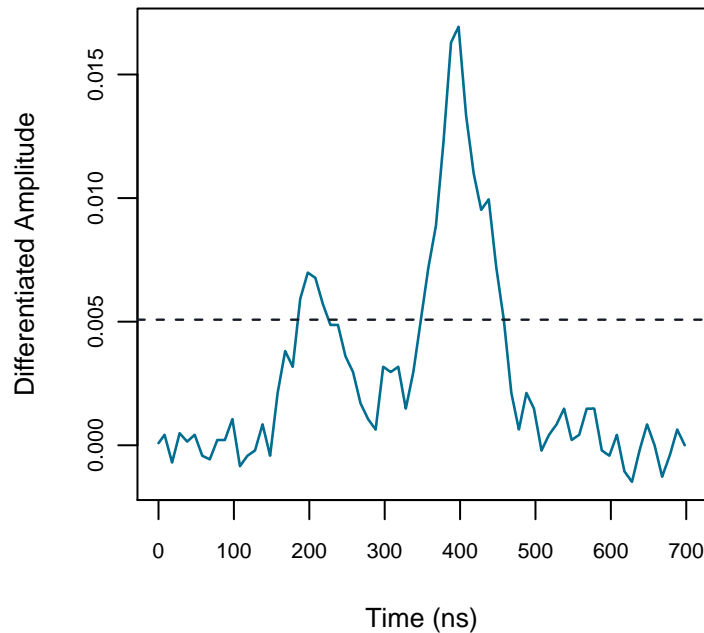

Figure 8.2: Differentiated pulse displaying a discontinuity in the rising edge. The veto threshold is placed at a value of 35 % the maximum height of the distribution.

The differentiated signal is stored in an array. The index of elements above the threshold are recorded and the differences between indices are used to determine the number of peaks.

If the threshold is too high (the maximum height of the signal) then almost all signals are seen to contain a single peak. If the threshold is too low then the noisy baseline shall be seen as multiple peaks and few events will pass this gate. As the threshold passes below the baseline more events shall be identified fold-1 as the entire signal lies above the threshold. The relationship between the threshold and fraction of events determined to be usable by PSA is displayed in Figure 8.3.
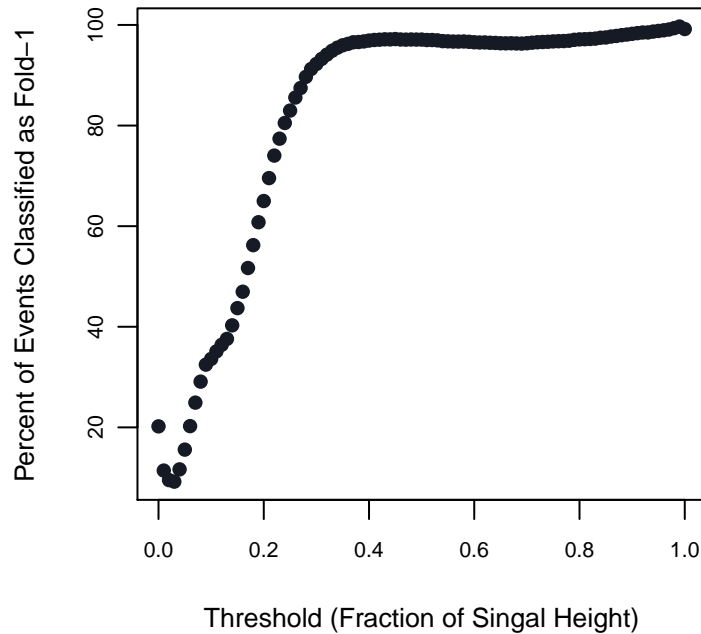

Figure 8.3: Relationship between chosen threshold and percentage of events determined to be usable by PSA.

Below 40 % of the maximum pulse height, the rate at which the percentage of usable fold-1 events decreases changes. The optimum value lies in this range. The final threshold was determined through a systematic variance to be 35 %. A set of pulses cleaned using this technique is displayed in Figure 8.4.
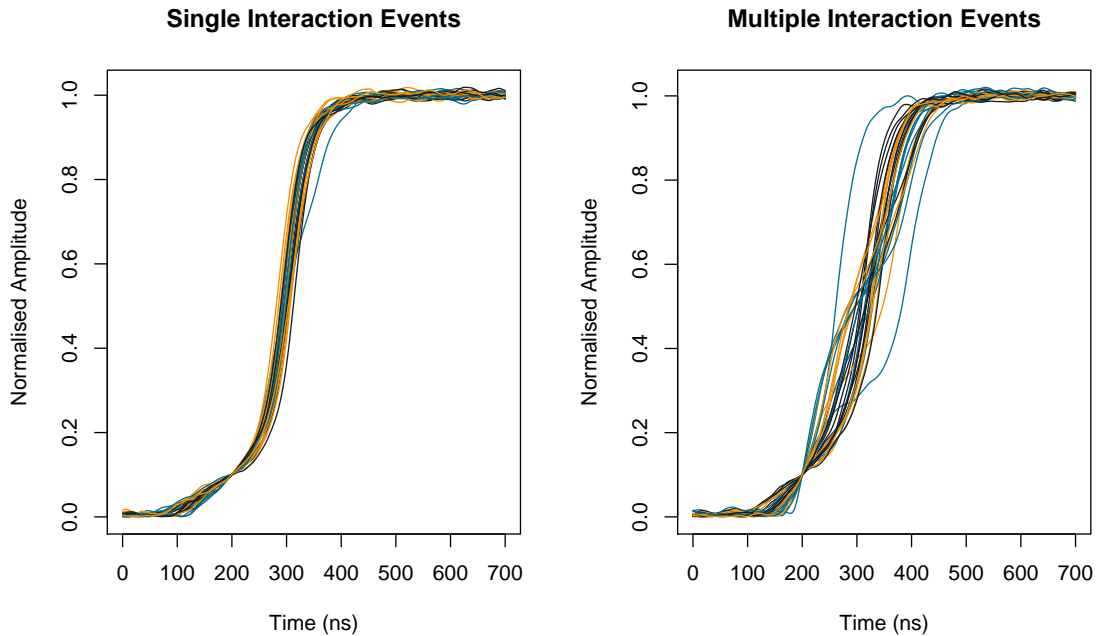
Figure 8.4: Events with one [left] and two [right] peaks in the differentiated spectra. Calculated using a threshold of 35 %.

This methodology is described for events which deposit 662 keV in the absorber detector. Events which deposit less energy shall show greater relative baseline fluctuation and the threshold will have to be optimised anew.

Decision on Channel Selection

A limited number of input channels are available in the V1495 CAEN global clock card. To accommodate this, three channels of GRI+ must be disconnected from the DAQ system. Figure 8.5 is a barplot displaying the percentage of reconstructible events lost when each individual channel of GRI+ is disconnected, produced from the GEANT4 simulation. Only the scatter channels are displayed, greater losses in efficiency were found for absorber channels. Channels selected for removal are highlighted in orange.
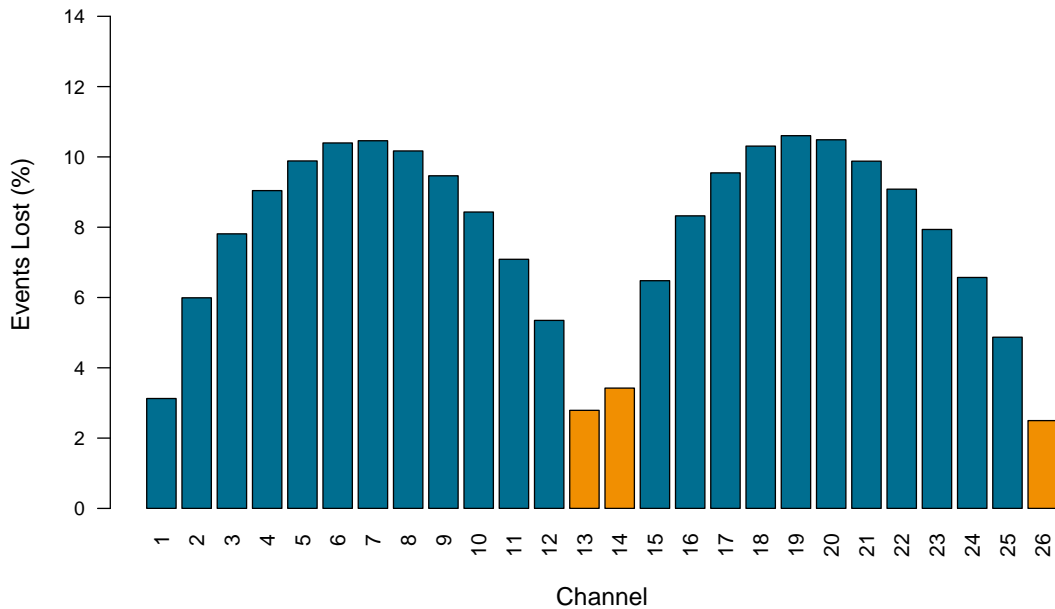
Figure 8.5: Percentage of reconstructible imaging events lost due to the removal of a channel from processing. Figure was produced using the GENAT4 simulation. Channels selected for removal are highlighted in orange.

Combining Compton Images with LIDAR point clouds

A method of combining reconstructed Compton data and a LIDAR (light detection And ranging) point cloud was developed for intuitive source visualisation. It was not included in the main bulk of the thesis because the perspex box encasing the phantom reflects LIDAR beams. However, it is of use in other imaging applications. The area surrounding the Compton camera was mapped using a Faro X330 LIDAR system [40]. Reference objects, in the form of spheres and square card were placed around the system and used to stitch multiple scans together. The resulting point cloud was displayed in the FARO SCENE software where a coordinate system was developed from identifying the position of several collinear points. Simultaneously, data was acquired by GRI+ of a Cs-137 point source 10 cm from the front of the detector. The analytical code was used to reconstruct slices every millimetre up to 20 cm from the detector, and the maximum Compton overlap from each slice was stored. These values are displayed in Figure 8.6.
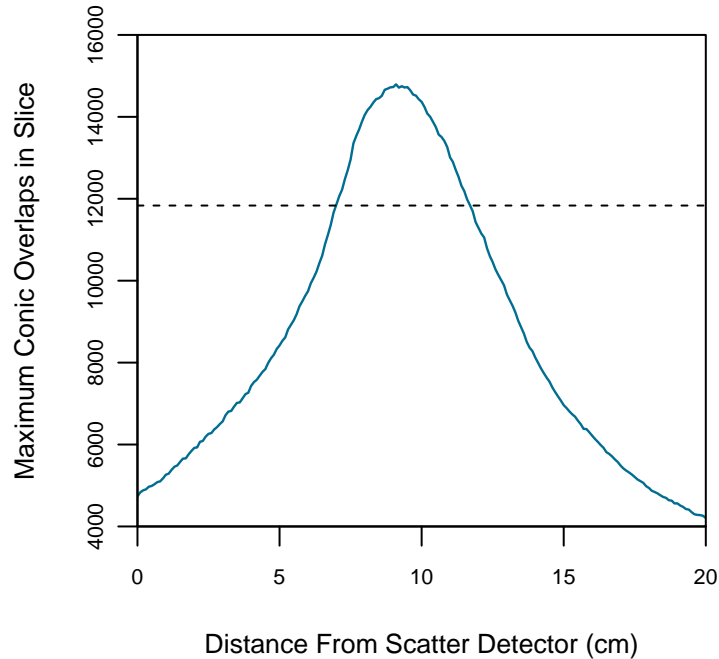
Figure 8.6: Maximum conic overlaps from several reconstructed Cs-137 slices over a range of 20 cm from the detector. A threshold is placed on the maximum number of overlaps, displayed as a dashed horizontal line.

The maximum overlap values were used to select a threshold, displayed as a horizontal line in Figure 8.6, below which the overlap points were removed. Typically, a threshold of 80% of the maximum Compton overlap value is chosen, but this is varied depending on the degree of statistical fluctuation in the distribution. The individual slices were combined into a 3D matrix of points which could be imported into the SCENE software as a text file. The 3D point cloud representing the Cs-137 point source, 10 cm from the detector, is shown in Figure 8.7 before and after the application of the threshold.
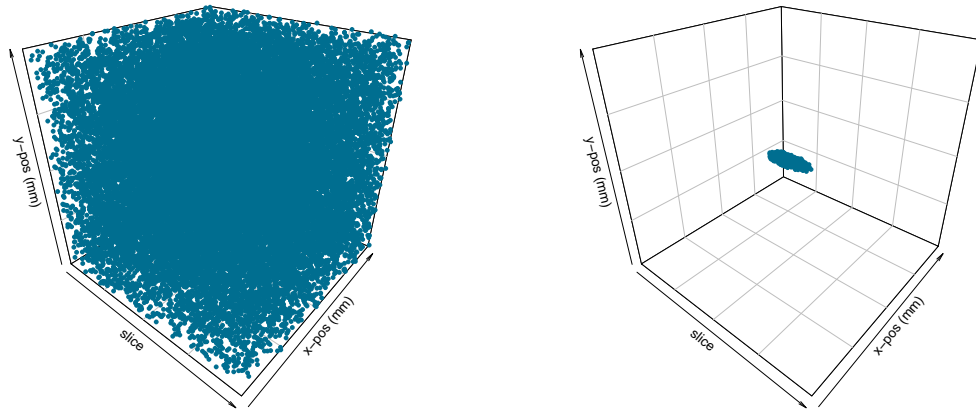
Figure 8.7: Point cloud representation of the Cs-137 point source before [left] and after [right] a threshold is applied to the maximum Compton overlap value.

Once the source point cloud was imported, the SCENE software allowed for the environment to be explored in order to obtain the best view of the radioactive emitter. An example of the Cs-137 point source within the SCENE software is displayed in Figure 8.8.
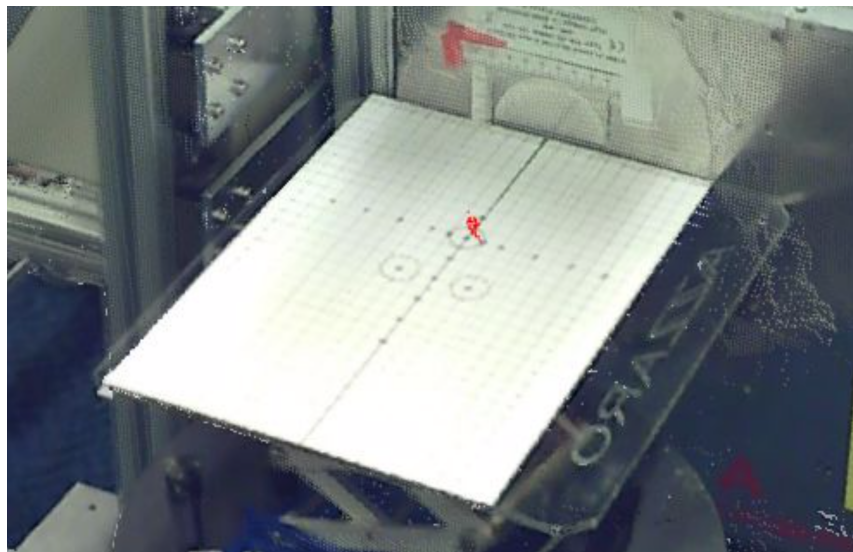

Figure 8.8: Combined LIDAR and Compton reconstruction of a Cs-137 point source [red].

This methodology worked well for near-field point sources, but more research must be conducted into threshold selection and its impact upon the combined images. The elongation of point sources, discussed in section 5.2.3, also greatly impacts the final result, making

this approach best suited for stand-off distances less than ~ 15 cm from the detector. I believe future work should be concentrated on the projection of cones into the environmental point cloud, creating filled contour plots on the surfaces of any intersecting objects. This method avoids the effects of source elongation and has displayed great promise when implemented [41].
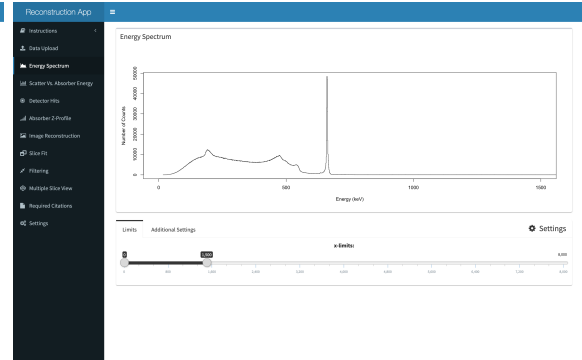
R GUI Imaging App

The GRI+ Compton camera is used by a number of people of different skill levels. To ensure the system is accessible to everyone, an intuitive application was developed to reconstruct processed data. The stand-alone application was developed in R, using the shiny library [42], and distributed using chromium and electron, as described on the Columbus-Collaboratory GitHub page [43]. The actions the application can perform are:

- Display energy spectra

- Display share of energy between the detectors

- Analyse interaction positions

- Reconstruct data using the analytical of SOE codes
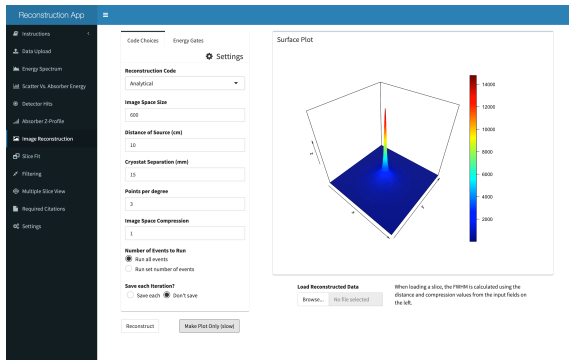
- Apply high-pass and low-pass filters to the data

Several screenshots from the application are displayed in Figure 8.9.
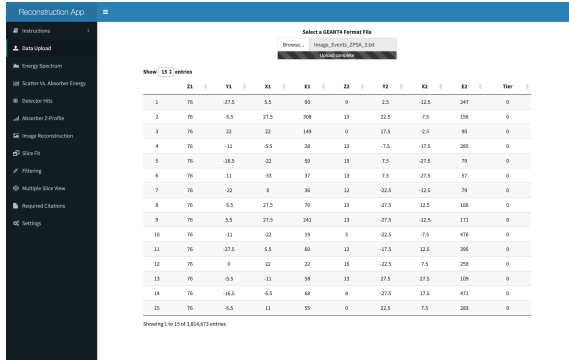
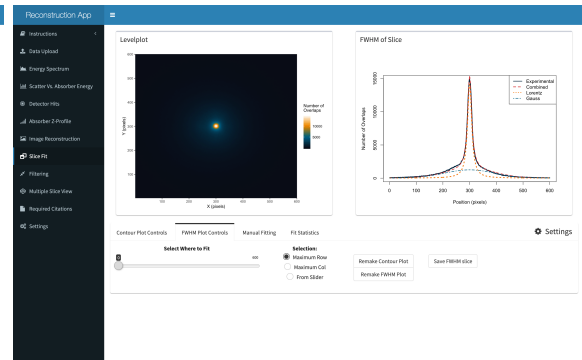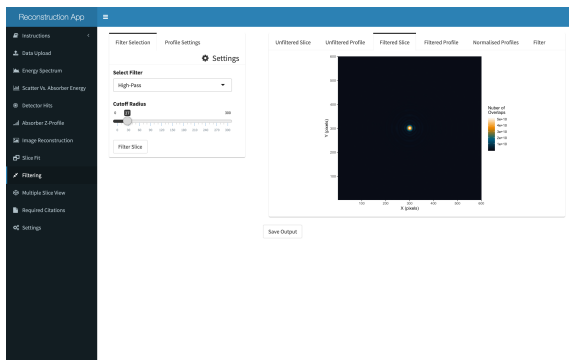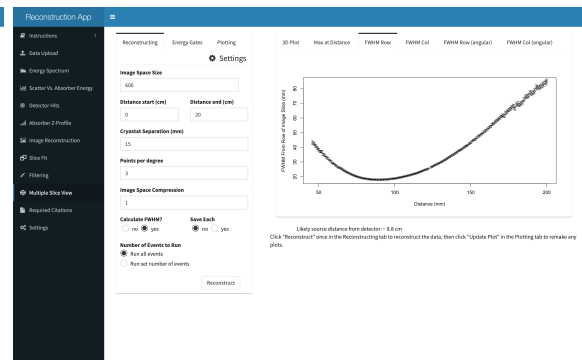**(a)** Data input

(b) Energy spectra

(c) Reconstruction options

(d) Reconstructed image

(e) FFT filtering

(f) Multiple slice reconstruction

Figure 8.9: Several screenshots from different pages of the imaging app.

Bibliography

[1] United Nations Treaty. Treaty on the non-proliferation of nuclear weapons (npt), 1968, available from: https://www.un.org/disarmament/wmd/nuclear/npt/.

[2] INTERNATIONAL ATOMIC ENERGY AGENCY. *Safeguards Techniques and Equipment:*. Number 1 (Rev. 2) in International Nuclear Verification Series. INTERNATIONAL ATOMIC ENERGY AGENCY, Vienna, 2011.

[3] Kenneth S Krane. *Introductory nuclear physics*, volume 465.

[4] Glenn F Knoll. *Radiation detection and measurement*. John Wiley & Sons, 2010.

[5] Oskar Klein and Yoshio Nishina. The scattering of light by free electrons according to dirac's new relativistic dynamics. *Nature*, 122(3072):398, 1928.

[6] William Shockley. Currents to conductors induced by a moving point charge. *Journal of applied physics*, 9(10):635–636, 1938.

[7] Simon Ramo. Currents induced by electron motion. *Proceedings of the IRE*, 27(9):584–585, 1939.

[8] ORTEC. *Preamplifier Introduction, charge sensitive preamplifiers*, Available at `https://www.ortec-online.com/-/media/ametekortec/other/preamplifier-introduction.pdf?la=en`.

[9] Mohammad Nakhostin. *Signal processing for radiation detectors*. John Wiley & Sons, 2017.

[10] LE Peterson and RL Howard. Gamma-ray astronomy in space in the 50-kev to 3-mev region. *IRE Transactions on Nuclear Science*, 8(4):21–29, 1961.

[11] Manbir Singh. An electronically collimated gamma camera for single photon emission computed tomography. part i: Theoretical considerations and design criteria. *Medical Physics*, 10(4):421–427, 1983.

[12] Manbir Singh and David Doria. An electronically collimated gamma camera for single photon emission computed tomography. part ii: Image reconstruction and preliminary experimental measurements. *Medical Physics*, 10(4):428–435, 1983.

[13] Nicolas Dedek, Robert D Speller, Paul Spendley, and Julie A Horrocks. Performance evaluation of 98 czt sensors for their use in gamma-ray imaging. *IEEE Transactions on Nuclear Science*, 55(5):2689–2697, 2008.

[14] Atsushi Harayama, Yuto Ichinohe, Hirokazu Odaka, Shin Watanabe, Tadayuki Takahashi, Hiroyasu Tajima, Kei Genba, Daisuke Matsuura, Hiroshi Ikebuchi, Yoshikatsu Kuroda, et al. A portable si/cdte compton camera and its applications to the visualization of radioactive substances. *Nuclear Instruments and Methods in Physics Research Section A: Accelerators, Spectrometers, Detectors and Associated Equipment*, 787:207–211, 2015.

[15] Gary W Phillips. Gamma-ray imaging with compton cameras. *Nuclear Instruments and Methods in Physics Research Section B: Beam Interactions with Materials and Atoms*, 99(1-4):674–677, 1995.

[16] LJ Harkness, DS Judson, AJ Boston, HC Boston, JR Cresswell, PJ Nolan, A Sweeney, J Beau, M Lampert, B Pirard, et al. Characterisation of a si (li) orthogonal-strip detector. *Nuclear Instruments and Methods in Physics Research Section A: Accelerators, Spectrometers, Detectors and Associated Equipment*, 726:52–59, 2013.

[17] MIRION. *Preamplifier Introduction, charge sensitive preamplifiers.* MIRION, Available at `https://www.ortec-online.com/-/media/ametekortec/other/preamplifier-introduction.pdf?la=en`.

[18] CAEN. *CAEN V1724 Digitiser Information site.* CAEN, Available at, `http://www.caen.it/csite/CaenProd.jsp?parent=11&idmod=483`.

[19] VFE Pucknell. The midas multi instance data acquisition system, 1995.

[20] Valentin T Jordanov, Glenn F Knoll, Alan C Huber, and John A Pantazis. Digital techniques for real-time pulse shaping in radiation measurements. *Nuclear Instruments and Methods in Physics Research Section A: Accelerators, Spectrometers, Detectors and Associated Equipment*, 353(1-3):261–264, 1994.

[21] John Cresswell and Janet Sampson. Mtsort language-edoc033. 2010.

[22] Brian Kernighan and Dennis M Ritchie. *The C programming language*. Prentice hall, 2017.

[23] Reynold James Cooper. *Performance of the SmartPET Positron Emission Tomography System for Small Animal Imaging*. PhD thesis, University of Liverpool, 2007.

[24] Dr Ellis Rintoul. Side scan of absorber detector - private communication.

[25] RJ Cooper, AJ Boston, HC Boston, JR Cresswell, AN Grint, LJ Harkness, PJ Nolan, DC Oxley, DP Scraggs, I Lazarus, et al. Charge collection performance of a segmented planar high-purity germanium detector. *Nuclear Instruments and Methods in Physics Research Section A: Accelerators, Spectrometers, Detectors and Associated Equipment*, 595(2):401–409, 2008.

[26] Guido Van Rossum et al. Python programming language. In *USENIX Annual Technical Conference*, volume 41, page 36, 2007.

[27] R Core Team. *R: A Language and Environment for Statistical Computing*. R Foundation for Statistical Computing, Vienna, Austria, 2016.

[28] Stefan Behnel, Robert Bradshaw, Craig Citro, Lisandro Dalcin, Dag Sverre Seljebotn, and Kurt Smith. Cython: The best of both worlds. *Computing in Science & Engineering*, 13(2):31–39, 2011.

[29] D.S. Judson, L.J. Harkness-Brennan, A.J. Boston, H.C. Boston, J. Dormand, S.J. Colosimo, J.R. Cresswell, P.J. Nolan, A.Patel, and C. Unsworth. A novel, computationally lightweight, compton imaging algorithm. *JINST*, Awaiting publication.

[30] Rene Brun and Fons Rademakers. Root—an object oriented data analysis framework. *Nuclear Instruments and Methods in Physics Research Section A: Accelerators, Spectrometers, Detectors and Associated Equipment*, 389(1-2):81–86, 1997.

[31] Mlem iterative reconstruction code - private communication.

[32] Timur V Elzhov, Katharine M Mullen, A Spiess, and B Bolker. R interface to the levenberg-marquardt nonlinear least-squares algorithm found in minpack. *Plus Support for Bounds*, 2010.

[33] Voichiţa Maxim. Filtered backprojection reconstruction and redundancy in compton camera imaging. *IEEE Transactions on Image Processing*, 23(1):332–341, 2014.

[34] Christofer Willman, Ane Håkansson, Otasowie Osifo, Anders Bäcklin, and Staffan Jacobsson Svärd. Nondestructive assay of spent nuclear fuel with gamma-ray spectroscopy. *Annals of Nuclear Energy*, 33(5):427–438, 2006.

[35] Antonio Dambrosio, Marek Ruščák, Guido Mazzini, and Alis Musa. Neutronic analysis of the lvr-15 research reactor using the parcs code. *Annals of Nuclear Energy*, 117:145–154, 2018.

[36] Helen MO'D Parker and Malcolm J Joyce. The use of ionising radiation to image nuclear fuel: A review. *Progress in Nuclear Energy*, 85:297–318, 2015.

[37] Jamie Dormand. *The proof of concept of a fused radiometric and optical stereoscopic imaging system*. PhD thesis, University of Liverpool, 2014.

[38] Bjarne Stroustrup. *The C++ programming language*. Pearson Education India, 2000.

[39] Sea Agostinelli, John Allison, K al Amako, John Apostolakis, H Araujo, P Arce, M Asai, D Axen, S Banerjee, G 2 Barrand, et al. Geant4—a simulation toolkit. *Nuclear instruments and methods in physics research section A: Accelerators, Spectrometers, Detectors and Associated Equipment*, 506(3):250–303, 2003.

[40] Faro x330 lidar scanner info. page: http://www.faro.com/en-us/products/3d-surveying/faro-focus3d/overview, December 2016.

[41] Andrew Haefner, Ross Barnowski, Paul Luke, Mark Amman, and Kai Vetter. Handheld real-time volumetric 3-d gamma-ray imaging. *Nuclear Instruments and Methods in Physics Research Section A: Accelerators, Spectrometers, Detectors and Associated Equipment*, 857:42–49, 2017.

[42] Winston Chang, Joe Cheng, JJ Allaire, Yihui Xie, and Jonathan McPherson. *shiny: Web Application Framework for R*, 2018. R package version 1.2.0.

[43] Collumbuscollaboratory github project: https://github.com/columbuscollaboratory/electron-quick-start, 2019.